THE COLLOIDAL GLASS TRANSITION UNDER CONFINEMENT

A DISSERTATION

SUBMITTED TO THE FACULTY OF THE GRADUATE SCHOOL

OF THE UNIVERSITY OF MINNESOTA

BY

BO ZHANG

IN PARTIAL FULFILLMENT OF THE REQUIREMENTS

FOR THE DEGREE OF

DOCTOR OF PHILOSOPHY

ADVISOR: XIANG CHENG, PH.D.

MAY, 2018

Acknowledgements

Firstly, I would like to express my sincere gratitude to my advisor Prof. Xiang Cheng for the continuous support of my PhD study and for his patience, motivation, and immense knowledge. I especially appreciate his help on the development of my writing and communication skills. His guidance helps me during all the time of research and writing of this thesis.

Besides my advisor, I would like to thank Prof. Chris Macosko, Prof. Lorraine Francis, Prof. Dave Odde, Prof. Kevin Dorfman, and Prof. Eric Weeks for their insightful discussions and also for their support and encouragement. In particular, I am grateful to Prof. Huan Pang for enlightening me the first glance of research.

My sincere thanks also goes to my fellow labmates Dr. Yi Peng, Dr. Bai Lian, Dr. Shuo Guo, Dr. Liangliang Gu, Dr. Kyle Welch, Dr. Leonardo Gordillo, Dr. Devranjan Samanta, Yu Abe, Seunghwan Shin, Truong Pham, Zhengyang Liu, Ou Yang, Qianyun Zhang, Runchen Zhao, and Yangming Kou for the stimulating discussions and for all the nice memories we have had in the past years. I also thank three undergraduates who worked with me: Wei Seng Pui, Zhisen Chong, and Feifan Du.

I would also like to show my gratitude to all other professors and staff in Department of Chemical Engineering and Materials Science. I would also like to thank the developers who developed this LaTex version of thesis template, which saves me from tedious typesetting.

I thank the ACS Petroleum Research Fund (Grant No. 54168-DNI9) and the NSF MRSEC Program (Grant No. DMR-1420013) for the financial support of my PhD study.

Last but not least, I would like to thank my beloved family and friends, especially my mom and my girlfriend for supporting me spiritually all these years.

Dedication

To my beloved family for supporting me over the years.

Abstract

Understanding the nature of the glass transition is one of the most challenging problems in condensed matter physics. Although ubiquitous and technically important, glasses still elude a universally accepted theoretical description. Here, we use colloidal particles as hard-sphere models and experimentally study particle dynamics of colloidal suspensions under different confinements near the glass transition.

In three dimension (3D), we design a colloidal system, where particles are confined inside spherical cavities with an amorphous layer of particles pinned at the boundary. Using this novel system, we capture the amorphous-order particle clusters proposed in the framework of the random first-order transition (RFOT) theory and demonstrate the development of a static correlation near the glass transition. Moreover, by investigating the dynamics of spherically confined samples, we reveal a profound influence of the static correlation on the relaxation of colloidal liquids. In analogy to glass-forming liquids with randomly pinned particles, we propose a simple relation for the change of configurational entropy of confined colloidal liquids, which quantitatively explains our experimental findings and illustrates a divergent static length scale during the colloidal glass transition.

In two dimension (2D), we prepare quasi-2D confined colloidal liquids with optical tweezers. We confirm the existence of a divergent static length in quasi-2D liquids. We further use the confinement as a tool to probe the Mermin-Wagner long-wavelength fluctuations. We find that the fluctuations have a logarithmic dependence on the system size in quasi-2D when the system approaches to the glass transition. Ellipsoidal and rodlike particles are also used to directly compare the translational and rotational dynamics. We show a decoupling between translational and rotational dynamics and the

decoupling is not affected by the confinement. What's more, constant values of critical volume fractions are observed regardless of types of particle aspect ratios, measurement methods, fitting functions, and values of structural factors.

Lastly, we have also conduct an experimental study on the 1D dynamic self-assembly of charged colloidal particles in microfluidic flows. Using high-speed confocal microscopy, we systematically investigate the influence of flow rates, electrostatics and particle polydispersity on the observed string structures. By studying the detailed dynamics of stable flow-driven particle pairs, we quantitatively characterize interparticle interactions. Based on the results, we construct a simple model that explains the intriguing non-equilibrium self-assembly process. Our study shows that the colloidal strings arise from a delicate balance between attractive hydrodynamic coupling and repulsive electrostatic interaction between particles. Finally, we demonstrate that, with the assistance of transverse electric fields, a similar mechanism also leads to the formation of 2D colloidal walls.

Our study provides key experimental evidences to support the development of RFOT theory to better understand the glass transition in both 3D and 2D. The fundamental differences of particle dynamics between 3D and 2D are also studied. In addition to providing experimental results for assessing general glass transition theories and particle self-assembly, our studies also provide new insights into the dynamics of confined colloidal liquids and may shed light on the behavior of atomic/molecular liquids under nano-confinements.

Contents

List of Figures

Chapter 1

Introduction

- Chapter 1 briefly provides the physics background of the glass transition.
- Chapter 2 concisely presents the experimental background of important techniques used in this thesis.
- Chapter 3 studies the colloidal glass transition under 3D confinement. Large portions of this chapter have been published in Ref.[1] (APS copyright).
- Chapter 4 shows the colloidal glass transition under 2D confinement. This work is under preparation for submission.
- Chapter 5 presents an additional research of the particle self-assembly in a simple fluid flow. This work is conducted with a close collaboration with Yu Abe and some other researchers. Large portions of this chapter have been published in Ref.[2]. Yu Abe, Bo Zhang, Xiang Cheng and Lorraine F Francis conceived the experiment. Yu Abe and Bo Zhang built the experimental setup and performed the experiment. Bo Zhang provided IDL algorithm for data analysis. Yu Abe and Bo Zhang analyzed data. All authors contributed to the model development and writing of the manuscript.

- Chapter 6 summarizes the whole work and discusses briefly about the future research directions.
- Appendix A concisely documents different particle synthesis methods used in this thesis or other unpublished work.
- Appendix B briefly discusses fluorescent labelling methods of the colloids synthesized in Appendix A.

1.1 Glass and Glass Transition

1.1.1 The Glass Transition

Glasses are disordered metastable materials that lack the periodicity of crystals but have mechanically properties like solids [3]. Silicate glass is one of the best-known examples of such amorphous solids. Composed mostly of sand, lime and soda, the transparent window glass has a typical tensile strength of 41 to 180 Mpa, which makes it a very popular architectural material [4, 5, 6]. Besides the window glass, optical fibers, many engineering plastics, and some metallic materials are glasses [7, 8, 9]. Historically, glasses are also one of the oldest materials used by human society. Stone-age humans are believed to use cutting tools and arrowheads made of a natural glass called obsidian. Manufactured glasses have also been found in ancient Egyptian tombs [10].

Even though glasses are known by human for a very long time and are widely used in our daily lives and industries, the quantitatively understanding of the glass and the glass transition is still one of the major scientific challenges in condensed matter physics and materials science [4, 11, 12, 13, 14]. Fig. 1.1 shows a schematic representation of the specific volume or enthalpy as a function of temperature for a liquid at a constant pressure [4, 11, 12]. Upon cooling from a high temperature to the melting temperature T_m, molecular motion slows down and molecules reorganize into a ordered crystalline

structure. However, if the liquid is cooled sufficiently fast, the crystallization can be avoided and the liquid becomes a supercooled liquid [11, 15, 16]. The molecular dynamics further slow down with the decreasing temperature and eventually the supercooled liquid vitrifies into a glass. The intersection of specific volume or enthalpy of the supercooled liquid and that of the vitrified glass versus temperature gives one of the widely accepted definitions of the glass transition temperature T_g [4, 11, 12]. Depending on the cooling rate, the glass transition temperature temperature T_g may shift to lower (slower cooling rate) or higher (faster cooling rate) temperature.

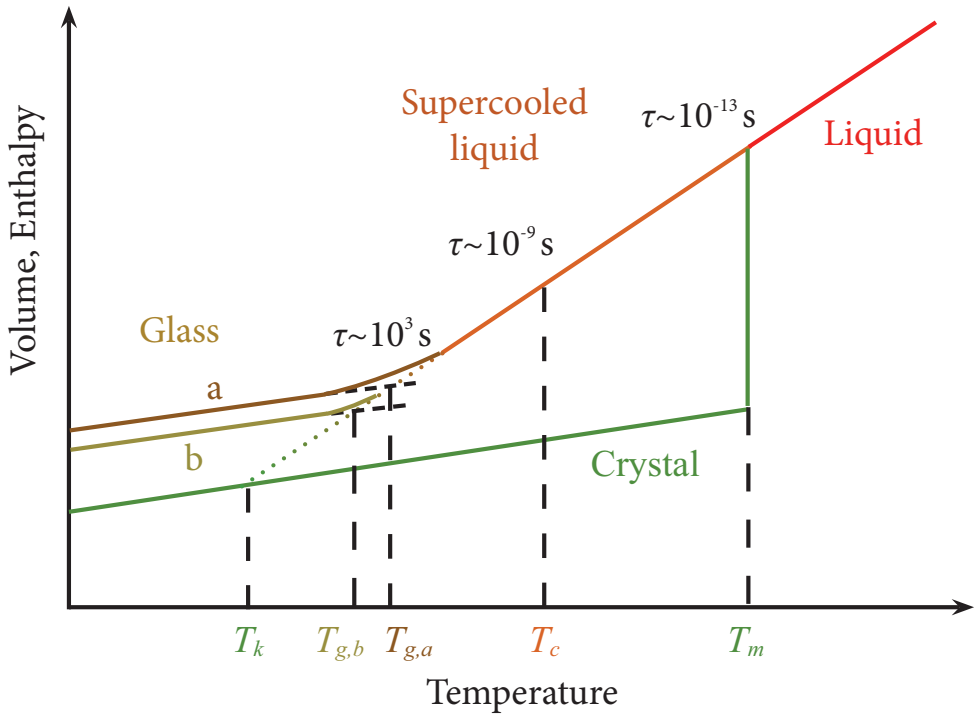

Figure 1.1: Temperature dependence of a liquid's specific volume or enthalpy at a constant pressure. T_m is the melting temperature. T_g is the glass transition temperature and it depends on the cooling rate (a and b curves). a has a faster cooling rate than b. T_k is the Kauzmann's entropy crisis temperature.

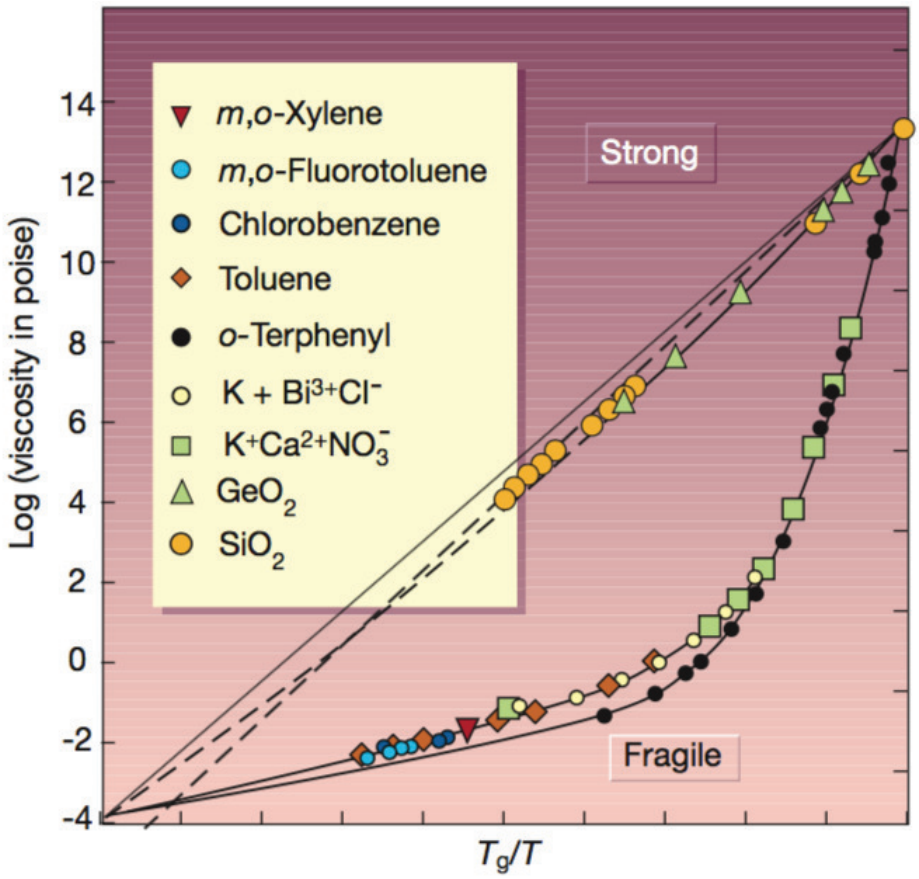

Figure 1.2: Viscosities as a function of rescaled temperature T_g/T for strong and fragile liquids. The image is reprinted from Ref.[3] with permission from Springer Nature.

Another useful definition of T_g is the temperature where the shear viscosity η goes to 10^{13} poise or the relaxation time τ_R reaches to 10^3 s [4]. Based on the Maxwell model, $\eta = G_\infty \tau_R$, and G_∞ is the infinite frequency shear modulus [12]. The viscosity and thus the relaxation time has a sensitive dependence on the temperature (the relaxation time changes from 10^{-13} s to 10^3 s) as shown in Fig. 1.1. The viscosity may change over 2 - 4 orders of magnitude when the temperature only changes several decades of degrees close to the glass transition temperature. Hence, the above definition of T_g can be fairly accurate, even though T_g is cooling-rate dependent.

Quantitatively, Fig. 1.2 shows viscosities of some materials as a function of T_g-scaled temperature T_g/T [3, 4, 11]. For some so-called strong liquids such as GeO_2 and SiO_2, the viscosity of the materials has an exponential dependence on T_g/T. This so-called Arrhenius behavior can be described by:

$$\eta = A\exp(E/k_B T), \tag{1.1}$$

where, A is a constant, E is the activation energy and k_B is the Boltzmann's constant [4]. Since $\eta \sim \tau_R$, the activation energy is temperature-independent and proportional to $\mathrm{d}(\ln \tau_R)/\mathrm{d}(1/T)$.

Other materials (fragile liquids such as $o-$Terphenyl, Fig. 1.2) have a stronger temperature dependence close to the T_g. Such a super-Arrhenius behavior can be approximately described by the Vogel-Tammann-Fulcher (VFT) relation:

$$\eta = A\exp(B/(T - T_k)), \tag{1.2}$$

where A and B are constant and T_k is the Kauzmann's entropy crisis temperature at which the configurational entropy density vanishes and the ideal glass forms [3, 4, 11].

1.1.2 The Quest for a Correlation Length

Notice that for the fragile liquids, the apparent activation energy (also the potential energy barrier) ($\sim$ d(ln τ_R)/d(1/T)) is not longer constant and increases sharply and may even diverge when T is close to T_k. In a system with short range interactions, molecular particle relaxation must be local in space [12]. According to the Adam-Gibbs theory, the activation energy arises because the growth of the size of the "cooperatively rearranging region (CRR)" during the glass transition [17]. The potential energy barriers between different local minimums on the free energy landscape increase due to more and more molecular particles rearrange cooperatively in order for the system to relax [12]. The size ξ of the CRR is a long-pursued correlation length during the glass transition.

However, both liquids and glasses are amorphous. Fig. 1.3 shows typical microscopic images of a colloidal liquid, crystal and glass and their fast Fourier transform (FFT) images. When a liquid crystallizes into a crystal, the system symmetry is broken. FFT images of concentric circles changes to six-order symmetric dots (Fig. 1.3b, d). During this phase transition, spacial correlations are formed. However, when a liquid vitrifies into a glass, the translational symmetry of the system persists (Fig. 1.3b, f) and no apparent spacial correlations are found. Thus, even though the idea that the growth of the size ξ of the CRR during the glass transition is widely accepted, a way to measure ξ is still actively under debate [4, 11, 12, 13, 14, 17, 18, 19, 20, 21, 22, 23, 24, 25].

1.1.3 Random First-Order Transition Theory

The Random First-Order Transition (RFOT) theory (also called the mosaic theory) has been developed to probe such a hidden correlation length ξ since later 1980s [12, 22, 23, 24, 25, 26]. According to this theory, a finite dimensional system may have many different amorphous states. An free energy cost exists due to the presence of interfaces

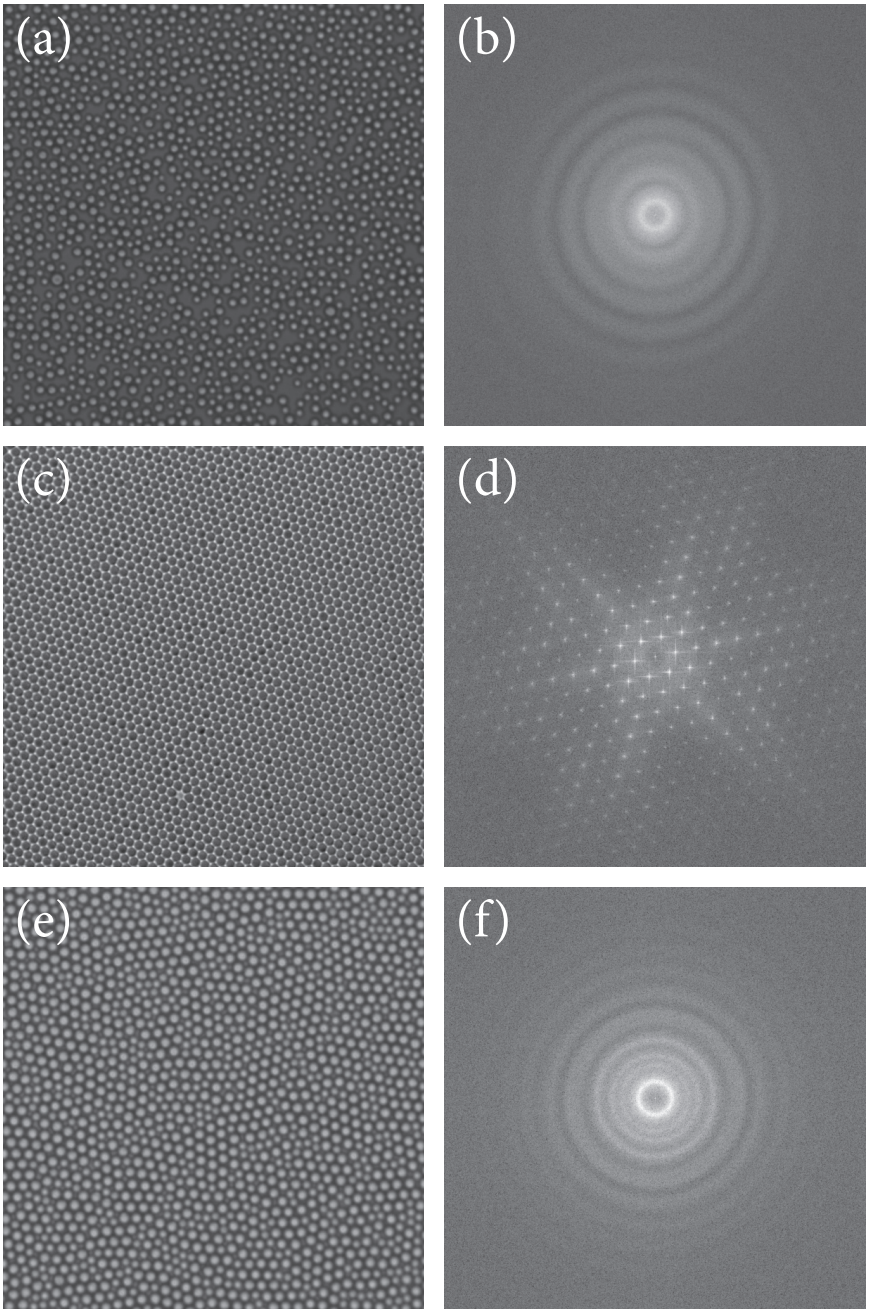

Figure 1.3: Microscopic images of a colloidal liquid (a), crystal (c) and glass (e) and their FFT images (b, d, and f).

separating different states. Assume the system is in α state at first. As the temperature of the system decreases, there is a new β phase with size of R nucleates in the original α phase. Assume the surface tension is the main part of the free energy barriers between state and thus the free energy cost is given by,

$$\Delta F_{\text{cost}} = YR^{\theta}, \quad \theta \leq d-1, \tag{1.3}$$

where Y is a "generalized" surface tension and d is the dimensionality of the system. The new phase with size of R also has an exponentially increased number of available states. The appearance of the new state β is thus driven by the configurational entropy. There is a free energy cost if the region only stays in α state but a free energy gain if the region can also explore other states such as β from the entropy point of view. Therefore, the thermodynamic drive is the free energy gained by the total available configurational entropy is:

$$\Delta F_{\text{gain}} = -Ts_c(T)R^d, \tag{1.4}$$

where T is temperature and s_c is configurational entropy density. Combining Eqn 1.3 and Eqn 1.4, a critical length ξ can be obtained when the energy cost equals the energy gain:

$$\xi = \left(\frac{Y(T)}{Ts_c(T)}\right)^{\frac{1}{d-\theta}}, \tag{1.5}$$

where both surface tension $Y(T)$ and configurational entropy $s_c(T)$ are temperature-dependent. According to FROT, ξ is the typical size of the CRR discussed above.

Based on the arguments above, a gedankenexperiment (thought experiment) has been proposed to detect such an amorphous phase in the supercooled liquids during the glass transition. In a liquid (Fig. 1.4 a), a cavity with a size of R is created (Fig. 1.4 b). The liquid particles out of the cavity including those on the surface of the cavity

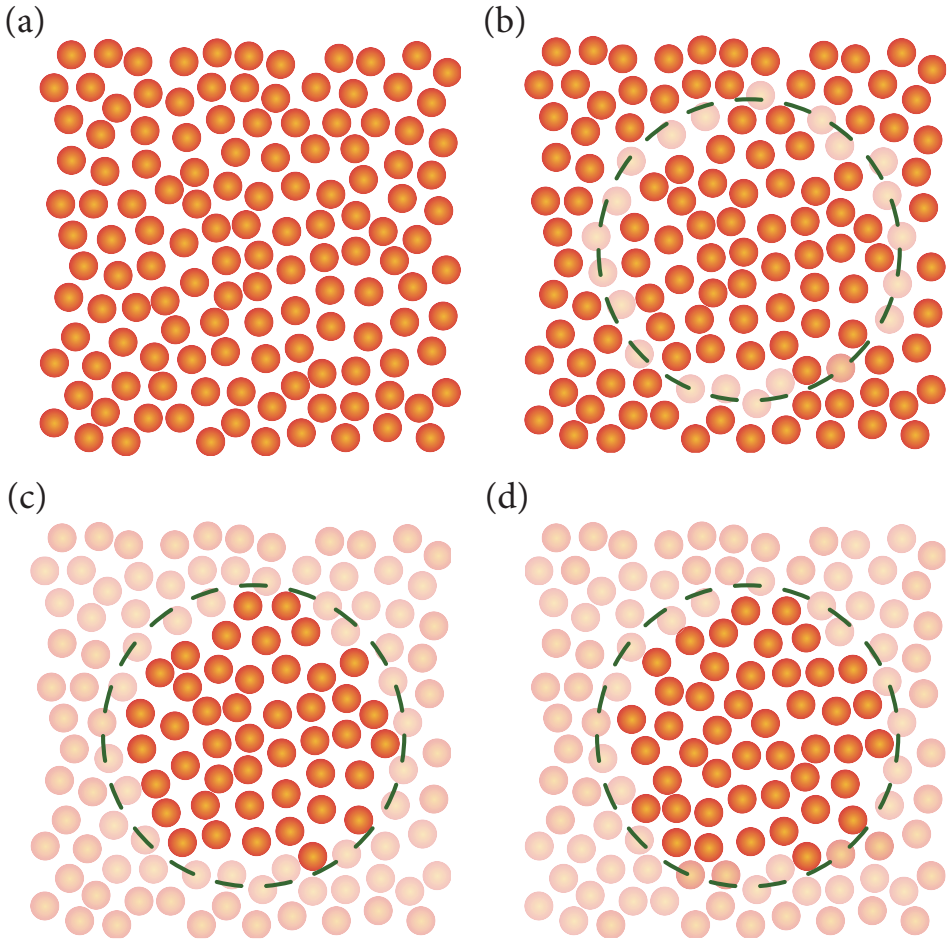

Figure 1.4: Illustration of the RFOT theory. The orange balls indicates individual particles. The green dashed line represent the pinned boundary and the grayish orange balls are trapped particles and frozen particles outside.

are frozen (Fig. 1.4 c). The liquid particles inside of the cavity can still freely evolve while the particles outside are kept still and produce a pinning field at the interface to retain the liquid in the original states α. After certain time, the free liquid particles inside can evolve into another state β (Fig. 1.4 d). Since both states are amorphous, the standard correlation functions that measure the correlation between different points of the system cannot measure the structural difference and correlation between the amorphous α and β phases. A special correlation function, the so-called point-to-set correlation, is introduced to measure the correlation between one point (the center of the cavity) and a set of particles (the boundary and outer frozen particles) among different states. The point-to-set correlation is defined as:

$$q_c(R,t) = \frac{\sum_i \langle n_i(t_0) n_i(t_0+t)\rangle}{\sum_i \langle n_i(t_0)\rangle}, \tag{1.6}$$

where the average is taken over the initial time t_0. n_i is the number of particles in a box near the center of the cavity at $\vec{x_i}$. The box size is chosen to be smaller than the diameter of the particles. Thus, n_i is either 0 or 1. When $R > \xi$, q_c decays to 0, which means there is no correlation between two states in the liquid. When R decreases and is smaller than ξ, q_c becomes non-zero (partially correlated) or even 1 (totally correlated). Such non-zero correlations have been observed in the simulations in supercooled liquids close to the glass transition [22, 27]. The key point is that $q_c(R)$ decays significantly slower when T is lower, and thus ξ increases when T decreases to T_g. The growing thermodynamic length scale indicates the existence of the amorphous order the supercooled liquids.

In Chapter 3 and Chapter 4, we experimentally fulfill the gedankenexperiment and prove the existence of the non-zero correlations and thus the amorphous order in the 3D and 2D confined supercooled liquids during the glass transition. Notice that many

other theories and concepts have also been developed to pursue the length scale such as p-spin model, dynamic heterogeneity, and dynamical facilitation [12, 28, 29, 30, 31, 32]. Even though we use RFOT to explain our results, the experimental results are independent of specific theories and should serve as an experimental benchmark for theoretical understanding of the glass transition.

1.2 Dynamics of Colloids

1.2.1 Colloidal Suspensions

A colloid suspension is a mixture in which the insoluble particles dispersed in a continuous medium. The size of the insoluble particles is roughly in the range of 1 nm - 1 µm. Base on the states (gas, liquid or solid) of the dispersed phases and dispersed media, colloids can be classified as 8 different categories. We see these different classes of colloids in our daily life such as fog (liquid in gas), smoke (solid in gas), cream (gas in liquid), milk (liquid in liquid), ink (solid in liquid), foam (gas in solid), gelatin (liquid in solid), and cranberry glass (solid in solid) [33]. Besides these everyday items, colloids also plays a very important role in the field of soft matter. There are many diverse research areas such as crystal/glass transition, self-assembly, transport, rheology, active matter and so on [34, 35, 36, 37, 38, 39].

Due to small sizes of particles, the thermal fluctuations of the order of k_BT are strong enough to perturb particle dynamics and cause random collisions between colloidal particles and fluid molecules, which leads to the well-known Brownian motion [40]. From a physics point of view colloids are characterized by observable Brownian motion. The random walk of Brownian motion along with other particle-particle interactions contributes to the rich and complex particle dynamics in colloids [35, 39, 41, 42, 43]. Particularly relevant to our research, colloids are widely used as a hard-sphere model

to study the glass transition [1, 44, 45, 46].

1.2.2 Hard Sphere Model

Hard-sphere interaction is the most simple particle-particle interaction and provides the simplest model for studying particle dynamics during the glass transition. The potential between two hard spheres is given by

$$U(r) = \begin{cases} \infty, \text{ if } r \leq 2a \\ 0, \text{ if } r > 2a, \end{cases} \tag{1.7}$$

when r is the distance between two sphere centers and a is the radius of the hard spheres [47]. In this hard-sphere model, particles cannot overlap with each other and all possible configurations has zero potential energy. The system is athermal. Thus the free energy of the system $-TS$ is entirely governed by the entropy S [47, 48, 49].

The total entropy for a liquid can be divided into the vibrational entropy S_{vib} and the configurational entropy S_c [50]. S_{vib} comes from the vibrations of particles near their positions whereas S_c is that part of the total entropy of a liquid which is determined by the number of possible packing states or the number of local minimums on the free-energy landscape [51]. S_{vib} can be further divided into the vibrational entropy of a fixed structure (such as a crystal) $S_{\text{vib, cry}}$ and the excess part of the vibrational entropy $S_{\text{vib, ex}}$. Thus the excess entropy which governs the glass transition can be written as $S_{\text{ex}} = S_{\text{vib, ex}} + S_c$. Since S_c is proportional to or treated equal to S_{ex}, the configurational entropy is commonly used to present the excess entropy such as in Adam-Gibbs equation [51].

For a stable or metastable system such as liquids, supercooled liquids and crystals, particles explore all possible configurations to minimize the system free energy. Near

the glass transition, according to Adam-Gibbs relation,

$$s_c = K(\phi_c - \phi), \tag{1.8}$$

where, s_c is the configurational entropy density (configurational entropy normalized by volume) and K is a constant [17]. ϕ is the volume fraction of the system and ϕ_c is the critical volume fraction where s_c vanishes. For a monodispersed hard-sphere system, the only control parameter is the volume fraction ϕ defined as:

$$\phi = \frac{4\pi N a^3}{3V}. \tag{1.9}$$

N is the number of spheres and V is the volume of the system [47, 49, 52, 53].

Particle dynamics of hard spheres are ergodic. For a hard sphere system in the dilute limit ($\phi \to 0$), the translational diffusion coefficient D_T is accurately described by the famous Stokes-Einstein-Sutherland equation:

$$D_T = \frac{k_B T}{6\pi\eta a}. \tag{1.10}$$

k_B is Boltzman constant, T is the temperature and η is the viscosity of the solvent [54, 55, 47]. The translational diffusive time (or translational relaxation time) τ_D of the particle thus can be defined as:

$$\tau_D = \frac{a^2}{6D} = \frac{\pi\eta a^3}{k_B T}. \tag{1.11}$$

As the volume fraction ϕ increases, the hard spheres show a more complicated phase diagram (Fig. 1.5) [47, 56]. Below $\phi = 0.494$, the colloidal suspension is liquid. When ϕ increases slowly above 0.494, the system goes through the liquid-crystal phase transition. The system shows a co-existence of liquid and crystal when $0.494 < \phi < 0.545$. The

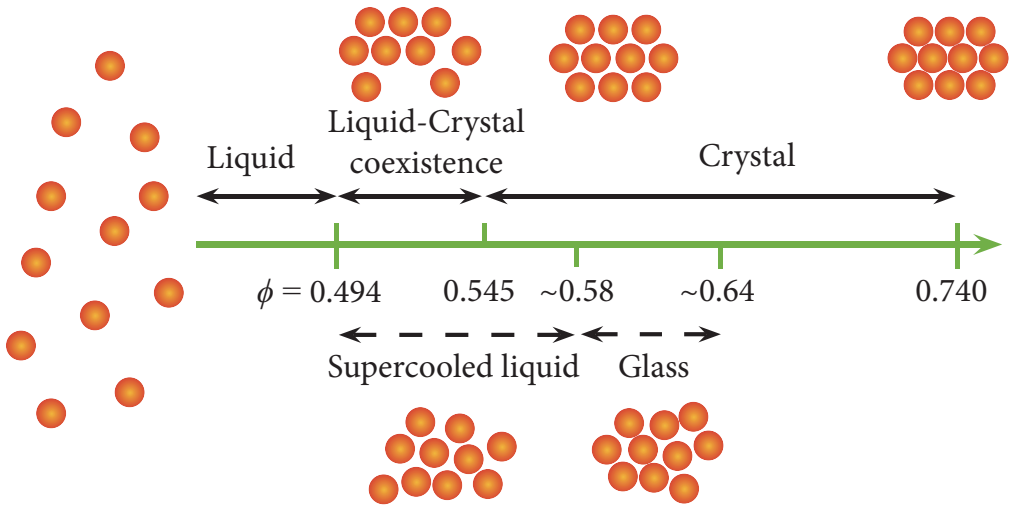

Figure 1.5: Hard-sphere phase diagram. The orange balls indicate hard-sphere particles showing typical organizations of particles at certain volume fractions ϕ.

whole system will be crystal when $\phi > 0.545$. However, when the volume fraction ϕ increases rapidly around 0.494 (such as by fast evaporation or sedimentation), the hard spheres do not have enough time to reorganize and crystalize. Thus, the system stays at the equilibrated liquid state as the supercooled liquid. The supercooled liquid eventually vitrifies into the glass when $\phi > 0.58$.

A key experiment performed by Pusey and van Megan first demonstrated that monodispersed poly(methymethacrylate) (PMMA) colloidal spheres could be treated as hard spheres and have the crystal transition and glass transition purely driven by entropy ϕ [34]. This pioneering work promotes the applications of the colloids as model hard spheres. Nowadays, colloidal particles such as PMMA, polystyrene (PS), and silica spheres under special solvent conditions are frequently used as hard spheres [1, 2, 34, 41, 57, 58].

Due to the ubiquitous presence of van de Waals attractions between colloidal particles, the stabilization of system usually requires steric repulsions by oligomers on

spheres' surfaces or charge repulsions by like charges on spheres' surfaces [59]. The PMMA spheres used by Pesey and van Megan are sterically stabilized by poly-12-hydroxy-stearic acid (PHSA) oligomers, while some other PMMA, PS or silica particles dispersed in the water are stabilized by like-charge repulsions [34].

In order to weaken the van de Waals forces among particles, the solvent should be carefully chosen to match the refractive index of particles to reduce the Hamaker constant [59]. For PHSA stabilized PMMA spheres used in our experiments (Chapter 3 and 5), a mixture of decahydronaphthalene (decalin) and cyclohexyl bromide (CXB) is commonly used to match the refractive index [41, 60]. The mixture of decalin and CXB can also match the density the PMMA particles simultaneously, which prevents sedimentation of particles.

Since the late 1960s, many experiments have demonstrated the similarities of particle dynamics between the glass transition in colloidal suspensions and those in atomic systems [61, 62, 63]. Treating hard-sphere colloidal particles as hard spheres can certainly simplify the study of the complex glass transition. Colloidal suspensions provide further advantages to study the glass transition. Traditionally, the dynamics of colloidal suspensions are studied by the light scattering [64, 65]. However, the light scattering can only be used on bulk samples and provide the average information. In order to study confined samples (such as blood cells in veins) or systems with heterogeneous dynamics, novel measurements with single-particle resolution are needed. To study the single-particle dynamics, a proper spacial resolution and temporal resolution of the measurements are needed. The typical size of colloidal particles used in experiments is in the range of 100 nm - 1 µm, which gives the diffusion time τ_D (Eqn 1.11) in the range of 1 ms - 1 s. The video microscopy such as video optical microscopy can perfectly meet the requirements [41, 66, 44]. In this thesis, we use colloidal particles as hard spheres to study the glass transition by video optical microscopy such as the

bright-field microscopy and the confocal laser scanning microscopy. With the help of the camera recording and computer-aided imaging data analysis, the information of particles such as spacial positions and their time evolutions can be accurately obtained at the single-particle level. More information about video optical microscopy and imaging data analysis will be discussed in Chapter 2.

Even though colloids can be very useful to study the glass transition, the differences between the colloidal glass and atomic glass should be noticed [40]. Firstly, in colloids, there are dispersed phases (colloidal particles) and dispersed media (solvents). The dynamics of particles are dissipative. The hydrodynamic effects affect the particle dynamics [67, 68]. While in atomic systems, there is usually one phase and particle dynamics are ballistic between collisions [47]. Secondly, colloidal suspensions are controlled by volume fractions, whereas atomic and molecular fluids are controlled by temperature. Thirdly, as a hard-sphere model, colloidal particles do not have complex particles shapes and particle-particle interactions as those of atoms and molecules. But for many cases of interests, especially the study of the glass transition, the hard-sphere model can still provides many useful insights. There are also many experiments exploring particle dynamics of non-sphere colloids and colloids with more complicated interparticle potentials [20, 69, 70, 71]. Lastly, colloidal particles are always polydispersed ($\sim 5\%$), which may shift the phase transition to higher values. However, the polydispersity of the colloidal particles is not always troublesome. The polydispersity can frustrate the crystallization and help the vitrification of colloidal suspensions. In fact, many experimental and simulation studies of colloidal glass transitions add the polydispersity on purpose [1, 72, 73, 74].

1.2.3 Self-assembly of Colloids

Besides used as a hard-sphere model to study the colloidal glass transition (Chapter 3 and 4), colloids are also used to study particle self-assembly (Chapter 5) [2, 35, 75, 76, 77, 78, 79]. Even though particle self-assembly is not a main topic in this thesis, this work does show the diverse research areas in colloidal science.

1.3 Mermin-Wagner Fluctuations

1.3.1 Mermin-Wagner Fluctuations in 1D and 2D

Dimensionality is important in materials science. Low dimensional (D $\leq$ 2) materials, such as graphene and nanoparticles, show very novel and interesting material properties compared to the bulk 3D materials [80, 81, 82, 83, 84, 85, 86]. Even though a lot of low dimensional materials are called crystals, they are not perfect crystals due to many issues such as finite sizes or dynamic fluctuations beyond 2D. It has been widely accepted that there is no perfect crystal in low dimensional (D $\leq$ 2) materials. Peierls and Landau first considered this problem and concluded that there was no 1D or 2D crystalline long-range order [87, 88, 89]. In 1960s, Mermin and Wagner published a series of papers discussing the quantum spin system, classical lattice spin system and classical particle systems on a 2D lattice [90, 91, 92]. The absense of spontaneous symmetry breaking in lower dimensional (D $\leq$ 2) systems was also rigorously proved by Coleman in quantum field theory and Hohenberg in statistical physics [93, 94]. Based on these work, the Mermin-Wagner theorem (also known as Mermin-Wagner-Hohenberg theorem or Coleman theorem) was established as: continuous symmetries cannot be spontaneously broken at finite temperature in 1D or 2D systems with sufficiently short-range interactions [90, 91, 92].

Let's first consider Peierls' 1D model (Fig. 1.6) [87]. Assume a string of N atoms at

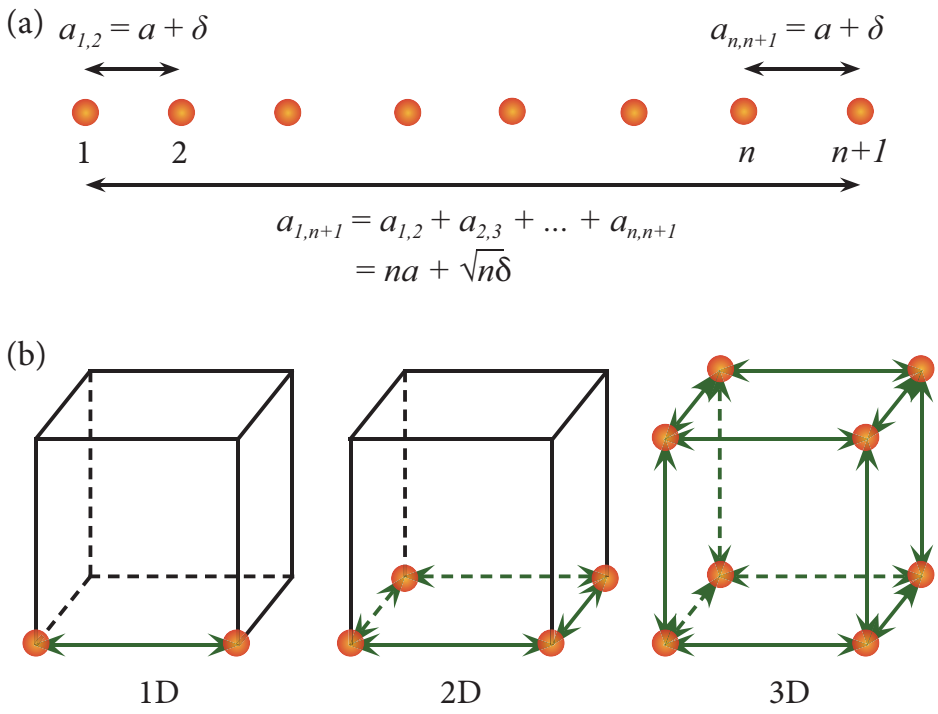

Figure 1.6: Illustration of Mermin-Wagner fluctuations. (a) Illustration of fluctuations in a 1D periodic crystal. (b) Different pathways to relax fluctuations in 1D, 2D and 3D.

some finite temperature in 1D. The interactions are short-range and only exist between two adjacent particles, which means the equilibrated position of each atom is only determined by its local environment, i.e., instantaneous positions of its neighbors. The lattice constant is a and there is a fluctuation of the position δ between two adjacent atoms due to thermal fluctuations. We further assume the interatomic forces are harmonic. The atomic displacement of atom n, δ_n, can be written in terms of normal modes of vibration:

$$x_n - na = (Nm)^{-1/2} \sum_k V_k \exp[i(\omega_k t - kna)], \tag{1.12}$$

where t is time, m is the mass of an atom, k is the wavevector, ω_k is the frequency and V_k is the amplitude of the mode [95]. Then the square of the amplitude of the fluctuations $\langle \delta_n^2 \rangle$ can be expressed as:

$$\langle \delta_n^2 \rangle = \frac{4}{Nm} \sum_k \langle |V_k|^2 \rangle \sin^2(kna/2). \tag{1.13}$$

c is the velocity. Considering that the string is very long and the normal mode spectrum is quasi continuous, the thermal average $\langle \delta_n^2 \rangle$ can be simplified as:

$$\langle \delta_n^2 \rangle = na^2 k_B T / 2mc^2, \tag{1.14}$$

or

$$\sqrt{\langle \delta_n^2 \rangle} \sim \sqrt{n}. \tag{1.15}$$

Thus, the amplitude of the long-wavelength fluctuation $\sqrt{\langle \delta_n^2 \rangle}$ goes infinite as the size of the system goes to infinite, resulting an unstable 1D crystal. The system losses spacial correlations and thus there is no perfect crystal with short-range interactions at finite temperature in 1D system [87, 92, 95].

Similar arguments can be applied to a 2D system and the amplitude of the long-wavelength fluctuations follows:

$$\sqrt{\langle \delta_n^2 \rangle} \sim \sqrt{\ln(n)}. \tag{1.16}$$

In this case, $\sqrt{\langle \delta_n^2 \rangle}$ is still increasing with the system size in 2D. $\sqrt{\langle \delta_n^2 \rangle}$ develops a logarithmic dependence on the system size. The dependence of the amplitude of fluctuations on the system size in 2D (Eqn. 1.15) is weaker than that in 1D (Eqn. 1.16) [92, 95]. If same procedures are applied to a 3D system, it turns out $\langle \delta_n^2 \rangle$ is independent on n [95].

Fig. 1.6 b shows simplified arguments for the fluctuations in systems [96]. In 1D the fluctuations can only relax among two neighbors, whereas in 2D the fluctuations have to be correlated along four neighbors. However, in 3D, the fluctuations can relax among six neighbors. The total amplitude of the fluctuations stays same order as the fluctuations between two adjacent atoms. Thus there is no perfect crystals in 1D and 2D systems due to the Mermin-Wagner fluctuations, whereas there are perfect crystals in 3D systems [95].

1.3.2 Mermin-Wagner Fluctuations in 2D Amorphous Colloidal Systems

Recently, Illing *et al.* experimentally demonstrated that the Mermin-Wagner fluctuations also exist in 2D glass [96]. 2D crystal, 2D glass and 3D glass were compared by measuring both actual dynamics such as mean square displacements (MSD) and self-intermediate scattering functions (F_s) and relative dynamics compared with neighbors such as cage-relative MSD (CR-MSD) and bond-orientational correlation functions

(C_Ψ). Actual dynamics measurements are influenced by the Mermin-Wagner fluctuations whereas relative dynamics measurements are not. They showed that actual motions and the relative motions were same in 3D glass whereas they became different in 2D crystal and 2D glass. Based the observations, they claimed that such differences between the actual motions and the relative motions are caused by the existence of the long wavelength Mermin-Wagner fluctuations in the 2D systems. Similar behaviors were also observed independently by the Weeks group in Emory Univerisity [97].

Illing *et al.* further showed numerically that the square root of heights of MSD at inflection points $\sqrt{\text{MSD}}$ grows logarithmically with system size $\sqrt{N}$. At the plateau of MSD curves (indicated by the inflection points), each particle is confined by its neighbors. Thus each particle is most likely moving with its neighbors and the height of the plateau of the MSD curve should indicates the actual displacement influenced by the Mermin-Wagner fluctuations. Thus the change of $\sqrt{\text{MSD}}$ with system size provides a way to measure the amplitude of the long-wavelength fluctuations in 2D glass.

In Chapter 4, we use optical tweezers to systematically change system sizes and measure the influence of the Mermin-Wagner fluctuations on our particles dynamics in 2D. We show experimentally that the amplitude of the fluctuations quantified by $\sqrt{\text{MSD}}$ follows a logarithmic dependence on the system size R. Another approach to measure the fluctuations is also developed, which further confirms the logarithmic dependence on sizes of 2D amorphous colloidal systems.

Chapter 2

Experimental Background

2.1 Confocal Laser Scanning Microscopy

Optical microscopy has been a powerful tool to study soft matter, fluid dynamics, polymer science and many other research fields [1, 2, 41, 98, 99, 100]. Fig. 2.1a shows the schematic diagram of a typical optical microscope [101, 102]. A light coming from an external light source shines upon a sample. The light may be reflected, scattered or absorbed by materials in the sample. A optical microscope can be either bright-field (collecting light transmitted through the sample) or dark-field (collecting light scattered by the sample). Notice that the reflection, scattering and absorption of light usually happens at same time.

It is extremely helpful to obtain accurate positions of target materials in order to study dynamics or mechanisms. Even though the normal optical microscopy is very useful, there are two major limitations that could cause many troubles when pursuing accurate positions. Firstly, due to the image contrast coming from the reflection, scattering and absorption of light, the observed objects have to have a large enough dielectric constant difference (or refractive index difference) from the background [101].

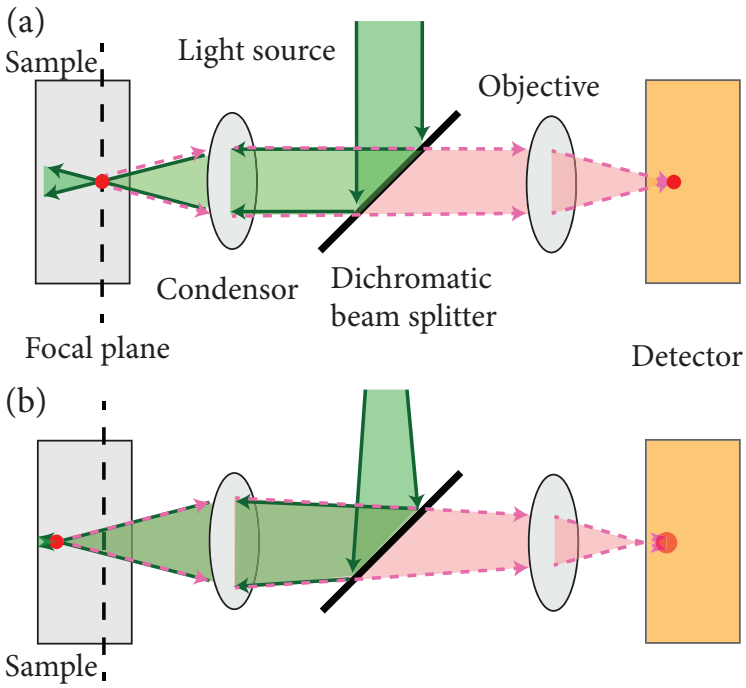

Figure 2.1: Schematic diagrams of optical/fluorescence microscopy with the observed objects (a) at the focal plane and (b) out of the focal plane. The image of objects at the focal plane shows clear and sharp figures while those out of the focal plane shows blurry and exaggerating figures. The schematic diagrams are only used to show the principle of the microscopy. The actual setup may be different and has more components.

Thus, the normal microscope is helpless when being used to image some polymer blends, liquid crystals or biological cells and tissues with similar refractive indices. Secondly, out-of-focus light can make images blurry and may exaggerate figures. Fig. 2.1b shows the light paths scattered by an observed object away from the focal plane. Different from the clear and sharp image in Fig. 2.1a, the image of the observed object away from the focal plane has much less image clarity. The situation will get even worse when it comes to samples with high concentration of objects, which is very common is soft matter. The images of the objects from the focal plane and out of the focal plane may be superimposed and make the detection almost impossible.

Fluorescence microscopy (FM) has been used to overcome the first limitation. The principle is based on the phenomena of fluorescence and phosphorescence (Fig. 2.2a) [101, 103]. Photons absorbed by a fluorescent or phosphorescent molecule can change the electronic, vibrational and rotational states of an electron in the outermost orbitals of the molecule. With enough light energy absorbed, the electrons at the ground state can jump to higher-energy excited states. Fluorescence (spontaneous emission) and phosphorescence (delayed emission) happen when the electrons at the excited states return to the ground states and release the emission light. Notice that the electrons always start from the the electronic level of the energy but may end at different vibrational levels of the energy. Thus, the emission light usually has a lower energy and longer wavelength than the excitation light. The difference is called as the Stokes shift [101].

The Stokes shift is the key to fluorescence microscopy because the shift makes it possible to distinguish the excitation light and emission light. Fig. 2.2b shows the excitation and emission spectrums of Nile Red (phospholipid), which is used in this work. From the plot, we can see that the emission spectrum shifts to the longer wavelength (lower energy). A light source with the wavelength close to the peak the excitation

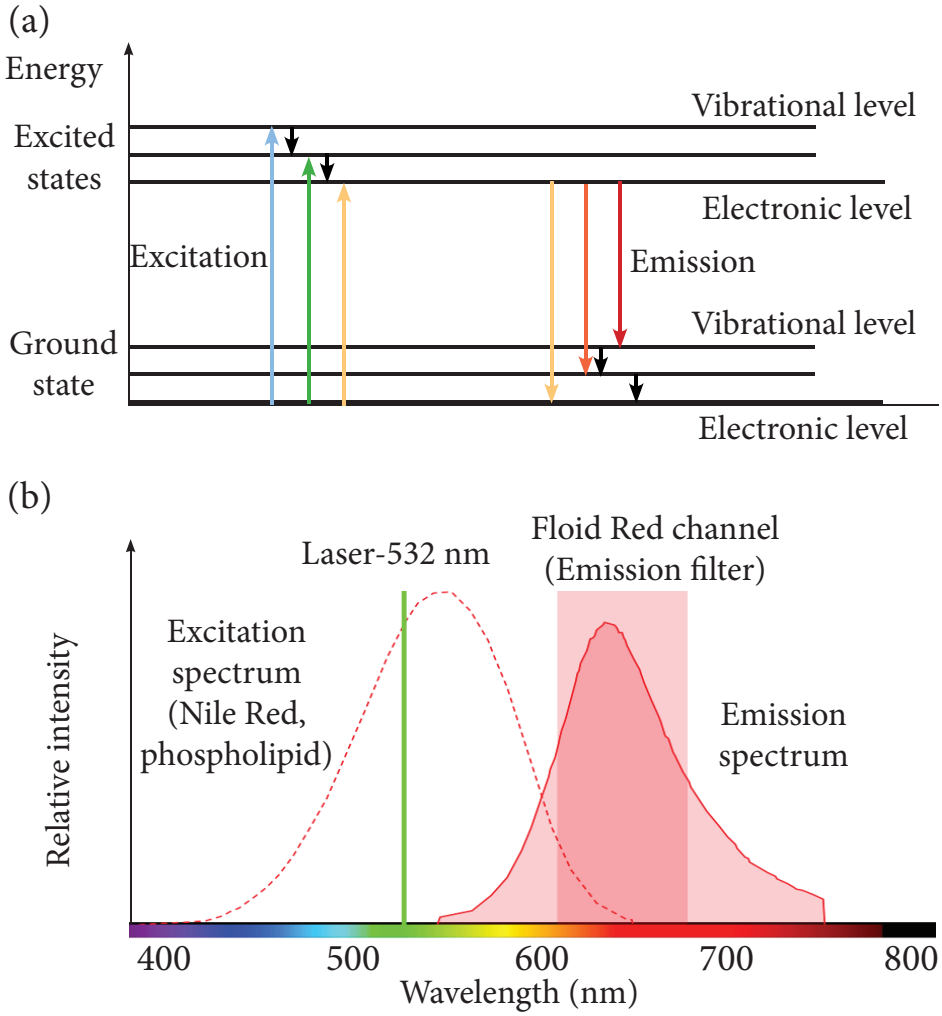

Figure 2.2: Excitation and emission spectrum for a fluorescent-labeled observed object. (a) Schematic diagram of the energy state changes of the fluorescent chemicals' electrons in the outermost orbitals with the influence of the light. The color of the lines roughly indicates the energy change between states and the colors of lights. From blue to red, the energy changes decrease. (b) Excitation and emission spectrum of Nile Red (phospholipid). The spectrum data is generated by the online "Fluorescence SpectraViewer" provided by Thermo Fisher Scientific (https://www.thermofisher.com/us/en/home/life-science/cell-analysis/labeling-chemistry/fluorescence-spectraviewer.html). The laser with wavelength of 532 nm is used to excite Nile Red in this work. The real excitation and emission spectrum may be altered by the dispersed medium. The data here is only for demonstration and may be different from the real spectrums for our Nile Red labeled PMMA particle suspended in decalin and CXB mixture.

spectrum (such as the laser with wavelength of 532 nm used in our work) is chosen to maximize the excitation. By choosing a right emission filter (such as Floid Red channel), the image is created only by the excitation light from the fluorescent-labeled objects with the light from the light source filtered out (Fig. 2.1a). In this way, with the observed objects labeled by a proper fluorescent dye, fluorescent images with high contrast can be obtained. Fluorescence microscopy has been widely used in many research areas where the observed objects have close dielectric constant to the medium or background. However, fluorescence microscopy still has the same limitation as the normal optical microscopy–blurry image caused by the out-of-focus light (Fig. 2.1b).

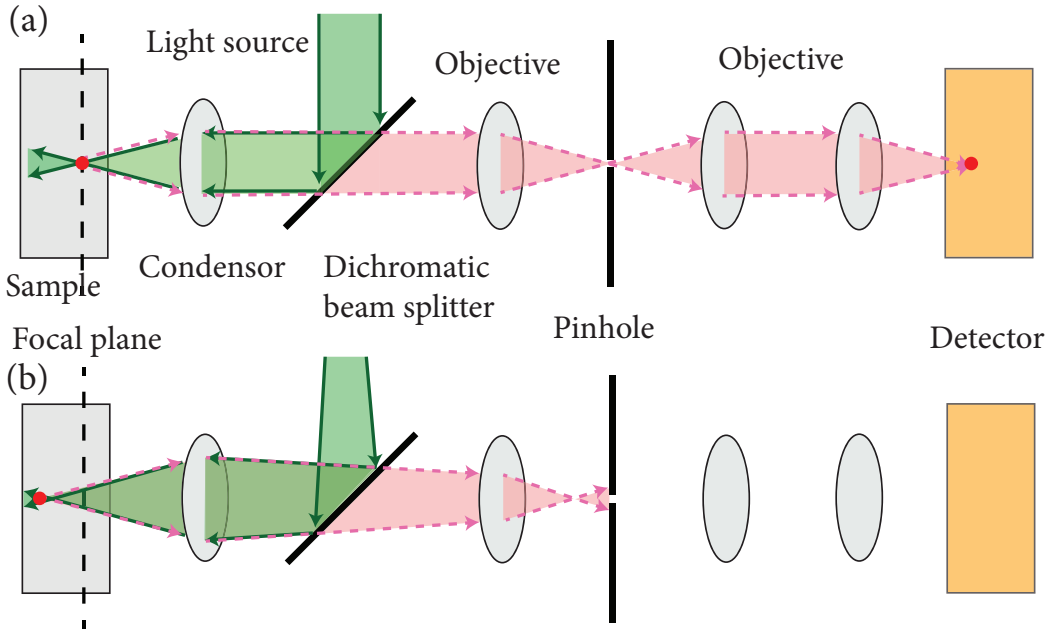

Figure 2.3: Schematic diagrams of confocal laser scanning microscopy with the observed objects (a) at the focal plane and (b) out of the focal plane. The image of objects at the focal plane shows clear and sharp figures while those out of the focal plane are blocked by the pinhole. The schematic diagrams are only used to show the principle of the confocal microscopy. The actual setup may be different and has more components.

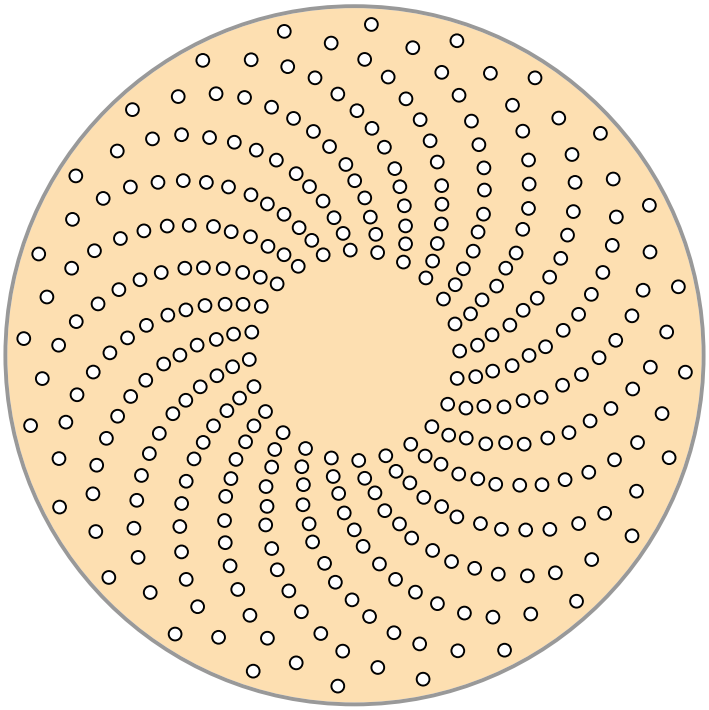

Figure 2.4: Schematic diagram of one type of spinning disk of the spinning-disk confocal microscope. A pair of spinning disks is used synchronously to accelerate the process of data collection. The figure is redrawn based on the geometry shown on one research website of University of New South Wales (https://cellbiology.med.unsw.edu.au/cellbiology/index.php/Group_6_Project_-_Confocal_Microscopy).

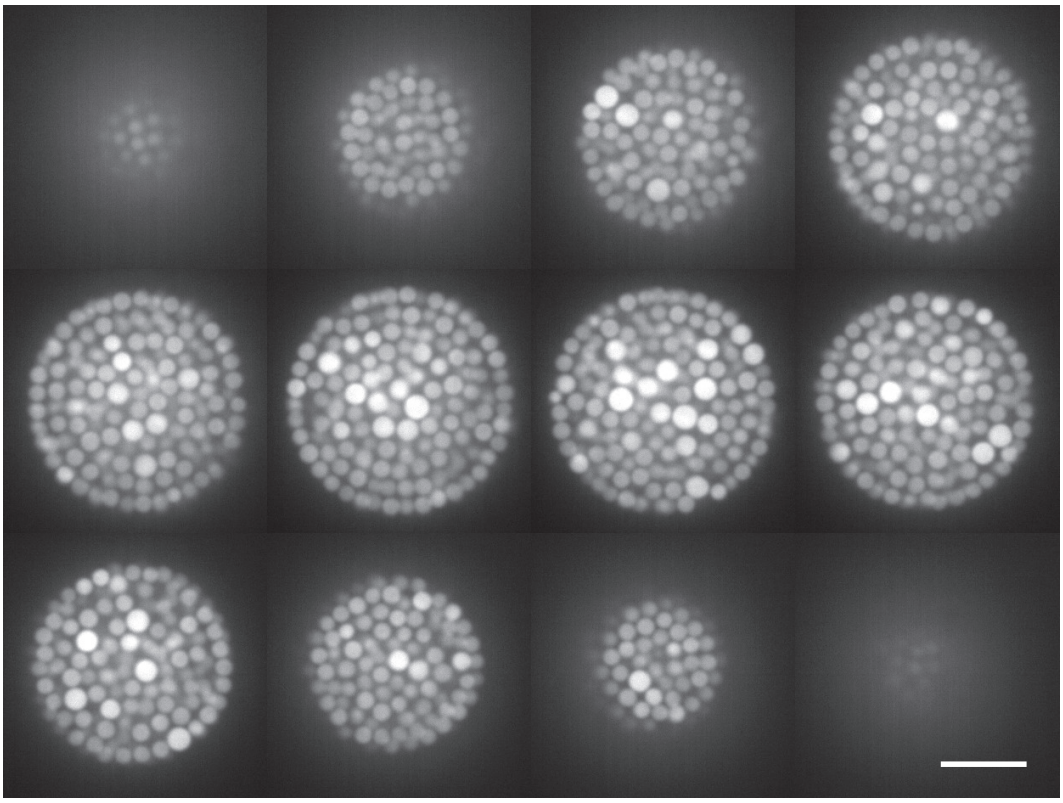

Figure 2.5: Z-stack image sequence of a spherical droplet of PMMA suspensions scanned from the top to the bottom. The step distance in z direction between two adjacent z-stack images is 1.5 µm. Two different sizes of PMMA particles are used. The diameter of particles are $d_s = 1.29$ µm and $d_l = 1.64$ µm. The scale bar is 5 µm. In our real experiment, the step distance between two adjacent z-stack images is set to be 0.1-0.3 µm in order to have multiple cross-section images of each particle. The scale bar is 10 µm.

In order to solve this problem, confocal laser scanning microscopy (CLSM) has been developed [98, 102, 101, 103, 104, 105]. Fig. 2.3a shows schematic diagrams of CLSM. The geometry of CLSM is very similar FM. The biggest change in CLSM is to add an opaque disk with a pinhole between the sample and the detector to screen the out-of-focus light. When the observed object is at the focal plane, the emission light excited from the fluorescent-labeled object by the external light (laser) can pass through the dichromatic beam splitter, condense at the pinhole and eventually focus on the detector (Fig2 2.3a). However, when the observed object is away from the focal plane, the emission light can still pass through the dichromatic beam splitter but condense before or after the pinhole and thus is blocked by the opaque disk. On contrary to the normal optical microscopy, for CLSM, the dielectric constant or the refractive index of the observed objects should be matched to that of the medium or background to further eliminate the scattering light due to refractive index differences. The ideally obtained image shows the 2D cross-section of the observed objects without the influence of the out-of-focus light, while in reality the depth of field is on the order of 100 nm and influenced by the numerical aperture of objectives. However, there comes another issue with the present of the pinhole. Instead of collecting all the light information in the field of view simultaneously, CLSM with a pinhole has to scan objects point by point, which provides high resolution images but greatly slows down the image collection process. In order to solve this problem, a spinning disk is introduced to the CLSM to replace the opaque disk with a pinhole (Fig. 2.4). The spinning disk confocal microscope uses a pair of the spinning disk synchronously to accelerate the data collection. The speed can go as high as 100 frames per second (FPS) for a field of view 1000 $\times$ 1000 pixels. A higher speed is limited by the concentration of fluorescent dyes and the efficiency and the power of the light source.

With the help of CLSM, a sample with refractive index matched with the medium

now can be nearly perfectly imaged at each focal plane. If we take a z-stack image sequence by quickly changing the position of the focal plane in z direction (perpendicular to the focal plane), 3D information of the observed objects can be obtained after 3D reconstruction. Fig. 2.5 shows a z-stack image sequence of a spherical droplet of PMMA suspensions with a step distance of 1.5 µm. The confocal images can be used to nearly perfectly calculate 3D information (positions, brightness, *et al.*) of PMMA particles. In our experiments, the step distance is usually set to be 0.1-0.3 µm in order to have at least 5-10 pixels resolution of each particle in z direction for accurate analysis. The 3D information can be further used to calculate particle dynamics or other useful quantities. More details about the experiments will be discussed in Chapter 2.3 and Chapter 3.

2.2 Optical Tweezers

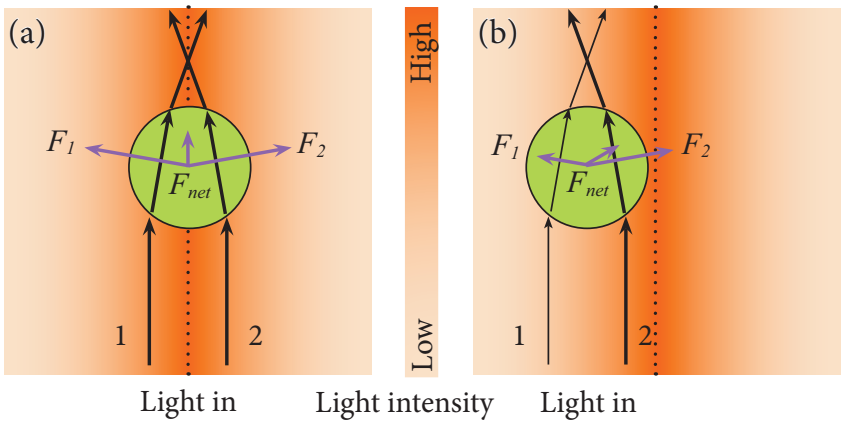

Figure 2.6: Ray optics explanation of forces on a particle in an unfocused but symmetric light field. The particle has a high refractive index (dielectric constant) than the suspended medium (liquid or gas). (a) When the particle stays at the center line, it will be pushed away along the incident light direction. (b) When the particle stays away from the center line, it will be pushed toward the center while pushed away along the incident light direction.

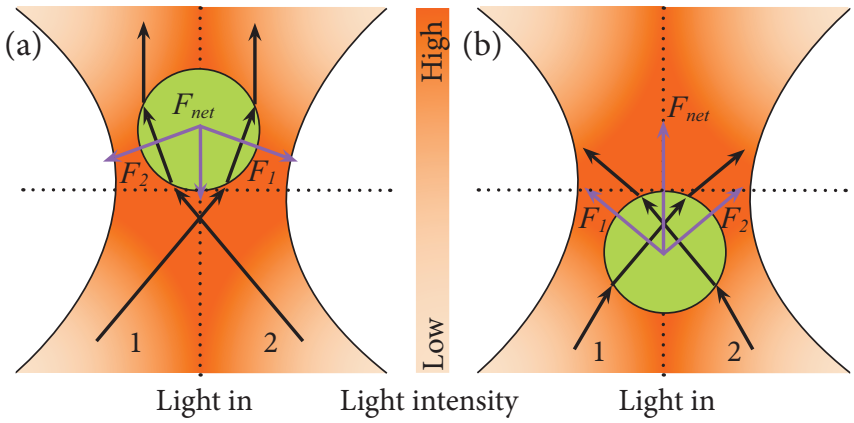

Figure 2.7: Ray optics explanation of forces on a particle in a focused and symmetric light field. The particle has a high refractive index (dielectric constant) than the suspended medium (liquid or gas). (a) When the particle stays above the center, the net force on the particle will have the inverse incident light direction. The particle will be push toward the center. (b) When the particle stays below the center, the net force on the particle will have the incident light direction. The particle will be push toward the center.

When passing through a transparent dielectric particle, incident light can be partially scattered or absorbed. Thus the linear and angular momentums of the light are transferred on the particle and the net force on the particle may be non-zero. Based on this phenomena, starting from early 1970s, Arthur Ashkin and his co-workers pioneered the field of laser-based optical tweezers (or named as optical trapping) [106, 107, 108, 109, 110]. The ability to apply femtonewtons to nanonewtons forces onto nanometer-sized to micron-sized dielectric particles makes optical tweezers a perfect manipulative tool in many research areas such as molecular motors and soft matter physics [111, 112, 113, 114].

Theoretical explanations of optical trapping of dielectric particles are sufficiently complex. Two extreme cases of Mie particles ($a \gg \lambda$, a is the particle radius) and Raleigh particles ($a \ll \lambda$) are well-understood, while many theories have been developed

to explain the case where $a \sim \lambda$ [111]. Here we use the Mie particle to qualitatively explain the formation of optical traps.

When a dielectric particle is placed in a gradient light field, besides a scattering force in the direction of light propagation, a gradient force in the direction of the spatial light gradient is applied on the particle [108, 111]. Fig. 2.6 shows two simple cases where a particle with higher dielectric constant than the medium stays in an unfocused but symmetric light field. The gradient force arises because in an inhomogeneous light field the laser induces dipoles in the dielectric particle and the dipoles (thus the particle) feel a force in the direction of the field gradient [108, 111]. The scattering force is positively correlated to the light intensity. The gradient force is proportional to the light intensity gradient and also the polarizability of the dielectric.

When the particle stays at the center line, the net force on the particle will be parallel to the initial light direction (Fig. 2.6a). The net force is the total force of F_1 and F_2. F_1 and F_2 are the total force of the scattering force and gradient force from ray 1 and ray 2. The particle will be pushed away along the incident light direction. When the particle stays away from the center line, the longitudinal part of the net force still points the incident light direction (Fig. 2.6b). However, the non-zero lateral part of the net force points to the center where the light intensity is stronger. Hence, the particle will be pushed toward the center while pushed away along the incident light direction. In both cases, the particle can not be optically trapped.

In order to firmly trap a particle, an objective lens of high numerical aperture (NA) is needed to focus the laser to generate a light field with a large gradient. Fig. 2.7 presents the ray optics explanation of force on a particle in a focused and symmetric light field. When the particle stays above the center, the net force on the particle will have the inverse incident light direction. The particle will be push toward the center. When the particle stays below the center, the net force on the particle will have the

incident light direction. The particle will be pushed toward the center. Combined with the arguments in Fig. 2.6, with a strong enough light intensity gradient the particle will be trapped at the location slightly higher than the center point of the light field. An stable optical trap is formed.

In sum, a powerful laser light source, an objective lens with a high numerical aperture and a large refractive index (RI) difference between the particle and its suspended medium are the three key components of optical tweezers. For our experiments, the maximum power of the 1064 nm Infrared radiation (IR) laser used for trapping is 5 W. A 60× oil immersion objective lens has NA = 1.25. PMMA (RI = 1.49), PS (RI = 1.55-1.59) and fused silica (RI = 1.46) particles are suspended in water (RI =1.33). The combinations can provide stable multiple traps. More details about the experiment using optical tweezers will be discussed in Chapter 4.

2.3 Computational Analysis

In order to study single-particle dynamics in colloidal suspensions, accurate information such as particle positions as a function of time is needed. Many well-known and public-domain algorithms have been developed over the last two decades. In this work, we use the widely used algorithms developed by John Crocker, David Grier and Eric Weeks [115, 116]. Based on these algorithms, custom-made algorithms for special purposes have also been developed and used for the image data analysis. Algorithms for single-particle dynamics are first to locate particle positions, then link same particles at different time frames and lastly calculate desired physical quantities such as MSD. Same algorithms can be achieved on different languages (IDL, MATLAB, Python *et al.*).

Fig. 2.8 shows a typical procedure of locating positions of spherical particles (pre-tracking). The original image needs to be inverted if particles are black (Fig. 2.8b). Then the background noise is removed by a spatial bandpass filter. After the filtration,

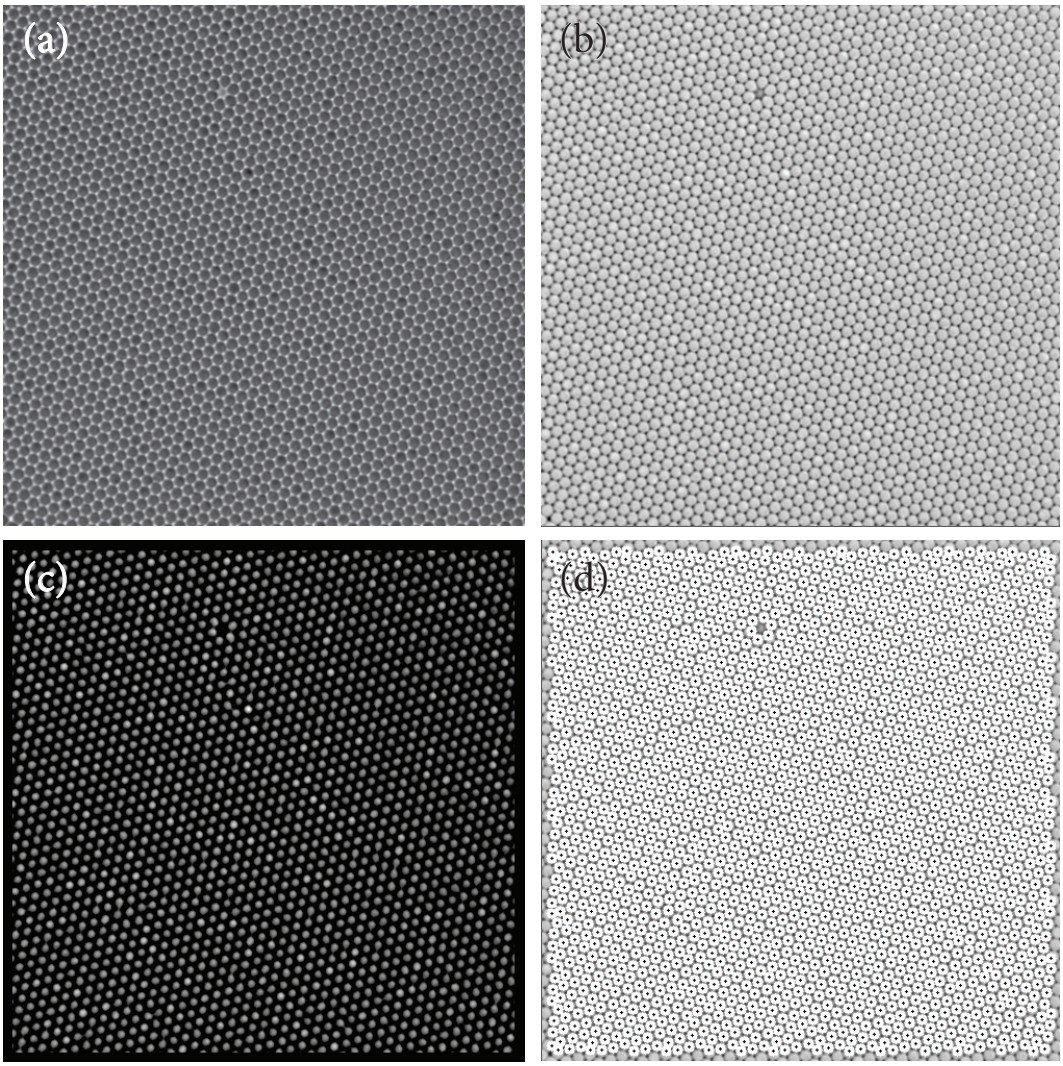

Figure 2.8: Demonstration of algorithms of image analysis. (a) A original image of PMMA particles with diameter of 2.08 µm collected by a microscope. (b) The inverted image to make particles as bright spots. (c) the image after a spatial bandpass filter is applied on the inverted image in (b). The spatial bandpass filter is used to smooth the image and subtract the background noise. (d) The detected particles are superimposed on the top of the inverted image to verify analysis results. The white spots and their black-cross centers presents locations of the detected particles. Notice that sizes of the white spots are default and not same as real particle sizes.

an image with clear background and individual white spots can be obtained (Fig. 2.8c). Lastly, a circular mask with an estimated size same as particles is created. The brightness of the mask follows 2D Gaussian distribution. Correlations between the brightness of the mask and the brightness of every position with same size on the image are calculated and compared. If the correlation achieves a local maximum, the position of the circular mask will be marked as one particle position. Same procedures will be applied to all positions until all features are found and marked (Fig. 2.8d). As shown in Fig. 2.8d, all particles except those near edges are accurately located. No particle is found in the location of the vacancy detect in the colloidal crystal. The accuracy of the positions is at the sub-pixel level (less than 50 nm). The high accuracy of the pre-tracking is essential for particle tracking velocimetry (PTV).

The next step is to link the same particles at different time frames (tracking). An image time series is recorded by a CCD camera on a normal optical microscope or a confocal laser scanning microscope. The interval time of the image time series should be smaller enough so that each particle will not diffuse more than one particle radius away from its previous position during each time interval. Having all positions at all frames from the pre-tracking procedure, same particles are then linked through the time series based on the factor that the displacement of each particle between two adjacent frames is smaller than one particle radius. Same particles are identified and labeled by the same numbers (IDs). The IDs are stored together with particles' other information, such as positions, sizes, *et al.*. Fig 2.9 shows a typical single-particle trajectory of the Brownian motion of a particle in a dilute quasi-2D suspension. Particle suspensions under more complicated situations such as flows can also be analyzed by similar procedures (Chapter 5).

After the tracking procedure, the spacial and temporal information of each particle can be obtained. Useful physical quantities such as mean square displacements (MSD),

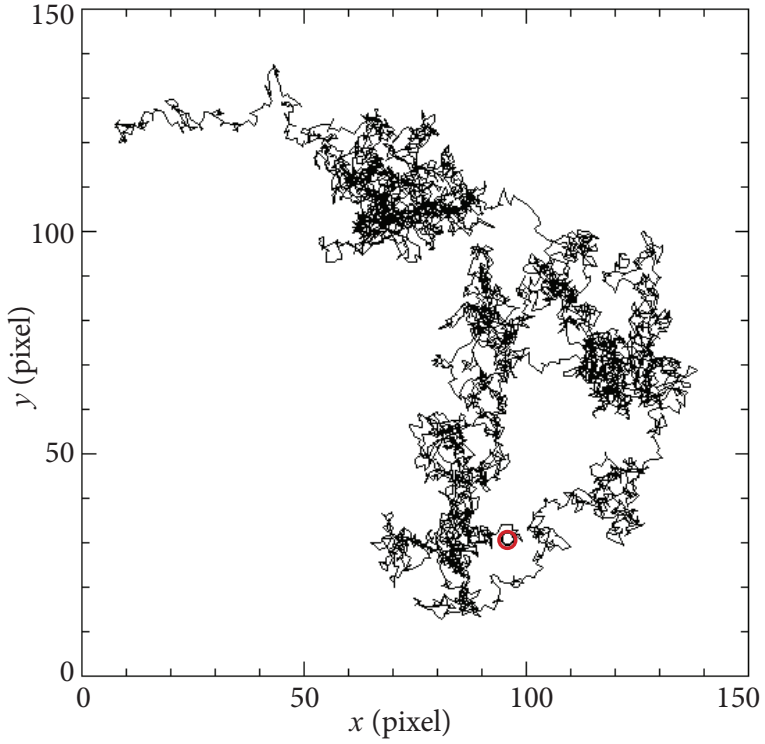

Figure 2.9: A typical single-particle trajectory of the Brownian motion of a particle in a dilute 2D suspension. The red circle indicates the initial position. The interval time of each step is 0.1 s and the total time is 600 s. 1 pixel = 0.095 µm. The diameter of the PMMA particle is 2.08 µm.

pair correlation functions ($g(r)$), and self-intermediate scattering functions (F_s) can be further calculated, which will be used to understand many phenomena in this work. More details will be discussed in the following chapters (Chapter 3, Chapter 4, and Chapter 5).

Chapter 3

3D Confinement*

3.1 Introduction

Understanding the nature of the glass transition is one of the most challenging problems in condensed matter physics [117, 118, 119, 120]. Although ubiquitous and technically important, glasses still elude a universally accepted theoretical description. A molecular glass forms when the temperature of a liquid is quenched below its glass transition temperature T_g. Near the transition, the relaxation of a liquid can slow down by many orders of magnitude with only a modest decrease of temperature by a factor of 2 or 3. The classical thermodynamic theory of Adam and Gibbs suggests that such a super-Arrhenius temperature dependence arises from cooperative particle rearrangements in localized regions that are related to the configurational entropy of supercooled liquids [3, 17].

*Reproduced in part with permission from (Bo Zhang and Xiang Cheng, "Structures and dynamics of glass-forming colloidal liquids under spherical confinement", *Physical review letters*, American Physical Society).

To illustrate the static correlations associated with these localized regions, "point-to-set" correlations have recently been proposed in the framework of the random first-order transition theory (RFOT) [14, 22, 121, 122], which is a modern development of the Adam-Gibbs theory unifying physical insights from the mode coupling theory and the spin glass theory [117, 118]. In the RFOT, a gedankenexperiment was conceived [22], where particles outside a cavity of radius R in a supercooled liquid are suddenly frozen while the particles inside the cavity are allowed to freely evolve. The point-to-set correlation length, ξ, is defined as the minimal R such that the particles at the center of cavity are not affected by the pinning field imposed by the boundary. A cavity with $R < \xi$ constrains the system into a local minimum of the free-energy landscape and captures an "amorphous order" particle configuration nucleated within the liquid. Numerical simulations on molecular glass-forming liquids have demonstrated an increase of ξ close to T_g [14, 22, 121, 122]. More recently, following a different protocol, Nagamanasa *et al.* have investigated semi-infinite 2D colloidal liquids with a wall of particles pinned in an equilibrated configuration and have experimentally confirmed the existence of static point-to-set correlations away from the pinning wall [122, 123].

Nevertheless, important questions remain unanswered. First, it is still an open question if and how the static correlation develops in 3D experimental systems similar to the gedankenexperiment. Second, recent theory has suggested that, instead of frozen equilibrated boundaries, confined systems with conventional boundaries exhibit a qualitatively similar trend for the development of static correlations [24]. Although confined systems have been extensively studied in probing the dynamics of glass-forming liquids [46, 74, 124, 125, 126, 127, 128, 129, 130], it has yet to be verified if the predicted static correlation exists in these supposedly familiar systems. Lastly, there still lack systematic experiments that examine how the configurational entropy associated with

static correlations varies when a confined colloidal liquid approaches the glass transition. Quantitative understanding of the variation of the configurational entropy is of great importance in shaping the glass transition theory [17, 117]. Our experiments aim to address these questions.

3.2 Methods

3.2.1 Fluorescent Label of PMMA Particles

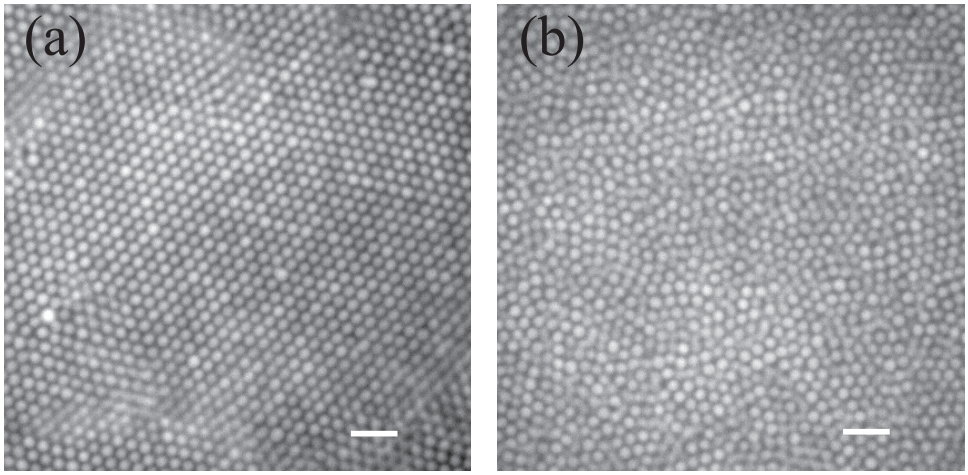

Figure 3.1: Confocal images of synthesized Nile Red labeled PMMA colloidal particles in the form of crystal (a) and glass (b). The scale bar is 5 μm.

The colloidal particles used this chapter are poly(methyl methacrylate) (PMMA) spheres we synthesize in our lab. The PMMA spheres are sterically stabilized by the covalently bonded poly(1,2-hydroxy stearic acid) (PSHA) polymer brushes with a typical length about 20 nm on particle surfaces [131, 132, 133, 134, 135, 136]. The PSHA brushes can efficiently prevent particle aggregations due to van de Waals forces when charges on particle surfaces are sufficiently screened by adding salts. PMMA particles are fluorescently labeled by Nile Red during the synthesis to provide a good fluorescence

function for the imaging by a confocal microscope. More information about the fluorescence and confocal microscopy, please refer to Chapter 2.1. For more details about the particle synthesis and fluorescent labelling, please refer to Appendix A.1 and B.2.

Fig 3.1 shows typical confocal images of Nile Red labeled PMMA particles. Individual particles can be distinguished and analyzed by methods described in Chapter 2.3. In our experiments, we use PMMA colloidal particles of two different sizes $d_s = 1.29$ μm and $d_l = 1.64$ μm (Figs. 3.4 a, b), which effectively prevent the crystallization in the system. The polydispersity of each size is smaller than 5% and the number ratio of particles is fixed at 2:1. PMMA particles are suspended in a mixture of decahydronaphthalene (decalin, 15 wt%) and cyclohexyl bromide (CXB, 85 wt%) that matches both the density and refractive index of the particles. The solvent is saturated with tetrabutylammonium bromide salt (TBAB) to screen the charge to minimize electrical repulsions between particles and make the particles perform as near hard-sphere particles [133, 134, 135, 136].

3.2.2 Sample Preparation

The PMMA suspensions then are transferred to a gelatin and sugar aqueous solution at $T = 70$ °C (Fig. 3.2). After mixed by hand shaking or vortex, oil/water emulsions are generated. The sizes of droplets have a broad distribution from several micrometers up to several millimeters, which are controlled by the strength of shaking or vortex. The emulsions are then injected into a sample cell (Fig. 3.3). When the temperature is cooled down to the room temperature, the aqueous phase solidifies through gelation, which traps one layer of particles at the oil-water interface. The sample cell is sealed by a UV adhesive (NOA 81, Norland Products, Inc.) to prevent any further evaporations during experiments. The sample can maintain same for more than a month if it is sealed well. The gelatin is added to solidify the aqueous phase while the sugar can increase the

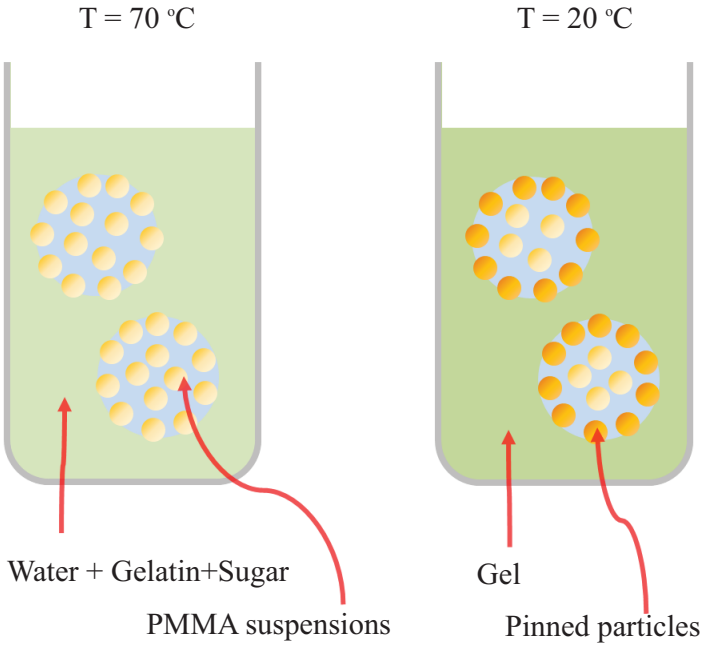

Figure 3.2: Construction of 3D spherical confinement by solidifying the aqueous phase of O/W emulsions. Gelatin is added to solidify the aqueous phase through the gelation when the temperature decreases from 70 °C to 20 °C. Sugar is added to increase the refractive index of the aqueous phase from 1.33 (water) to 1.48 to match the refractive index of the oil phase (PMMA suspensions, 1.49). Sugar is oversaturated in room temperature but the whole system stays uniform within a month.

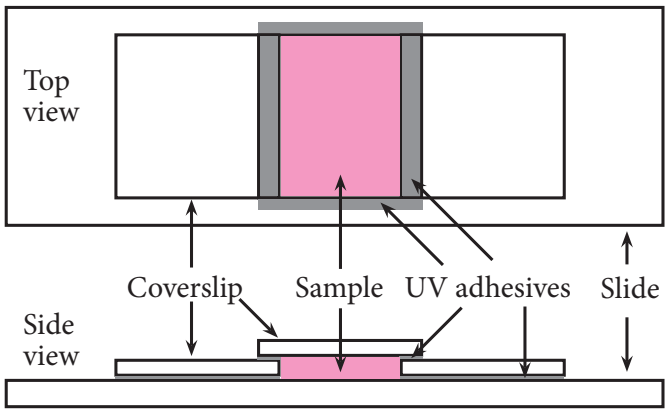

Figure 3.3: Geometry of a typical sample cell. Two coverslips are bonded on a glass slide by a UV adhesive. Then another coverslip is attached on the top of two lower coverslips. The sample is injected from one open side to remove any air inside of the cell and both open sides are sealed after the injection.

refractive index of the aqueous phase to match the refractive indices of PMMA particles and the solvent mixture.

3.2.3 Data Collection

After the injection of the sample and the sample being totally solidified, the sample cell is placed inverted on a confocal microscope. The sample is usually left at least overnight for the solidification process. A 100× oil immersion objective with a working distance about 100 μm is used for imaging. Fig 3.4a shows a confocal image of the cross section of a droplet along its equator. The image time series are recorded by a CCD camera with the speed 0.5 - 10 FPS (frames per second) for 10 min - 4 h depending on the volume fractions of droplets. For the study in this chapter, particle dynamics are all calculated based on the information at cross sections. Since the spherical droplet is highly symmetric, the dynamics at the cross sections should provides similar information as these based on whole 3D confined droplets.

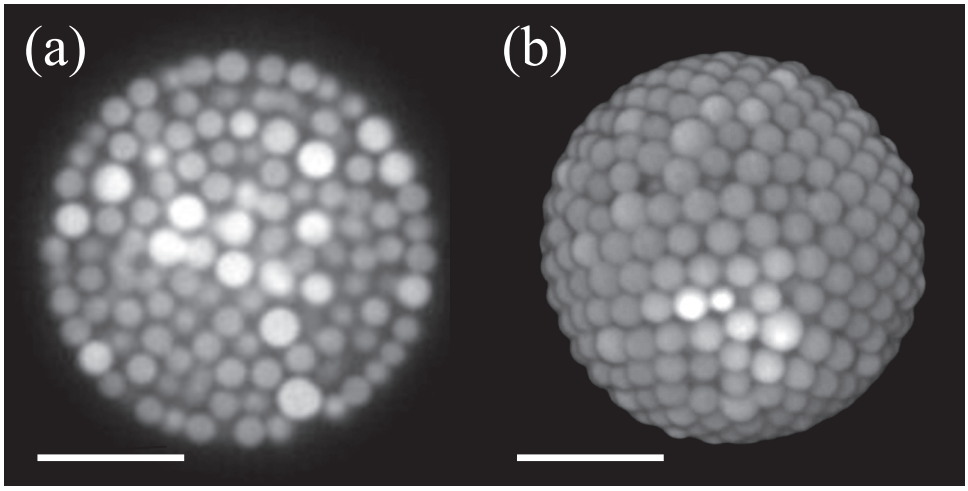

Figure 3.4: Imaging data collected by confocal microscopy. (a) Confocal image of a cross section of a droplet along its equator. (b) 3D reconstruction of the z-stack confocal images of the droplet. The scale bar is 5 μm.

3.2.4 Volume Fraction Measurements

Although it is difficult, if not impossible, to measure the absolute value of volume fraction ϕ to within a few percent, the uncertainty on the relative ϕ of our samples (compared to other samples using same batch of particles) is smaller than 0.6 % [137]. The uncertainty on the absolute value of volume fractions is mainly due to the uncertainty on the size of particles and the undetermined interparticle interactions such as residual electrostatic repulsion and particle softness. As pointed out by Poon, Weeks and Royall in their well-written review paper [137], the problem of the large uncertainty on particle volume fractions is faced by almost all the colloidal experiments. Specifically for experiments on confined colloidal liquids [46, 74, 127, 128, 130], the presence of the confining boundary introduces extra uncertainty in determining volume fractions. Below, we explain the detailed procedure we adopted in determining the volume fraction of our samples. As suggested by Poon *et al.*, although it is difficult to remove the experimental uncertainty on volume fractions, the detailed information on the experimental

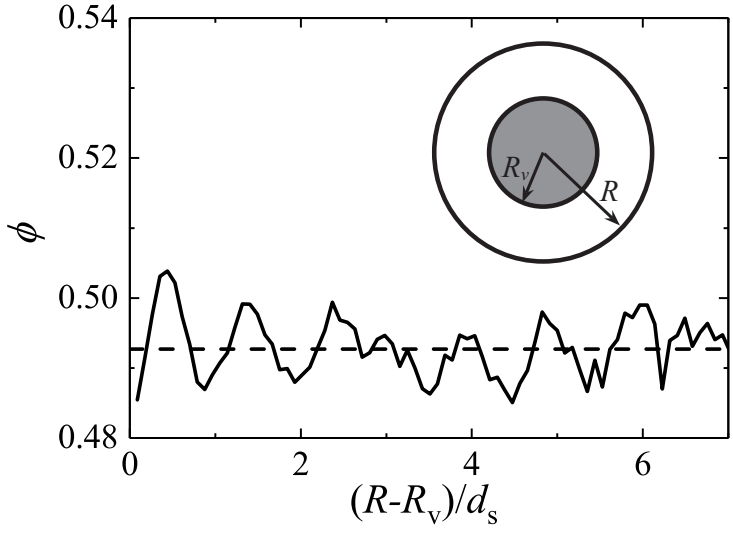

Figure 3.5: Measurement of the volume fraction of a confined sample with $R = 20d_s$. $(R - R_v)/d_s$ is the distance away from the pinned boundary. The volume fraction is measured based on the particles within the radius of R_v. The dashed line indicates the average volume fraction of the confined sample near the center of the droplet.

procedure will help to clarify how we determine the volume fractions, so that a similar procedure can be used, or at least be considered, when our results are compared with results from other experiments and simulations [137].

The whole droplet is imaged with a z-stack scanning to calculate the (relative) volume fraction of the droplets. (Fig 2.5, Fig 3.4b). From the z-stack images, the total volume can be obtained and the numbers of larger particles and small particles are counted with the help of the image analysis (Chapter 2.3). Then the volume fraction ϕ of the droplet is calculated by:

$$\phi = \frac{4\pi(N_l a_l^3 + N_s a_s^3)}{3V}, \tag{3.1}$$

where, a_l and a_s are the radii of the larger and smaller particles and N_l and N_s are the numbers of the larger and smaller particles in the volume of V. The number ratio of the larger and smaller particle is fixed at 1/2.

The large uncertainty up to a few percentage on the volume fraction of colloidal samples arises from the difficulty in precisely determining the size of particles, which is compounded by particle polydispersity and possible residual interparticle interactions [137]. By contrast, measurements on the number of large and small particles have much less uncertainties. We obtain the number of particles and the type of particles (i.e. small vs large) based on the standard 3D particle finding algorithm [116]. We then visually crosscheck the finding results with the raw images of all our samples. After the crosscheck and subsequent correction, we estimate the error on the value of N_s and N_l is smaller than 0.6 %, i.e., one particle in a few hundred particles may be misidentified. The absolute value of volume fractions depends on a_s and a_l, which have large uncertainties. However, because the same colloid batch is used in our experiments, the relative volume fractions between two samples under different confinements is given

by $\phi_1/\phi_2 = N_{s1}/N_{s2}$ independent a_s and a_l and, therefore, has much less uncertainties.

Although the absolute volume fractions have large uncertainty up to a few percentage, we nevertheless provide the best estimate of the absolute volume fraction of our samples. Specifically, we determine the average size of small and large particles from the location of the first peak of the pair correlation function of the corresponding close-packed bulk samples. Averaging over large numbers of particles, pair correlation functions provide one of the most accurate methods for determining particle sizes from confocal microscopy [137].

Although we use two different size particles to reduce the degree of particle layering, a certain degree of particle layering does occur in our system near the confining boundary, which is typical for confined colloidal experiments [46, 74, 130]. In our experiments, to reduce the influence of these boundary layers, we limit our measurement to the central region of cavities. To determine the volume fraction of samples inside cavities, we measure the volume fraction as a function of distance away from the boundary (Fig. 3.5). The volume fraction shows a smooth oscillation near the boundary due to the presence of particle layers. The more noise-like oscillation near the center of the cavity arises due to the loss of the layering order and due to the statistical noise from the finite size effect. Note that the number of particles reduces when the volume fraction is measured in a smaller region near the center of the cavity (Fig. 3.5 inset).

Specifically, in our experiments, we determine the volume fraction of confined samples by averaging the oscillatory volume fractions near the center of cavities. For the data shown in Fig. 3.5, the method gives $\phi = 0.493 \pm 0.004$ (black dashed line). The error here is the standard deviation from the average. Apparently, as the radius of cavities increases, this averaging method naturally leads to the volume fraction of bulk samples.

3.3 Results

3.3.1 3D Confined Geometry Built by Pinned Particles

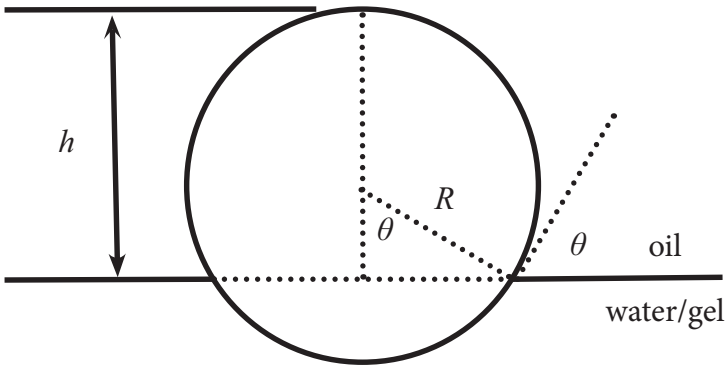

Figure 3.6: Protrusion of PMMA particles at the oil-water interface.

In addition to preventing the crystallization, particles of different sizes randomly trapped at the boundary of cavities also roughen the boundary surface. Since the contact angles of particles at the oil-water interface are the same for both big and small PMMA particles, from a simple geometrical consideration (Fig. 3.6), the height of interfacial particles protruded into cavities is given by

$$h = R(1 + \cos\theta), \tag{3.2}$$

where R is the radius of PMMA particles and θ is the contact angle between particles and the oil composed of the mixture of decalin and CXB. θ is estimated to be $0° < \theta \leq 15°$ [135]. Thus, interfacial particles of different sizes protrude into cavities with different heights, h, and lead to rough, rather than smooth, surfaces.

It should be emphasized that the rough boundaries in our system are not the exactly same as the equilibrium boundaries of the gedankenexperiment proposed in the RFOT

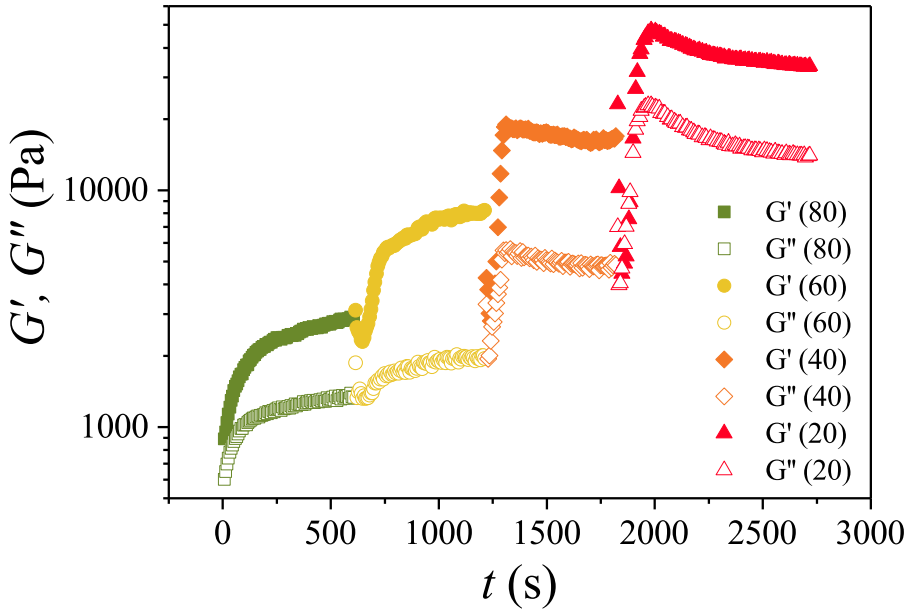

Figure 3.7: Rheology measurements of the gelatin aqueous solution/gel at different temperatures. Solid symbols show the elastic moduli and hollow symbols are viscous moduli at different temperatures shown in the legend with the unit of °C. The high elastic modulus at room temperature ($T = 20$°C) indicates that the aqueous phase is solid.

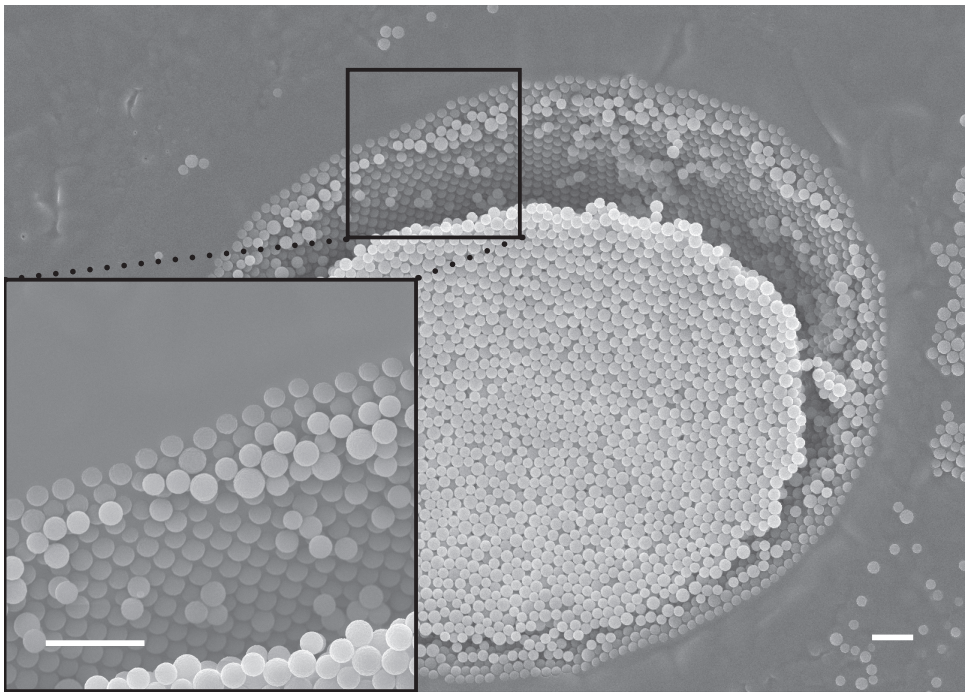

Figure 3.8: A SEM image of a large cavity. The inset shows an enlarged view of the boundary. A layer of particles pinned at the interface can be identified. The asymmetric shape is caused by the shear stress from the cutting when the sample is prepared for SEM imaging. The scale bar is 5 μm.

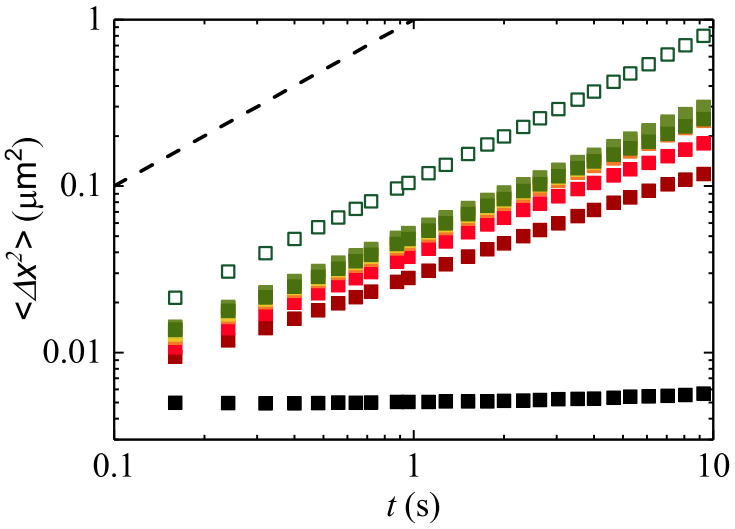

Figure 3.9: Mean square displacements, $\langle \Delta x^2 \rangle$, of particles at different distances, r, away from the boundary in a cavity of $R = 32.5 d_s$. From bottom to top, $r = 0 d_s$ (the pinned boundary layer), $1 d_s$, $2 d_s$, $3 d_s$, $4 d_s$, $5 d_s$, $7 d_s$, $9 d_s$, $11 d_s$, $13 d_s$, $15 d_s$, $17 d_s$ and $19 d_s$. The empty squares are for a bulk sample of the same ϕ. The suspension has $\phi = 0.425$. The boundary layer shows zero motions with the constant indicating the noise level of our tracking algorithm.

[22]. For equilibrium boundaries where interfacial particles are fixed in equilibrium positions, when the size of the system is smaller than the point-to-set correlation length, the system is trapped into a single state, i.e., the ideal glass state [22, 24]. By contrast, for rough boundaries of our system, the pinning boundary allows multiple states compatible with the positions of fixed particles. These states all have comparable "surface energy" around k_BT, arising from the free-energy mismatch at the boundary. Thus, the rough boundaries allow the interstate dynamics. However, the rough boundaries do significantly reduce the number of possible states, which leads to non-zero $(q_c - q_{rand})$ as shown in Fig. 3.15. Indeed, recent theoretical studies by Cammarota *et al.* have showed that, when the system goes through the glass transition, the divergence of the "point-to-set" length measured in confined systems exhibits a quantitatively similar trend as the true point-to-set correlation length of the RFOT gedankenexperiment [24]. As such, these authors suggested that confinement provides a direct tool for probing the amorphous order of the glass transition [24].

The gel has an elastic modulus $G' > 10$ kPa, leading to a yield energy, $G'd_s^3$, 10^6 times larger than the thermal energy k_BT. Thus, particles across the interface are permanently pinned, as confirmed by both scanning electron microscopy (SEM) (Fig. 3.8) and mean square displacement (MSD) measurements (Fig. 3.9). Particle dynamics inside the cavities are recorded using a spinning-disk confocal microscope. The radius of the cavities, R, is measured from the average position of the centers of the pinned particles (Fig. 3.12). We exclude the pinned layer when measuring the volume fraction of the samples, ϕ.

MSDs show a sharp gradient in the slowdown of the particle dynamics near the confining surface. Three particle diameters away from the pinned layer, the particles already exhibit slow yet uniform dynamics (Fig. 3.9), consistent with the particle dynamics in emulsion droplets with high-viscosity outer fluids [130]. Thus, the particle

dynamics near the center of the cavities reveals the true confinement effect, instead of the wall-induced interfacial effect that is usually present in confined colloidal systems [46, 74, 125, 126, 127, 128, 129, 130].

3.3.2 Particle Structures in Confined Samples

The pair correlation function, $g(r)$, of a confined sample near the center of a cavity is shown in Fig. 3.10a. We find that $g(r)$ of confined samples is qualitatively the same as amorphous bulk samples. To show the angle-dependent structures, we also measure the 2D pair correlation functions, $g(x, y)$ (Fig. 3.10b and c). Similarly, the confined sample near the center of a cavity shows a qualitatively similar structure as that of a bulk sample of a similar volume fraction. Since we probe particle dynamics and structures near the center of cavities, these structural measurements show that the influence of particle layering near the confining boundary is small in our measurement regions.

The structural factor S(Q) of bulk colloidal suspensions composed of the small particles at $\phi = 0.43$ is shown in Fig. 3.11. The first peak of $S(Q)$ locates at $Q = 7.4/d_s$, which is used for measuring $F_s(t)$ (Eqn. 3.5 below). $S(Q)$ is calculated from the Fourier integral of the 2D pair correlation function of the sample, $g(r)$:

$$S(Q) = 1 + 2\pi\rho \int_0^\infty r(g(r) - 1)\frac{\sin(Qr)}{Qr}dr. \tag{3.3}$$

3.3.3 The Static Length Scale

With these specially prepared cavities, we measure the correlation of configurations between the particles at the center of the cavities and the set of particles pinned at the boundary, i.e., the point-to-set correlation. Following the RFOT protocol [22], we choose an area of size $3.7d_s \times 3.7d_s$ at the center of the cavities excluding the particles with non-uniform dynamics near the boundary (Fig. 3.12). The area is further divided into

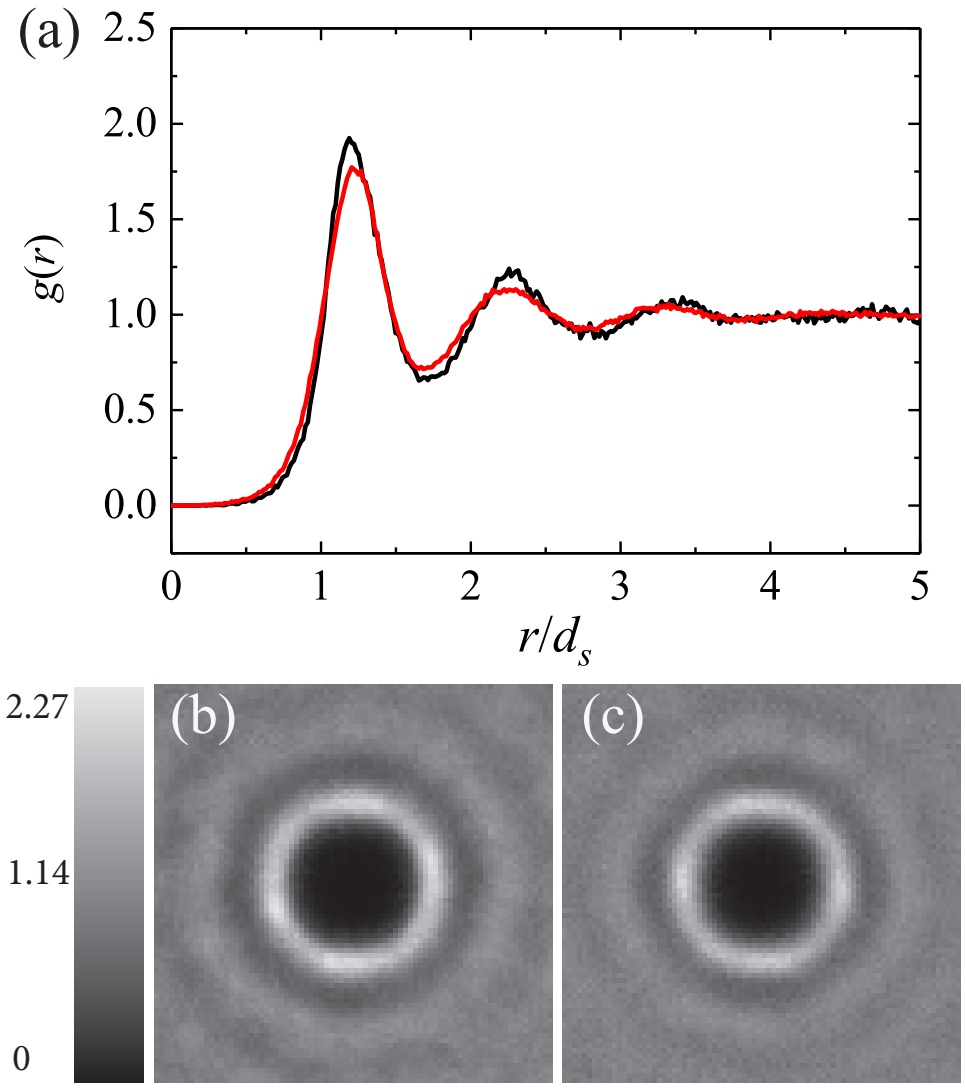

Figure 3.10: Particle structure in confined and bulk samples. (a) The pair correlation function, $g(r)$, of colloidal suspensions with $\phi = 0.50$ for a confined sample with $R = 8.5d_s$ (black line) and a bulk sample (red line). 2D pair correlation function $g(x,y)$, of colloidal suspensions in the same (b) confined sample and (c) bulk sample.

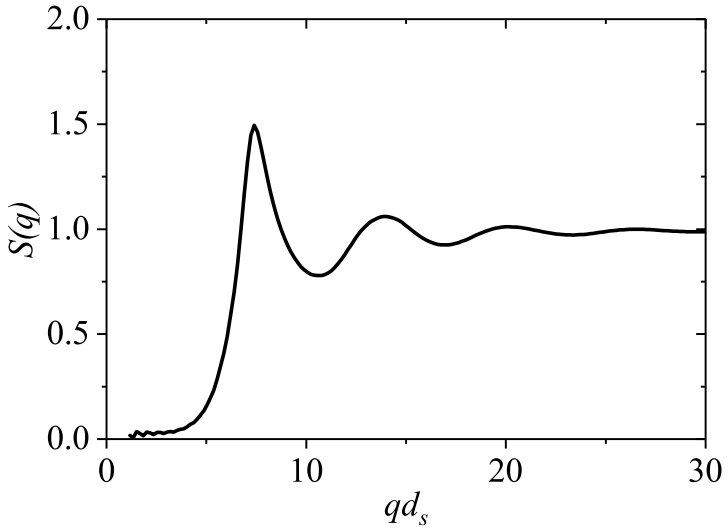

Figure 3.11: Structural factor $S(Q)$ of bulk colloidal suspensions composed of the small particles at $\phi = 0.43$.

10-by-10 small boxes. The box size is small enough such that the number of particles in the box j is either $n_j = 0$ or 1. The overlap function that quantifies the correlation between the initial configuration and the configuration after a time interval t is defined as:

$$q_c(R,t) = \frac{\sum_j \langle n_j(t_0) n_j(t_0+t)\rangle}{\sum_j \langle n_j(t_0)\rangle}, \tag{3.4}$$

where the average is taken over the initial time t_0. Fig. 3.13 shows $q_c(R,t)$ at two different ϕ. At $\phi = 0.41$, q_c decays to a plateau, which shows a weak dependence on the degree of confinement. However, at $\phi = 0.54$, the confinement exerts a stronger influence on q_c. For small cavities with $R \leq 16.5 d_s$, q_c decays slowly across the entire time window of our experiments.

Two factors determine the time variation of q_c: (*i*) the development of a true static point-to-set correlation; (*ii*) the slowdown of particle dynamics near the glass transition, which deteriorates further due to the effect of confinement [46, 74, 127]. To characterize

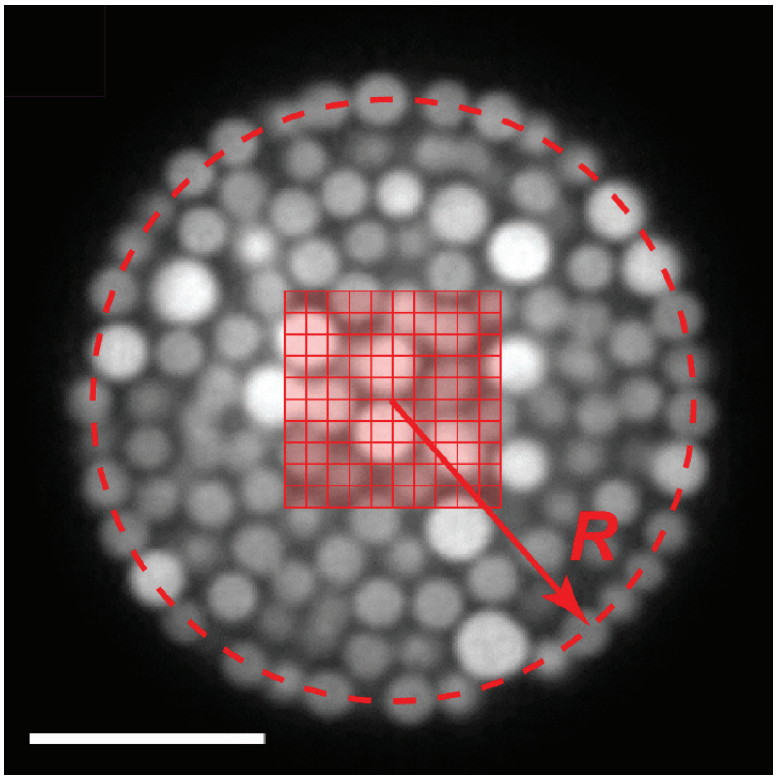

Figure 3.12: Illustration of boxes used in q_c measurements. The 10-by-10 boxes at the center is the whole area used for the calculation. The size of each box is $0.37d_s \times 0.37d_s$.

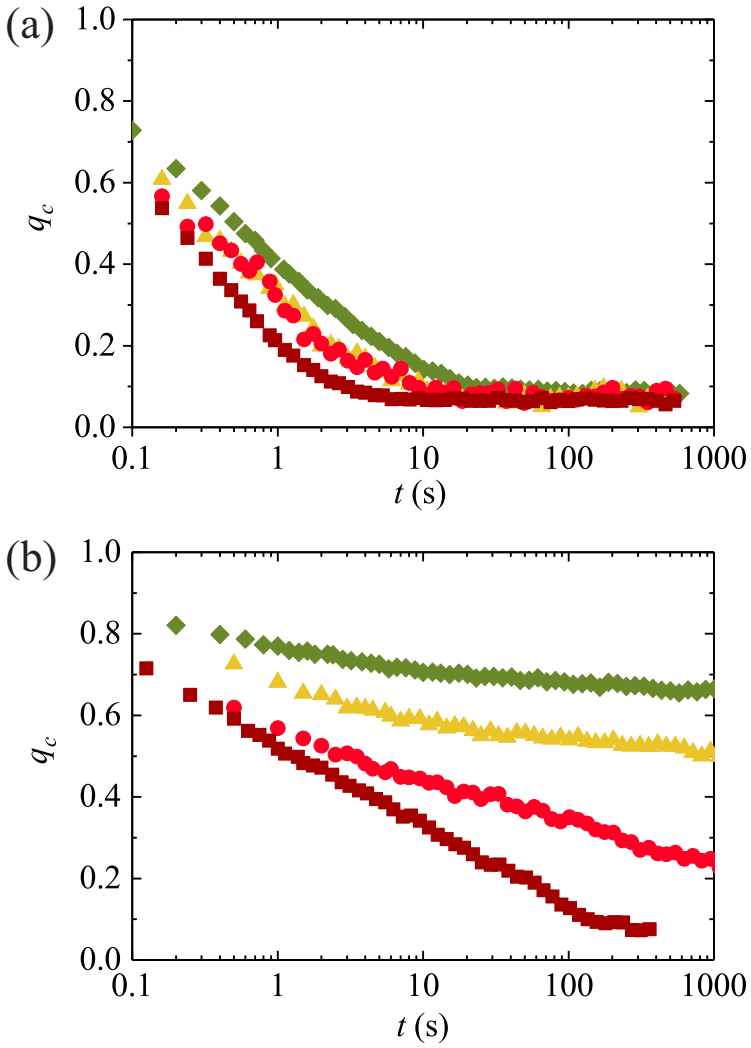

Figure 3.13: Point-to-set correlations in confined colloidal liquids. The time variation of the overlap function, q_c, for different cavities with $\phi = 0.41$ (a) and $\phi = 0.54$ (b). From top to bottom, $R = 8.5d_s$ (green diamonds), $16.5d_s$ (yellow triangles), $32.5d_s$ (red circles) and bulk (dark red squares).

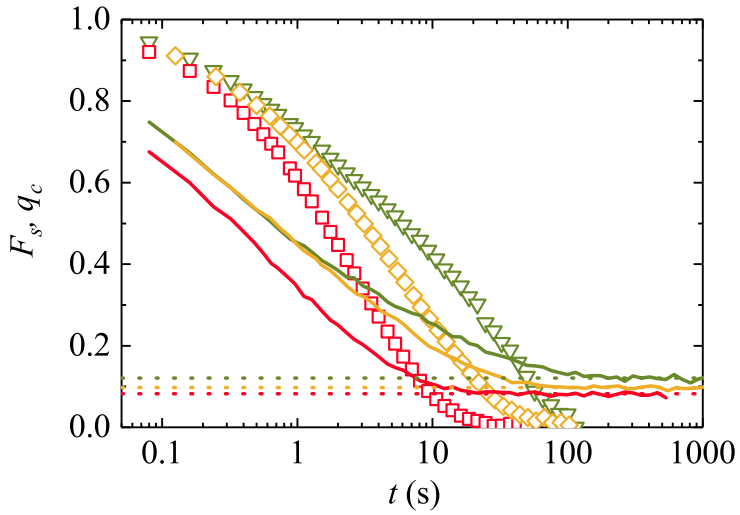

Figure 3.14: Comparison of self-intermediate scattering functions, $F_s(t)$ (symbols), and $q_c(t)$ (solid lines) at $\phi = 0.475$. $R = 4.5d_s$ (green triangles), $8.5d_s$ (yellow diamonds) and bulk (red squares). F_s reaches 0 when q_c decays to non-zero plateaus (dotted lines).

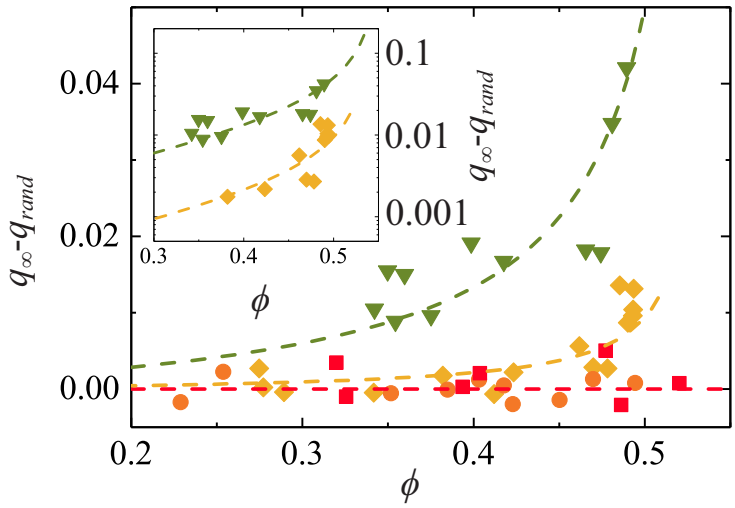

Figure 3.15: Equilibrium overlap function, $(q_\infty - q_{rand})$, versus ϕ in the linear scale (main plot) and the semi-log scale (inset). $R = 4.5d_s$ (green triangles), $8.5d_s$ (yellow diamonds), $32.5d_s$ (orange circles) and bulk (red squares). The dashed lines are visual guides.

and then exclude the influence of slow particle dynamics on $q_c(t)$, we investigate single particle dynamics through the self-intermediate scattering function:

$$F_s(Q,t) = \langle \frac{1}{N} \sum_j \cos\left(Q \cdot [x_j(t_0+t) - x_j(t_0)]\right) \rangle, \tag{3.5}$$

where we choose $Q = 7.4 d_s^{-1}$ from the position of the first peak of the structural factor $S(Q)$, $x_j(t)$ is the location of particle j at time t and N is the number of particles in the studied area. Note that, different from q_c, F_s represents a self-correlation, equivalent to the self-overlap function $q_c^{self} \equiv \sum_j \langle n_j^s(t_0) n_j^s(t_0+t) \rangle / \sum_j \langle n_j^s(t_0) \rangle$, where $n_j^s(t_0) n_j^s(t_0 + t) = 1$ only when the *same* particle occupies the cell j at time t_0 and $t_0 + t$. F_s exhibits a characteristic two-step relaxation above a certain $\phi(R)$ (Fig. 3.18). We find that q_c reaches the plateau when F_s decays to 0 (Fig. 3.14) [122, 138]. Accordingly, we measure the equilibrium overlap, $q_\infty = q_c(R, t = t^*)$ at a time t^* when $F_s = 0$. The protocol ensures that our measured q_∞ is a true thermodynamic quantity reflecting the structural rather than the dynamic signatures of the system. Specifically, we average the plateaued q_c in a time window over 200 s to reduce statistical errors. Since a bulk sample does not develop the static correlation before the ideal glass transition [22, 24], q_∞ of bulk samples defines $q_{rand}(\phi)$—the overlap between two uncorrelated configurations at a given ϕ. $q_{rand}(\phi)$ forms the baseline for comparison, which we obtain from both experiments and theoretical and numerical calculations.

Fig. 3.15 shows $[q_\infty(\phi) - q_{rand}(\phi)]$ for different confinements. q_∞ deviates from q_{rand} at $\phi \approx 0.47$ for the cavities of $R = 8.5 d_s$, indicating a static point-to-set correlation length $\xi \gtrsim 8.5 d_s$, similar to that found in unconfined 2D systems [123]. Compared with bulk samples of the same ϕ, particles inside a small cavity equilibrate and sample fewer numbers of states that are compatible with the constraint of pinned boundaries, which, therefore, leads to a larger overlap [24]. Different from equilibrated boundaries that

pin particles in a single state when $R < \xi$, our confining boundaries allow degenerate states and interstate dynamics. Consistent with the RFOT, the increase of q_∞ with ϕ becomes more drastic as R is reduced (Fig. 3.15). Since the size of the amorphous-order particle clusters increases with ϕ, a smaller cavity captures the emergence of the clusters at lower ϕ and, thus, exhibits a larger q_∞.

3.3.4 Influence of the Depth of Field on Point-to-Set Correlations

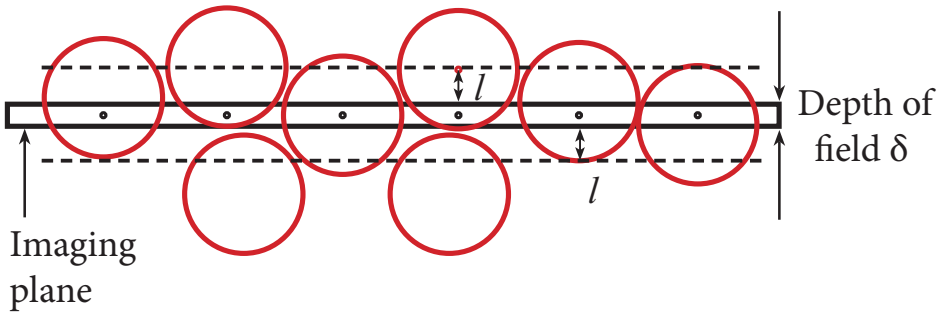

Figure 3.16: Schematic showing the experimental imaging method. The red dots indicate the center of particles and the black dots are the projection of the particle centers on the imaging plane, which are the particle positions measured in our experiments. Particles are identified by the image analysis algorithm only when the centers of particles are within the distance l of the imaging plane between two dashed lines.

To explain the detailed experimental procedure for measuring the overlap function q_c (Eqn 3.4), it is necessary to clarify our experimental imaging method. We adopt the standard method for measuring colloidal dynamics near the glass transition with confocal microscopy, where 2D particle dynamics in 3D samples, rather than full 3D particle dynamics, are imaged [46, 74, 127, 128, 130]. Confocal microscopy has a depth of field on the order of the wavelength of light, smaller than the size of particles we

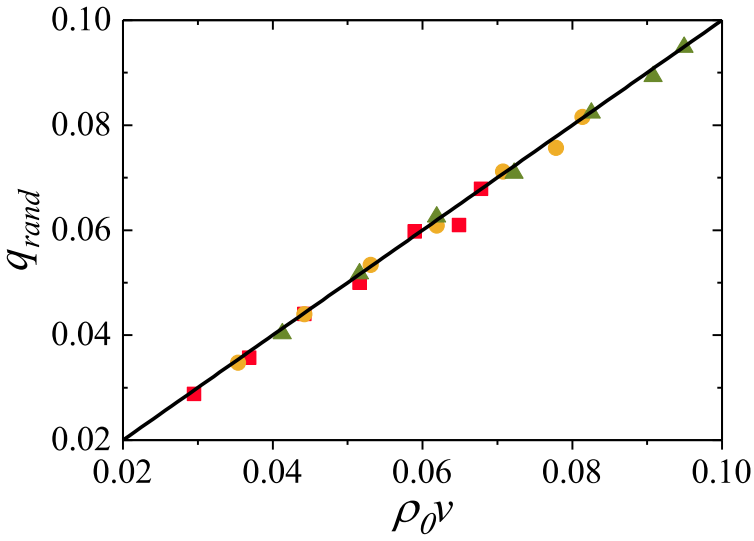

Figure 3.17: q_{rand} of equilibrated colloidal suspensions of different ϕ from simulations. $l = 0.39d_s$ (red squares), $0.47d_s$ (yellow circles), and $0.54d_s$ (green triangles). The solid line indicates $q_{rand} = \rho_0 v$.

used. Hence, the imaging essentially measures the projection of the center of particles onto a 2D plane, which is chosen at the equatorial plane of cavities in our experiments (see the schematic shown in Fig. 3.16). The red dots in the schematic indicate the center of particles, whereas the black dots indicate the position of the center of particles projected onto the 2D plane we measure in our experiments. As a result, our experiments resolve 2D particle dynamics within the imaging plane. Since the dynamics of particles are isotropic and the three translational degrees of freedom are independent, the 2D dynamics show the same characteristics as the 3D particle dynamics. Lastly, it should be emphasized that, before each dynamics measurement, we scan each sample in 3D to acquire a static 3D structure of the sample. The volume fractions of our samples are calculated based on the 3D particle positions obtained from these 3D scan measurements.

Our experimental method shown above determines that the shape of each small box

for calculating the overlap function q_c in our study is equivalent to a cuboid with the dimension $0.37d_s \times 0.37d_s \times 2l$. Here, l is the maximal distance between the center of a particle and the location of the imaging plane, where the cross-section of the particle at the imaging plane is large enough to be identified by the particle finding algorithm (Fig. 3.16). $2l$ arises from the fact that particles on both sides of the imaging plane need to be considered. We investigate the value of l in detail. By comparing our experimental results with simulations on random colloidal samples of the same volume fraction (we shall show the detail of the procedure below), we find that l is a weak function of confinements. This is presumably due to the slightly mismatched index refraction between the gel phase and the oil phase, which affects the image quality at different R and modifies the minimum particle sizes we can identify with our algorithm. We find l increases from $0.43d_s$ for bulk samples to $0.5d_s$ for highly confined samples. Since q_{rand} is proportional to the volume of the small box (shown in Fig. 3.17), the change of l indeed induces a systematic error in $(q_\infty - q_{rand})$. To remove this error, we obtain $q_{rand}(\phi, l(R))$ from numerical and theoretical calculations for each R (shown in Fig. 3.17) and then calculate $[q_\infty(\phi, R) - q_{rand}(\phi, l(R))]$ (Fig. 3.15).

Theoretically, $q_{rand} = v\rho_0$, where v is the volume of the small box and ρ_0 is the particle number density [139, 122, 123]. To verify this relation in our study with cuboidal boxes and to obtain the theoretical value of $q_{rand}(\phi, l(R))$, we perform Monto Carlo simulations to generate a large number of equilibrated random hard-sphere packs at different ϕ. These equilibrated random packs compose of hard-sphere particles of two different sizes with the size ratio and the number ratio matching those of our experiments. A typical system in our simulations contains 4000 particles with periodic boundary conditions. After creating these packs, we obtain the 2D particle positions following our experimental procedure shown in Fig. 3.16 with l taken as a control input parameter. The value of l in our experiments can thus be determined by matching the 2D

particle density in the imaging plane from our experiments with that from simulations of random packs of the same ϕ. (Note that since ϕ is measured based on 3D particle positions in both experiments and simulations, ϕ is independent of l.) l thus obtained is consistent with our estimates based on the image quality and the accuracy of the particle finding algorithm [116]. We find l increases slightly for confined samples, as we have explained above. Finally, with the 2D particle positions, $q_{rand}(\phi, l)$ can be directly calculated using the definition of the overlap function (Eqn. 3.4). The large box of $0.37d_s \times 0.37d_s \times 2l$ for q_c measurements is chosen at the center of simulated packs, away from the periodic boundaries.

Regarding the results. Firstly, we find that q_{rand} obtained from simulations equals to $v\rho_0$, where $v = 0.37d_s \times 0.37d_s \times 2l$, agreeing quantitatively with theoretical predictions (Fig. 3.17). More importantly, we find that the theoretical q_{rand} confirmed by our simulations matches quantitatively with q_{rand} from our experiments (i.e., q_∞ of bulk samples) (Fig. 3.15). Lastly, $(q_\infty - q_{rand})$ is shown in Fig. 3.15, which unambiguously demonstrate the non-zero $(q_\infty - q_{rand})$ for confined samples at high ϕ and the development of a true static correlation. We find that samples with $R = 32.5d_s$ (diameter $D = 65d_s$) show zero $(q_\infty - q_{rand})$, whereas samples with smaller R show non-zero $(q_\infty - q_{rand})$. This is consistent with previous experiments on confined colloidal liquids, where the dynamics of confined samples reach the bulk limit at the length $\sim 30d_s$ [74].

3.3.5 Influence of the Static Correlation on Particle Dyanmics

Next, we investigate the influence of the static correlation on the relaxation of confined colloidal liquids. We obtain the relaxation time of the liquids, τ_α, by fitting the α relaxation of F_s with stretched exponential functions, $F_s(t) = A\exp[-(t/\tau_\alpha)^\beta]$, where A is the Debye-Waller factor (Fig. 3.18). τ_α as a function of ϕ for different R is shown in Fig. 3.19. Although the relaxation is much slower for samples under confinement

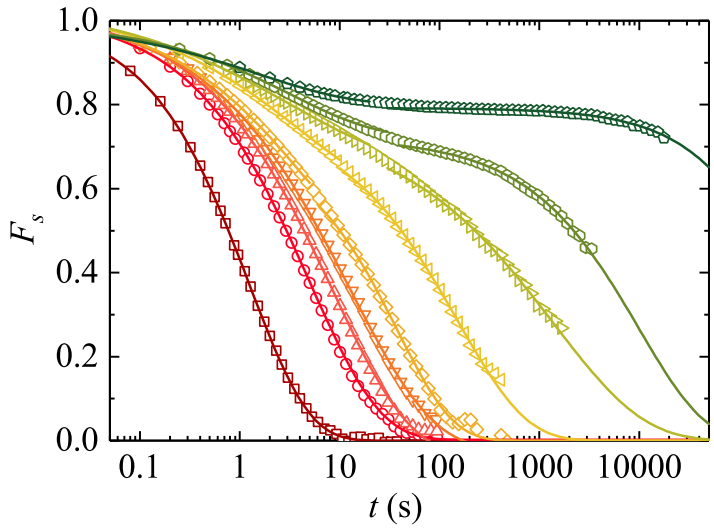

Figure 3.18: Relaxation of confined colloidal liquids $F_s(t)$ for $R = 16.5d_s$. From left to right: $\phi = 0.390$, 0.445, 0.485, 0.505, 0.509, 0.510, 0.515, 0.525 and 0.545. The solid lines are the stretched exponential fittings. Fittings on the highest volume fraction samples serve only as a visual guide.

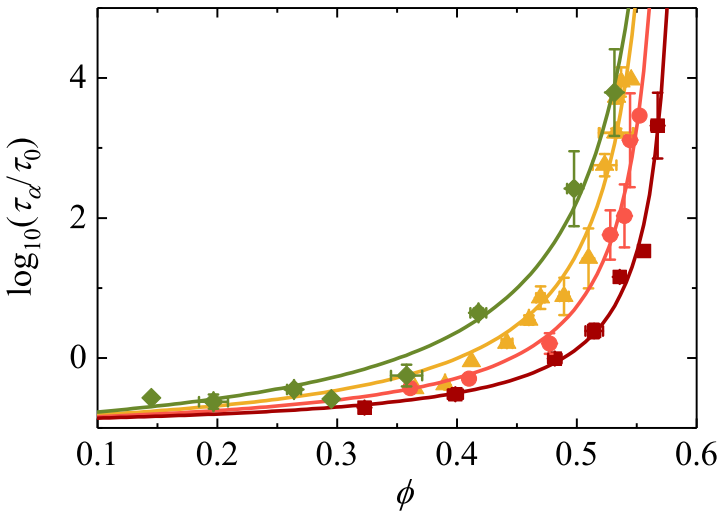

Figure 3.19: The α relaxation time, τ_α, as a function of ϕ. From top to bottom, $R = 8.5d_s$, $16.5d_s$, $64.5d_s$ and bulk. $\tau_0 = 2.87$ s is the Brownian relaxation time of small particles in the dilute limit. The solid lines are the VFT fittings.

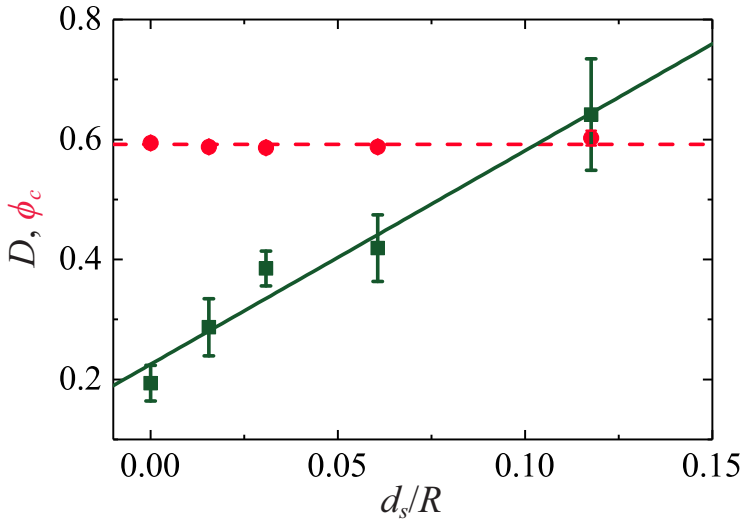

Figure 3.20: Critical volume fraction ϕ_c (red disks) and the fragility index D (green squares) as a function of d_s/R. The dashed line indicates $\phi_c = 0.592$ and the solid line is a linear fit.

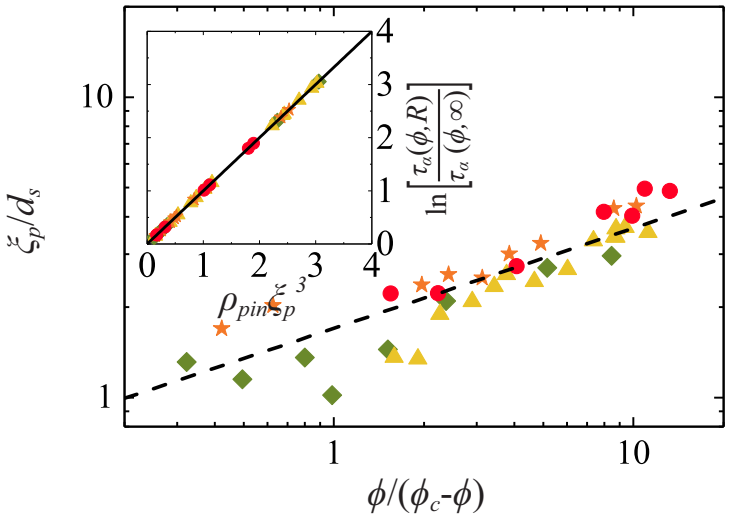

Figure 3.21: Pinning length ξ_p/d_s vs $\phi/(\phi_c - \phi)$. Besides the same symbols used in Fig. 3.18, the stars indicate $R = 32.5d_s$. The dashed line indicates the 1/3 scaling. The inset shows the collapse of $\ln[\tau_\alpha(\phi, R)/\tau_\alpha(\phi, \infty)]$ with a rescaled variable, $\rho_{pin}\xi_p^3$. The solid line is a linear fit.

[74, 127, 46], we find that a fitting of $\tau_\alpha(\phi)$ using the Vogel-Fulcher-Tammann (VFT) relation, $\tau_\alpha(R,\phi) = \tau_0 \exp[D\phi/(\phi_c - \phi)]$, gives a constant $\phi_c = 0.59 \pm 0.01$, independent of R (Fig. 3.20). ϕ_c is the volume fraction of the apparent divergence of the relaxation time and indicates the ideal glass transition in the Adam-Gibbs theory. Moreover, we find that the fragility index, D, increases linearly with $1/R$, following $D(R) = D(\infty)+c(d_s/R)$ with $c = 3.56$ (Fig. 3.20). Bulk samples have the smallest D and exhibit the most fragile behaviors. In addition to the confinement, the change of the fragility of glass-forming liquids has also been reported in experiments varying particle stiffness [140] and in simulations varying the curvature of space [141], the degree of polydispersity [142] and interparticle potentials [143]. Although our results are qualitatively similar to previous experiments on 2D confined vibrated granular particles [129], it is worth noting that the change of fragility in our 3D colloidal system is not due to the slowdown of particle dynamics near the wall as proposed in the previous study. When analyzing q_c and F_s, we only consider particles with uniform dynamics in the center of the cavities excluding the slow particles near the boundary (Fig. 3.9).

With due caution in interpreting the extrapolated data [117, 119], we can gain a quantitative understanding of the configurational entropy of confined colloidal liquids. From the Adam-Gibbs theory, the relaxation of a supercooled liquid is given by $\tau_\alpha \sim \exp[A_0\phi/s_c]$, which leads to the VFT relation when the configurational entropy density of the liquid $s_c = K(\phi_c - \phi)$, where K is a numerical constant and the fragility index $D = A_0/K$ [17, 50]. τ_α diverges when $s_c = 0$ and $\phi = \phi_c$. Our experiments show that the configurational entropy of colloidal liquids vanishes at a constant ϕ_c, independent of confinement. This result agrees with numerical studies on glass-forming liquids with randomly pinned particles [144], where the extrapolated Kauzmann temperature T_K is independent of the concentration of pinned particles, ρ_{pin}. Note that $\rho_{pin} \approx (d_s/R)(1/d_s^3)$ in our confined system.

Inspired by this similarity, we propose the following formula for the configurational entropy density of confined colloidal liquids [144]: $s_c(\phi, R) = F(R) \cdot s_c(\phi, \infty) = F(R) \cdot K(\phi_c - \phi)$, where $s_c(\phi, \infty)$ is the configurational entropy density of bulk samples at ϕ, and $F(R) \in (0, 1]$ is an increasing function of R with $F(\infty) = 1$. The relation is consistent with our experiments, i.e., $s_c(\phi, R) = 0$ at a constant ϕ_c independent of R. Furthermore, at a finite R, the system has a reduced number of states with $s_c(\phi, R) < s_c(\phi, \infty)$, resulting in a non-zero $(q_\infty - q_{rand})$ (Fig. 3.15). More importantly, under the Adam-Gibbs assumption, the relation leads to $\tau_\alpha(\phi, R) \sim \exp\left(A_0\phi / \left[F(R)K(\phi_c - \phi)\right]\right)$ with the confinement-dependent fragility, $D(R) = A_0/[F(R)K]$, which successfully interprets the decrease of $D(R)$ with increasing R (Fig. 3.20). Quantitatively, we have

$$\begin{aligned} \ln\left[\frac{\tau_\alpha(\phi, R)}{\tau_\alpha(\phi, \infty)}\right] &= [D(R) - D(\infty)]\left(\frac{\phi}{\phi_c - \phi}\right) \\ &= \left([D(R) - D(\infty)]\,\frac{R}{d_s}\right)\rho_{pin}\left(\frac{\phi d_s^3}{\phi_c - \phi}\right) \\ &= c\rho_{pin}\left(\frac{\phi d_s^3}{\phi_c - \phi}\right). \end{aligned} \tag{3.6}$$

Here, we use the experimental result, $[D(R) - D(\infty)] = c(d_s/R)$ (Fig. 3.20). Eqn. 3.6 can be further written in a scaling form [144]:

$$\ln\left[\frac{\tau_\alpha(\phi, R)}{\tau_\alpha(\phi, \infty)}\right] = f(\rho_{pin}\xi_p^3), \tag{3.7}$$

where $f(x) = x$ and

$$\xi_p/d_s = \left[c\phi/(\phi_c - \phi)\right]^{1/3}. \tag{3.8}$$

ξ_p represents a static length scale—the so-called pinning length—which is related to the point-to-set correlation length ξ through $\xi_p/d_s \sim (\xi/d_s)^{1/3}$ near the random-first-order transition and $\xi_p/d_s \sim \xi/d_s$ away from the transition [144, 145, 23]. To directly verify

the ξ_p scaling, we manage to collapse $\ln[\tau_\alpha(\phi, R)/\tau_\alpha(\phi, \infty)]$ by using a rescaled variable $\rho_{pin}\xi_p^3$ (Fig. 3.21 inset). $\xi_p(\phi)$ thus obtained indeed follows the predicted 1/3 scaling (Fig. 3.21). Note that $\xi_p(\phi)$ is an intrinsic property of colloidal liquids, independent of confinement [23, 144, 145]. Furthermore, the estimate of ξ based on the q_c measurement gives $\xi \gtrsim 8.5d_s$ at $\phi \approx 0.47$ (Fig. 3.15), leading to $\xi > \xi_p \approx 2.5d_s$, consistent with the scaling relation between the two length scales.

3.4 Discussion and Conclusion

3.4.1 The Issue of Equilibrium

We start our measurements a couple of hours after the samples have been equilibrated at room temperature, which provides sufficient time for the gelation of the aqueous phase. This waiting time allows most of our samples, except the highest volume-fraction samples under the strongest confinements, reach the equilibrium before measurements. Here, the relaxation time of samples can be directly estimated from the F_s measurements shown in Fig. 3.18. However, surprisingly, we find that even for samples of the highest volume fractions we use in our study, the dynamics of the systems seem to be independent of the waiting time. When performing experiments, we measure particle dynamics in different cavities in a random order. Thus, the samples with the highest volume fractions can be measured with the waiting-time difference as much as 24 hours. Such time-independent dynamics indicate that the samples have already reached equilibrium before our measurements. Presumably, this is because before the gelation completes, the liquid interface of emulsion droplets, instead the solid interface of cavities, allows for a much faster particle relaxation – an effect that has been demonstrated in previous experiments [130].

Indeed, the experimental procedure itself helps us to select equilibrated samples.

For very high volume-fraction samples, the structural relaxation of samples is so slow that the cavities containing such samples would not be able to relax back to a spherical shape under the influence of capillary forces before the completion of gelation. Note that during the emulsification process, the emulsion droplets created by vigorous mixing have highly non-spherical shapes initially. To restore the spherical shape, particles contained inside droplets need to move more than one particle diameter on average, which facilitates sample relaxation. Hence, by studying spherical cavities, our measurements are naturally limited only to equilibrated samples. Within the range of volume fractions we study in our experiments, the majority of cavities have spherical shapes after gelation. Experimentally, it is hard to create spherical cavities for very high volume fraction suspensions, which limits the highest volume fraction we can obtain for confined samples.

3.4.2 Conclusion

Our experiments may help to resolve controversies over static correlations in the glass transition. First, we confirm the numerical and theoretical predictions on the 1/3 scaling of the pinning length [23, 144, 145] and illustrate a divergent static length scale in the colloidal glass transition when $\phi \to \phi_c$. Moreover, we show that glass-forming liquids with randomly pinned particles show quantitatively similar dynamics as colloidal liquids under spherical confinement [122, 144, 138, 24]. Thus, the RFOT can be applied for understanding confined colloidal liquids—an extensively studied subject in colloidal science [74, 125, 126, 127, 128, 129, 46, 130]. Our findings contradict the numerical study on hard-sphere particles, where the increase of static correlations is found to be negligible [145]. The results are also different from the theoretical prediction, where ϕ_c moves to lower ϕ under pinning or confinement [23, 24].

It should be emphasized that although we interpret our results within the context

of the RFOT, the experimental findings are independent of specific theoretical descriptions. Therefore, it is necessary to check if our experiments can be explained by other competing theories including dynamical facilitation and geometric frustration models [119, 120]. For example, the large curvature of small cavities induces strong geometric frustrations in particle packings [146, 147], which modify the particle dynamics that may link to our observations [120, 146]. In addition to providing experimental results for assessing general glass-transition theories, our study also provides new insights into the dynamics of confined colloidal liquids and may shed light on the behavior of atomic/molecular liquids under nano-confinements [124].

Chapter 4

2D Confinement

4.1 Introduction

The quest of a structural signature, especially a growing static correlation length during the glass transition plays a central role in developing thermodynamic theories of the glass transition. The classical Adam-Gibbs theory proposes that super-Arrhenius behavior of the relaxation during the glass transition arises from cooperative rearrangement regions, according to the classic Adam-Gibbs theory [3, 17]. More recently, the static length scale associated with such regions was predicted by the random first-order transition (RFOT) theory [14, 22, 23, 24, 138]. In this framework, the confinement is used ingeniously as a tool to probe the structural correlation in supercooled liquids. A so-called "point-to-set" correlation length ξ is proposed to quantify the static length scale. Numerical simulations on the glass-forming liquids under confinement have shown the increase of ξ when the system approaches T_g [22, 27, 122]. The existence of static point-to-set correlations has been also confirmed by experimental studies on confined colloidal glass in two dimensions (2D) and our previous work in three dimensions (3D) as discussed in Chapter 3 [1, 123]. In the previous experiment in 3D, we also investigate the influence

of the static correlation on the relaxation of confined colloidal liquids. And we further use the modified Adam-Gibbs relation to explain our experimental results and further find a divergent pinning length ξ_p, which is related with ξ by $\xi_p \sim \xi^{1/3}$ near the random first-order transition [23, 144, 145].

The RFOT theory predicts that the structural correlation may depend on the dimensionality of systems, d [23, 117]. The free-energy penalty due to the mismatch between the amorphous state of particles within a cavity of R and the equilibrium state outside R is $\Delta F_{\rm cost} = Y(T)R^{\theta}$, where $Y(T)$ is a generalized surface tension and $\theta \leq d-1$. The free-energy gain from the formation of different amorphous states is $\Delta F_{\rm gain} = -Ts_c(T)R^d$, where s_c is the configurational entropy density. s_c decreases linearly to zero as T approaching T_K, $s_c = K(T - T_K)$, where $T_K < T_g$ is the Kauzmann temperature and K is a constant. Balancing the total free energy leads to a prediction of ξ,

$$\xi = \left[\frac{Y(T)}{Ts_c(T)}\right]^{1/(d-\theta)} = \left[\frac{Y(T)}{TK(T-T_K)}\right]^{1/(d-\theta)}. \tag{4.1}$$

$\theta = 2$ and $3/2$ have been reported in 3D simulations [26, 148]. It is certainly interesting to investigate structural correlations in experiments of different dimensionalities.

The dimensionality of systems is very important in soft condensed matter. It brings many interesting phenomena such as crystal melting and self-assembly in fluid flows [2, 42, 149]. The differences between glassy dynamics in 2D and 3D are also widely studied [69, 150, 151]. Recently, two individual groups argued that the existence of the Mermin-Wagner long-wavelength fluctuations in colloidal glass-forming liquids might be the cause of dynamic differences between 2D and 3D [96, 97]. The amplitude of the long-wavelength fluctuations grows logarithmically with the size of system in 2D at finite temperatures. While, in 3D, the fluctuations cannot accumulate independently and remains same order of magnitude [90, 92, 96].

However, systematically studies of the fluctuations in 2D colloidal suspensions are insufficient, especially experimental verifications of the logarithmic dependence of the fluctuations on system sizes. Secondly, better ways instead of directly comparing relaxation curves are needed to present the fluctuations and to extract more information about the influence on dynamics. Furthermore, due to the existence of the long-wavelength fluctuations in 2D systems, whether the modified Adam-Gibbs relation can still be used to explain the relaxation in 2D has yet to be verified. We have shown the confinement as a useful tool to probe the static pinning length ξ as it can conveniently vary system sizes. Due to this unique advantage, the confinement can also be used to study the fluctuations in 2D systems. Last but not least, the influence of the long-wavelength fluctuations on the dynamics of anisotropic particles lacks of systematically studies. Compared with colloidal spherical particles, anisotropic particles can better mimic real atoms and molecules with non-spherical shapes and complex inter-particle interactions and thus provide us more insights to the glass transition [20, 69, 152, 153].

In this chapter, we address the above questions by experimentally studying the structural correlations and the long-wavelength fluctuations in quasi-2D colloidal suspensions under circular confinement.

4.2 Methods

4.2.1 Preparation of Ellipsoidal and Rodlike Particles

For the experiments under quasi-2D confinement, spherical, ellipsoidal and rodlike PMMA or PS particles are used. For spherical particles, we use non-cross-linked polymethylmethacrylate spheres (PMMA, Microparticles GmbH, Berlin) of two different sizes $d_s = 2.21$ µm and $d_l = 2.81$ µm, which effectively prevent the crystallization when the system approaches the glass transition. Ellipsoidal particles are synthesized

by stretching the smaller PMMA spheres [69, 154]. And rodlike particles are prepared by stretching PS particles with a size of $d = 2.00$ µm (Polyscience, Inc.).

Fig. 4.1 shows a typical preparation procedure of ellipsoidal particles. 3.0 g of polyvinyl alcohol (PVA, MW $\sim$ 90,000) and 25 ml of water are added to a 100 mL Erlenmeyer flask. The Erlenmeyer flask is sealed by a rubber stopper and heated on a hotplate with the setting temperature as 150 °C. The mixture is also mixed by a magnetic stir bar simultaneously with a rotational rate of 300 rpm (round per minute) for 1 h to fully dissolve PVA into water (Fig. 4.1a). The temperature of the solution is about 80 °C. Then 0.3 mL of PMMA spherical particles (10 % solid) is added to the solution. The temperature of the hotplate is changed to be 100 °C. The mixture is stirred for another 1 h and then poured on a clean flat glass surface (Fig. 4.1b) . The mixture is allowed to evenly cover an area about 12 cm $\times$ 10 cm. The glass is placed on a horizontal table and left at least overnight to dry the film at room temperature (Fig. 4.1c). A typical thickness of the film is about 200 µm. After dried, the film is cut into multiple smaller strips with size about 2 cm $\times$ 5 cm. The strips are stretched in an oven with inside temperature 130 - 140 °C at a stretching rate about 0.3 mm/s (Fig. 4.1d, e). The temperature is set above the glass transition temperatures but less the melting temperatures of both PVA matrix ($T_g = 85$°C) and PMMA particles ($T_g = 105$°C). The slow stretching rate makes sure both PVA matrix and PMMA particles are evenly deformed during this process. After stretched to a desired aspect ratio, the strip is cooled down naturally. The uniformly stretched parts of strips are collected and dissolved in water with the hotplate temperature set as 120 °C. The temperature of the solution is about 65 - 70 °C. Then PMMA suspensions are washed about 10 times by centrifugation to remove PVA residues. Microscopic images of both original particles and stretched particles are shown in Fig. 4.2. The aspect ratios of particles are controlled by both stretching ratios and properties of materials. The polydispersity (the standard deviation

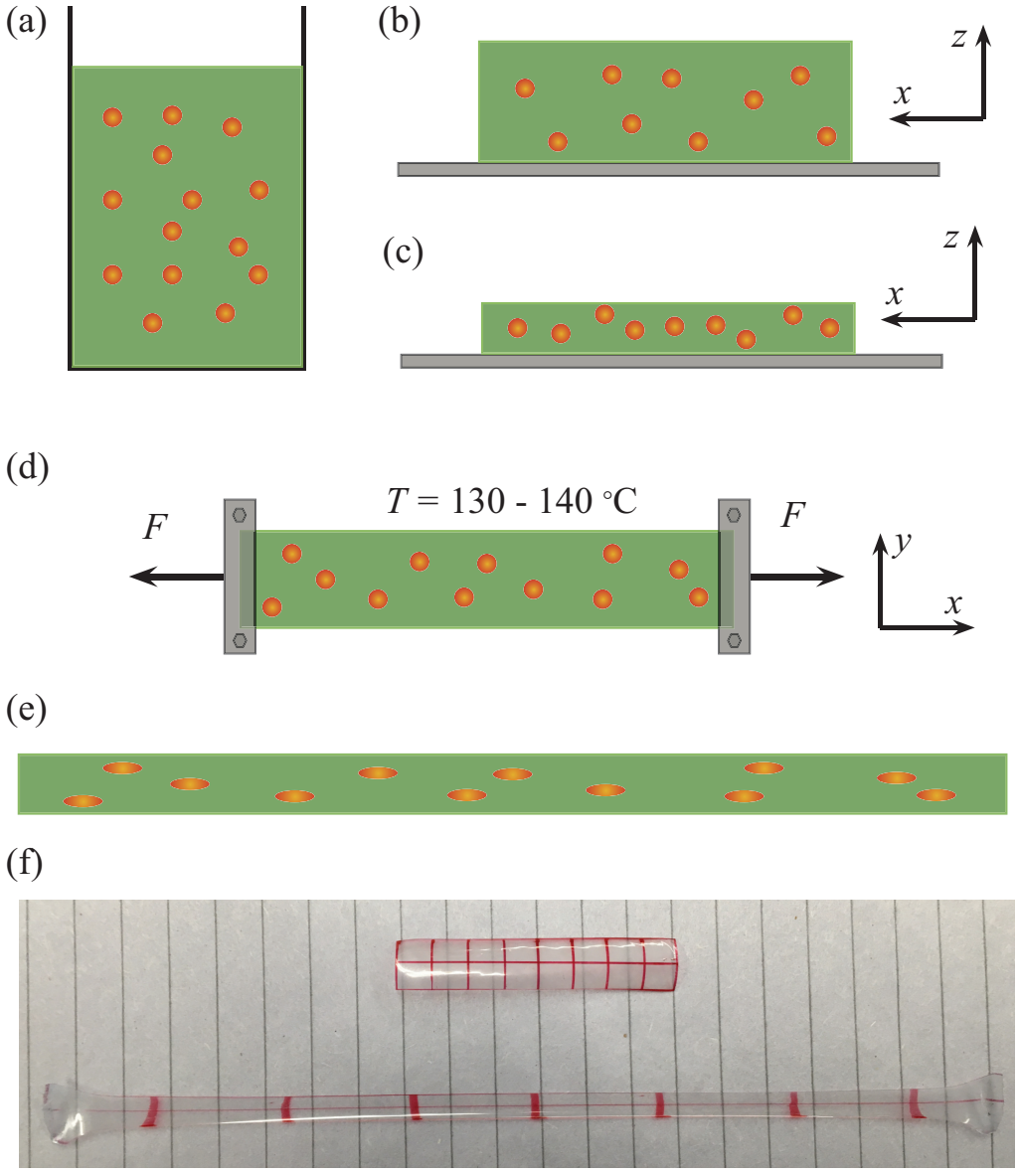

Figure 4.1: Schematics of the preparation of ellipsoidal and rodlike particles. (a) Colloidal particles are mixed with PVA suspensions. (b) The mixture is poured onto a flat glass surface. (c) Leave the sample to dry at room temperature overnight. (d) Dried film strips are stretched uniformly at a temperature between 130 - 140 °C. (e) Film strips after being stretched are allowed to cool down to the room temperature. (f) Photographic image of an unstretched film strip (upper) and a stretched film strip (lower) with same original lengths. The uniform distribution of red lines indicates a uniform deformation of the film strip during stretching.

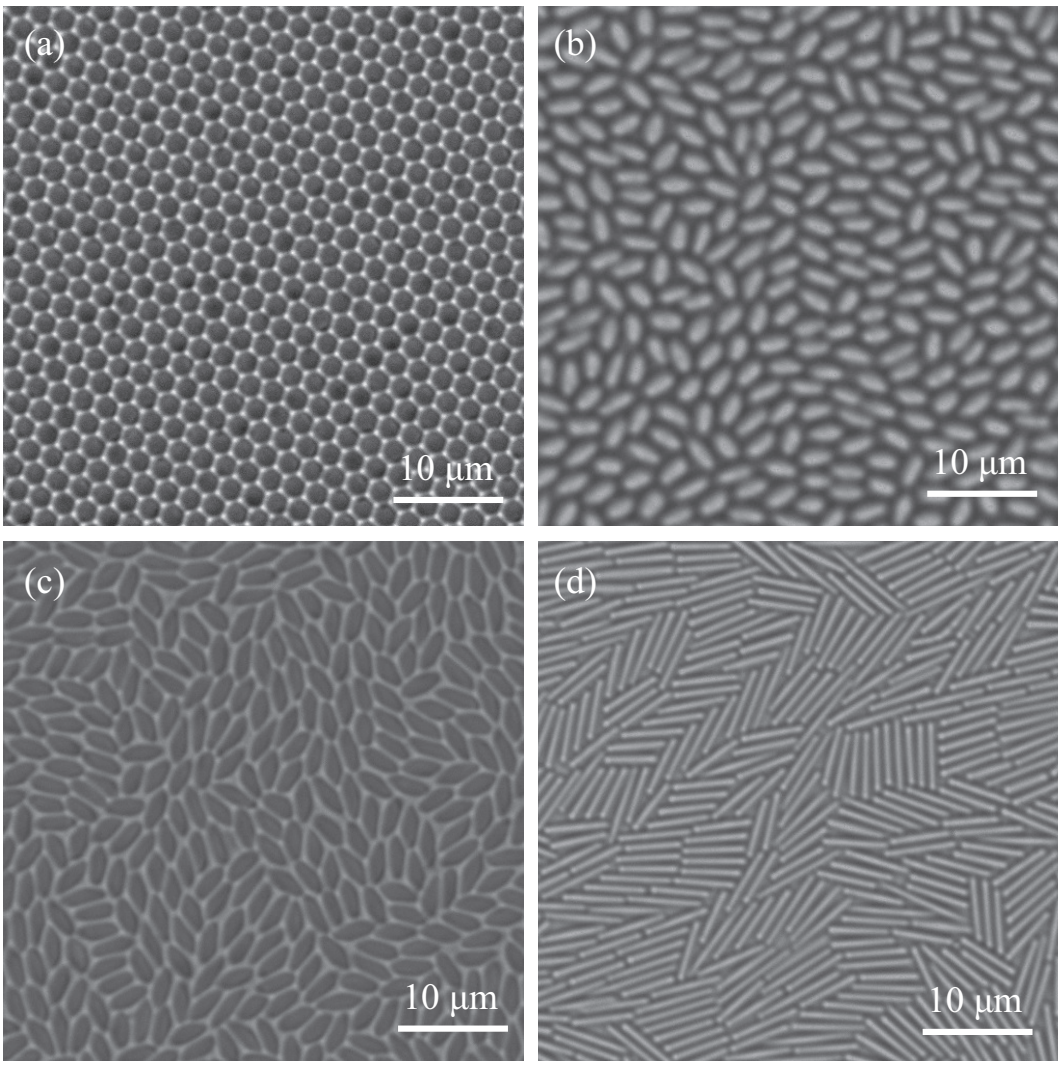

Figure 4.2: Microscopic images of spherical (a), ellipsoidal (b, c), and rodlike (d) particles with different aspect ratios. The aspect ratios of the particles are 1 (a), 1.4 (b), 1.9 (c) and 8.0 (d) respectively.

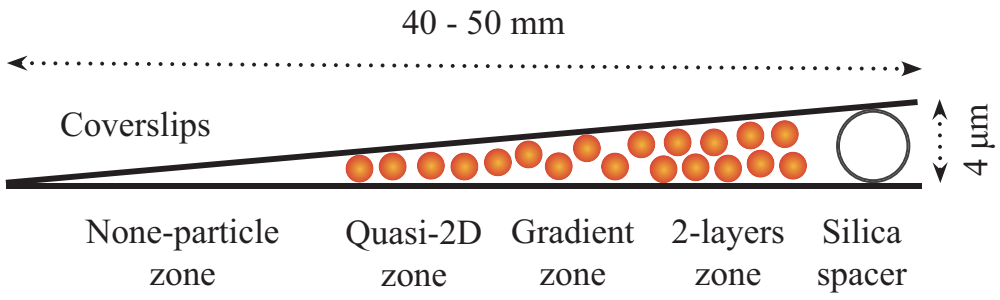

Figure 4.3: Preparation of quasi-2D samples in wedge-shaped cells. A layer of silica particle of 4 µm is place at one end of the bottom coverslip to serve as spacers. Four different zones can be defined based on the gap size and the particle size. All image data is taken at the quasi-2D zone.

of particle sizes) of each type of particles is about 5%. Particles then are suspended in a 7 mM of sodium dodecyl sulfate (SDS) aqueous solution. SDS is added to stabilize particles and also make the Debye length of particles less than 20 nm to be treated as hard spheres [69].

4.2.2 Quasi-2D Sample Preparation

The quasi-2D sample is prepared by spherically confining a monolayer of colloidal particles between two glass coverslips (Fig. 4.3)[20, 69, 155]. The coverslips are vigorously cleaned by the piranha solution (3 parts of 95 - 98 % sulfuric acid and 1 part of 30 % hydrogen peroxide solution) at least overnight. A dilute layer of silica particle of 4 µm is placed near one end of the bottom coverslip to serve as spacers. After the silica suspension is dried and silica particles are attached to the coverslip surface due to the van de Waals attraction, 3 µL of SDS solution is added on the surface of the bottom coverslip and then the top coverslip is put on carefully to remove all bubbles inside.

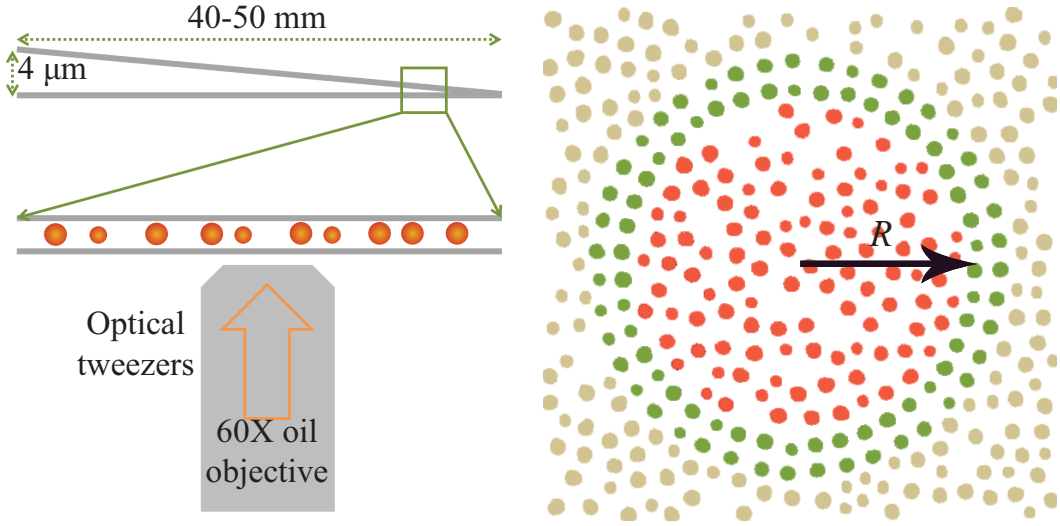

Figure 4.4: Preparation of 2D confined samples by optical tweezers. (a) The imaging system is consisted of a bright-field optical microscope and optical tweezers. Multiple optical traps are used to pin two circles of particles at the same time. (b) A modified microscopic image to show the inner particles (red), pinned particles (green) and outer particles (light brown). Two circles of particles are pinned by optical tweezers to reduce the influence of outer particles on inner particles. Each pinned particle is trapped by an optical trap at a same trapping strength for different system size R.The radius $R = 9.0d_s$.

The coverslips are then transferred onto a microscope slide. Three sides of the coverslips are sealed together with the microscope slide by a UV adhesive (NOA 81, Norland Products, Inc.) except the one with silica spacers. Then 0.5 - 1 µL of PMMA or PS suspensions is injected from the open side, which is sealed by a UV adhesive afterwards. The wall separation varies less than 100 nm per 1 mm, which makes two glass walls nearly parallel within the field of view. Due to the gradient change of the gap size, there are different zones: none-particle zone, quasi-2D zone, gradient zone and 2-layers zone. Only particles at the quasi-2D zone are used for the quasi-2D experiments.

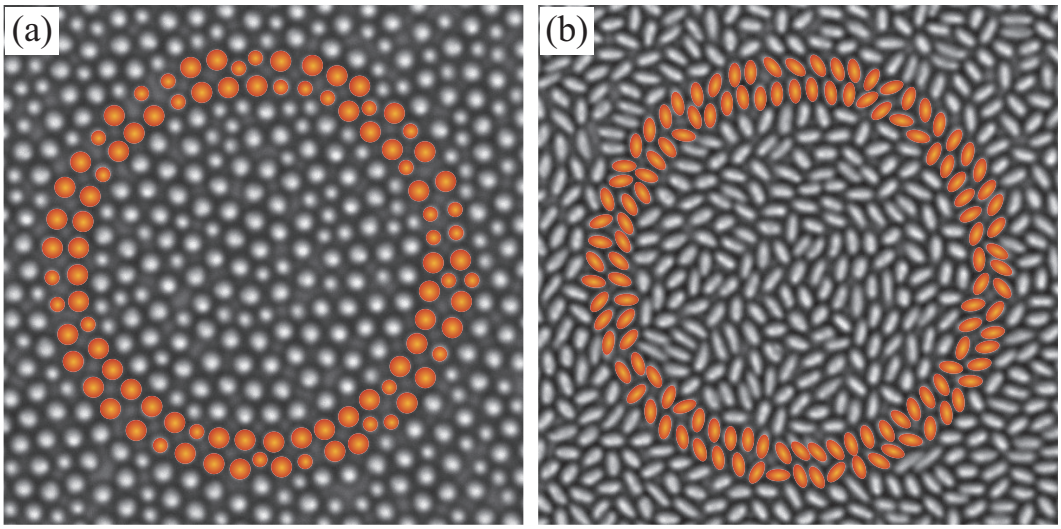

Figure 4.5: Microscopic images of 2D confined systems of (a) binary spherical particles and (b) ellipsoidal particles with an aspect ratio of 1.9. Same as the geometry in Fig. 4.4b, two circles of particles (orange) are pinned for each case. The pinned particles do not leave but can semi-freely rotate at the pinned positions during the experiment.

4.2.3 2D Spherical Confinement by Optical Tweezers

The 2D confinement is created by pinning two circles of particles in quasi-2D samples using optical tweezers with a 60× oil immersion lens on a bright-field microscope (Fig. 4.4). Only the quasi-2D zone is used for the experiments. The system size R can be conveniently changed up to 60 µm, which is only limited by the working range of optical tweezers. Since the boundary mobility affects the glassiness of confined colloidal liquids, the strength of each trap on each particle for all different system size R is kept same for all experiments to prepare boundaries with same mobility [156]. During the experiment, trapped particles can only vibrate around trapped positions but never leave the positions. The trapped particles build an unpenetrated boundary between inner and outer particles, so that inner particles can freely evolve without the influence of outer particles.

4.2.4 Image Data Collection

The samples prepared following the procedures in Chapter 4.2.2 are left vertically for one to two days to let particles sediment to the smaller gap side. The sample is then put horizontally on the microscope stage overnight to allow the system reach the equilibrium before any used images are taken. No obvious drifts are found and the area fractions are same during the experiment. The microscopic images are taken at the place (quasi-2D zone, Fig. 4.3) close to the smaller gap of the sample cell. For all experiments, special attentions are paid to keep the wall separation nearly constant and slightly larger than the size of larger spherical particles or the short axis of ellipsoidal particles.

The image time series are recorded by a CCD camera with a speed of 0.5 - 10 FPS (frames per second) for 10 min - 2 h depending on the area fractions. Then the images are analyzed using standard image processing algorithms [116]. Two layers of particles near the pinned layer is excluded from data analysis to eliminate the wall-induced interfacial effect or influence of optical tweezers other than the true confinement effect [46, 74, 126, 128, 129, 130].

4.3 Results

4.3.1 The Static Length Scale in 2D

With the quasi-2D confined system, we follows similar procedure as our previous 3D confinement experiment discussed in Chapter 3 [1]. We use the self-intermediate scattering function F_s to study the influence of the confinement on the relaxation of binary spherical colloidal liquids:

$$F_s(Q,t) = \langle \frac{1}{N} \sum_j \cos\left(Q \cdot [x_j(t_0+t) - x_j(t_0)]\right) \rangle, \tag{4.2}$$

where $Q = 5.8d_s^{-1}$ obtained from the position of the first peak of the structural factor $S(Q)$, $x_j(t)$ is the location of particle j at time t and N is the total number of particles [157]. Fig. 4.6 shows several typical F_s curves. The area fraction ϕ is increasing from left to right. For small ϕ, F_s has a single-step relaxation called α relaxation. Whereas for high ϕ closing the critical area fraction ϕ_c, F_s expresses two-step relaxation behavior. F_s first decays to some non-zero plateau by β relaxation then decays to zero by α relaxation. The appearance of β relaxation is due to particle dynamics hindered by neighbor particles at higher ϕ (caging behavior).

By fitting the α relaxation part of F_s curve with a stretched exponential function, $F_s(t) = A_0 \exp[-(t/\tau_{\alpha,F_s})^{\beta}]$, we have the relaxation time, τ_{α,F_s}. Fig. 4.7 shows τ_{α,F_s} as a function of ϕ for different confinement sizes R. The relaxations of colloidal liquids under different confinements all show the Super-Arrhenius behaviors and the system under a stronger confinement has a larger fragility index and the colloidal liquid is stronger. The α relaxation time τ_{α,F_s} in the stronger confined systems is longer than that in less confined or bulk systems. The existence of the pinned boundary dramatically slows down particle dynamics inside.

When fitting the $\tau_{\alpha,F_s}(\phi)$ with the classic Vogel-Fulcher-Tammann (VFT) relation:

$$\tau_{\alpha,F_s}(R,\phi) = \tau_0 \exp[D\phi/(\phi_c - \phi)], \tag{4.3}$$

we find the constant critical area fraction $\phi_c = 0.89 \pm 0.01$ for all sizes (Fig. 4.8). D is the fragility index. According to the Adam-Gibbs theory, the relaxation of supercooled liquids can be quantified as:

$$\tau_{\alpha,F_s} \sim \exp[A_0\phi/s_c], \tag{4.4}$$

where the configurational entropy density $s_c = K(\phi_c - \phi)$ and A_0 is a constant. This equation can further directly justify the VFT relation (Eqn. 4.3) with $D = A_0/K$.

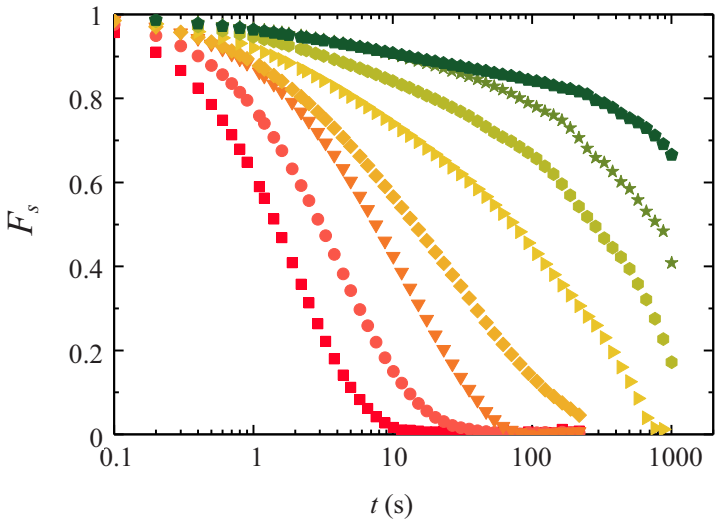

Figure 4.6: Self-intermediate scattering function $F_s(t)$ for bulk samples. From left to right: the area fraction $\phi = 0.229$, 0.534, 0.695, 0.776, 0.814, 0.826, 0.838, 0.851.

When $\phi \to \phi_c$, $s_c \to 0$ and $\tau_{\alpha,F_s} \to \infty$. ϕ_c is the idea glass transition point where the configurational entropy goes to zero and the relaxation time divergents when the system goes through the ideal glass transition. Furthermore, the fragility index D increases linearly with $1/R$:

$$D(R) = D(\infty) + c(d_s/R), \tag{4.5}$$

where $c = 1.42$ (Fig. 4.8). When systems are stronger confined (smaller R), the liquids show less super-Arrhenius behaviors and become stronger. The confinement can strongly alter particle dynamics.

Considering that the classic Adam-Gibbs relation (Eqn. 4.4) only deals with bulk

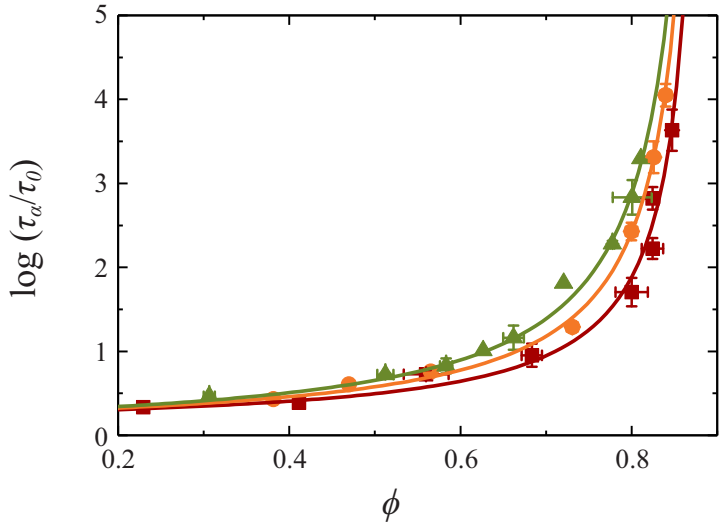

Figure 4.7: α relaxation time calculated from F_s, τ_{α,F_s}, as a function of ϕ. From top to bottom, $R = 4.5d_s$, $9.0d_s$ and bulk. $\tau_0 = 1.04$ s is the Brownian relaxation time of smaller particles in the dilute limit. The solid lines are from VFT fittings.

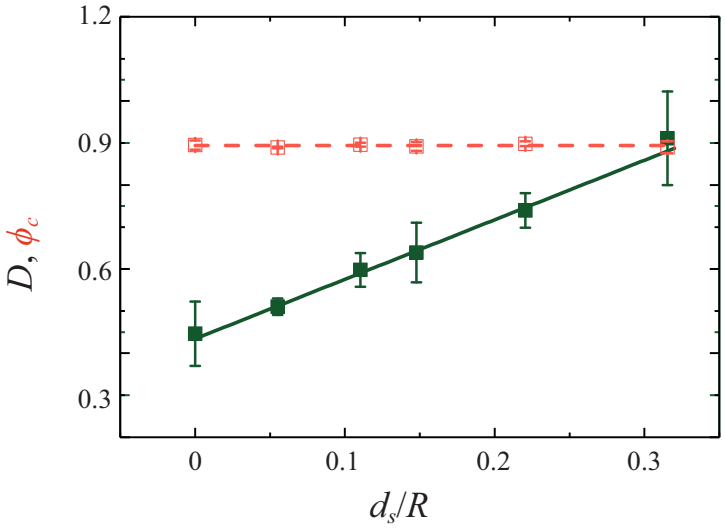

Figure 4.8: The critical area fraction ϕ_c (red squares) and the fragility index D (green squares) as functions of d_s/R. The dashed line indicates $\phi_c = 0.895$. The solid line is a linear fit and the slope $c = 1.42$.

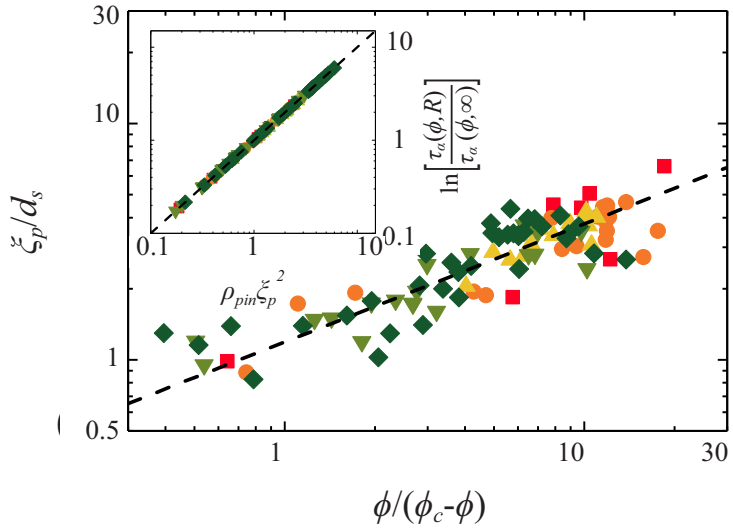

Figure 4.9: The pinning length ξ_p/d_s versus $\phi/(\phi_c - \phi)$. Different symbols represent different sizes R. The dashed line is $\xi_p/d_s = c^{1/2}(\phi/(\phi_c - \phi))^{1/2}$ and c is the slope from Fig. 4.8. The inset shows the collapse of $\ln[\tau_\alpha(\phi, R)/\tau_\alpha(\phi, \infty)]$ with a rescaled variable, $\rho_{pin}\xi_p^2$. The dash line is a linear fit.

samples, we introduce a new parameter $F(R)$ into the relation to quantify the confinement effect on the configurational entropy density:

$$\begin{aligned} s_c(\phi, R) &= F(R) \cdot s_c(\phi, \infty) \\ &= F(R)K(\phi_c - \phi), \end{aligned} \tag{4.6}$$

where $F(R) \in (0, 1]$ is an increasing function of R [1, 144]. Thus, we have

$$\tau_{\alpha,F_s}(\phi, R) \sim \exp\left(A_0\phi / \left[F(R)K(\phi_c - \phi)\right]\right). \tag{4.7}$$

Compared with the VFT function (Eqn. 4.3), the fragility index can be written as: $D(R) = A_0/[F(R)K]$, which successfully explains the our previous result that $D(R)$ increases with decreasing R. If $R \to \infty$, $F(\infty) = 1$ and s_c becomes same as the one for bulk samples. For confined samples, s_c is smaller and τ_{α,F_s} is larger than those of bulk samples, which means there is less local minimums on the free energy landscape and the system relaxes slower among less available energy minimums.

Now with the newly introduced $F(R)$, we compare the relaxation of samples under confinement with that of bulk samples:

$$\begin{aligned} \ln\left[\frac{\tau_\alpha(\phi, R)}{\tau_\alpha(\phi, \infty)}\right] &= \left[D(R) - D(\infty)\right]\left(\frac{\phi}{\phi_c - \phi}\right) \\ &= c\rho_{pin}\left(\frac{\phi d_s^2}{\phi_c - \phi}\right) \\ &= \rho_{pin}\xi_p^2, \end{aligned} \tag{4.8}$$

where,

$$\xi_p/d_s = \left[c\phi/(\phi_c - \phi)\right]^{1/2}. \tag{4.9}$$

Here, ξ_p is the pinning length, which is directly related to the static point-to-set correlation length ξ in the framework of the random first-order transition (RFOT) theory [23, 144, 145]. The only change of this equation from the previous equation in 3D (Eqn. 3.8) is that the power is changed form 1/3 to 1/2. And when $\phi \to \phi_c$, the pinning length $\xi_p \to \infty$, which indicates ξ_p is the long-pursued divergent static length during the glass transition. Notice that our system is in 2D. Thus, the concentration of pinned particles is quantified as $\rho_{pin} \approx (d_s/R)(1/d_s^2)$, instead of $(d_s/R)(1/d_s^3)$ in 3D [1]. To verify whether above theoretical arguments can be applied to our 2D confined systems, we collapse $\ln[\tau_\alpha(\phi, R)/\tau_\alpha(\phi, \infty)]$ using Eqn. 4.8 to obtain ξ_p for all confined sizes (Fig. 4.9 inset). We show that $\xi_p(\phi)$ follows both the 1/2 scaling and $c^{1/2} = 1.19$ (Fig. 4.9), which are exactly what the above theory (Eqn. 4.9) predicts. Our modified Adam-Gibbs theory can well explain our 2D experimental results as well as the 3D experimental results (Chapter 3). The static length ξ_p becomes divergent when $\phi \to \phi_c$, unveiling the divergent static length during the glass transition in 2D systems.

4.3.2 Influence of Mermin-Wagner Fluctuations on Spherical Particles

However, the differences between 2D and 3D are much more than just the change of power in the Eqn 4.9. Recently there are active discussions about whether dimensionality changes particle dynamics near the glass transition [96, 97, 150]. By directly comparing the self-intermediate scattering functions F_s and bond-orientational correlation functions C_Ψ in both 2D and 3D, Flenner and Szamel showed the fundamental differences between glassy dynamics in 2D and 3D [150]. Then, two individual groups argued that the Mermin-Wagner long-wavelength fluctuations existing in 2D might cause the differences of dynamics in 2D and 3D [96, 97]. Using the heights of the plateaus of simulated MSD curves to quantify the amplitudes of the long-wavelength fluctuations, Illing *et al*. found the amplitudes have a lorgarithmic dependence on system size $\sqrt{N}$.

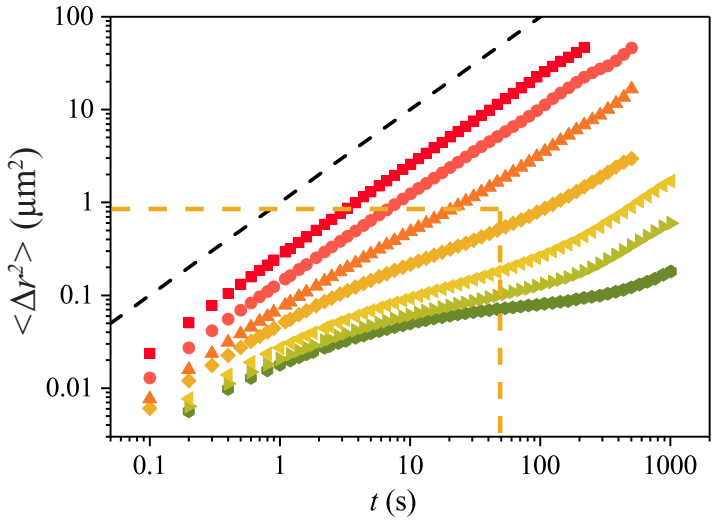

Figure 4.10: Mean square displacement of typical bulk samples. From top to bottom, the area fractions $\phi = 0.229, 0.538, 0.695, 0.785, 0.815, 0.822, 0.840$. The orange dashed lines show the position of the inflection point and the height of the plateau of the MSD curve. The black dashed line has a slope of 1.

N is the number of particles in the system. They further showed that the glass transitions in 2D and 3D were still similar if the long-wavelength fluctuations were removed by measuring particle displacements relative to the average displacements of each particle's nearest neighbors (cage-relative mean square displacements, CR-MSD).

Here we systematically study the influence of the Mermin-Wagner fluctuations on particle dynamics using the quasi-2D systems discussed above. A typical MSD curve is shown in Fig. 4.10. For higher ϕ, the curve shows a plateau indicating the caging behavior of particle dynamics as discussed above. At the plateau, particle dynamics are hindered by their neighbor particles and the particles are most likely to move along with their neighbors if there is long-wavelength fluctuations such as the Mermin-Wagner fluctuations in the system. The fluctuations could push the particles away from their original locations and MSD values get higher. Thus, the height of the plateau could be

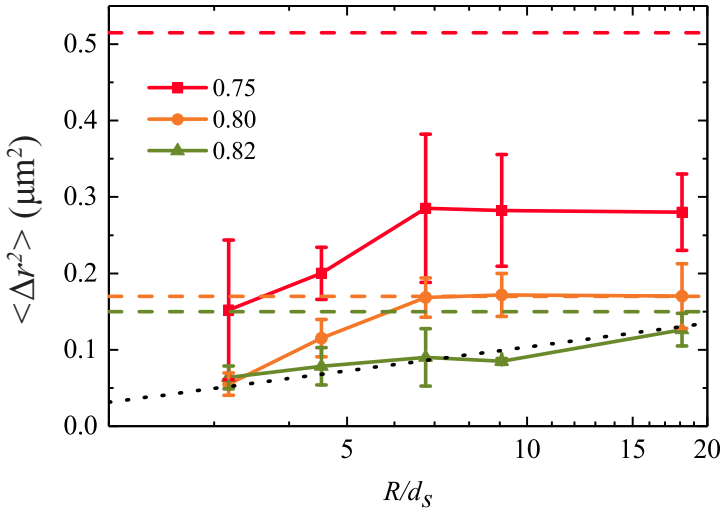

Figure 4.11: Plateau values of MSD as functions of system size R for different area fractions with a range of $\pm$ 0.1. The legends show three typical area fractions. The dashed lines indicate the value of the bulk sample for each area fraction (same color). The black dotted line is a visual guide line which indicates the logarithmic dependence of the plateau values on system sizes for $\phi = 0.82$.

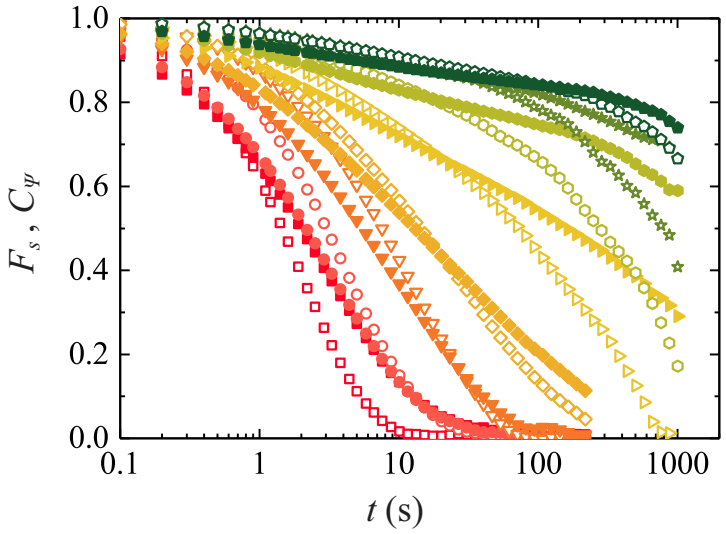

Figure 4.12: C_Ψ (solid symbols) and F_s (open symbols) as a function of time t for different ϕ in bulk samples. Same colors represent same ϕ as in Fig. 4.6.

used to compare the influence of the long-wavelength fluctuations on particle dynamics.

With the plateau values obtained from MSD curves, the amplitudes of the long-wavelength fluctuations for different system sizes and different area fractions can be compared (Fig. 4.10). The plateau values increases as the area fraction ϕ decreases and the system size R increases. For highest ϕ ($\phi = 0.82$), the plateau values have a roughly logarithmic dependence on R, which is in agreement with the theoretical predictions [87, 88, 89, 90, 91, 92, 93, 94].

Next, we investigate the influence of the long-wavelength fluctuations on particles dynamics in 2D confined colloidal liquids. Unlike the actual transitional measurements such as MSD or F_s, the orientational order measurements such as the bond-orientational correlation functions C_Ψ are not affected by the long-wavelength fluctuations [97, 150]. C_Ψ is defined as:

$$C_\Psi(\Delta t) = \frac{\langle \sum_j [\Psi_6^j(t)]^* [\Psi_6^j(t+\Delta t)] \rangle}{\langle \sum_j |\Psi_6^j(t)|^2 \rangle}, \tag{4.10}$$

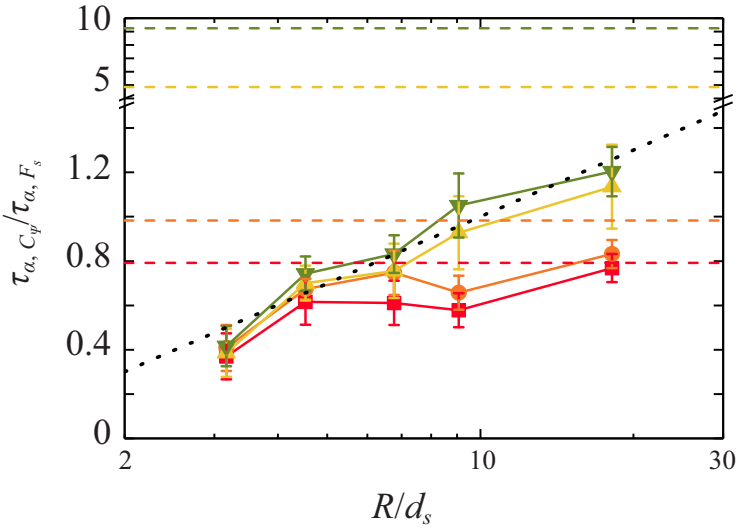

Figure 4.13: The relaxation time ratio $\tau_{\alpha,C_\Psi}/\tau_{\alpha,F_s}$ depends on the system size R. The ratio is used to quantified the long-wavelength fluctuations in the system. The area fractions are $\phi = 0.70$ (red squares), 0.75 (orange circles), 0.80 (yellow upper triangles), 0.82 (green lower triangles). There is a $\pm$ 0.1 variation range for each ϕ. The same colored dashed lines indicates the ratios for bulk samples. The black dotted line is $\tau_{\alpha,C_\Psi}/\tau_{\alpha,F_s} = \log(R/d_s)$.

and

$$\Psi_6^j(t) = \sum_k (N_b^j)^{-1} e^{i6\theta_{jk}}. \tag{4.11}$$

N_b^j is number of nearest neighbors k of particle j and θ_{jk} is the angle between particles j and k [150]. $\Psi_6^j(t)$ is the local director field in time, which is defined based on the relative angle change of nearest neighbors. C_Ψ measures time correlations of the local director fields. C_Ψ is equal to 1, if neighbors maintain same relative angular positions and decreases if the relative angular positions change. Since C_Ψ quantifies the relative rotational dynamics and C_Ψ is not influenced by the long-wavelength fluctuations in 2D, the differences between F_s and C_Ψ can be used to quantify the influence of the long-wavelength fluctuations on particle dynamics near the glass transition.

Fig. 4.12 compares typical F_s and C_Ψ as functions of interval time t for different ϕ in bulk samples. The same F_s curves are also shown in Fig. 4.6. At lower ϕ, C_Ψ curves have similar decay trends, which might be caused by the quick change of nearest neighbors. For the discussions below, we only use data with $\phi > 0.5$. At intermediate ϕ, F_s and C_Ψ show similar relaxation trends. At higher ϕ, C_Ψ starts to show slower relaxation over time than F_s, which indicates that the long-wavelength fluctuations enhance the dynamical relaxation. Recent experiments also confirmed the different relaxation trends between F_s and C_Ψ in 2D while similar relaxation trends in 3D [97, 150, 96]. Both F_s and C_Ψ have single-step relaxations at lower ϕ and two-step relaxations at higher ϕ.

By fitting the α relaxation parts with the VFT relation (Eqn. 4.3), α relaxation time from C_Ψ, τ_{α,C_Ψ}, can be obtained similar as τ_{α,F_s}. Here, the time ratio $\tau_{\alpha,C_\Psi}/\tau_{\alpha,F_s}$ is used to quantitively measure the influence of the long-wavelength fluctuations on particle dynamics in 2D systems (Fig. 4.13). The time ratios for different ϕ are similar for smaller R, whereas for larger R the time ratios for higher ϕ are larger than those of lower ϕ. For lower area fractions ($\phi = 0.70$ or 0.75), the time ratio for both confined systems

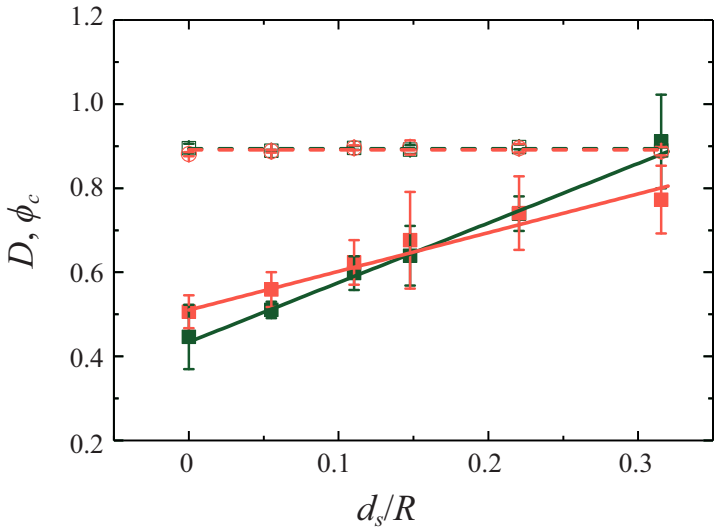

Figure 4.14: Comparison of the critical area fraciton ϕ_c (open symbols) and the fragility index D (solid symbols) obtained from C_Ψ (red) and F_s (green). The dashed lines shows constant fittings and the solid lines have the linear fittings versus d_s/R with slopes of c_{C_Ψ} and c_{F_s}, respectively.

and bulk systems are in the same order of magnitude. The time ratios increase with the system sizes R and eventually saturated at the ratios of bulk samples. For higher area fractions ($\phi = 0.80$ or 0.82), the time ratios of bulk systems are one order of magnitude higher than those of confined systems. The time ratio has a logarithmic dependence on the system size (the dashed line). The logarithmic dependence on system sizes is the fingerprint of the Mermin-Wagner long-wavelength fluctuations [96]. So $\tau_{\alpha,C_\Psi}/\tau_{\alpha,F_s}$ well detects influence of the fluctuations on particle dynamics.

Due to the existence of the long-wavelength fluctuations in 2D system, it is worthy to double check the influence of the fluctuations on the divergent static length discussed previously. The critical area fraction ϕ_{c,C_Ψ} and the fragility index D_{C_Ψ} for different R can also obtained by fitting $\tau_{\alpha,C_\Psi}(\phi)$ with the VFT relation (Eqn. 4.3). While $\phi_{c,C_\Psi}(R)$ is constantly same as $\phi_{c,F_s}(R)$, $D_{C_\Psi}(R)$ shows a weaker linear dependence on d_s/R than

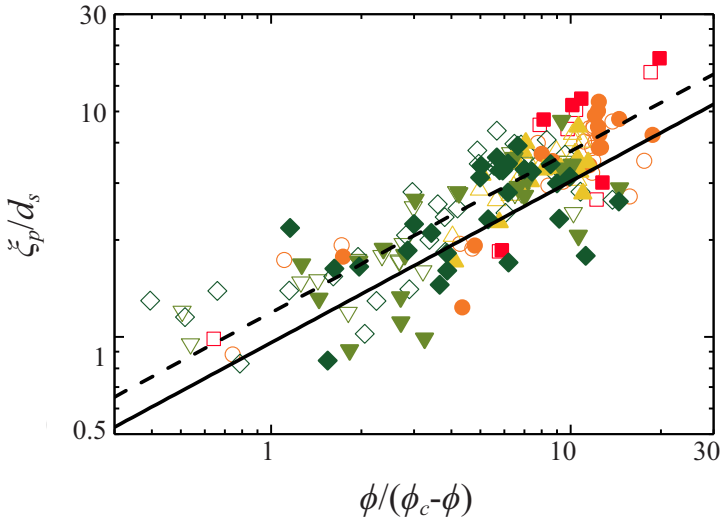

Figure 4.15: The pinning length ξ_p/d_s vs $\phi/(\phi_c - \phi)$ measured by C_Ψ (solid symbols) and F_s (open symbols). Different symbols represent different sizes R. Both the solid line (C_Ψ) and dashed line (F_s) are $\xi_p/d_s = c^{1/2}(\phi/(\phi_c - \phi))^{1/2}$, while c is the slope from Fig. 4.14.

D_{F_s} (Fig. 4.14). This is exactly the outcome of the Mermin-Wagner fluctuations in 2D. Since D_{F_s} is influenced by the fluctuations (Fig. 4.12) and the fluctuations strongly depend on R (Fig. 4.13), D_{F_s} is expected to have a stronger dependence on R than D_{C_Ψ}.

With same constant $\phi_{c,C_\Psi}(R)$ and linear changing $D_{C_\Psi}(1/R)$, the pinning length ξ_{p,C_Ψ} still has a linear dependence on $(\phi/(\phi_c - \phi))^{1/2}$ (Fig. 4.15). Both ξ_{p,C_Ψ} and ξ_{p,F_s} lines have a power of 1/2 and heights are directly determined by $c^{1/2}$ from $D(R)$. The ξ_{p,C_Ψ} line is slightly lower than the ξ_{p,F_s} line, which corresponds the smaller slope of D_{C_Ψ} than that of D_{F_s}. As discussed in Chapter 3.3.5 and Chapter 4.3.1, the pinning length ξ_p is positively related to the point-to-set correlation length ξ which is usually probed under confinement. ξ is the critical size of the amorphous "glasslites" in supercooled liquids proposed by the RFOT, above which the system vitrifies. ξ is probed by the mean of confinements. Larger ξ_{p,F_s} indicates that particle dynamics quantified by F_s can sense the confinement earlier than that by C_Ψ due to the long-wavelength feature of the Mermin-Wagner fluctuations. No matter whether F_s or C_Ψ is used to measure the dynamics, the modified Adam-Gibbs relation can still well explain our 2D experimental results and a divergent static length is unveiled when $\phi \to \phi_c$.

4.3.3 Influence of 2D confinement on Anisotropic Particles

Spherical colloidal particles are an outstanding hard-sphere model for the studies of the glass transition since a single-particle resolution of particle dynamics can be achieved when combined with video microscopy and particle tracking algorithms [41, 98, 103, 104, 115, 116]. Compared to the much simpler and more popular studies of the glass transition of colloidal spherical particles, the studies of anisotropic particles are much less [20, 69, 155, 152]. However, compared to spherical colloidal particles, anisotropic particles can better mimic real atoms and molecules with non-spherical shapes and

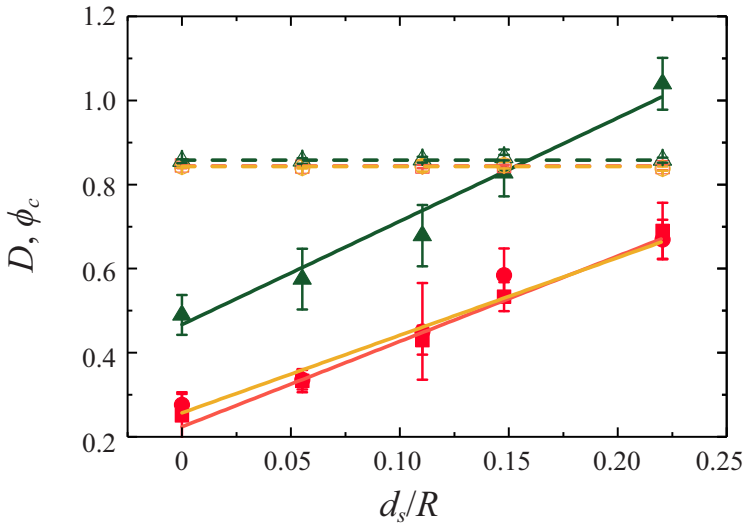

Figure 4.16: ϕ_c (open symbols) and D (solid symbols) from F_s (red), C_Ψ (orange) and L_n (green) as functions of system size R for ellipsoids with an aspect ratio of 1.90.

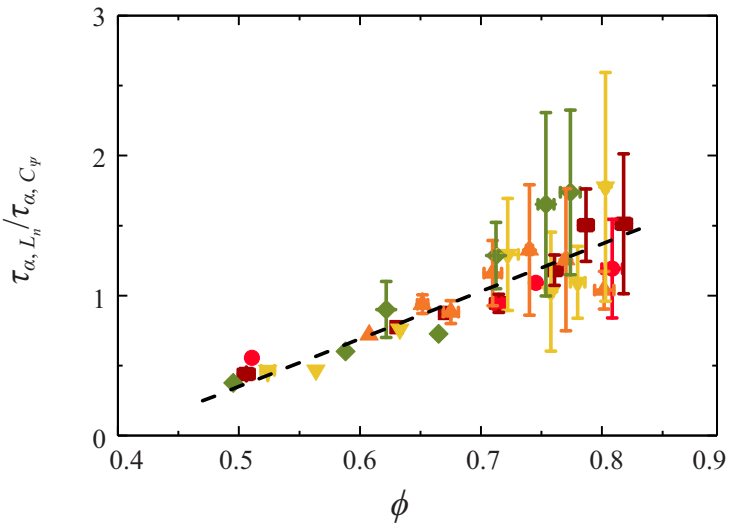

Figure 4.17: Relaxation time ratios from $L_n(\phi)$ and $C_\Psi(\phi)$. Different symbols represent different sizes R. The black dashed line shows the visual increasing trend.

complex inter-particle interactions [20, 69, 152, 153]. Within anisotropic particles, ellipsoidal and rodlike particles are among the simplest cases of studies. Relatively easy to synthesize and do imaging data analysis make ellipsoidal and rodlike particles popular candidates to study many topics such as the rotational dynamics and decoupling between translational and rotational dynamics by both experiments and simulations [69, 152, 158, 159, 160].

Here we study the influence of the 2D confinement on particle dynamics of ellipsoidal particles (preparation methods in Chapter 4.2.1). As we discussed above (Chapter 4.3.2), particle translational dynamics are affected by the Mermin-Wagner fluctuations in 2D systems. We first compare C_Ψ and F_s in ellipsoidal particle liquids with an aspect ratio $P = 1.9$ under confinement (Fig. 4.16). The critical area fractions ϕ_c are constant regardless of the size of confinement for both F_s and C_Ψ. And the values are same within the error regardless of measurement methods. Whereas D_{F_s} and D_{C_Ψ} both show linear dependences on $1/R$, $D_{C_\Psi}(R)$ has a slightly smaller slope c, which is due to the existence of the long-wavelength fluctuations in ellipsoidal particle liquids as we discussed in Chapter 4.3.2.

C_Ψ measures the change of relative angular positions of neighbors, which intrinsically still measure the translational dynamics of particles like F_s. In 2D due to the existence of the long-wavelength fluctuations, C_Ψ, unlike F_s, can detect the translational dynamics without the influence of the long-wavelength fluctuations. With ellipsoidal particles, we can also measure the rotational dynamics of a single particle by the orientational correlation function:

$$L_n(t) = \langle \frac{1}{N} \sum_j \cos[n(\theta_j(t) - \theta_j(0))] \rangle, \tag{4.12}$$

where $\theta_j(t)$ is the orientation of ellipsoid j at time t and N is the total number of

particles. n is added to better present the orientational relaxation by magnifying the change of orientations and $n = 6$ here. Different choices of n yield the same glass transition points [20]. ϕ_{c,L_n} is independent of system sizes and equals to both ϕ_{c,C_Ψ} and ϕ_{c,F_s}. The fragility index D has a linear dependence on $1/R$. Both constant ϕ_c and linear dependence of $D(1/R)$ indicate that not only the dynamics quantified by C_Ψ and F_s but also the behavior of L_n under confinement can be quantitively explained by the modified Adam-Gibbs relation we have shown above. Different measurement methods only provides different aspects of the same particle dynamics.

The decoupling describe the behavior in glass-forming materials that rotational diffusion coefficient D_R remains coupled with viscosity η as $D_R \propto \eta^{-1}$, while the translational diffusion coefficient D_T develops a fractional dependence on η as $D_T \propto \eta^{-n}$ with $n < 1$ [45, 161, 162]. Since η has a positive relation with ϕ in colloidal suspensions while the diffusion coefficient has a negative relation with the α relaxation time τ_α, we use more easily measured ϕ and τ_α to represent η and the diffusion coefficient D [45]. Thus, the decoupling between translational and rotational dynamics in colloidal suspension can be presented more accurately by comparing the ratio of the relaxation time from L_n and C_Ψ versus ϕ (Fig. 4.17). The ratio of the relaxation time increases with ϕ, which indicates the translational and rotational dynamics decoupled when the system approaches the glass transition similar to other observations [20, 21, 45, 163]. It is interesting to point out that the dependence of the ratio of relaxation time on ϕ is not affected by the confinement. Unlike the influence of area fractions, the confinement slow down translational and rotational dynamics at same level for ellipsoidal particles with an aspect ratio of 1.9. Similar trends (Fig. 4.16, Fig. 4.17) are also observed for ellipsoidal particles with an aspect ratio of 1.4.

The aspect ratios of ellipsoidal particles are another factor that may change particle dynamics. The critical area fractions ϕ_{c,C_Ψ} are same for translational dynamics of two

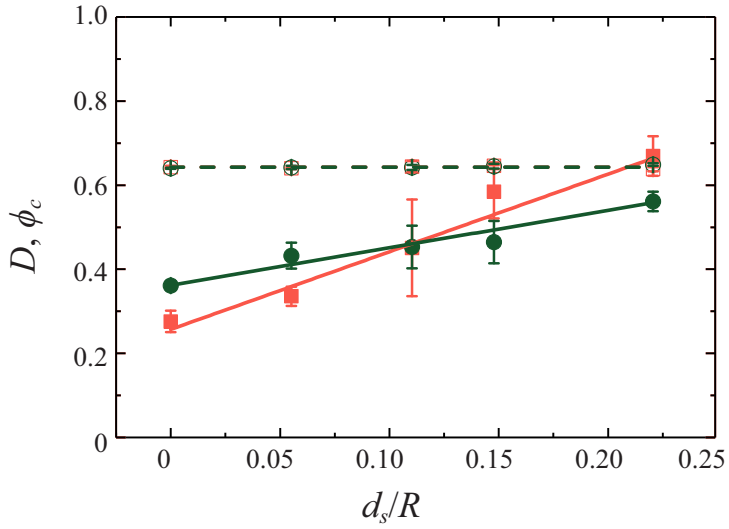

Figure 4.18: ϕ_{c,C_Ψ} (hollow symbols) and D_{C_ψ} (solid symbols) from particles with aspect ratios of 1.4 (green) and 1.9 (red). The dashed lines indicates the constant ϕ_c for different system sizes and the solid lines shows the linear dependence of D on the inverse system size d_s/R.

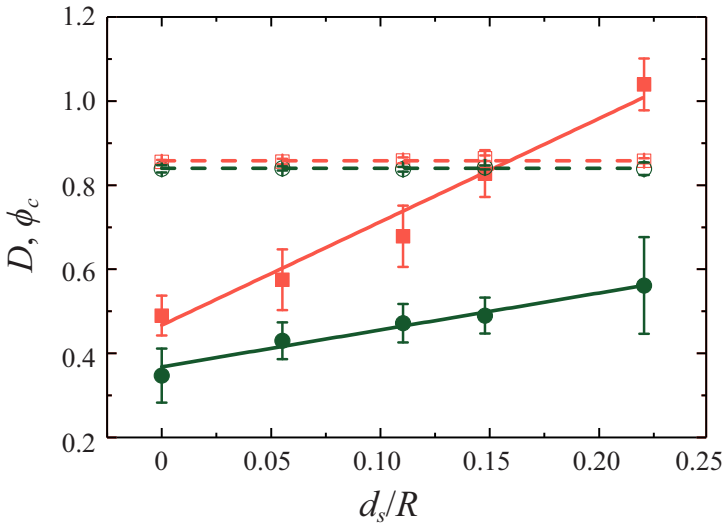

Figure 4.19: ϕ_{c,L_n} (hollow symbols) and D_{L_n} (solid symbols) from particles with aspect ratios of 1.4 (green) and 1.9 (red). The dashed lines indicates the constant ϕ_c for different system sizes and the solid lines shows the linear dependence of D on the inverse system size d_s/R.

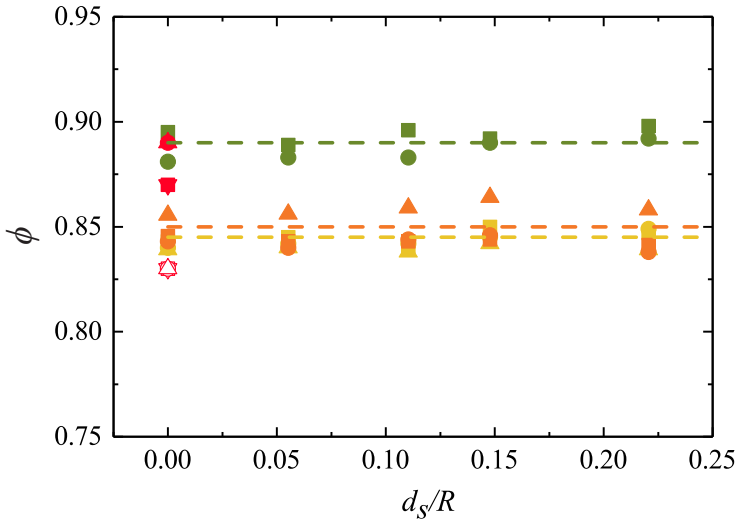

Figure 4.20: Critical area fractions ϕ_c as functions of the inverse system size d_s/R for spherical particles (green symbols), ellipsoidal particles with aspect ratios of 1.4 (yellow) and 1.9 (orange), and rodlike particles with an aspect ratio of 8.0 (red). ϕ_c is calculated from different physical measurements: F_s (solid squares), C_Ψ (solid circles), L_n (solid upper triangles). For rodlike particles, calculations are also done on F_s of bulk samples with another $Q = 0.28$ (solid lower triangles). The dashed lines indicate the average ϕ_c for different aspect ratios. All area fractions above are obtained by VFT fittings. Area fractions from the power law fittings are also shown (hollow symbols) for bulk samples of rodlike particles.

aspect ratios of particles (Fig. 4.18), which is in agreement with the previous prediction of ellipsoids with aspect ratios smaller than 3.5 [20]. The fragility index D still has the linear dependence on $1/R$. However ellipsoidal particles with an aspect ratio $P = 1.4$ have smaller slope than those with $P = 1.9$ for $D_{C_\Psi}(R)$. Particles with a larger aspect ratio have longer long axis and need to interact with less neighbor particles to feel the confinement by the boundary. The constant ϕ_{c,L_n} and linear increasing $D_{L_n}(1/R)$ are also observed in rotational dynamics (Fig. 4.19). The similarity between the measurements from C_Ψ and F_s is another evidence showing that the translational and rotational dynamics are obstructed by the confinement at same level (Fig. 4.17).

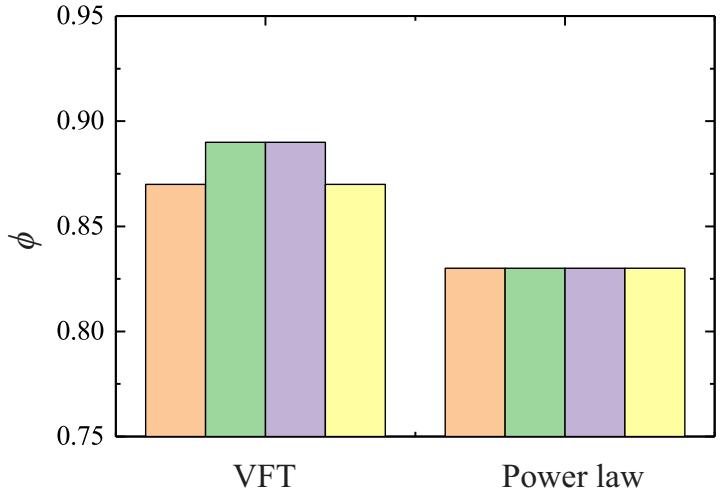

Figure 4.21: Critical area fraction ϕ_c from different fitting methods for bulk samples of rodlike particles. ϕ_c is calculated from different physical measurements: $F_s(Q = 0.57)$ (brown), C_Ψ (green), L_n (purple) and $F_s(Q = 0.28)$ (yellow). The ϕ_c values are also plotted in Fig. 4.20 as red symbols.

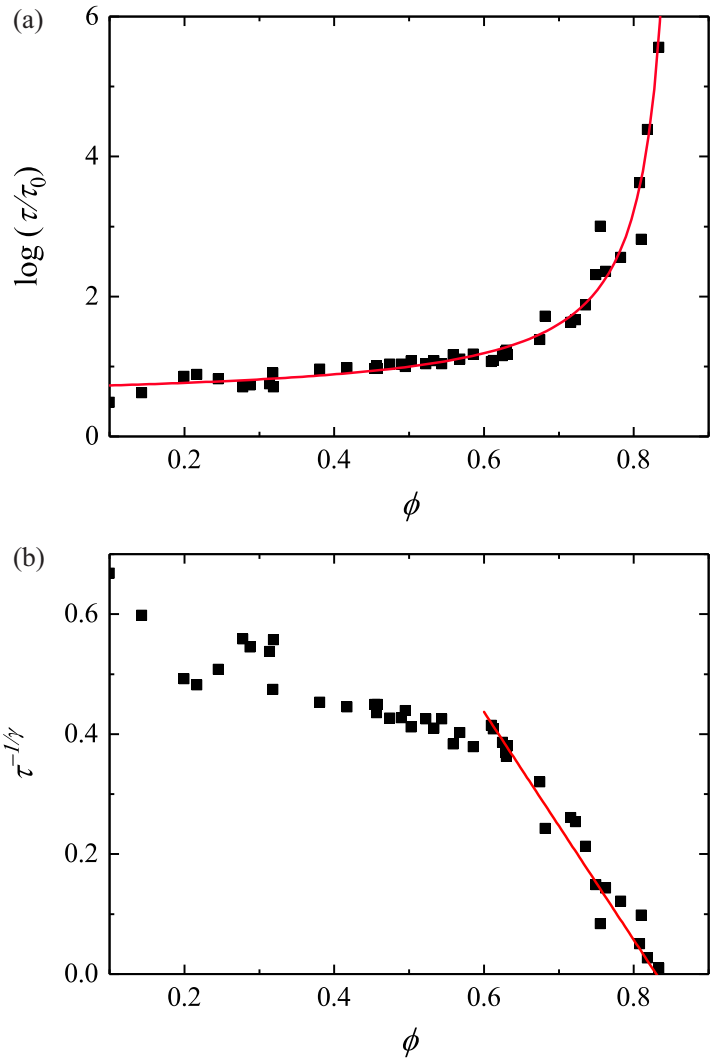

Figure 4.22: VFT fittings (a) and power law fittings (b) of $\tau_{\alpha,F_s(Q=0..28)}$ for bulk samples of rodlike particles with $P = 8.0$. For the power law fitting, data points only with $\phi > 0.6$ are used.

Besides different dependences on viscosity η for D_R and D_T, the decoupling between translational and rotational dynamics is also shown by the different ϕ_c calculated from F_s and L_n for ellipsoidal particles with large aspect ratios ($P > 3.5$) [20]. Fig. 4.20 summaries all the critical area fractions ϕ_c we measured in the experiments. For spherical particles and ellipsoidal particles with smaller aspect ratios ($P = 1.4$ and 1.9), different measurements methods yield same ϕ_c for bulk samples as well as confined samples. The deviations of ϕ_c are usually less than 0.01. The differences of ϕ_c between spherical particles and ellipsoidal particles are caused by the different highest close packed area fractions due to the change of particle shapes. The same ϕ_c for each type of particles is consistent with other observations of ellipsoids with small aspect ratios ($P < 3.5$) [20].

We further conduct measurements of rodlike PS particle with a much larger aspect ratio ($P = 8.0$). Fig. 4.21 shows the critical area fraction ϕ_c using VFT fitting function (Eqn. 4.3). All ϕ_c values are same within the error, which is quite different from the previous result that the difference between ϕ_{c,F_s} and ϕ_{c,L_n} could be as high as 0.1 for ellipsoids with larger aspect ratios ($P = 6.0$ and 9.0) [20]. To further confirm this unexpected result, we also use another power law relation to fit our α relaxation time:

$$\tau_\alpha(\phi) \sim (\phi_c - \phi)^{-\gamma}, \tag{4.13}$$

where γ is obtained from fitting relaxation curves and ϕ_c is the critical glass transition point. This relation is predicted by mode-coupling theory (MCT) [20, 157]. Note that the ϕ_c here is different from the ϕ_c obtained from the VFT relation (Eqn. 4.3). $\phi_{c,\mathrm{VFT}}$ indicates the ideal glass transition point where the number of local minimums on the free energy landscape dereases to one and the configurational entropy vanishes (Chapter 3). Fig. 4.22 presents both the VFT fittings and power law fittings of $\tau_{\alpha,F_s(Q=0..28)}$ for bulk samples of rodlike particles. Same procedures are done for τ_{α,C_Ψ} and τ_{α,L_n}, which are

together shown in Fig. 4.20 and Fig. 4.21. ϕ_c from the power law fitting is lower than that from the VFT fitting due to different physical meanings. All ϕ_c values obtained by power fittings of different measurements are still same within the error, which are same as the results from VFT fittings. Different values of Q from F_s definition are also compared. $Q = 0.57$ is directly calculated from the position of the first peak of the structural factor $S(Q)$ and $Q = 0.28$ is one half of it. For both VFT and power fittings, different choices of Q do not change ϕ_{c,F_s} (Fig. 4.21).

In sum, regardless of the type of physical measurements (F_s, C_Ψ or L_n), fitting functions (VFT or power law), and Q values for F_s (0.57, or 0.28), the critical area fractions ϕ_c for rodlike particles with an aspect ratio of 8.0 are always constant. This is different from other observations in ellipsoidal particle systems [20, 155, 164, 165, 166]. The reason of the differences is not clear now. One possibility is due to the different structures of ellipsoidal particles and rodlike particles at high ϕ. Ellipsoidal particles usually have splay structures while rodlike particles prefer staying parallel to their neighbor particles (Fig. 4.2) [20]. And the different local structures may affect the ϕ_c measured from translational and rotational dynamics. More experimental data for ellipsoidal particles with larger aspect ratios is needed to explain the unexpected results.

4.4 Conclusion and Discussion

Our experiments use the confinement as a tool to probe the Mermin-Wagner long-wavelength fluctuations and show the fluctuations have a logarithmic dependence on the system size when the system approaches to the glass transition. We argue that the bond-orientational correlation function C_Ψ is a better option to quantified translational dynamics in 2D considering that the more widely used self-intermediate scattering function F_s is altered by the long-wavelength fluctuations. We further systematically study

the effect of the fluctuations on particle dynamics near the glass transition. We confirm the predication of the 1/2 power scaling of the pinning length and unveil a divergent static length scale when $\phi \to \phi_c$ with and without the fluctuations in 2D, while the fluctuations make the pinning length slightly larger. Ellipsoidal particles are also used to directly compare translational and rotational dynamics to show the decoupling between translational and rotational dynamics and the decoupling is not affected by the confinement. For rodlike particles with a large aspect ratio ($P = 8.0$), constant values of ϕ_c are observed regardless of the type of physical measurements, fitting functions, and Q values, which is different from other observations [20]. We demonstrate that the success of RFOT theory and modified Adam-Gibbs relations in 3D can also be applied to 2D, showing the similarities between 2D and 3D like previous articles [96, 97]. It also should be emphasized that the glass transition is an active research area but far from understood. There is no unified theory to explain the mystical behaviors. Even though we use RFOT and the modified Adam-Gibbs theory to explain our results, similar colloidal experiments can also be explained by other approaches [14, 47, 167]. Our results are independent of theories. And the unique approach by confinement provides new insights into the dynamics near the glass transition.

Chapter 5

1D Strings*

5.1 Introduction

Due to its broad applications such as photonics, materials synthesis and biomedical engineering, self-assembly of colloidal particles in both equilibrium and non-equilibrium has drawn more and more attentions from researchers in different fields [78, 168]. Compared to the more well-studied and well-understood colloidal self-assembly in equilibrium, our understanding of non-equilibrium self-assembly of colloidal particles is still of lack [71, 76, 169, 170]. The non-equilibrium dynamic self-assembly provides us a fertile ground to exploring non-equilibrium statistical mechanics as well as a powerful tool for designing novel colloidal materials with unusual mesoscopic structures.

Due to the rapid growth of microfluidic techniques, flow-driven particle self-assembly especially in one dimension (1D) is particularly attractive among all different non-equilibrium systems. [171, 172, 173, 174, 175]. 1D colloidal strings with regular particle spacing offer precise control over the positions of colloidal particles such as cells and

*Reproduced in part with permission from (Yu Abe, Bo Zhang, Leonardo Gordillo, Alireza Mohammad Karim, Lorraine F Francis, and Xiang Cheng, "Dynamic self-assembly of charged colloidal strings and walls in simple fluid flows", *Soft Matter*, Royal Society of Chemistry).

droplets, which is crucial for flow cytometry, cell separation and diagnostics, and microfluidic computation and encryption [176, 177, 178, 179, 180, 181, 182, 183, 184, 185, 186, 187]. Nevertheless, compared with a myriad of methods for creating 2D or 3D colloid structures, fewer approaches are available for assembling 1D colloidal strings. Due to the isotropic nature of interparticle interactions of colloidal spheres, 1D colloidal strings are usually constructed through special processes. In equilibrium, 1D colloidal strings have been assembled via template-directed colloidal epitaxy and electromagnetic field-assistant self-assembly [170, 188, 189, 190]. In fluid flows, Colloidal strings self-assembling along the vorticity direction of shear flows has been reported in both viscoelastic fluids and Newtonian fluids under strong confinement [176, 177, 179, 180, 181]. Flow-aligned colloidal strings along the flow direction have also been observed at finite Reynolds numbers ($Re > 1$) when the effect of inertia is significant [178]. However, such high-Re condition cannot be easily satisfied in many microfluidic applications. As a result, for many applications, flow-aligned colloidal strings are normally created manually in microfluidics. Particles are injected into microfluidic channels at externally-controlled regular time intervals [191, 192, 193]. However, the string structures obtained from such methods are metastable, and susceptible to external perturbations [191].

In this chapter, we report a simple experimental method to prepare 1D colloidal crystals. Charged colloidal particles under unidirectional flows self-assemble into flow-aligned strings with regular particle spacing near a solid boundary. We use fast confocal microscopy to study particle dynamics of the self-assembly process. we optimize the condition for the formation of colloidal strings by systematically varying key control parameters such as the flow rate, the strength of electrostatic interactions, the size and polydispersity of particles and the dimension of micro-fluidic channels. Based on our experimental observation, we propose a simple model that explains the intriguing non-equilibrium self-assembly process. Being minimalistic with crude approximations,

our model is nevertheless capable of capturing the essential mechanism for the origin of colloidal strings. As such, our experiments demonstrate the possibility of assembling flow-aligned 1D ordered colloidal structures at low Re through the balance of hydrodynamic coupling and electrostatic repulsion. Compared with previous methods, our study provides a much simpler approach to prepare a large number of stable flow-aligned colloidal strings, showing a great potential for different microfluidic applications. Lastly, we show that this approach also leads to the formation of 2D colloidal walls when a moderate transverse alternating current (AC) electric field is applied to the same colloidal system.

5.2 Methods

5.2.1 Fluorescent Label of PMMA Particles

We synthesize poly(methyl methacrylate) (PMMA) spheres as our colloidal particles, which are fluorescently labeled with Nile Red [131, 132]. The particles are stabilized by covalently bonding polymer brushes made of poly(1,2-hydroxy stearic acid) (PHSA). Most of our experiments are conducted using particles of average diameter $d = 1.36\,\mu m$, although two other batches of particles with $d = 1.56\,\mu m$ and $1.86\,\mu m$ are also used to test the effect of polydispersity. The polydispersities of particles in these particle batches are below 11 %. Particle sizes and polydispersities are determined from dynamic light scattering (DLS). PMMA particles are suspended in a mixture of decahydronaphthalene (decalin, 27.2 wt%) and cis + trans cyclohexyl bromide (CXB, 72.8 wt%), which matches both the density and refractive index of the particles. The density and the viscosity of the mixture are $\rho = 1.20$ g/cm^3 and $\eta = 1.74$ mPa·s, respectively. Its relative dielectric constant is $\epsilon_r = 5.6$. The volume fraction of suspensions is fixed at $\phi = 1$ % for most of our experiments. We obtain the surface charge of PMMA particles in the decalin/CXB

mixture via electrophoresis [136]. The electrophoretic mobility of particles in a DC field of 6 V/mm is measured, which can be converted into the zeta potential and the surface charges of particles based on a theory by Carrique et al. [194]. The numbers of positive surface charges on the three batches of PMMA particles with increasing d are similar with $Z = 158 \pm 8.2$, 152 ± 12 and 160 ± 4.7, respectively. Note that we use a Debye screening length $\kappa^{-1} \approx 1.3\,\mu\text{m}$ in our calculation, which is derived from the measured conductivity of the mixture at 218 $\text{pS}\cdot\text{cm}^{-1}$ [136]. The screening length can be changed when salt is added into the solvent. All our measurements are conducted at room temperature.

5.2.2 Fabrication of Microfluidic Channels

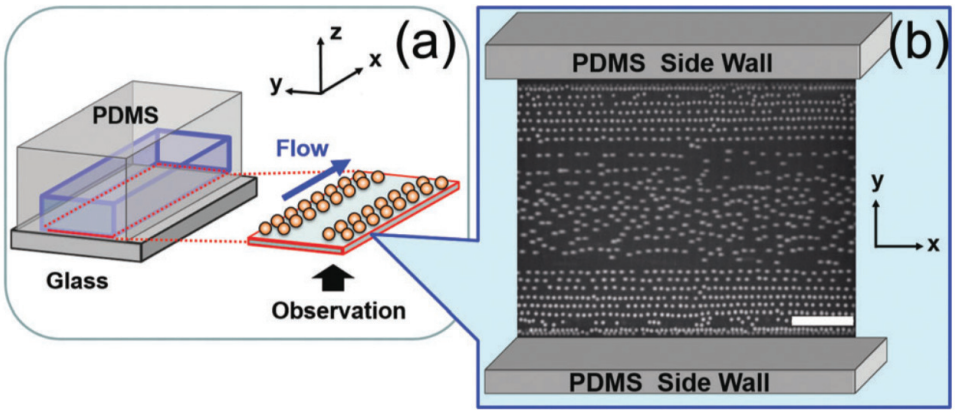

Figure 5.1: Formation of colloidal strings in microfluidic flows. (a) A schematic showing the geometry of our experiments. A coordinate system is defined in the upper left. (b) An example of colloidal strings in the narrow channel next to the glass bottom. Flow is along the x direction. The average diameter of particles is 1.36 µm and the flow rate is 3.0 µL min^{-1}. The scale bar is 25 µm.

We fabricate microfluidic channels from poly(dimethylsiloxane) (PDMS) using conventional photolithography. The channels have rectangular cross-sections with two different inner dimensions. A narrow channel has a width of $W = 99.6 \pm 1.4$ µm, whereas

a wide channel has a width of $W = 299.7 \pm 2.1$ µm. All channels have a similar height of $H = 104.8 \pm 9.2$ µm and a length of $L \approx 4$ cm. We define a Cartesian coordinate system such that x is the flow direction along the channel length, y is along the width direction with -$W/2 \leq W/2$ and z is along the height direction with $0 \leq z \leq H$ (Fig. 5.1a). The cell is sealed at the bottom by a glass microscope coverslip, allowing for direct confocal imaging. Colloidal suspensions are injected into the channels using a syringe pump with a controlled volumetric flow rate ranging from 2.0 to 9.0 µL·min^{-1}. The uncertainties on flow rates are less than 0.5 %. Within this range, the particle Reynolds number, $Re \equiv \rho v_p d/\eta < 5 \times 10^{-4}$, where v_p is the velocity of particles near the bottom wall. Finally, to probe the effect of transverse electric fields on the self-assembly process, we also fabricate a small microfluidic channel of 100×15 µm^2 ($W \times H$), where the bottom and top walls of the channel are made of indium tin oxide (ITO) coated glasses.

5.2.3 Acquisition of Image Data

We use an inverted spinning-disk confocal microscope to image the dynamics of particles near the center of a microfluidic channel away from its inlet and outlet. The images are recorded at 100 frames per second. Particle dynamics at different heights z above the bottom wall are taken by varying the focal plane of a 60× microscope objectives (NA = 1.4). To follow the dynamics of colloidal particles for the longest possible time, we translate the sample holder of the microscope in the direction opposite to the flow of suspensions at a controlled speed in certain experiments, so that particles at a given position can be imaged in their co-flowing frame. The positions of all particles in the field of view are then tracked over a long time using a widely-used particle tracking algorithm [116].

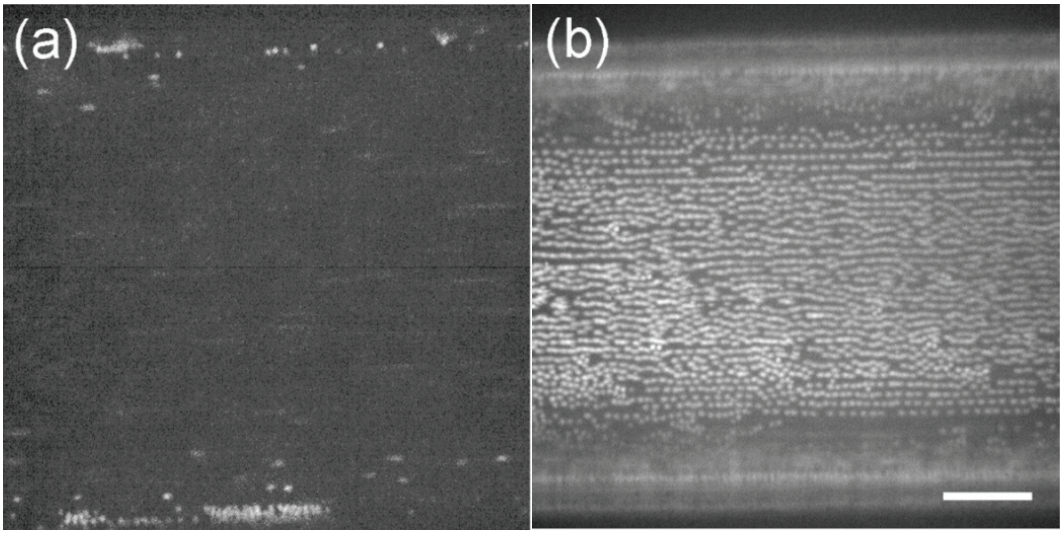

Figure 5.2: Colloidal strings at different heights. (a) String structure is absent away from the glass bottom. The height is $z = 5$ µm (b) Strings next to the top plate. Although particle concentration is fixed at 1%, more particles are attracted to the top PDMS surface than to the bottom glass surface (see Fig. 2). Flow rate is at 3.0 µL/min. The scale bar is 20 µm.

5.3 Results

A typical example of colloidal strings formed in our microfluidic channel is shown in Fig. 5.1b, where PMMA particles self-assemble into flow-aligned 1D strings at the boundary next to the glass bottom. The strings move along with the ambient flow but at significantly reduced speeds. Above the bottom layer, strings disappear, where particles simply move passively with the ambient flow as expected (Fig. 5.2a). The strings are also observed next to the top wall (Fig. 5.2b). In this study, we focus on the dynamics of particles next to the glass bottom at $z \approx d/2$ for the convenience of imaging. Nevertheless, the mechanism discussed should equally apply for strings next to the top wall. To reveal the origin of colloidal strings, we first investigate the influence of flow rates and the strength of electrostatic interactions on the string structure.

5.3.1 Flow Rate and Ionic Strength Dependence

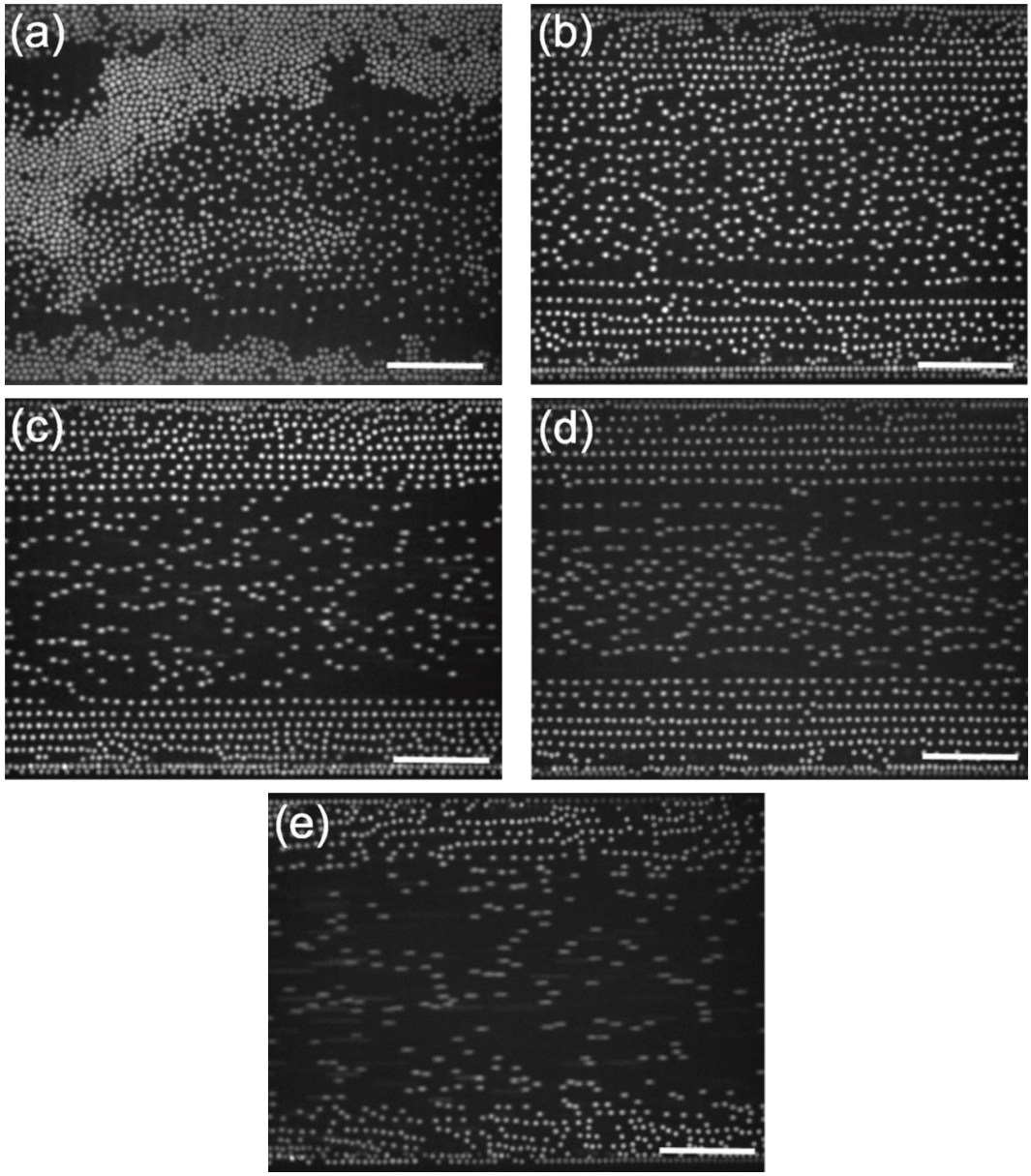

Figure 5.3: Colloidal strings at different flow rates in the narrow channel. Suspensions flow toward the right. From (a-e), the flow rates are 2.0, 2.2, 2.6, 3.0 and 3.6 µL·min^{-1}, respectively. The top and the bottom edges of the images correspond to the two side walls of the channel. The scale bars are 25 µm.

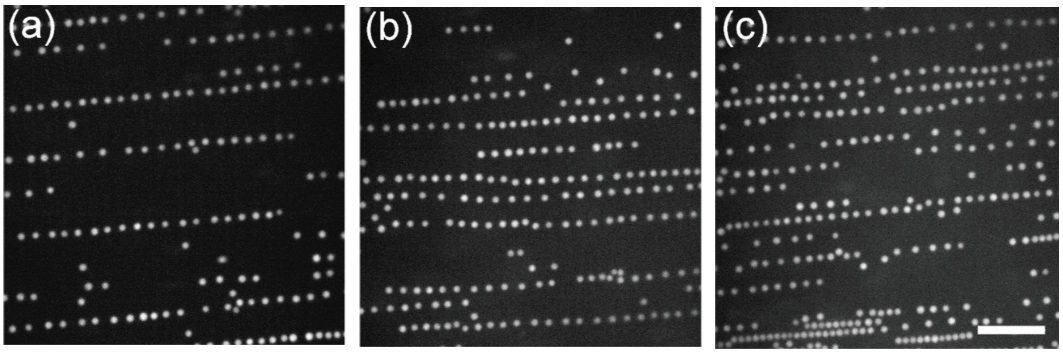

Figure 5.4: String structures at different particle concentrations. (a) 0.25 wt%, (b) 0.5 wt% and (c) 1.0 wt%. The wide channel of 300 × 100 μm^2 was used. The flow rate is 9.0 μL/min. The scale bar is 20 μm.

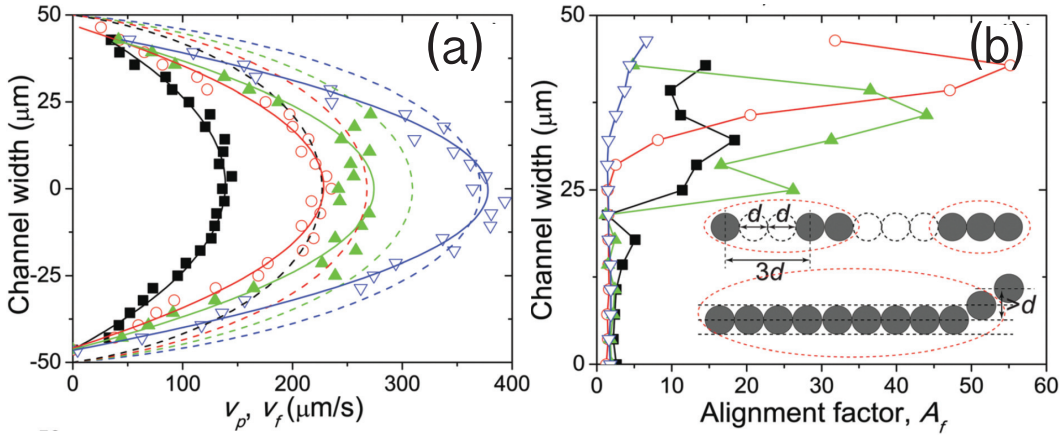

Figure 5.5: Degree of the string order at different flow rates. (a) Velocity of particles, v_p, across the width of the channel. From left to right, the flow rates are 2.2 (black squares), 2.6 (red circles), 3.0 (green up-pointing triangles) and 3.6 μL·min^{-1} (blue down-pointing triangles), respectively. The solid lines are fits with parabolic functions. The dashed lines are the calculated velocity of the unperturbed flows at $z = d/2$. (b) Alignment factor, A_f, across the width of the channel. Since the string order is symmetric, the results are shown only for the upper half of the channel. The symbols are the same as those used in (a). The inset illustrates the definition of strings. Particles in a dashed circle belong to one string. Neighboring particles in a string should have distances smaller than $3d$ along the x direction and smaller than d along the y direction.

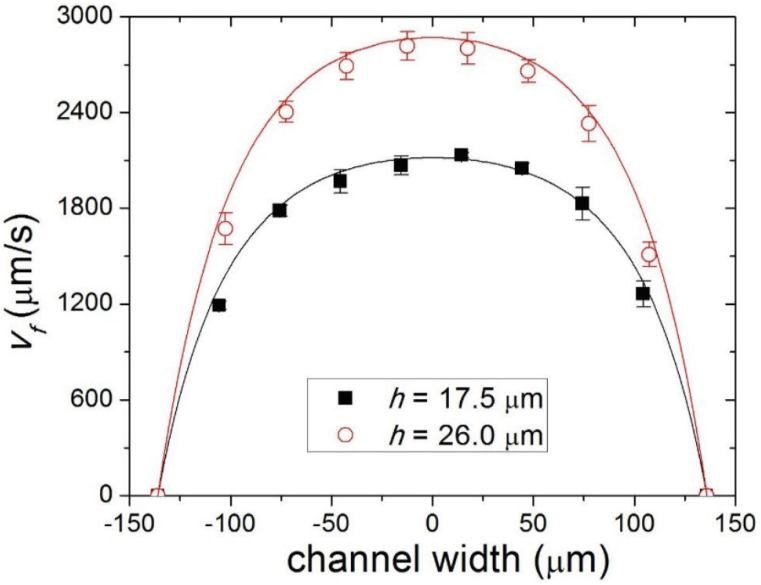

Figure 5.6: Comparison of calculated velocity profiles (solid lines) and measured velocity profiles (symbols). The channel has a cross-section area of 272 × 114 μm^2. The flow rate is 4 μL/min. h is the height above the bottom plate.

Flow rates show a strong effect on the formation of colloidal strings (Fig. 5.3). In the narrow channel, at a low flow rate of 2.0 μL·min^{-1}, most PMMA particles entering the channel near the glass bottom stick to the glass bottom resisting the drag from the ambient flow. Since the refractive index of the particles is close to that of the glass bottom, the effective Hamaker constant and, therefore, the van der Waals attraction between particles and the glass surface should be small [195]. The adhesion mainly arises from the electrostatic attraction as we shall demonstrate below. At this low flow rate, particles are attracted to the glass surface and form immobile clusters instead of moving strings (Fig. 5.3a). At a slightly higher flow rate of 2.2 μL·min^{-1}, strings start to form on the surface of the glass (Fig. 5.3b). At even higher flow rates of 2.6 μL·min^{-1} and 3.0 μL·min^{-1}, the string structure can be clearly identified near the side walls (Fig. 5.3c and d). Short and less regular strings can also be observed near the

center of the channel. The spacing between the strings along the y direction shows large variations. The average spacing between the strings decreases with increasing particle concentrations (Fig. 5.4). It is worth noting that the strings are very stable and robust against strong perturbations such as the presence of stuck particles on the surface and the variation of fluid flows. However, as we increase the flow rate further to 3.6 $\mu L \cdot min^{-1}$, colloidal strings collapse (Fig. 5.3e). At this high flow rate, particles move passively with the ambient flow.

To quantify the degree of the 1D string order across the width of the channel, we measure the alignment factor at different y values, $A_f(y)$, defined as

$$A_f = \frac{\sum_{L=1}^{\infty} N_L L^2}{\sum_{L=1}^{\infty} N_L L}, \tag{5.1}$$

where N_L is the number of strings that contain L particles [180]. Af is similar to the weight-average molecular weight of polymer chains. $A_f \geq 1$ and $A_f = 1$ when there are only isolated particles. Note that a string is defined such that all the neighboring particles in the string are within three particle diameters away from each other along the x direction and within one particle diameter away along the y direction (Fig. 5.5b lower inset).

The alignment factor, $A_f(y)$, the velocity of unperturbed ambient flows, $v_f(y)$, and the velocity of particles, $v_p(y)$, at different flow rates are shown in Fig. 5.5. Here, v_f is calculated based on the flow profiles of pressure-driven flows in rectangular ducts of given cross-sections at given flow rates [196]. No-slip boundary conditions at the walls of the microfluidic channels are assumed in these calculations. We verify our calculation by directly comparing the calculated velocity profiles with the measured velocity profiles above the glass bottom (Fig. 5.6). The relative error on v_f is about 7 %. The velocity of particles, v_p, is measured from experiments via particle tracking velocimetry. Note

that v_p reduces to zero at y slightly different from -$W/2$ and $W/2$ (Fig. 5.5a). As shown in Fig. 5.3, a layer of particles sticks to the side walls of the channel, leading to zero particle velocity near the side walls next to the glass bottom. However, away from the glass bottom, fewer particles stick to the side walls (Fig. 5.2).

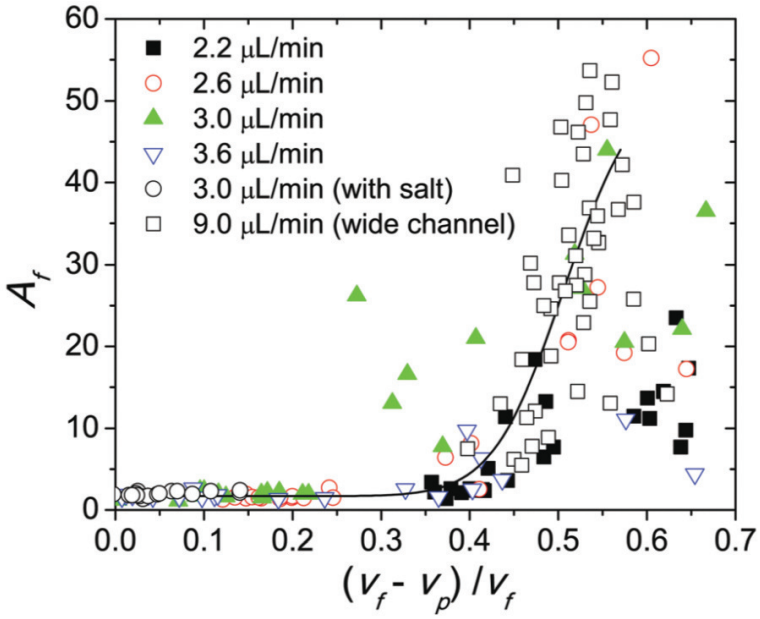

Figure 5.7: Alignment factor, A_f, as a function of the normalized velocity difference $(v_f - v_p)/v_f$. v_p is the particle velocity. v_f is the velocity of unperturbed ambient flows. Flow rates are indicated in the plot. The solid line provides a visual guide.

As the flow rate increases, the velocity difference between the particles and the unperturbed flow, $(v_f - v_p)$, decreases (Fig. 5.5a). The degree of the string order is strongest near the side walls of the channel, which increases with the flow rate at low flow rates and decreases at high flow rates (Fig. 5.5b). More importantly, we find a positive correlation between the degree of the string order and the velocity difference between the particles and the ambient flows (Fig. 5.7), when the velocity difference is small at $(v_f - v_p)/v_f < 0.55$. The strings disappear when $v_f \approx v_p$. At larger velocity differences, the degree of the string order may decrease, although the data show strong

fluctuations in this limit.

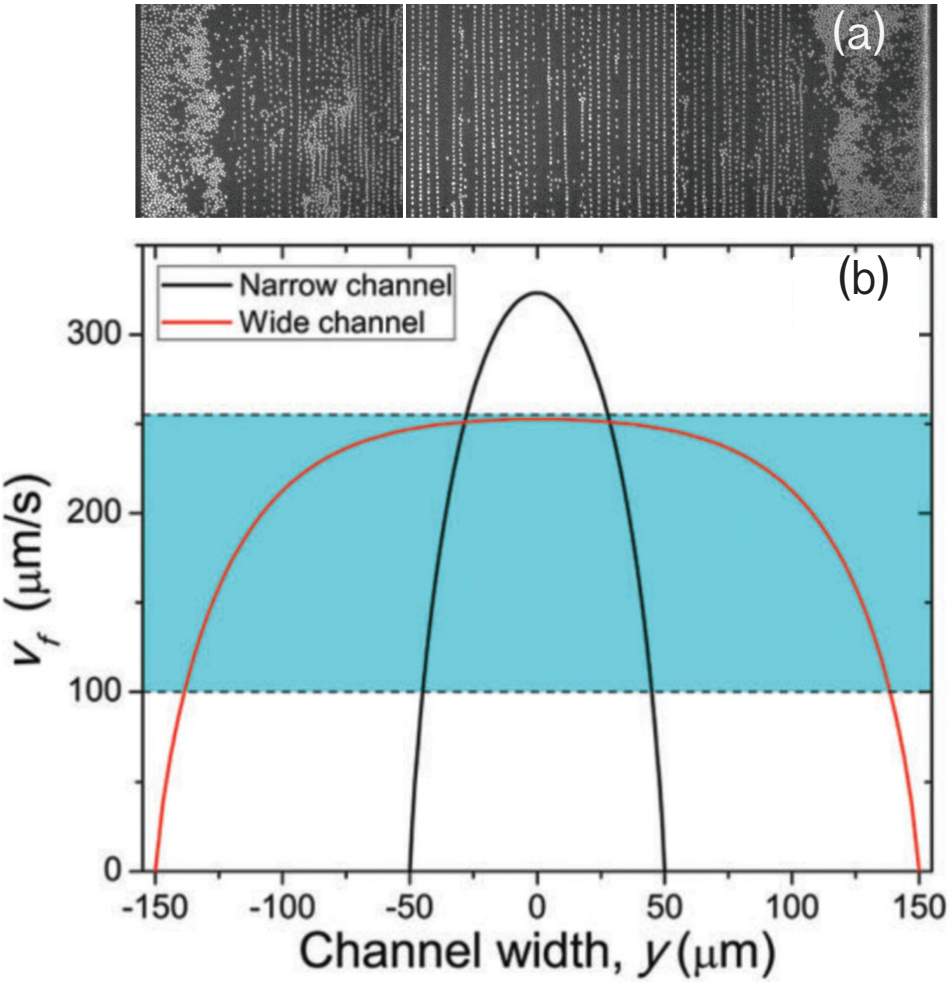

Figure 5.8: (a) Formation of colloidal strings in the wide channel. The suspension flows toward the right and the flow rate is 9.0 μL·min^{-1}. Since the width of the channel is larger than the field of view of our 60× objectives, the entire channel is imaged by tiling three separate images. The top and bottom edges of the image correspond to the two side walls of the channel. The scale bars are 25 μm. (b) Flow profiles in the narrow and wide channels at $z = d/2$. The flow rates are 3.0 μL·min^{-1} in the narrow channel and 9.0 μL·min^{-1} in the wide channel, which give the same flow rate per unit cross-section area. The blue area indicates qualitatively the region where the ambient flow velocities are in the right range for the formation of colloidal strings.

It is worth noting that the presence of the side walls and the shear gradients near

the side walls are not necessary for the formation of the strings. We have conducted experiments in the wide channel of 300 μm in width. The formation of strings can be clearly observed at the center of the channel (Fig. 5.8). The difference in particle structures in the narrow and wide channels can be explained from different velocity profiles in the two channels. With a fixed flow rate per unit cross-section area, the flow velocity near the center of the narrow channel is larger than that near the center of the wide channel. We show the velocity profiles in the two channels at a flow rate of 3 $\times$ 10^{-4} μL·(min·μm^2)$^{-1}$ (Fig. 5.8b), which corresponds to 3.0 μm·min^{-1} in the narrow channel (the flow rate used in Fig. 5.3d) and 9.0 μm·min^{-1} in the wide channel (the flow rate used in Fig. 5.3a). The velocity difference between particles and the ambient flow necessary for the formation of colloidal strings only establishes at intermediate ambient velocities, as illustrated qualitatively by the blue region in Fig. 5.8b. At lower ambient velocities below the blue region, the drag forces on particles are too weak. Particles stick to the glass bottom (Fig. 5.3a). At higher ambient velocities above the blue region, particles move with the ambient flow and the velocity difference reduces to zero (Fig. 5.3e). Based on the above picture, the strings form near the wall in the narrow channel (Fig. 5.8b). There exist small regions of one or two particle layers next to both side walls, where particles are immobile due to weak ambient flows (Fig. 5.5a). Near the center of the narrow channel, the flow velocities are too large and the velocity differences between particles and the flow are too small to form colloidal strings (Fig. 5.3d). In contrast, in the wide channel, the flow velocities away from the side walls all fall in the blue region. As such, colloidal strings form near the center of the wide channel. Particles are immobile in a larger region near the side walls due to the smaller velocity gradients near the walls of the wide channel (Fig. 5.8b). Quantitatively, the correlation between A_f and $(v_f - v_p)/v_f$ in the wide channel shows the similar trend as that in the narrow channel (Fig. 5.7). Thus, our results indicate that the velocity difference

between the particles and the ambient flows, instead of the shear gradient, is the key factor dictating the formation of the strings.

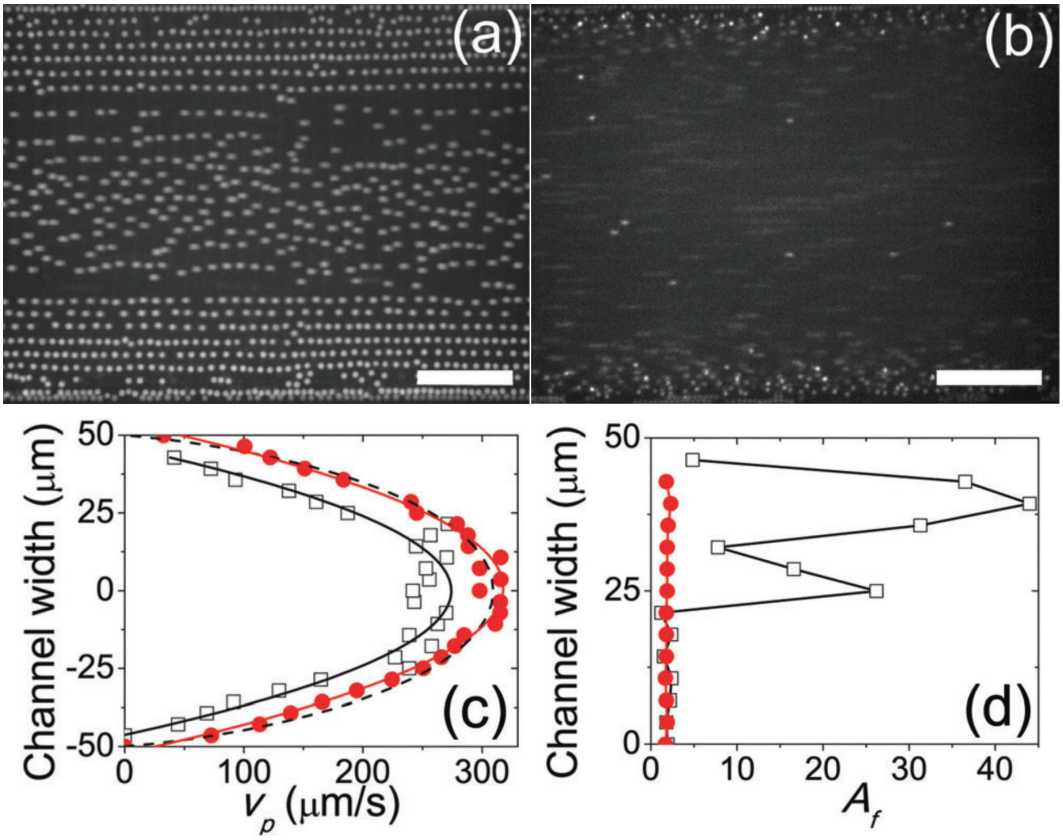

Figure 5.9: Colloidal structures at different ionic strengths. (a) Colloidal strings in the solvent without TBAB. (b) The collapse of strings in the solvent with 100 μM TBAB. The flow rate is 3.0 μL·min^{-1}. A comparison of particle velocity and alignment factor in the two cases are shown in (c) and (d), respectively. Empty squares are for the solvent without TBAB. Red disks are for the solvent with TBAB. The scale bars are 25 μm.

The formation of strings also depends on the electrostatics of particles. To reveal the effect of electrostatic interactions, we add 100 μM quaternary ammonium salt-tetrabutyl ammonium bromide (TBAB)-into the solvent, which according to a previous study reverses the sign of the surface charge of particles [133]. We also directly confirm the

reverse of the surface charge on PMMA particles in our experiments using electrophoresis. As a result, when the salt is added, PMMA particles do not stick to the glass bottom even at low flow rates. Due to the repulsive, instead of attractive, interactions between particles and the wall, the density of particles at the bottom is dramatically reduced (Fig. 5.9b). We cannot observe the formation of strings at any flow rate (Fig. 5.9b and d). Particle velocity also significantly increases. At 3.0 $\mu L \cdot min^{-1}$, the velocity of particles is almost the same as that of the unperturbed ambient flow (Fig. 5.9c). The finding indicates that without salt the electrostatic attraction between particles and the glass bottom induces frictional or lubrication forces on the particles, which slow down the motion of the particles relative to the ambient flow. With the reversed electrostatic interaction at high ionic strength, the repulsion between particles and the glass bottom eliminates the drag force from the bottom. As a result, the particles move passively with the flow with $(v_f - v_p)/v_f \approx 0$. The strings do not form (Fig. 5.9).

In summary, our experiments show that the velocity differences between the ambient flows and particles are important for the formation of colloidal strings. Such velocity differences lead to hydrodynamic coupling between particles, crucial for the bonding of particles in the strings. Moreover, the result with reversed electrostatic interactions suggests that the retarded motion of particles is induced by the electrostatic attraction between particles and the glass bottom. Charges on particles necessarily give rise to electrostatic repulsions between particles, a factor that also needs to be considered in modeling colloidal strings.

5.3.2 Dynamics of Stable Particle Pairs

To quantify the interparticle interactions, we study the dynamics of stable particle pairs. The formation of particle pairs is the precursor and the first step for the assembly of longer colloidal strings. To create stable particle pairs without interference from longer

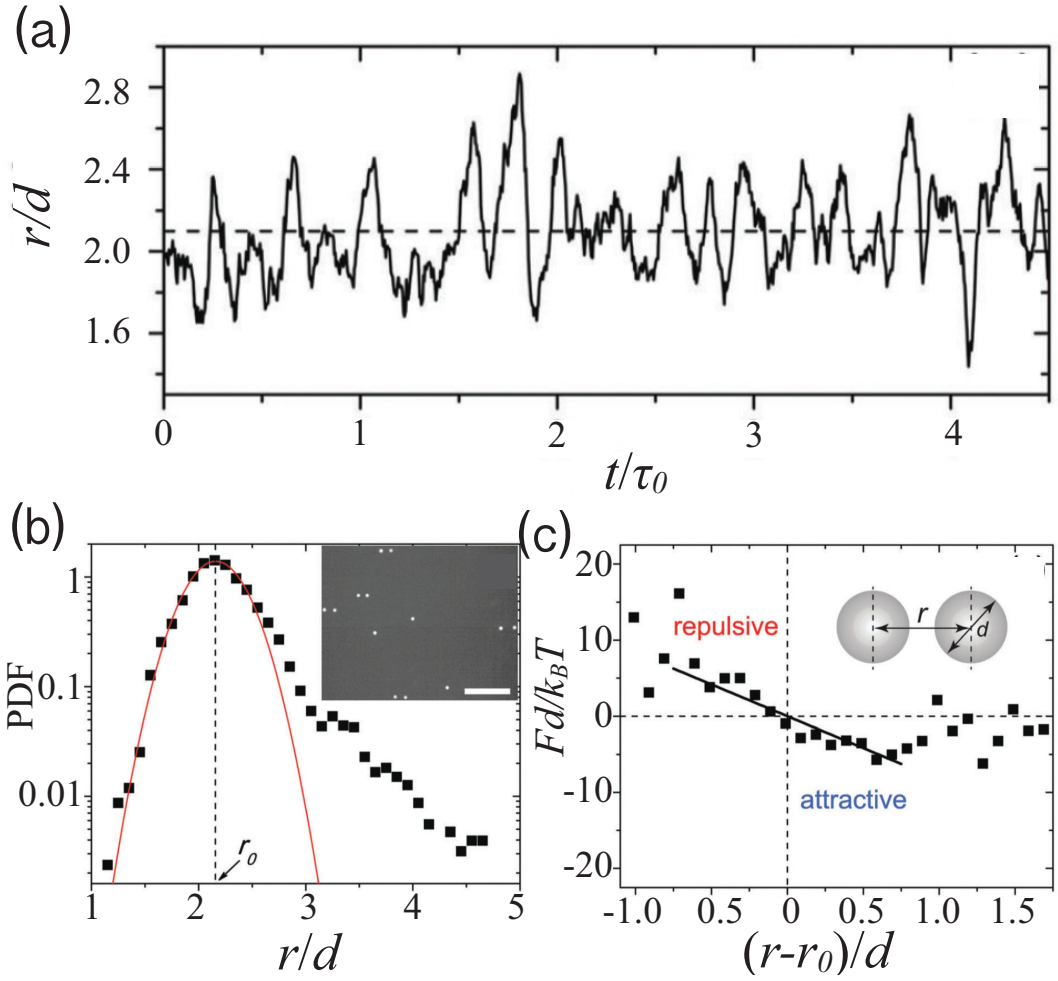

Figure 5.10: Dynamics of particle pairs in the wide channel. (a) Center-to-center distance between two particles in particle pairs, r, as a function of time, t. r is normalized by the average particle diameter d. r and d are defined in the inset of (c). t is normalized by the Brownian relaxation time of particles in the dilute limit, $\tau_0 = 6\pi\eta a^3/k_BT = 2.19$ s, where $\eta = 1.74$ mPa·s is the viscosity of the solvent and $a = d/2$ is the average radius of particles. The horizontal dashed line indicates the mean distance between particles. The flow rate is 2.6 µL·min^{-1}. (b) Probability distribution function (PDF) of r. The solid line is a fit of a Gaussian distribution using the data near the peak r_0 and $r < r_0$. The vertical dashed line indicates the peak of the distribution, r_0. The inset shows stable particle pairs in our experiments. The scale bar is 25 µm. (c) Effective force between particles, $F(r)$. F is normalized by k_BT/d. The black line shows the model result.

colloidal strings, we reduce the volume fractions of suspensions to $\phi = 0.01$ % in our experiments. Most particles form stable particle pairs in the wide microfluidic channel at such a low particle concentration (Fig. 5.10b inset). The dynamics of stable particle pairs next to the glass bottom around $y = 0$ in the wide channel are then measured, where the variation of the speeds of the ambient flow is small, thanks to the small velocity gradients near $y = 0$. We track the center-to-center distance between two particles in particle pairs, r, as a function of time (Fig. 5.10a and c inset). Fig. 5.10b shows the probability distribution function (PDF) of the distance. The maximal probability occurs at $r_0/d = 2.160 \pm 0.006$. Near r_0 and at short separations with $r < r_0$, the distribution can be well approximated by a Gaussian distribution with a standard deviation of $\sigma/d = 0.52 \pm 0.01$. The PDF shows a long tail at large r, indicating higher probabilities to find particle pairs at large separations.

In analogy to equilibrium systems, the Gaussian distribution near r_0 allows us to define an effective potential and, accordingly, an effective force between particles in this non-equilibrium flow-driven system.

$$\frac{U(r)}{k_B T} = \ln A - \ln(\mathrm{PDF}(r)), \tag{5.2}$$

$$F(r) = -\frac{\mathrm{d}U(r)}{\mathrm{d}r} = \frac{k_B T}{\mathrm{PDF}} \cdot \frac{\mathrm{dPDF}}{\mathrm{d}r}, \tag{5.3}$$

where $U(r)$ is the effective potential in the unit of thermal energy $k_B T$ and $F(r)$ is the effective force between particles in a particle pair. A is the normalization constant of the probability distribution. F(r) in the unit of $k_B T/d$ is shown in Fig. 5.10c. Near the equilibrium position $r = r_0$ where $F(r = r_0) = 0$, the harmonic potential gives rises to a spring-like force. When $r < r_0$, a repulsive force pushes the two particles apart, whereas at $r > r_0$ an attraction pulls the particles together. The force can be as large

as several k_BT/d and, therefore, can effectively suppress the thermal motion of particles and maintain the stability of the particle pair. When the distance between particles is one particle diameter away from the equilibrium position, $r > r_0 + d$, $F(r) \approx 0$. The particles are decoupled.

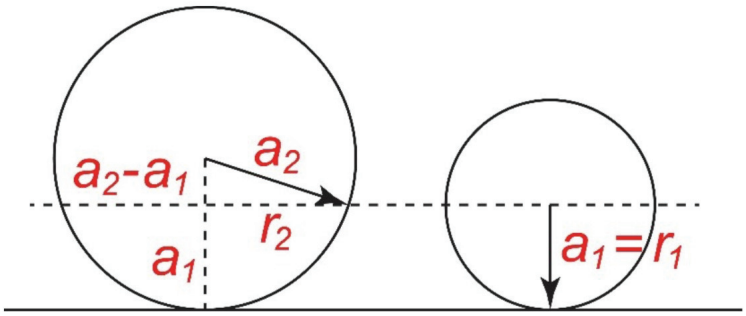

Figure 5.11: A schematic showing the calculation of the size ratio of two particles, a_2/a_1.

The results shown in Fig. 5.10b and c are obtained by averaging tens of particle pairs of different size ratios. A more detailed analysis shows that the equilibrium position r_0 depends on the size ratio of the two particles in a particle pair, a_2/a_1, where a_1 and a_2 are the radii of the leading and the trailing particles in the particle pair, respectively. Note that when calculating a_2/a_1, a correction has been made to consider the effect that the centers of small and large particles sit at slightly different heights above the glass bottom (Fig. 5.11). We estimate the errors on a_2/a_1 to be about 4. To probe a larger range of size ratios, we mix the $d = 1.36$ µm particle batch with two other batches of particles with $d = 1.56$ and 1.86 µm. The polydispersity of these particle batches allows us to obtain an almost continuous range of size ratios. We show r_0 as a function of a_2/a_1 in Fig. 5.12. r_0 decreases with increasing a_2/a_1. The change is most drastic at small a_2/a_1 when the size difference of the two particles in a particle pair is small. Note that when we set the average size ratio of particle pairs equal to the polydispersity of the particle batch, *i.e.*, $a_2/a_1 = 1.11$, we have $r_0 \approx 2.2$, consistent with our average

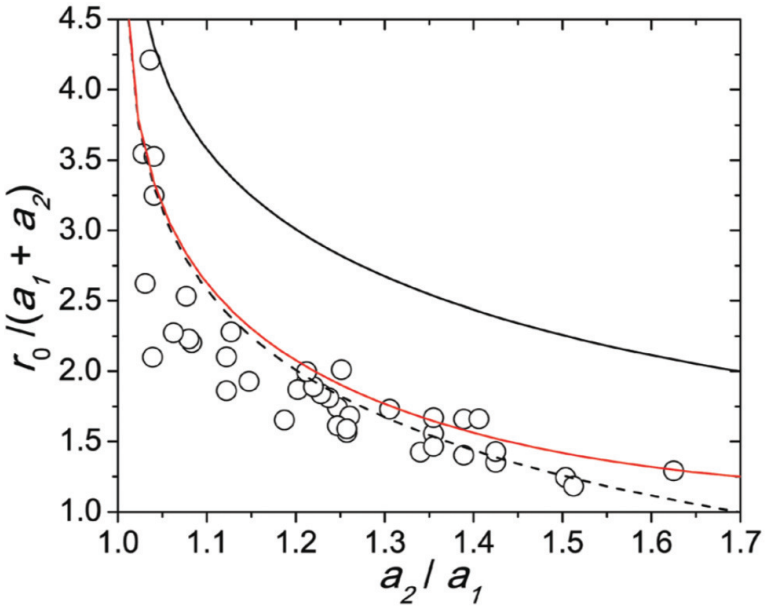

Figure 5.12: Average center-to-center distance, r_0, between two particles in particle pairs of different size ratios, a_2/a_1. r_0 is normalized by the mean diameter of particle pairs, $a_1 + a_2$. The black solid line is the normalized r_0 from the model. The dashed line shows the normalized r_0 - $(a_1 + a_2)$ from the model. The red solid line shows the normalized r_0 from the model when the effective distance $r_e = r_0$ - $(a_1 + a_2)$ is used in Eqn 5.7 and 5.8.

measurements shown in Fig. 5.10b.

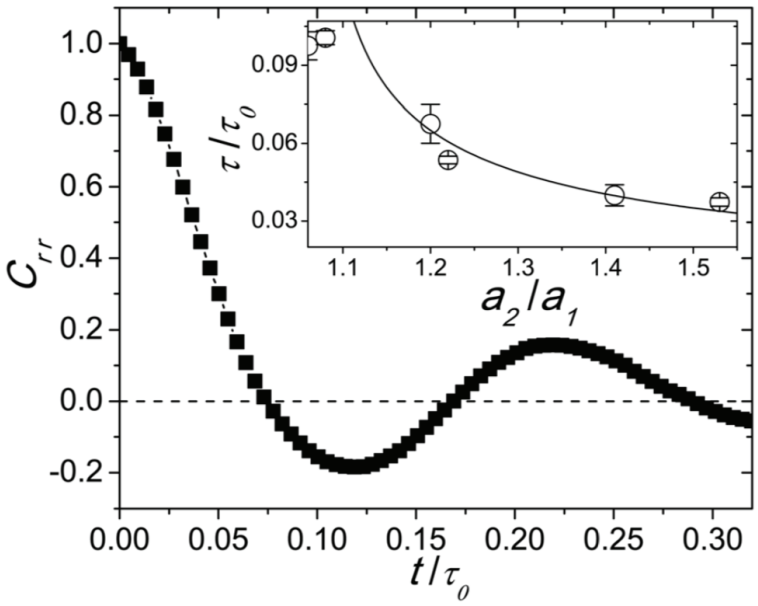

Figure 5.13: Autocorrelation of the center-to-center distance, $r(t)$, of a particle pair. The flow rate is 3.0 µL·min^{-1}. The size ratio of the two particles is $a_2/a_1 = 1.2$. Inset shows the correlation time, τ, as a function of a_2/a_1. τ is normalized by the Brownian relaxation time of particles, τ_0. The solid line is a fit from the model.

We also calculated the autocorrelation of the particle-pair dynamics (Fig. 5.13),

$$C_{rr}(t) = \frac{\langle (r(t+t_0) - \langle r \rangle)(r(t_0) - \langle r \rangle) \rangle}{\langle r^2 \rangle - \langle r \rangle^2}, \tag{5.4}$$

The average $\langle \cdots \rangle$ is taken over all the initial time t_0. $\langle r \rangle \approx r_0$. The vibration of the two particles in a particle pair around r_0 leads to the oscillation of C_{rr} at large t. The correlation time of the particle-pair dynamics, τ, can be defined by fitting C_{rr} at small t with an exponential function, exp(-t/τ). τ indicates the rigidity of the harmonic potential in Eqn 5.2 and 5.3. A smaller τ corresponds to a narrower and stiffer potential well. We find that τ is also a function of a_2/a_1 (Fig. 5.13 inset). A larger a_2/a_1 gives rise to a smaller τ and, therefore, a stiffer potential.

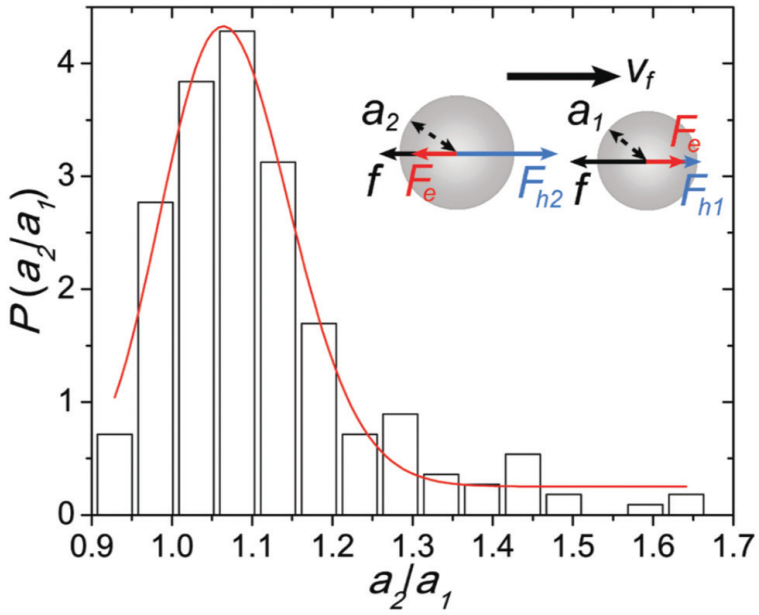

Figure 5.14: Probability distribution of the size ratio between the trailing and leading particles, $P(a_2/a_1)$. The red line is a fit using a log-normal function with the peak value at $a_2/a_1 = 1.064$. Inset shows the force diagram on a particle pair. The flow direction is indicated by v_f.

The dependence of r_0 and τ on a_2/a_1 indicates that particle polydispersity plays an important role in the formation of stable particle pairs. Indeed, we measured the size ratio between the leading particle and the trailing particle, a_2/a_1, over 220 particle pairs. Fig. 5.14 shows the probability distribution function of a_2/a_1. The distribution is clearly biased toward $a_2/a_1 > 1$ with the maximal probability occurring at $a_2/a_1 = 1.064$. In other words, the leading particle is smaller than the trailing particle in a particle pair.

5.3.3 A Minimalistic Model

Based on our experimental observations, we constructed a simple minimalistic model, which provides a semi-quantitative description of the dynamics of particle pairs. Our experiments have shown that hydrodynamic coupling and electrostatic interaction between particles are the key factors influencing the formation of stable colloidal pairs and strings. To induce the hydrodynamic coupling, the glass bottom provides the resistance force that slows down the motion of particles relative to the ambient flow.

A full theoretical description of the motion of solid spheres close to a solid boundary in a semi-infinite fluid medium cannot be achieved within the limit of low-Re Stokes hydrodynamics [197, 198]. To fully address the problem, complex factors including the roughness of particles' surface, the permeability and the stiffness of the layer of grafted PHSA polymer brushes, and even the cavitation of fluids underneath particles need to be considered, which is certainly beyond the scope of our current work [197, 199, 200, 201]. Instead, we try to build a simple model, aiming for an order-of-magnitude estimate of our observations. Surprisingly, the minimalistic model shows a semi-quantitative agreement with our experiments.

In our model, we reduce the complex effects of the bottom boundary on the motion of particles into one essential effect, *i.e.*, it provides a resistance force, f, slowing down the

motion of particles. The effect enables the hydrodynamic coupling between particles, crucial for the formation of colloidal strings. We further assume that f arises from the friction, instead of lubrication, between particles and the glass bottom and, therefore, is independent of the velocity of particles. Note that the density of particles matches that of the solvent. Hence, the normal force that results in the friction should arise from the electrostatic attraction between particles and the wall instead of the weight of the particles. Since the average surface charge of particles is approximately the same for different batches of particles, f should also be independent of the size of particles. The assumption is consistent with our experiments. At low flow rates, the drag on particles from the flow is below the threshold of static friction. Particles stick to the glass bottom and do not move (Fig. 5.3a). At higher flow rates, particles slide on the glass bottom. The kinetic friction f follows the Amonton-Coulomb law $f = \mu \mathrm{N}$, where μ is the friction coefficient between PMMA spheres and the glass bottom and N is the normal force induced by the electrostatic attraction between the spheres and the glass bottom. When salt is added into the solvent, the particle-wall interaction becomes repulsive, which removes the normal force. As a result, $f \approx 0$. Particles move passively with the flow (Fig. 5.9b). The hydrodynamic coupling is zero and the string structures cannot be observed.

Under the above approximation, the force balance of the two particles in a particle pair can be easily written (Fig. 5.14 inset). Note that at low Reynolds number, the total force on each particle is zero. Therefore, for the leading particle (particle 1), we have

$$F_{h1} + F_e = f. \tag{5.5}$$

For the trailing particle (particle 2), we have

$$F_{h2} = F_e + f. \tag{5.6}$$

Here, F_{hi} is the hydrodynamic force on particle i and F_e is the electrostatic repulsion between the two particles. $i = 1$ or 2.

For the hydrodynamic forces, we have

$$\frac{F_{h1}}{\eta K_1} = \frac{(v_f - v_{p1}) - [K_2(v_f - v_{p2})/4\pi r]}{1 - (K_1 K_2)/(4\pi r)^2}, \tag{5.7}$$

$$\frac{F_{h2}}{\eta K_2} = \frac{(v_f - v_{p2}) - [K_1(v_f - v_{p1})/4\pi r]}{1 - (K_1 K_2)/(4\pi r)^2}, \tag{5.8}$$

where r is the center-to-center distance between the two particles, v_f is the velocity of the unperturbed ambient flow at the center of particles and v_{pi} is the velocity of particle i [202]. For a stable particle pair, $v_{p1} = v_{p2}$. The two particles move together with the same speed. $K_i = 6\pi a_i$ is the coefficient of Stokes' drag of particle i. When $v_f = v_{pi}$, the hydrodynamic forces disappear. Further- more, as $r \to \infty$, F_{hi} reduces to $F_{hi} = \eta K_i(v_f - v_{pi})$, *i.e.*, the Stokes law of isolated particles. The two particles decouple in this limit.

For the electrostatic repulsion, the DLVO theory gives

$$F_e = \frac{Z_1 Z_2 e^2}{\epsilon_r \epsilon_0} \cdot \frac{\exp(\kappa a_1)}{1 + \kappa a_1} \cdot \frac{\exp(\kappa a_2)}{1 + \kappa a_2} \cdot \frac{(1 + \kappa r)}{r^2} \cdot \exp(-\kappa r), \tag{5.9}$$

where Z_i and a_i are the number of charges and the radius of particle i, e is the elementary charge, ϵ_r is the relative dielectric constant of the solvent, ϵ_0 is the vacuum permittivity and κ^{-1} is the screening length of the solvent. Since $Z_1 Z_2 > 0$, F_e is always repulsive.

The force balance (Eqn 5.5 and 5.6) leads to a simple relation,

$$F_{h2} - F_{h1} = 2F_e. \tag{5.10}$$

Eqn 5.10 gives a zero internal force between the particles, $(F_{h2} - F_{h1} - 2F_e)/2 = 0$. For

two particles of the same size, $F_{h1} = F_{h2}$. In this case, Eqn 5.10 can be satisfied only by $F_e = 0$ when the distance between the two particles is significantly larger than the screening length κ^{-1}. With the two particles traveling at the same speed, the particle pair thus formed is metastable, susceptible to random perturbations. For stable particle pairs with nonzero F_e, polydispersity is necessary. Since $F_e > 0$ and $F_{h1} < F_{h2}$, the leading particle should be smaller than the trailing particle in a particle pair, consistent with our observation (Fig. 5.13). Eqn 5.10 determines the equilibrium position r_0 of particle pairs.

The prediction of r_0 from Eqn 5.10 is compared with experimental results in Fig. 5.12. Since the leading particles are always small particles from the particle batch with average diameter $d = 1.36$ µm, we fix $\langle a_1 \rangle = d/2 = 0.68$ mm in our calculation. In addition, we use $\langle Z_{1,2} \rangle = 157$ and the average velocity difference between particles and the ambient flow at $\langle v_f - v_p \rangle = 65$ µm·s^{-1}, both of which are measured directly from experiments. The model qualitatively predicts the decreasing trend of r_0 with increasing a_2/a_1 (the black solid line in Fig. 5.12). The quantitative discrepancy may arise from the crude approximation we have made on the effects of the wall and also from the fact that the hydrodynamic forces in Eqn 5.7 and 5.8 are accurate only when the distances between particles are large $r0 \gg (a_1 + a_2)$ [202]. Interestingly, when we plot the surface-to-surface distance, $r_0 - (a_1 + a_2)$, from the model, it quantitatively agrees with our experiments on r_0 (the black dashed line in Fig. 5.12). The result indicates that the particle distance used in Eqn 5.7 and 5.8 may be replaced by an effective distance r_e when r_0 is comparable with $(a_1 + a_2)$. Considering the increasing contribution of the lubrication stress in the gap between particles and the hydrodynamic coupling, r_e should be smaller than the center-to-center distance r_0 and close to the surface-to-surface distance between particles. Indeed, when we replace r_0 with $r_e = r_0 - (a_1 + a_2)$ in Eqn 5.7 and 5.8, the result shows a quantitative agreement with our measurements

(the red line in Fig. 5.12).

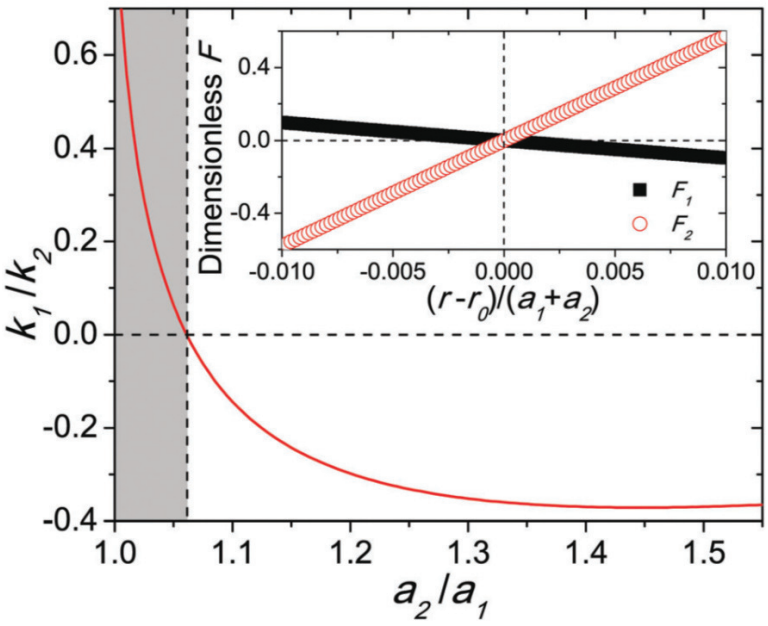

Figure 5.15: Effective spring-like forces on particle pairs from the model. The main plot shows the ratio of the effective spring constants, k_1/k_2, on two particles in particle pairs of different size ratios, a_2/a_1. The gray region indicates unstable particle pairs with $a_2/a_1 < 1.062$, where $k_1/k_2 > 0$. Inset shows the forces on the two particles in a particle pair with $a_2/a_1 = 1.11$ when the distance between the two particles r is slightly away from their equilibrium position r_0. The forces are normalized by $k_BT/(a_1 + a_2)$.

In addition to the equilibrium position r_0, the model also predicts that the approximately harmonic potential near r_0 is narrower and stiffer at larger a_2/a_1, leading to the decrease of the correlation time τ with a_2/a_1, consistent with our observation (Fig. 5.13 inset). Quantitatively, the force on the particle i in a particle pair can be approximated as a spring-like force $F_i = k_i(r - r_0)$ when the distance between the two particles is slightly different from r_0, $|r - r_0|/r_0 \ll 1$ (Fig. 5.15 inset), where k_i is the effective spring constant. F_i is balanced by the Langevin-type random force from thermal fluctuations. The two effective springs on the particles in a particle pair are in series. Thus,

the average spring constant of the effective force between the two particles can be simply estimated as $k = |k_1 k_2|/(|k_1| + |k_2|)$. When we set the average particle ratio at $a_2/a_1 = 1.11$, the polydispersity of the particle batch used in Fig. 5.10, the resulting spring-like force quantitatively matches our experiments (the black line in Fig. 5.10c). The correlation time can also be estimated as $\tau \sim 1/\sqrt{k}$. A fitting using this model prediction again agrees well with our experiments at large a_2/a_1 (Fig. 5.13 inset). The predicted τ, however, shows a sharper increase at small a_2/a_1. This discrepancy can be related to the limit of the stability of particle pairs at small a_2/a_1.

To have a stable particle pair, the sign of k_1 and k_2 must be opposite, so that the forces acting on the particles are attractive when $r > r_0$ and repulsive when $r < r_0$ (Fig. 5.15 inset). Based on the criterion, a particle pair becomes unstable or metastable when the size ratio of the two particles is smaller than 1.062 (Fig. 5.15). The potential well becomes infinitely soft and τ diverges at this lower bound of a_2/a_1. Due to the approximation taken in the model, the lower bound fails to explain the existence of particle pairs of small a_2/a_1 observed in our experiments, which may be metastable in nature. As a result, the predicted τ shows a sharper increase at small a_2/a_1 compared with experiments. Interestingly, the estimate lower bound quantitatively matches the size ratio of the most populous particle pairs found in our experiments at $a_2/a_1 = 1.064$ (Fig. 5.14).

Our simple minimalistic model is able to capture semi- quantitatively all the essential features of experimental observations. Although the slowdown of particle motions near the boundary is induced by the electrostatic attractions in our experiments, the model shows that any other attractive interactions such as those induced by commensurate polymer brushes attached to particles and walls can also lead to a similar mechanism for the assembly of colloidal strings [203]. The non-equilibrium self-assembly principle explored here should apply in much broader contexts.

5.3.4 Kinetics and Formation of Colloidal Strings

The size difference between the leading and trailing particles also explains the kinetics of formation of particle pairs. For an isolated particle, the particle velocity is given by $v_p = v_f - f/(6\pi\eta a)$ from the Stokes law, where f is the friction that is independent of the radius of the particle a. The larger size of the trailing particle results in a faster particle speed, which allows the large particle catch the small particle from behind and forms a stable particle pair (Fig. 5.16a).

Particle pairs serve as the nuclei for the formation of longer colloidal strings at higher particle concentrations. Due to the hydrodynamic coupling, the speed of particles in colloidal strings decreases with the length of strings (Fig. 5.17). For example, for a pair of equal-sized particles, the speed of particles is given by $v_p = v_f - cf/(6\pi\eta a)$, with $c = 1 + 3a/(2r) > 1$ (Eqn 5.7 and 5.8), which is smaller than the speed of isolated particles. As a result, a third isolated particle can approach a particle pair from behind and form a colloidal string of three particles (Fig. 5.16b). The same mechanism also applies for strings of four particles (Fig. 5.16c). As the process repeats, a long colloidal string eventually forms. The dynamic assembly of long colloidal strings can be seen as the nucleation and growth processes of 1D colloidal crystals in a flow-driven nonequilibrium system.

5.3.5 Construction of Colloidal Walls

The hydrodynamic coupling that is responsible for the formation of 1D colloidal strings can also lead to the assembly of 2D colloidal walls in fluid flows when a transverse electric field is applied. To apply a transverse AC field across the channel along the z direction, we construct a small microfluidic channel with an inner cross-section of 100 $\times$ 15 μm^2 ($W \times H$), where the top and bottom walls of the channel are made of ITO coated glasses. The small height of the channel was chosen here, so that we can apply a

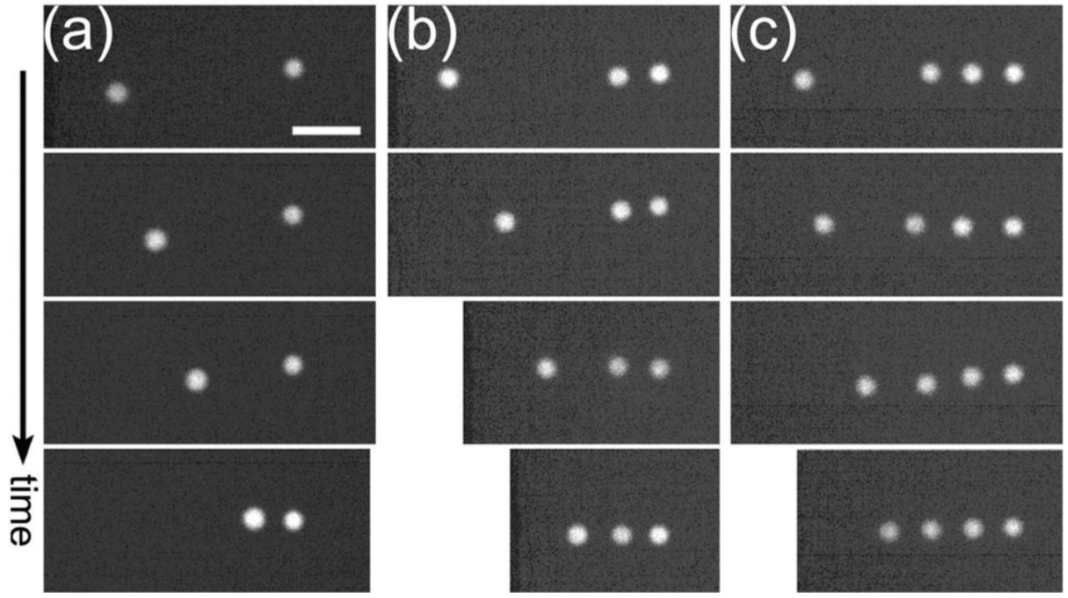

Figure 5.16: Nucleation and growth of 1D colloidal crystals. Fluid flows toward the right. (a) The time series showing the formation of a particle pair. The times of the frames are 0 s, 0.53 s, 0.9 s and 1.91 s, respectively. (b) The time series showing the formation of a colloidal string of three particles. The times of the frames are 0 s, 1.85 s, 2.89 s and 5.42 s, respectively. (c) The time series showing the formation of a colloidal string of four particles. The times of the frames are 0 s, 0.78 s, 1.58 s and 2.46 s, respectively. The flow rate is 3.0 µL·min^{-1} in the wide microfluidic channel. The scale bar is 7 µm.

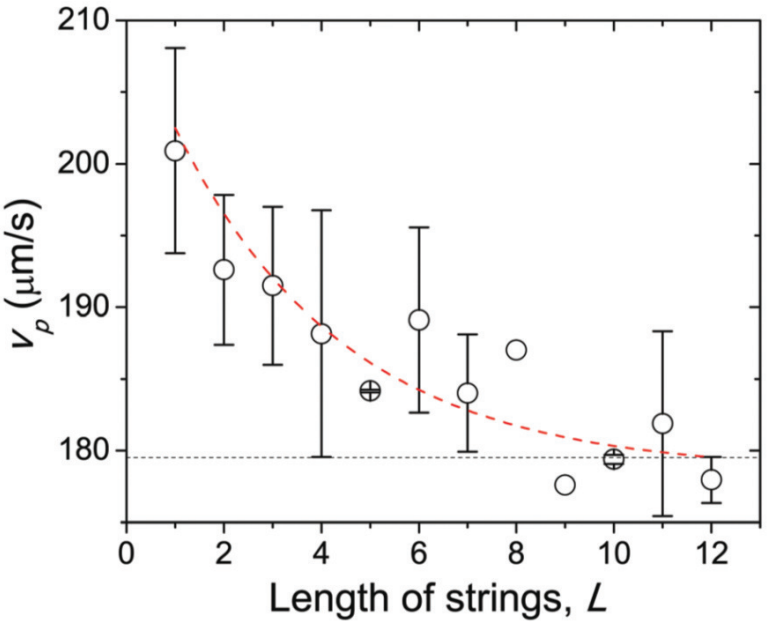

Figure 5.17: The speed of particles in strings of different lengths, L, in terms of the number of particles. Flow rate is 3.0 μL·min^{-1}. Particle speeds are measured at a fixed y location in the narrow channel. The horizontal dashed line indicates the average speed of particles in strings with $L \geq 16$. The red line is a fit of an exponential function as a visual guide.

field with a large enough voltage gradient across the channel. We fixed the peak-to-peak amplitude of the field at 20 V (voltage gradient at 1333.33 V·mm^{-1}) and the frequency at 50 kHz.

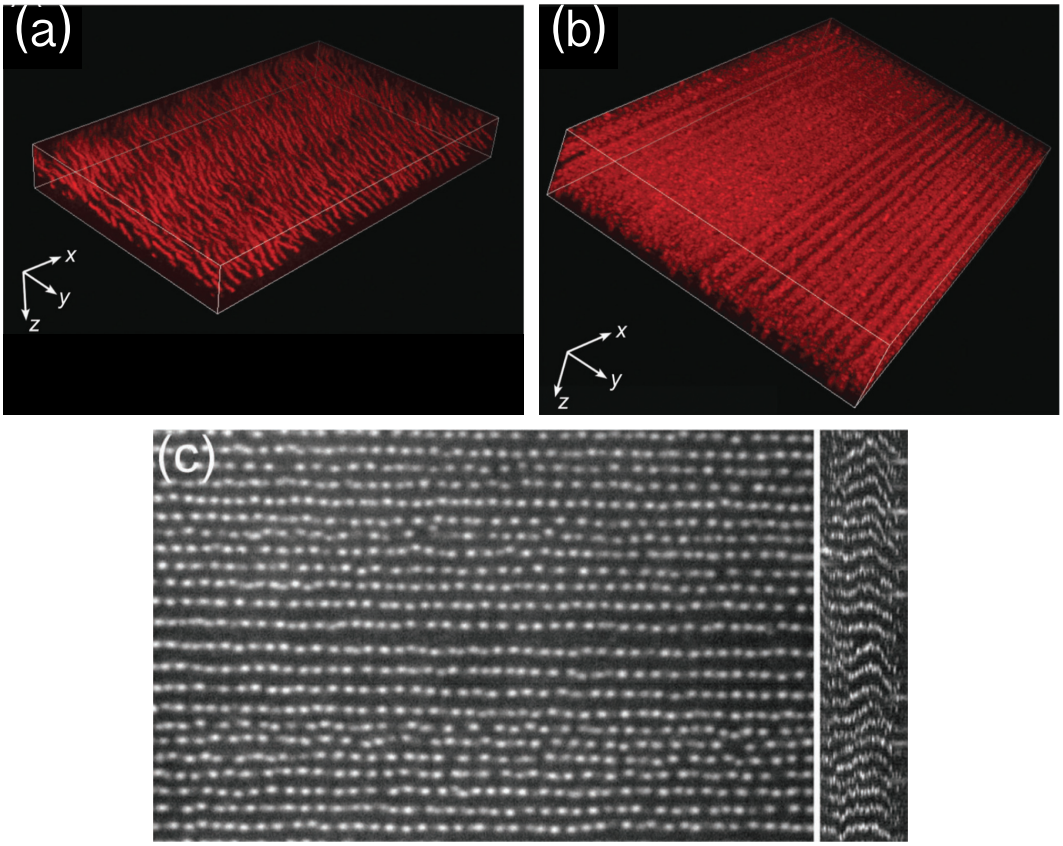

Figure 5.18: Formation of 2D colloidal walls in a transverse AC electric field. (a) A 3D view of colloidal chains formed in the AC field. The field of view is 120 × 75 × 14 µm^3 ($x \times y \times z$).The AC field is along the z direction. (b)A 3D view of colloidal walls formed in the AC field under a fluid flow. The field of view is 120 × 75 × 16 µm^3 ($x \times y \times z$).The AC field is along the z direction and the flow is along the x direction. The walls move at 132 µm·s^{-1} along the flow direction. (c) An orthogonal view of the colloidal walls near the center of the channel in the $x - y$ plane (left panel) and in the $z - y$ plane (right panel). The field of view of the left panel is 120 × 75 µm^2 and that of the right panel is 15 × 75 µm^2. The left and right edges of the right panel correspond to the bottom and top walls of the microfluidic channel made of ITO glasses.

Due to the field-induced dipolar interactions between particles, PMMA spheres suspended in CXB align into chains along the direction of the applied field (Fig. 5.18a) [189, 204, 205]. Note that we use pure CXB, instead of the CXB/decalin mixture, as our solvent in these experiments to enlarge the mismatch of dielectric constants between particles and the solvent, which increases the induced particle polarization. The formation of colloidal chains along the field direction results in the well-studied electrorheological effect [204, 205]. Without external fluid flows, the positions of the chains are completely random in the $x - y$ plane (Fig. 5.18a). To induce the hydrodynamic coupling between different chains, a fluid flow is created along the x direction by a syringe pump. Remarkably, under flow, the originally randomly-positioned chains align along with the flow direction and form 2D colloidal walls across the entire width of the channel in the y direction (Fig. 5.18b and c). The colloidal walls move along with the flow but with significantly slower speeds. The spacing between the walls is controlled by the particle concentration.

5.4 Discussion and Conclusion

5.4.1 Experimental Errors on Velocity Measurements

Experimentally, we determined the position of the center of a particle by adjusting the focal plane of the microscopic objectives until the diameter of the particle under study appears to be maximal and the particle is in clear focus in the image. The z position of the microscopic objectives can be controlled with a very high accuracy of 0.025 µm by using a objectives piezo. Thus, the error in z mainly arises from the determination of the size of particles, d. To accurately determine the size of a colloidal particle is notoriously difficult. We determined the diameter of the particle from the position where the light-intensity profile of the particle first reaches the background intensity (Fig 5.19). The

diameter of the particle thus measured is close to the four standard deviations of the Gaussian fit of the intensity profile of the particle. In other words, the radius of the particle is about two standard deviations away from the center of the particle. The diameter of particles has an error about 1.5 pixels from our measurements, which leads to an absolute error of Δd = $\pm$ 0.049 µm and a relative error of $\Delta d/d \approx 3.5\%$, consistent with the literature values. Alternatively, if the diameter of the particle is determined from the standard deviation of the Gaussian fit, the fitting error gives a similar relative error of $\Delta d/d \approx 3\%$. The uncertainty on particle sizes indeed gives rise to a relatively large error in the velocity of ambient flows due to the existence of high shear rates close to the boundary. Assuming the mean diameter of particles at 1.36 µm, the channel cross-section at 100 $\times$ 100 µm^2 and the flow rate at $Q = 3$ µL/min-the typical parameters of our experiments-the variation of particle diameter $\Delta d = \pm$ 0.049 µm leads to a relative error in ambient flow velocities of $\Delta v_f/v_f \sim 7$ % near the center of the channel next to the glass bottom. The difference between velocities at different z will be smaller when the particle is close to the side wall at $y = \pm$ 50 µm. This relatively large error of $\Delta v_f/v_f$ contributes, in a large part, to the scattering of data in Fig. 5.7. Nevertheless, this error is still significantly smaller than the range of velocity differences between particles and the ambient flow, $(v_f - v_p)/v_f$, we measured in our experiments. As such, the uncertainty should not qualitatively change our conclusions, *i.e.*, the existence of finite velocity differences between particles and the ambient flow.

5.4.2 Experimental Errors on Particle Size Measurements

Although the error on the size of one single particle is large, the relative error on the size ratio of two particles is small. To determine the size ratio a_2/a_1, we fit the intensity profiles of the two particles with two independent Gaussian distributions. Assuming the size of particles in the focal plane is proportional to the standard deviation of

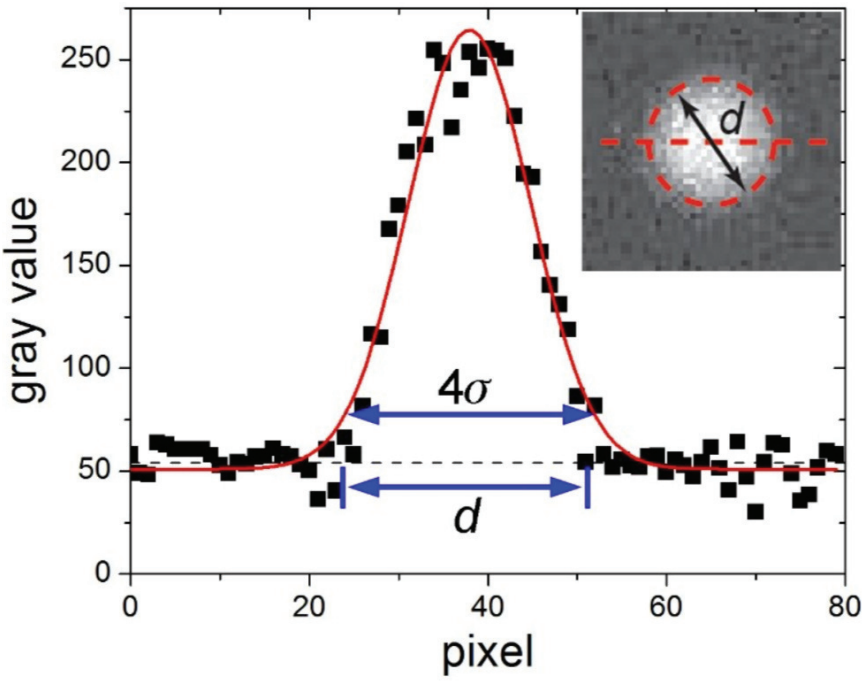

Figure 5.19: The light-intensity profile of a particle from confocal microscopy. The intensity is measured through the center of the particle along the horizontal dashed line (see inset). The center of the particle is obtained via a widely-used particle tracking algorithm, where a 2D Gaussian fit of the particle image is used to achieve a subpixel resolution. The horizontal black dashed line indicates the background intensity measured far away from the particle. The diameter of the particle, d, is then measured from the positions where the particle intensity first reaches the background intensity as indicated in the plot. The solid red line is a Gaussian fit of the profile. σ is the standard deviation of the Gaussian fit. 4σ is indicated in the plot.

the Gaussian distributions, we have $r_1 = c \cdot \sigma_1$ and $r_2 = c \cdot \sigma_2$, where c is an unknown constant, σ_1 and σ_2 are the standard deviations of the two Gaussian fits. Since the focal plane is chosen to be through the largest circle of the small particle, $a_1 = r_1 = c \cdot \sigma_1$. The radius of the large particle, Particle 2, can then be calculated through a simple geometry (Fig. 5.3), giving $a_2 = (r_2^2 + a_1^2)/(2a_1) = c(\sigma_1^2 + \sigma_2^2)/(2\sigma_1)$. Hence, the ratio $a_2/a_1 = (\sigma_1^2 + \sigma_2^2)/(2\sigma_1^2)$. The error of a_2/a_1 is then given by

$$\Delta(a_2/a_1) = \sqrt{\frac{\sigma_2^4}{\sigma_1^6}(\Delta\sigma_1)^2 + \frac{\sigma_2^2}{\sigma_1^4}(\Delta\sigma_2)^2}, \tag{5.11}$$

where $\Delta\sigma_1$ and $\Delta\sigma_2$ are the fitting errors of the Gaussian distributions. Since the measurements on the size of the two particles are independent, we should have $\sigma_1 \approx \sigma_2$ and $\Delta\sigma_1 \approx \Delta\sigma_2$. Thus, we have $\Delta(a_2/a_1) = \sqrt{2}(\Delta\sigma_1/\sigma_1)$. From a typical fitting result (see Fig. 5.19), we estimate $\Delta(a_2/a_1) \approx 4.1\%$.

5.4.3 Conclusion

We have conducted an experimental study on the dynamic self- assembly of charged colloidal particles in microfluidic flows. We showed that due to the balance of hydrodynamic coupling and electrostatic repulsion, colloidal particles can self-assemble into 1D colloidal strings close to the boundary of microfluidic channels. The strings are stable against strong perturbations in the system. Such a 1D ordered structure can be further extended into 2D colloidal walls when a transverse electric field is imposed. We systematically investigated both the dynamics and the kinetics of formation of 1D colloidal strings and constructed a simple minimalistic model that provides a semi-quantitative explanation of the self-assembly process. Our experiments demonstrate a new way for ordering micron-sized objects in low-Re flows, potentially useful for various diagnostic microfluidic devices. One possible strategy to exploit this unique non-equilibrium

self-assembly process is to construct microfluidic channels of narrow heights, which increase the surface-to-volume ratio of the channels and facilitate the boundary-induced self-assembly of colloidal strings.

A future experiment is planned to investigate the kinetics of the formation of 2D colloidal walls. Moreover, the complex effects of the boundary on the hydrodynamic coupling and electrostatic interaction need to be further studied, which will provide a better quantitative description of the dynamic self-assembly process.

Chapter 6

Summary and Outlook

6.1 Summary

In sum, particle dynamics of colloidal suspensions at a single-particle resolution under different confinements have been studied. The studies of colloidal glass transition have been conducted under 3D and 2D confinements. 1D particle self-assembly in a simple flow has also been observed and studied.

Our experiments under 3D and 2D confinements may help to resolve controversies over static correlations in the glass transition. First, we confirm the numerical and theoretical predictions on the 1/3 scaling in 3D and 1/2 scaling in 2D of the pinning length [23, 144, 145] and illustrate a divergent static length scale in the colloidal glass transition when $\phi \to \phi_c$. Moreover, we show that glass-forming liquids with randomly pinned particles show quantitatively similar dynamics as colloidal liquids under spherical confinement [24, 122, 144, 138]. Thus, the RFOT can be applied for understanding confined colloidal liquids—an extensively studied subject in colloidal science [46, 74, 125, 126, 127, 128, 129, 130].

We further use the confinement as a tool to probe the Mermin-Wagner long-wavelength

fluctuations and show that the fluctuations have a logarithmic dependence on the system size in 2D when the system approaches to the glass transition. We argue that the bond-orientational correlation function C_Ψ is a better option to quantified the translational dynamics in 2D considering that the more widely used self-intermediate scattering function F_s is altered by the long-wavelength fluctuations. Ellipsoidal and rodlike particles are also used to directly compare the translational and rotational dynamics to show the decoupling between translational and rotational dynamics. We find that the decoupling is not affected by the confinement. What's more, constant values of critical volume fractions are observed regardless of types of particle aspect ratios, measurement methods, fitting functions, and values of structural factors, which is different from other observations [20].

Besides using colloids to study the glass transition, we have also conducted an experimental study on the dynamic 1D self-assembly of charged colloidal particles in microfluidic flows. We show that due to the balance of hydrodynamic coupling and electrostatic repulsion, colloidal particles can self-assemble into 1D colloidal strings close to the boundary of microfluidic channels. Such a 1D ordered structure can be further extended into 2D colloidal walls when a transverse electric field is imposed. We systematically investigate both the dynamics and the kinetics of formation of 1D colloidal strings and construct a simple minimalistic model that provides a semi-quantitative explanation of the self-assembly process. Our experiments demonstrate a new way for ordering micron-sized objects in low-Re flows, potentially useful for various diagnostic microfluidic devices.

In addition to providing experimental results for assessing general glass-transition theories and particle self-assembly, our studies also provide new insights into the particle dynamics of confined colloidal liquids and may shed light on the behavior of atomic/molecular liquids under nano-confinements [124].

6.2 Outlook

6.2.1 Beyond Hard-Sphere Suspensions

In this thesis, we mainly use spherical colloidal particles as hard spheres to study particle dynamics, which indeed provides us plenty of useful insights. However, the differences between colloidal glasses and atomic glasses can not be ignored as we discussed Chapter 1.2.2. One of the most important differences is that hard spheres do not have the same complex shapes and directional interactions as their counterparts–real atoms or molecules. Thus, one exciting direction is to go beyond hard spheres and study particle dynamics of asymmetric particles and systems with more complex particle-particle interactions.

In Chapter 4, we have shown novel phenomena in ellipsoidal particles, which can not be observed in hard-sphere systems such as the decoupling between translational and rotational dynamics. Colloidal ellipsoids, rods, and dumbbells are widely used as the first meaningful attempts to explore non-hard-sphere interactions, as they are relative simpler than other asymmetric particles [20, 21, 69, 152, 155, 164, 206, 207, 208, 209]. However, most of experimental studies focus on 2D systems due to the difficulties to prepare asymmetric particles in a large quantity and much more complicated particle tracking algorithms in 3D. Asymmetric particles have been prepared by different methods, such as particle-stretching, microfluidic channel, electric-field, asymmetric coating, wet-chemistry, self-assembly, and lithography [75, 79, 154, 189, 208, 210, 211, 212, 213, 214, 215]. Unfortunately, these methods usually have either low yields or large polydispersity of particles. Thus preparation of colloidal particles with controllable shapes and sizes in large scales is urgently needed. What's more, even though some attempts have been made for asymmetric particle tracking, more robust and fast algorithms are to be developed to study particle dynamics at a single-particle resolution [45, 216].

Particle dynamics with different particle-particle interactions have also been studied [164, 176, 177, 217, 218]. One interesting direction is to prepare particles with directional bonds similar to covalent bonds. Wang *et al*. prepared patchy particles and functionalize the patchy points with DNA with single-stranded sticky ends [219]. The special patchy particles can form highly directional bonds and self-assemble into "colloidal molecules" such as "ethylene" structures and "copolymer" structures. Synthesis of colloidal particles with a variety of well-controlled directional interactions opens a wide spectrum of new structures for the study of particle dynamics and self-assembly.

More detailed information about particle synthesis and fluorescent labelling of particles explored during my Ph.D. study are presented in Appendix A and B.

6.2.2 Active Particles

So far, we are only dealing with passive Brownian particles. The world of colloids is much larger than just the passive particles. Different from passive particles driven by random thermal fluctuations, active particles (also known as self-propelled Brownian particles, micro-/nano-swimmers or micro-/nano-motors) can be either chemically self-propelled or propelled by external fields [220, 221]. For active particles in 2D, the stochastic equations of motions are:

$$\begin{cases} \dot{x} = \sqrt{2D_T}\xi_x + v\cos\phi, \\ \dot{y} = \sqrt{2D_T}\xi_y + v\sin\phi, \\ \dot{\phi} = \sqrt{2D_R}\xi_\phi + \omega, \end{cases} \tag{6.1}$$

where x and y are the particle positions and ϕ is the orientation. ξ_x, ξ_y, and ξ_ϕ are the random noises from the brownian motion. v and ω are the non-random velocity and the angular velocity, respectively [220]. Unlike zero average velocity for passive particles, the

average velocity for active particles is not longer equal to zero and the velocities do not obey the Gaussian distribution. The system is no longer thermally equilibrated. Thus, the study of active particles can shed light on non-equilibrated systems where many novel phenomena such as flocking, schooling are observed [220, 221, 222, 223]. Moreover, active particles also provides promising tools for many applications such as the cargo transport, biomedical applications and environmental remediation [220, 221, 222, 223]. To control and design the dynamics of active particles, understanding particle dynamics under different internal or external fields are essential, which provides us a good but challenging opportunity to apply our knowledge accumulated in passive colloidal systems to this rapidly growing field.

6.2.3 Down to Nanoscale Sizes

The sizes of colloidal particles are roughly in the range of 1 nm - 1 µm. Note that the lengths of steric polymeric hairs of colloids (such as PHSA on the surface of PMMA particles) are typical around 10 nm and the Debye lengths are from several nanometers to a few micrometers [69, 133, 137]. Down to nanoscale, colloidal particle can no longer be treated as hard spheres and sophisticated particle-particle interactions must be considered. What's more, particle dynamics could be much more vigorous. For a spherical Brownian particle, the translational diffusion coefficient $D_T = k_B T/6\pi\eta a$ and the rotational diffusion coefficient $D_R = k_B T/8\pi\eta a^3$. When the particle size decreases to 1/10, D_T increases 10 times and D_R increases 1,000 times. For an active particle, controllable dynamics are also become much more difficult. The competition between the random walks from Brownian motions and the designed directional diffusion is fierce [220]. All of these challenges request detailed studies of particle dynamics at nanoscale.

With the help of powerful video microscopy we can study particle dynamics of colloidal particles with sizes near the upper end ($\sim$ 1 µm). With particle sizes down to

nanoscale, due to the limitation of spacial resolutions, many colloidal particle dynamics cannot be directly studied by optical microscopy. While electron microscopy (such as SEM, TEM) has a much high spacial resolution, the temporal resolution can up to several seconds and it requires vacuum environments. Recently, there arises another imaging technique called liquid-phase TEM (LP-TEM), which can nicely make up this gap [224, 225, 226, 227, 228, 229]. LP-TEM has both a spacial resolution close to the traditional TEM (sub-nanometer) and a high temporal resolution (up to 400 FPS) [229]. Instead of putting dried samples in a vacuum chamber like traditional TEM, special sealed liquid cells are designed to contain liquid samples during experiments. Due to these advantages, LP-TEM has been used recently to study particle dynamics at nanoscale, such as nucleation and crystal growth, self-assembly, electrochemical systems, macromolecular complexes, *et al*. [224, 226, 228, 230, 231, 232].

In sum, it is promising but challenging to study colloidal science, especially particle dynamics, beyond hard spheres. Several directions are proposed here: complex shapes and interactions, active particles, and nanoscale sizes. From the fundamental side of view, these studies can further enrich our knowledge of colloidal science. From the more applied side of view, such studies and their derivative knowledge can be used to guide the design of smart materials and products in both industries and our daily lives.

Bibliography

[1] Bo Zhang and Xiang Cheng. Structures and dynamics of glass-forming colloidal liquids under spherical confinement. *Physical review letters*, 116(9):098302, 2016.

[2] Yu Abe, Bo Zhang, Leonardo Gordillo, Alireza Mohammad Karim, Lorraine F Francis, and Xiang Cheng. Dynamic self-assembly of charged colloidal strings and walls in simple fluid flows. *Soft Matter*, 13(8):1681–1692, 2017.

[3] Pablo G Debenedetti and Frank H Stillinger. Supercooled liquids and the glass transition. *Nature*, 410(6825):259–267, 2001.

[4] Pablo G Debenedetti, Thomas M Truskett, Catherine P Lewis, and Frank H Stillinger. Theory of supercooled liquids and glasses: Energy landscape and statistical geometry perspectives. *Advances in Chemical Engineering*, 2001.

[5] Keith J Kasunic. *Optomechanical systems engineering*. John Wiley & Sons, 2015.

[6] Charles Bray. *Dictionary of glass: materials and techniques*. University of Pennsylvania Press, 2001.

[7] Christopher J Ellison and John M Torkelson. The distribution of glass-transition temperatures in nanoscopically confined glass formers. *Nature materials*, 2(10):695, 2003.

[8] Jan Schroers. Bulk metallic glasses. *Physics today*, 66(2):32, 2013.

[9] Li Zhong, Jiangwei Wang, Hongwei Sheng, Ze Zhang, and Scott X Mao. Formation of monatomic metallic glasses through ultrafast liquid quenching. *Nature*, 512(7513):177–180, 2014.

[10] Eric Le Bourhis. *Glass: mechanics and technology*. John Wiley & Sons, 2014.

[11] Ml D Ediger, CA Angell, and Sidney R Nagel. Supercooled liquids and glasses. *The journal of physical chemistry*, 100(31):13200–13212, 1996.

[12] Andrea Cavagna. Supercooled liquids for pedestrians. *Physics Reports*, 476(4):51–124, 2009.

[13] Salvatore Torquato. Glass transition: hard knock for thermodynamics. *Nature*, 405(6786):521–523, 2000.

[14] Giulio Biroli and Juan P Garrahan. Perspective: The glass transition. *The Journal of chemical physics*, 138(12):12A301, 2013.

[15] David Turnbull. Under what conditions can a glass be formed? *Contemporary physics*, 10(5):473–488, 1969.

[16] Charles Austen Angell. Structural instability and relaxation in liquid and glassy phases near the fragile liquid limit. *Journal of non-crystalline solids*, 102(1-3):205–221, 1988.

[17] Gerold Adam and Julian H Gibbs. On the temperature dependence of cooperative relaxation properties in glass-forming liquids. *The journal of chemical physics*, 43(1):139–146, 1965.

[18] Mi D Ediger. Spatially heterogeneous dynamics in supercooled liquids. *Annual review of physical chemistry*, 51(1):99–128, 2000.

[19] Marcus T Cicerone, Qin Zhong, and Madhusudan Tyagi. Picosecond dynamic heterogeneity, hopping, and johari-goldstein relaxation in glass-forming liquids. *Physical review letters*, 113(11):117801, 2014.

[20] Zhongyu Zheng, Ran Ni, Feng Wang, Marjolein Dijkstra, Yuren Wang, and Yilong Han. Structural signatures of dynamic heterogeneities in monolayers of colloidal ellipsoids. *Nature communications*, 5, 2014.

[21] Chandan K Mishra and Rajesh Ganapathy. Shape of dynamical heterogeneities and fractional stokes-einstein and stokes-einstein-debye relations in quasi-two-dimensional suspensions of colloidal ellipsoids. *Physical review letters*, 114(19):198302, 2015.

[22] GBJP Biroli, J-P Bouchaud, Andrea Cavagna, Tomás S Grigera, and Paolo Verrocchio. Thermodynamic signature of growing amorphous order in glass-forming liquids. *Nature Physics*, 4(10):771–775, 2008.

[23] Chiara Cammarota and Giulio Biroli. Ideal glass transitions by random pinning. *Proceedings of the National Academy of Sciences*, 109(23):8850–8855, 2012.

[24] Chiara Cammarota, Giacomo Gradenigo, and Giulio Biroli. Confinement as a tool to probe amorphous order. *Physical review letters*, 111(10):107801, 2013.

[25] Giulio Biroli. Disordered solids: in search of the perfect glass. *Nature Physics*, 10(8):555–556, 2014.

[26] TR Kirkpatrick, D Thirumalai, and Peter G Wolynes. Scaling concepts for the dynamics of viscous liquids near an ideal glassy state. *Physical Review A*, 40(2):1045, 1989.

[27] Glen M Hocky, Thomas E Markland, and David R Reichman. Growing point-to-set length scale correlates with growing relaxation times in model supercooled liquids. *Physical review letters*, 108(22):225506, 2012.

[28] P-J_ Flory. Statistical thermodynamics of semi-flexible chain molecules. *Proc. R. Soc. Lond. A*, 234(1196):60–73, 1956.

[29] David J Thouless, Philip W Anderson, and Robert G Palmer. Solution of'solvable model of a spin glass'. *Philosophical Magazine*, 35(3):593–601, 1977.

[30] D Lancaster. D. lancaster and g. parisi, j. phys. a 30, 5911 (1997). *J. Phys. A*, 30:5911, 1997.

[31] Juan P Garrahan and David Chandler. Geometrical explanation and scaling of dynamical heterogeneities in glass forming systems. *Physical review letters*, 89(3):035704, 2002.

[32] Stephen Whitelam, Ludovic Berthier, and Juan P Garrahan. Dynamic criticality in glass-forming liquids. *Physical review letters*, 92(18):185705, 2004.

[33] Tsuneo Okubo. *Colloidal organization*. Elsevier, 2015.

[34] Peter N Pusey and W Van Megen. Phase behaviour of concentrated suspensions of nearly hard colloidal spheres. *Nature*, 320(6060):340–342, 1986.

[35] Qian Chen, Sung Chul Bae, and Steve Granick. Directed self-assembly of a colloidal kagome lattice. *Nature*, 469(7330):381, 2011.

[36] Peter J Yunker, Tim Still, Matthew A Lohr, and AG Yodh. Suppression of the coffee-ring effect by shape-dependent capillary interactions. *Nature*, 476(7360):308, 2011.

[37] Norman J Wagner and John F Brady. Shear thickening in colloidal dispersions. *Physics Today*, 62(10):27–32, 2009.

[38] Mengmeng Cui, Todd Emrick, and Thomas P Russell. Stabilizing liquid drops in nonequilibrium shapes by the interfacial jamming of nanoparticles. *Science*, 342(6157):460–463, 2013.

[39] Jörn Dunkel, Sebastian Heidenreich, Knut Drescher, Henricus H Wensink, Markus Bär, and Raymond E Goldstein. Fluid dynamics of bacterial turbulence. *Physical review letters*, 110(22):228102, 2013.

[40] Henk NW Lekkerkerker and Remco Tuinier. *Colloids and the depletion interaction*, volume 833. Springer, 2011.

[41] Eric R Weeks, John C Crocker, Andrew C Levitt, Andrew Schofield, and David A Weitz. Three-dimensional direct imaging of structural relaxation near the colloidal glass transition. *Science*, 287(5453):627–631, 2000.

[42] Yi Peng, Feng Wang, Ziren Wang, Ahmed M Alsayed, Zexin Zhang, Arjun G Yodh, and Yilong Han. Two-step nucleation mechanism in solid–solid phase transitions. *Nature materials*, 14(1):101–108, 2015.

[43] Ziren Wang, Feng Wang, Yi Peng, Zhongyu Zheng, and Yilong Han. Imaging the homogeneous nucleation during the melting of superheated colloidal crystals. *Science*, 338(6103):87–90, 2012.

[44] Eric R Weeks. Introduction to the colloidal glass transition. *ACS Macro Letters*, 2016.

[45] Kazem V Edmond, Mark T Elsesser, Gary L Hunter, David J Pine, and Eric R Weeks. Decoupling of rotational and translational diffusion in supercooled colloidal fluids. *Proceedings of the National Academy of Sciences*, 109(44):17891–17896, 2012.

[46] Kazem V Edmond, Carolyn R Nugent, and Eric R Weeks. Influence of confinement on dynamical heterogeneities in dense colloidal samples. *Physical Review E*, 85(4):041401, 2012.

[47] Gary L Hunter and Eric R Weeks. The physics of the colloidal glass transition. *Reports on Progress in Physics*, 75(6):066501, 2012.

[48] Aleksandar Donev, Frank H Stillinger, and Salvatore Torquato. Configurational entropy of binary hard-disk glasses: Nonexistence of an ideal glass transition. *The Journal of chemical physics*, 127(12):124509, 2007.

[49] Eugene Michael Terentjev and David A Weitz. *The Oxford handbook of soft condensed matter*. Oxford Handbooks, 2015.

[50] Srikanth Sastry. The relationship between fragility, configurational entropy and the potential energy landscape of glass-forming liquids. *Nature*, 409(6817):164–167, 2001.

[51] L-M Martinez and CA Angell. A thermodynamic connection to the fragility of glass-forming liquids. *Nature*, 410(6829):663, 2001.

[52] William G Hoover and Francis H Ree. Use of computer experiments to locate the melting transition and calculate the entropy in the solid phase. *The Journal of Chemical Physics*, 47(12):4873–4878, 1967.

[53] Francesco Sciortino. Potential energy landscape description of supercooled liquids and glasses. *Journal of Statistical Mechanics: Theory and Experiment*, 2005(05):P05015, 2005.

[54] William Sutherland. A dynamical theory of diffusion for non-electrolytes and the molecular mass of albumin. *The London, Edinburgh, and Dublin Philosophical Magazine and Journal of Science*, 9(54):781–785, 1905.

[55] Albert Einstein. Einstein, a., 1905, ann. phys.(leipzig) 31, 132. *Ann. Phys.(Leipzig)*, 31:132, 1905.

[56] Yogesh M Joshi. Dynamics of colloidal glasses and gels. *Annual review of chemical and biomolecular engineering*, 5:181–202, 2014.

[57] PN Segre, SP Meeker, PN Pusey, and WCK Poon. Viscosity and structural relaxation in suspensions of hard-sphere colloids. *Physical review letters*, 75(5):958, 1995.

[58] Xiang Cheng, Jonathan H McCoy, Jacob N Israelachvili, and Itai Cohen. Imaging the microscopic structure of shear thinning and thickening colloidal suspensions. *Science*, 333(6047):1276–1279, 2011.

[59] Jacob N Israelachvili. *Intermolecular and surface forces*. Academic press, 2011.

[60] Sébastien Wiederseiner, Nicolas Andreini, Gaël Epely-Chauvin, and Christophe Ancey. Refractive-index and density matching in concentrated particle suspensions: a review. *Experiments in fluids*, 50(5):1183–1206, 2011.

[61] P Anne Hiltner and Irvin M Krieger. Diffraction of light by ordered suspensions. *The Journal of Physical Chemistry*, 73(7):2386–2389, 1969.

[62] PA Hiltner, YS Papir, and IM Krieger. Diffraction of light by nonaqueous ordered suspensions. *The Journal of Physical Chemistry*, 75(12):1881–1886, 1971.

[63] Akira Kose, Masataka Ozaki, Kaoru Takano, Yoko Kobayashi, and Sei Hachisu. Direct observation of ordered latex suspension by metallurgical microscope. *Journal of Colloid and Interface Science*, 44(2):330–338, 1973.

[64] W Van Megen and PN Pusey. Dynamic light-scattering study of the glass transition in a colloidal suspension. *Physical review A*, 43(10):5429, 1991.

[65] W Van Megen and SM Underwood. Dynamic-light-scattering study of glasses of hard colloidal spheres. *Physical Review E*, 47(1):248, 1993.

[66] Rut Besseling, Lucio Isa, Eric R Weeks, and Wilson CK Poon. Quantitative imaging of colloidal flows. *Advances in colloid and interface science*, 146(1):1–17, 2009.

[67] E Di Cola, A Moussaïd, M Sztucki, T Narayanan, and E Zaccarelli. Correlation between structure and rheology of a model colloidal glass. *The Journal of chemical physics*, 131(14):144903, 2009.

[68] Christian Aponte-Rivera and Roseanna N Zia. Simulation of hydrodynamically interacting particles confined by a spherical cavity. *Physical Review Fluids*, 1(2):023301, 2016.

[69] Zhongyu Zheng, Feng Wang, Yilong Han, et al. Glass transitions in quasi-two-dimensional suspensions of colloidal ellipsoids. *Physical review letters*, 107(6):065702, 2011.

[70] William TM Irvine, Vincenzo Vitelli, and Paul M Chaikin. Pleats in crystals on curved surfaces. *Nature*, 468(7326):947–951, 2010.

[71] Mirjam E Leunissen, Christina G Christova, Antti-Pekka Hynninen, C Patrick Royall, Andrew I Campbell, Arnout Imhof, Marjolein Dijkstra, Rene Van Roij, and Alfons Van Blaaderen. Ionic colloidal crystals of oppositely charged particles. *Nature*, 437(7056):235, 2005.

[72] Walter Kob and Hans C Andersen. Testing mode-coupling theory for a supercooled binary lennard-jones mixture i: The van hove correlation function. *Physical Review E*, 51(5):4626, 1995.

[73] Walter Kob and Hans C Andersen. Testing mode-coupling theory for a supercooled binary lennard-jones mixture. ii. intermediate scattering function and dynamic susceptibility. *Physical Review E*, 52(4):4134, 1995.

[74] Carolyn R Nugent, Kazem V Edmond, Hetal N Patel, and Eric R Weeks. Colloidal glass transition observed in confinement. *Physical review letters*, 99(2):025702, 2007.

[75] Shan Jiang, Qian Chen, Mukta Tripathy, Erik Luijten, Kenneth S Schweizer, and Steve Granick. Janus particle synthesis and assembly. *Advanced materials*, 22(10):1060–1071, 2010.

[76] Qian Chen, Jonathan K Whitmer, Shan Jiang, Sung Chul Bae, Erik Luijten, and Steve Granick. Supracolloidal reaction kinetics of janus spheres. *Science*, 331(6014):199–202, 2011.

[77] SC Glotzer, MJ Solomon, and Nicholas A Kotov. Self-assembly: From nanoscale to microscale colloids. *AIChE Journal*, 50(12):2978–2985, 2004.

[78] Yoon S Lee. *Self-assembly and nanotechnology: a force balance approach*. John Wiley & Sons, 2008.

[79] Zhihong Nie, Wei Li, Minseok Seo, Shengqing Xu, and Eugenia Kumacheva. Janus and ternary particles generated by microfluidic synthesis: design, synthesis, and self-assembly. *Journal of the American Chemical Society*, 128(29):9408–9412, 2006.

[80] Rahul Raveendran Nair, Peter Blake, Alexander N Grigorenko, Konstantin S Novoselov, Tim J Booth, Tobias Stauber, Nuno MR Peres, and Andre K Geim. Fine structure constant defines visual transparency of graphene. *Science*, 320(5881):1308–1308, 2008.

[81] Sasha Stankovich, Dmitriy A Dikin, Geoffrey HB Dommett, Kevin M Kohlhaas, Eric J Zimney, Eric A Stach, Richard D Piner, SonBinh T Nguyen, and Rodney S Ruoff. Graphene-based composite materials. *nature*, 442(7100):282, 2006.

[82] Gunter Schmid et al. *Nanoparticles*. Wiley VCH, 2005.

[83] Daniel L Fedlheim and Colby A Foss. *Metal nanoparticles: synthesis, characterization, and applications*. CRC press, 2001.

[84] Yugang Sun and Younan Xia. Shape-controlled synthesis of gold and silver nanoparticles. *Science*, 298(5601):2176–2179, 2002.

[85] Huan Pang, Bo Zhang, Jimin Du, Jing Chen, Jiangshan Zhang, and Sujuan Li. Porous nickel oxide nanospindles with huge specific capacitance and long-life cycle. *RSC Advances*, 2(6):2257–2261, 2012.

[86] Chengzhen Wei, Huan Pang, Bo Zhang, Qingyi Lu, Shuang Liang, and Feng Gao. Two-dimensional β-mno 2 nanowire network with enhanced electrochemical capacitance. *Scientific reports*, 3:2193, 2013.

[87] RE Peierls. Peierls, re, 1935, ann. inst. henri poincaré 5, 177. *Ann. Inst. Henri Poincaré*, 5:177, 1935.

[88] Lev Davidovich Landau. On the theory of phase transitions. *Ukr. J. Phys.*, 11:19–32, 1937.

[89] LD Landau. Zur theorie der phasenumwandlungen ii. *Phys. Z. Sowjetunion*, 11(545):26–35, 1937.

[90] N David Mermin and Herbert Wagner. Absence of ferromagnetism or antiferromagnetism in one-or two-dimensional isotropic heisenberg models. *Physical Review Letters*, 17(22):1133, 1966.

[91] N David Mermin. Absence of ordering in certain classical systems. *Journal of Mathematical Physics*, 8(5):1061–1064, 1967.

[92] N David Mermin. Crystalline order in two dimensions. *Physical Review*, 176(1):250, 1968.

[93] Sidney Coleman. There are no goldstone bosons in two dimensions. *Communications in Mathematical Physics*, 31(4):259–264, 1973.

[94] Pierre C Hohenberg. Existence of long-range order in one and two dimensions. *Physical Review*, 158(2):383, 1967.

[95] Jay G Dash. Helium films from two to three dimensions. *Physics Reports*, 38(4):177–226, 1978.

[96] Bernd Illing, Sebastian Fritschi, Herbert Kaiser, Christian L Klix, Georg Maret, and Peter Keim. Mermin–wagner fluctuations in 2d amorphous solids. *Proceedings of the National Academy of Sciences*, 114(8):1856–1861, 2017.

[97] Skanda Vivek, Colm P Kelleher, Paul M Chaikin, and Eric R Weeks. Long-wavelength fluctuations and the glass transition in two dimensions and three dimensions. *Proceedings of the National Academy of Sciences*, 114(8):1850–1855, 2017.

[98] Anthony D Dinsmore, Eric R Weeks, Vikram Prasad, Andrew C Levitt, and David A Weitz. Three-dimensional confocal microscopy of colloids. *Applied optics*, 40(24):4152–4159, 2001.

[99] Lian Bai, John W Fruehwirth, Xiang Cheng, and Christopher W Macosko. Dynamics and rheology of nonpolar bijels. *Soft Matter*, 11(26):5282–5293, 2015.

[100] Lian Bai, Radhika Sharma, Xiang Cheng, and Christopher W Macosko. Kinetic control of graphene localization in co-continuous polymer blends via melt compounding. *Langmuir*, 2017.

[101] Elton N. Kaufmann. *Characterization of Materials.* John Wiley & Sons, Inc, Hoboken, New Jersey, 2012.

[102] Tony Wilson and Colin Sheppard. *Theory and practice of scanning optical microscopy*, volume 180. Academic Press London, 1984.

[103] Robert L Price and W Gray Jay Jerome. *Basic confocal microscopy.* Springer Science & Business Media, 2011.

[104] Vikram Prasad, Denis Semwogerere, and Eric R Weeks. Confocal microscopy of colloids. *Journal of Physics: Condensed Matter*, 19(11):113102, 2007.

[105] Matthew C Jenkins and Stefan U Egelhaaf. Confocal microscopy of colloidal particles: towards reliable, optimum coordinates. *Advances in colloid and interface science*, 136(1-2):65–92, 2008.

[106] Arthur Ashkin. Acceleration and trapping of particles by radiation pressure. *Physical review letters*, 24(4):156, 1970.

[107] Arthur Ashkin and JM Dziedzic. Optical levitation by radiation pressure. *Applied Physics Letters*, 19(8):283–285, 1971.

[108] Arthur Ashkin, James M Dziedzic, JE Bjorkholm, and Steven Chu. Observation of a single-beam gradient force optical trap for dielectric particles. *Optics letters*, 11(5):288–290, 1986.

[109] Arthur Ashkin, James M Dziedzic, and T Yamane. Optical trapping and manipulation of single cells using infrared laser beams. *Nature*, 330(6150):769, 1987.

[110] Arthur Ashkin. History of optical trapping and manipulation of small-neutral particle, atoms, and molecules. *IEEE Journal of Selected Topics in Quantum Electronics*, 6(6):841–856, 2000.

[111] Keir C Neuman and Steven M Block. Optical trapping. *Review of scientific instruments*, 75(9):2787–2809, 2004.

[112] Arthur Ashkin and James M Dziedzic. Optical trapping and manipulation of viruses and bacteria. *Science*, 235(4795):1517–1520, 1987.

[113] Jennifer E Curtis, Brian A Koss, and David G Grier. Dynamic holographic optical tweezers. *Optics communications*, 207(1-6):169–175, 2002.

[114] David G Grier. A revolution in optical manipulation. *nature*, 424(6950):810, 2003.

[115] John C Crocker and Eric R Weeks. Particle tracking using idl. *Retreived from http://www. physics. emory. edu/faculty/weeks//idl*, 2018.

[116] John C Crocker and David G Grier. Methods of digital video microscopy for colloidal studies. *Journal of colloid and interface science*, 179(1):298–310, 1996.

[117] Ludovic Berthier and Giulio Biroli. Theoretical perspective on the glass transition and amorphous materials. *Reviews of Modern Physics*, 83(2):587, 2011.

[118] Peter G Wolynes and Vassiliy Lubchenko. *Structural Glasses and Supercooled Liquids: Theory, Experiment, and Applications*. John Wiley & Sons, 2012.

[119] David Chandler and Juan P Garrahan. Dynamics on the way to forming glass: Bubbles in space-time. *Annual review of physical chemistry*, 61:191–217, 2010.

[120] Gilles Tarjus, Steven A Kivelson, Z Nussinov, and Pascal Viot. The frustration-based approach of supercooled liquids and the glass transition: a review and critical assessment. *Journal of Physics: Condensed Matter*, 17(50):R1143, 2005.

[121] Jean-Philippe Bouchaud and Giulio Biroli. On the adam-gibbs-kirkpatrick-thirumalai-wolynes scenario for the viscosity increase in glasses. *The Journal of chemical physics*, 121(15):7347–7354, 2004.

[122] Ludovic Berthier and Walter Kob. Static point-to-set correlations in glass-forming liquids. *Physical Review E*, 85(1):011102, 2012.

[123] K Hima Nagamanasa, Shreyas Gokhale, AK Sood, and Rajesh Ganapathy. Direct measurements of growing amorphous order and non-monotonic dynamic correlations in a colloidal glass-former. *Nature Physics*, 11(5):403–408, 2015.

[124] R Richert. Dynamics of nanoconfined supercooled liquids. *Annual review of physical chemistry*, 62:65–84, 2011.

[125] Jeetain Mittal, Jeffrey R Errington, and Thomas M Truskett. Thermodynamics predicts how confinement modifies the dynamics of the equilibrium hard-sphere fluid. *Physical review letters*, 96(17):177804, 2006.

[126] Jeetain Mittal, Thomas M Truskett, Jeffrey R Errington, and Gerhard Hummer. Layering and position-dependent diffusive dynamics of confined fluids. *Physical review letters*, 100(14):145901, 2008.

[127] Prasad S Sarangapani and Yingxi Zhu. Impeded structural relaxation of a hard-sphere colloidal suspension under confinement. *Physical Review E*, 77(1):010501, 2008.

[128] Prasad S Sarangapani, Andrew B Schofield, and Yingxi Zhu. Direct experimental evidence of growing dynamic length scales in confined colloidal liquids. *Physical Review E*, 83(3):030502, 2011.

[129] Keiji Watanabe, Takeshi Kawasaki, and Hajime Tanaka. Structural origin of enhanced slow dynamics near a wall in glass-forming systems. *Nature materials*, 10(7):512–520, 2011.

[130] Gary L Hunter, Kazem V Edmond, and Eric R Weeks. Boundary mobility controls glassiness in confined colloidal liquids. *Physical Review Letters*, 112(21):218302, 2014.

[131] L Antl, JW Goodwin, RD Hill, Ronald H Ottewill, SM Owens, S Papworth, and JA Waters. The preparation of poly (methyl methacrylate) latices in non-aqueous media. *Colloids and Surfaces*, 17(1):67–78, 1986.

[132] C Pathmamanoharan, K Groot, and JKG Dhont. Preparation and characterization of crosslinked pmma latex particles stabilized by grafted copolymer. *Colloid and Polymer Science*, 275(9):897–901, 1997.

[133] CP Royall, ME Leunissen, and A Van Blaaderen. A new colloidal model system to study long-range interactions quantitatively in real space. *Journal of Physics: Condensed Matter*, 15(48):S3581, 2003.

[134] Anand Yethiraj and Alfons van Blaaderen. A colloidal model system with an interaction tunable from hard sphere to soft and dipolar. *Nature*, 421(6922):513–517, 2003.

[135] Mirjam E Leunissen, Alfons Van Blaaderen, Andrew D Hollingsworth, Matthew T Sullivan, and Paul M Chaikin. Electrostatics at the oil–water interface, stability, and order in emulsions and colloids. *Proceedings of the National Academy of Sciences*, 104(8):2585–2590, 2007.

[136] Marjolein N van der Linden, Johan CP Stiefelhagen, Gülşen Heessels-Gürboğa, Jessi ES van der Hoeven, Nina A Elbers, Marjolein Dijkstra, and Alfons van Blaaderen. Charging of poly (methyl methacrylate)(pmma) colloids in cyclohexyl bromide: Locking, size dependence, and particle mixtures. *Langmuir*, 31(1):65–75, 2014.

[137] Wilson CK Poon, Eric R Weeks, and C Patrick Royall. On measuring colloidal volume fractions. *Soft Matter*, 8(1):21–30, 2012.

[138] Misaki Ozawa, Walter Kob, Atsushi Ikeda, and Kunimasa Miyazaki. Equilibrium phase diagram of a randomly pinned glass-former. *Proceedings of the National Academy of Sciences*, 112(22):6914–6919, 2015.

[139] Walter Kob, Sándalo Roldán-Vargas, and Ludovic Berthier. Non-monotonic temperature evolution of dynamic correlations in glass-forming liquids. *Nature Physics*, 8(2):164, 2012.

[140] J Mattsson, HM Wyss, A Fernandez-Nieves, K Miyazaki, Z Hu, DR Reichman, DA Weitz, JC Conrad, S Manley, V Trappe, et al. Glasses and gels. *Nature*, 462(7269):83, 2009.

[141] François Sausset, Gilles Tarjus, and Pascal Viot. Tuning the fragility of a glass-forming liquid by curving space. *Physical review letters*, 101(15):155701, 2008.

[142] Takeshi Kawasaki and Hajime Tanaka. Structural origin of dynamic heterogeneity in three-dimensional colloidal glass formers and its link to crystal nucleation. *Journal of Physics: Condensed Matter*, 22(23):232102, 2010.

[143] Anshul DS Parmar and Srikanth Sastry. Kinetic and thermodynamic fragilities of square well fluids with tunable barriers to bond breaking. *The Journal of Physical Chemistry B*, 119(34):11243–11252, 2015.

[144] Saurish Chakrabarty, Smarajit Karmakar, and Chandan Dasgupta. Dynamics of glass forming liquids with randomly pinned particles. *Scientific reports*, 5, 2015.

[145] Benoit Charbonneau, Patrick Charbonneau, and Gilles Tarjus. Geometrical frustration and static correlations in a simple glass former. *Physical review letters*, 108(3):035701, 2012.

[146] David R Nelson. *Defects and geometry in condensed matter physics*. Cambridge University Press, 2002.

[147] AR Bausch, MJ Bowick, A Cacciuto, AD Dinsmore, MF Hsu, DR Nelson, MG Nikolaides, A Travesset, and DA Weitz. Grain boundary scars and spherical crystallography. *Science*, 299(5613):1716–1718, 2003.

[148] Silvio Franz. First steps of a nucleation theory in disordered systems. *Journal of Statistical Mechanics: Theory and Experiment*, 2005(04):P04001, 2005.

[149] Klaus Zahn, R Lenke, and Georg Maret. Two-stage melting of paramagnetic colloidal crystals in two dimensions. *Physical review letters*, 82(13):2721, 1999.

[150] Elijah Flenner and Grzegorz Szamel. Fundamental differences between glassy dynamics in two and three dimensions. *Nature communications*, 6, 2015.

[151] Matthias Schmidt and Hartmut Löwen. Phase diagram of hard spheres confined between two parallel plates. *Physical Review E*, 55(6):7228, 1997.

[152] Peter J Yunker, Ke Chen, Zexin Zhang, Wouter G Ellenbroek, Andrea J Liu, and Arjun G Yodh. Rotational and translational phonon modes in glasses composed of ellipsoidal particles. *Physical Review E*, 83(1):011403, 2011.

[153] RC Kramb, R Zhang, KS Schweizer, and CF Zukoski. Glass formation and shear elasticity in dense suspensions of repulsive anisotropic particles. *Physical review letters*, 105(5):055702, 2010.

[154] Julie A Champion, Yogesh K Katare, and Samir Mitragotri. Making polymeric micro-and nanoparticles of complex shapes. *Proceedings of the National Academy of Sciences*, 104(29):11901–11904, 2007.

[155] Chandan K Mishra, K Hima Nagamanasa, Rajesh Ganapathy, AK Sood, and Shreyas Gokhale. Dynamical facilitation governs glassy dynamics in suspensions of colloidal ellipsoids. *Proceedings of the National Academy of Sciences*, 111(43):15362–15367, 2014.

[156] Ian Williams, Erdal C Oguz, Thomas Speck, Paul Bartlett, Hartmut Löwen, and C Patrick Royall. Transmission of torque at the nanoscale. *Nature Physics*, 12(1):98–103, 2016.

[157] Giovanni Brambilla, Djamel El Masri, Matteo Pierno, Ludovic Berthier, Luca Cipelletti, George Petekidis, and Andrew B Schofield. Probing the equilibrium dynamics of colloidal hard spheres above the mode-coupling glass transition. *Physical review letters*, 102(8):085703, 2009.

[158] Ali Mohraz and Michael J Solomon. Direct visualization of colloidal rod assembly by confocal microscopy. *Langmuir*, 21(12):5298–5306, 2005.

[159] Deshpremy Mukhija and Michael J Solomon. Translational and rotational dynamics of colloidal rods by direct visualization with confocal microscopy. *Journal of colloid and interface science*, 314(1):98–106, 2007.

[160] Skanda Vivek and Eric R Weeks. Decoupling of translational and rotational diffusion in quasi-2d colloidal fluids. *The Journal of Chemical Physics*, 147(13):134502, 2017.

[161] Marco G Mazza, Nicolas Giovambattista, H Eugene Stanley, and Francis W Starr. Connection of translational and rotational dynamical heterogeneities with the breakdown of the stokes-einstein and stokes-einstein-debye relations in water. *Physical Review E*, 76(3):031203, 2007.

[162] Jeongmin Kim and Bong June Sung. Tracer shape and local media structure determine the trend of translation-rotation decoupling in two-dimensional colloids. *Physical review letters*, 115(15):158302, 2015.

[163] Stephen M Anthony, Minsu Kim, and Steve Granick. Translation-rotation decoupling of colloidal clusters of various symmetries. *The Journal of chemical physics*, 129(24):244701, 2008.

[164] Chandan K Mishra, Amritha Rangarajan, and Rajesh Ganapathy. Two-step glass transition induced by attractive interactions in quasi-two-dimensional suspensions of ellipsoidal particles. *Physical review letters*, 110(18):188301, 2013.

[165] Wen-Sheng Xu, Xiaozheng Duan, Zhao-Yan Sun, and Li-Jia An. Glass formation in a mixture of hard disks and hard ellipses. *The Journal of Chemical Physics*, 142(22):224506, 2015.

[166] Wen-Sheng Xu, Zhao-Yan Sun, and Li-Jia An. Relaxation dynamics in a binary hard-ellipse liquid. *Soft matter*, 11(3):627–634, 2015.

[167] Jeppe C Dyre. Colloquium: The glass transition and elastic models of glass-forming liquids. *Reviews of modern physics*, 78(3):953, 2006.

[168] Hailin Cong, Bing Yu, Jianguo Tang, Zejing Li, and Xuesong Liu. Current status and future developments in preparation and application of colloidal crystals. *Chemical Society Reviews*, 42(19):7774–7800, 2013.

[169] Noel A Clark, Alan J Hurd, and Bruce J Ackerson. Single colloidal crystals. *Nature*, 281(5726):57, 1979.

[170] Djamal Zerrouki, Jean Baudry, David Pine, Paul Chaikin, and Jérôme Bibette. Chiral colloidal clusters. *Nature*, 455(7211):380, 2008.

[171] Jan Vermant and MJ Solomon. Flow-induced structure in colloidal suspensions. *Journal of Physics: Condensed Matter*, 17(4):R187, 2005.

[172] MD Haw, WCK Poon, and PN Pusey. Direct observation of oscillatory-shear-induced order in colloidal suspensions. *Physical Review E*, 57(6):6859, 1998.

[173] Itai Cohen, Thomas G Mason, and David A Weitz. Shear-induced configurations of confined colloidal suspensions. *Physical review letters*, 93(4):046001, 2004.

[174] Yu Ling Wu, Didi Derks, Alfons van Blaaderen, and Arnout Imhof. Melting and crystallization of colloidal hard-sphere suspensions under shear. *Proceedings of the National Academy of Sciences*, 106(26):10564–10569, 2009.

[175] TH Besseling, M Hermes, A Fortini, M Dijkstra, A Imhof, and A Van Blaaderen. Oscillatory shear-induced 3d crystalline order in colloidal hard-sphere fluids. *Soft Matter*, 8(26):6931–6939, 2012.

[176] Alberto Montesi, Alejandro A Peña, and Matteo Pasquali. Vorticity alignment and negative normal stresses in sheared attractive emulsions. *Physical review letters*, 92(5):058303, 2004.

[177] Chinedum O Osuji and David A Weitz. Highly anisotropic vorticity aligned structures in a shear thickening attractive colloidal system. *Soft Matter*, 4(7):1388–1392, 2008.

[178] Wonhee Lee, Hamed Amini, Howard A Stone, and Dino Di Carlo. Dynamic self-assembly and control of microfluidic particle crystals. *Proceedings of the National Academy of Sciences*, 107(52):22413–22418, 2010.

[179] Xiang Cheng, Xinliang Xu, Stuart A Rice, Aaron R Dinner, and Itai Cohen. Assembly of vorticity-aligned hard-sphere colloidal strings in a simple shear flow. *Proceedings of the National Academy of Sciences*, 109(1):63–67, 2012.

[180] Rossana Pasquino, Daniele Panariello, and Nino Grizzuti. Migration and alignment of spherical particles in sheared viscoelastic suspensions. a quantitative determination of the flow-induced self-assembly kinetics. *Journal of colloid and interface science*, 394:49–54, 2013.

[181] Neil YC Lin, Xiang Cheng, and Itai Cohen. Biaxial shear of confined colloidal hard spheres: the structure and rheology of the vorticity-aligned string phase. *Soft Matter*, 10(12):1969–1976, 2014.

[182] Dongeun Huh, Wei Gu, Yoko Kamotani, James B Grotberg, and Shuichi Takayama. Microfluidics for flow cytometric analysis of cells and particles. *Physiological measurement*, 26(3):R73, 2005.

[183] Ryan Tewhey, Jason B Warner, Masakazu Nakano, Brian Libby, Martina Medkova, Patricia H David, Steve K Kotsopoulos, Michael L Samuels, J Brian Hutchison, Jonathan W Larson, et al. Microdroplet-based pcr enrichment for large-scale targeted sequencing. *Nature biotechnology*, 27(11):1025, 2009.

[184] Bishnubrata Patra, Chien-Chung Peng, Wei-Hao Liao, Chau-Hwang Lee, and Yi-Chung Tung. Drug testing and flow cytometry analysis on a large number of uniform sized tumor spheroids using a microfluidic device. *Scientific reports*, 6:21061, 2016.

[185] Michael J Fuerstman, Piotr Garstecki, and George M Whitesides. Coding/decoding and reversibility of droplet trains in microfluidic networks. *Science*, 315(5813):828–832, 2007.

[186] Manu Prakash and Neil Gershenfeld. Microfluidic bubble logic. *Science*, 315(5813):832–835, 2007.

[187] Michinao Hashimoto, Ji Feng, Roger L York, Audrey K Ellerbee, Greg Morrison, Samuel W Thomas Iii, L Mahadevan, and George M Whitesides. Infochemistry: encoding information as optical pulses using droplets in a microfluidic device. *Journal of the American Chemical Society*, 131(34):12420–12429, 2009.

[188] Laurent Malaquin, Tobias Kraus, Heinz Schmid, Emmanuel Delamarche, and Heiko Wolf. Controlled particle placement through convective and capillary assembly. *Langmuir*, 23(23):11513–11521, 2007.

[189] Hanumantha Rao Vutukuri, Ahmet Faik Demirörs, Bo Peng, Peter DJ van Oostrum, Arnout Imhof, and Alfons van Blaaderen. Colloidal analogues of charged and uncharged polymer chains with tunable stiffness. *Angewandte Chemie*, 124(45):11411–11415, 2012.

[190] Mingsheng Wang, Le He, and Yadong Yin. Magnetic field guided colloidal assembly. *Materials Today*, 16(4):110–116, 2013.

[191] Tsevi Beatus, Tsvi Tlusty, and Roy Bar-Ziv. Phonons in a one-dimensional microfluidic crystal. *Nature Physics*, 2(11):743, 2006.

[192] Dhananjay Dendukuri and Patrick S Doyle. The synthesis and assembly of polymeric microparticles using microfluidics. *Advanced Materials*, 21(41):4071–4086, 2009.

[193] Bingqing Shen, Joshua Ricouvier, Florent Malloggi, and Patrick Tabeling. Designing colloidal molecules with microfluidics. *Advanced Science*, 3(6), 2016.

[194] F Carrique, FJ Arroyo, and AV Delgado. Electrokinetics of concentrated suspensions of spherical colloidal particles with surface conductance, arbitrary zeta potential, and double-layer thickness in static electric fields. *Journal of colloid and interface science*, 252(1):126–137, 2002.

[195] William Bailey Russel, Dudley Albert Saville, and William Raymond Schowalter. *Colloidal dispersions*. Cambridge university press, 1989.

[196] FM White. *Viscous Fluid Flow*. McGraw-Hill, New York, 1991.

[197] Arthur Joseph Goldman, Raymond G Cox, and Howard Brenner. Slow viscous motion of a sphere parallel to a plane wall—i motion through a quiescent fluid. *Chemical engineering science*, 22(4):637–651, 1967.

[198] AJ Goldman, RG Cox, and H Brenner. Slow viscous motion of a sphere parallel to a plane wall—ii couette flow. *Chemical engineering science*, 22(4):653–660, 1967.

[199] Neil YC Lin, Ben M Guy, Michiel Hermes, Chris Ness, Jin Sun, Wilson CK Poon, and Itai Cohen. Hydrodynamic and contact contributions to continuous shear thickening in colloidal suspensions. *Physical review letters*, 115(22):228304, 2015.

[200] AA Potanin and WB Russel. Hydrodynamic interaction of particles with grafted polymer brushes and applications to rheology of colloidal dispersions. *Physical Review E*, 52(1):730, 1995.

[201] J Ashmore, C Del Pino, and T Mullin. Cavitation in a lubrication flow between a moving sphere and a boundary. *Physical review letters*, 94(12):124501, 2005.

[202] John Happel and Howard Brenner. *Low Reynolds number hydrodynamics: with special applications to particulate media*, volume 1. Springer Science & Business Media, 2012.

[203] Anna C Balazs, Todd Emrick, and Thomas P Russell. Nanoparticle polymer composites: where two small worlds meet. *Science*, 314(5802):1107–1110, 2006.

[204] Alice P Gast and Charles F Zukoski. Electrorheological fluids as colloidal suspensions. *Advances in Colloid and Interface Science*, 30:153–202, 1989.

[205] Mukund Parthasarathy and Daniel J Klingenberg. Electrorheology: mechanisms and models. *Materials Science and Engineering: R: Reports*, 17(2):57–103, 1996.

[206] Bing Liu, Thijs H Besseling, Michiel Hermes, Ahmet F Demirörs, Arnout Imhof, and Alfons Van Blaaderen. Switching plastic crystals of colloidal rods with electric fields. *Nature communications*, 5:3092, 2014.

[207] Anke Kuijk, Dmytro V Byelov, Andrei V Petukhov, Alfons van Blaaderen, and Arnout Imhof. Phase behavior of colloidal silica rods. *Faraday discussions*, 159(1):181–199, 2012.

[208] Anke Kuijk, Arnout Imhof, Margriet HW Verkuijlen, Thijs H Besseling, Ernst RH van Eck, and Alfons van Blaaderen. Colloidal silica rods: Material properties and fluorescent labeling. *Particle & Particle Systems Characterization*, 31(6):706–713, 2014.

[209] Patrick M Johnson, Carlos M van Kats, and Alfons van Blaaderen. Synthesis of colloidal silica dumbbells. *Langmuir*, 21(24):11510–11517, 2005.

[210] CC Ho, A Keller, JA Odell, and RH Ottewill. Preparation of monodisperse ellipsoidal polystyrene particles. *Colloid and Polymer Science*, 271(5):469–479, 1993.

[211] AS Utada, El Lorenceau, DR Link, PD Kaplan, HA Stone, and DA Weitz. Monodisperse double emulsions generated from a microcapillary device. *Science*, 308(5721):537–541, 2005.

[212] Jin-Woong Kim, Ryan J Larsen, and David A Weitz. Synthesis of nonspherical colloidal particles with anisotropic properties. *Journal of the American Chemical Society*, 128(44):14374–14377, 2006.

[213] Jin-Gyu Park, Jason D Forster, and Eric R Dufresne. High-yield synthesis of monodisperse dumbbell-shaped polymer nanoparticles. *Journal of the American Chemical Society*, 132(17):5960–5961, 2010.

[214] Stefano Sacanna, WTM Irvine, Paul M Chaikin, and David J Pine. Lock and key colloids. *Nature*, 464(7288):575, 2010.

[215] Jason P Rolland, Benjamin W Maynor, Larken E Euliss, Ansley E Exner, Ginger M Denison, and Joseph M DeSimone. Direct fabrication and harvesting of monodisperse, shape-specific nanobiomaterials. *Journal of the American Chemical Society*, 127(28):10096–10100, 2005.

[216] TH Besseling, M Hermes, A Kuijk, B De Nijs, TS Deng, M Dijkstra, A Imhof, and A Van Blaaderen. Determination of the positions and orientations of concentrated rod-like colloids from 3d microscopy data. *Journal of Physics: Condensed Matter*, 27(19):194109, 2015.

[217] VERONIQUE Trappe, V Prasad, Luca Cipelletti, PN Segre, and DAVID A Weitz. Jamming phase diagram for attractive particles. *Nature*, 411(6839):772–775, 2001.

[218] Guangnan Meng, Natalie Arkus, Michael P Brenner, and Vinothan N Manoharan. The free-energy landscape of clusters of attractive hard spheres. *Science*, 327(5965):560–563, 2010.

[219] Yufeng Wang, Yu Wang, Dana R Breed, Vinothan N Manoharan, Lang Feng, Andrew D Hollingsworth, Marcus Weck, and David J Pine. Colloids with valence and specific directional bonding. *Nature*, 491(7422):51, 2012.

[220] Clemens Bechinger, Roberto Di Leonardo, Hartmut Löwen, Charles Reichhardt, Giorgio Volpe, and Giovanni Volpe. Active particles in complex and crowded environments. *Reviews of Modern Physics*, 88(4):045006, 2016.

[221] Hong Wang and Martin Pumera. Fabrication of micro/nanoscale motors. *Chemical reviews*, 115(16):8704–8735, 2015.

[222] Samuel Sánchez, Lluís Soler, and Jaideep Katuri. Chemically powered micro-and nanomotors. *Angewandte Chemie International Edition*, 54(5):1414–1444, 2015.

[223] Flory Wong, Krishna Kanti Dey, and Ayusman Sen. Synthetic micro/nanomotors and pumps: fabrication and applications. *Annual Review of Materials Research*, 46:407–432, 2016.

[224] Niels De Jonge and Frances M Ross. Electron microscopy of specimens in liquid. *Nature nanotechnology*, 6(11):695, 2011.

[225] Jong Min Yuk, Jungwon Park, Peter Ercius, Kwanpyo Kim, Daniel J Hellebusch, Michael F Crommie, Jeong Yong Lee, A Zettl, and A Paul Alivisatos. High-resolution em of colloidal nanocrystal growth using graphene liquid cells. *Science*, 336(6077):61–64, 2012.

[226] James J De Yoreo and Nico AJM Sommerdijk. Investigating materials formation with liquid-phase and cryogenic tem. *Nature Reviews Materials*, 1(8):16035, 2016.

[227] Michael H Nielsen and James J De Yoreo. *Liquid phase TEM investigations of crystal nucleation, growth, and transformation*. Springer, 2017.

[228] Binbin Luo, John W Smith, Zihao Ou, and Qian Chen. Quantifying the self-assembly behavior of anisotropic nanoparticles using liquid-phase transmission electron microscopy. *Accounts of chemical research*, 50(5):1125–1133, 2017.

[229] Byung Hyo Kim, Jiwoong Yang, Donghoon Lee, Back Kyu Choi, Taeghwan Hyeon, and Jungwon Park. Liquid-phase transmission electron microscopy for studying colloidal inorganic nanoparticles. *Advanced Materials*, 30(4), 2018.

[230] Hong-Gang Liao, Danylo Zherebetskyy, Huolin Xin, Cory Czarnik, Peter Ercius, Hans Elmlund, Ming Pan, Lin-Wang Wang, and Haimei Zheng. Facet development during platinum nanocube growth. *Science*, 345(6199):916–919, 2014.

[231] Dongsheng Li, Michael H Nielsen, Jonathan RI Lee, Cathrine Frandsen, Jillian F Banfield, and James J De Yoreo. Direction-specific interactions control crystal growth by oriented attachment. *Science*, 336(6084):1014–1018, 2012.

[232] Maria T Proetto, Anthony M Rush, Miao-Ping Chien, Patricia Abellan Baeza, Joseph P Patterson, Matthew P Thompson, Norman H Olson, Curtis E Moore, Arnold L Rheingold, Christopher Andolina, et al. Dynamics of soft nanomaterials captured by transmission electron microscopy in liquid water. *Journal of the American Chemical Society*, 136(4):1162–1165, 2014.

[233] Andrew I Campbell and Paul Bartlett. Fluorescent hard-sphere polymer colloids for confocal microscopy. *Journal of Colloid and Interface Science*, 256(2):325–330, 2002.

[234] Gilles Bosma, Chellapah Pathmamanoharan, Els HA de Hoog, Willem K Kegel, Alfons van Blaaderen, and Henk NW Lekkerkerker. Preparation of monodisperse, fluorescent pmma–latex colloids by dispersion polymerization. *Journal of Colloid and Interface Science*, 245(2):292–300, 2002.

[235] Parag Desai, Clare Dibble, Mike Kogan, and Laura Sherda. Handbook of poly-12 hydroxystearic acid stabilized poly(methyl methacraylate) synthesis, 2005.

[236] RH Pelton and P Chibante. Preparation of aqueous latices with n-isopropylacrylamide. *Colloids and Surfaces*, 20(3):247–256, 1986.

[237] Brian R Saunders and Brian Vincent. Microgel particles as model colloids: theory, properties and applications. *Advances in colloid and interface science*, 80(1):1–25, 1999.

[238] Jianzhong Wu, Bo Zhou, and Zhibing Hu. Phase behavior of thermally responsive microgel colloids. *Physical review letters*, 90(4):048304, 2003.

[239] Ahmed M Alsayed, Mohammad F Islam, Jian Zhang, Peter J Collings, and Arjun G Yodh. Premelting at defects within bulk colloidal crystals. *Science*, 309(5738):1207–1210, 2005.

[240] Yi Peng, Ziren Wang, Ahmed M Alsayed, Arjun G Yodh, and Yilong Han. Melting of colloidal crystal films. *Physical review letters*, 104(20):205703, 2010.

[241] Bo Li, Di Zhou, and Yilong Han. Assembly and phase transitions of colloidal crystals. *Nature Reviews Materials*, 1(2):15011, 2016.

[242] Peter J Yunker, Ke Chen, Matthew D Gratale, Matthew A Lohr, Tim Still, and AG Yodh. Physics in ordered and disordered colloidal matter composed of poly (n-isopropylacrylamide) microgel particles. *Reports on Progress in Physics*, 77(5):056601, 2014.

[243] Roberto FS Freitas and EL Cussler. Temperature sensitive gels as extraction solvents. *Chemical Engineering Science*, 42(1):97–103, 1987.

[244] Todd R Hoare and Daniel S Kohane. Hydrogels in drug delivery: Progress and challenges. *Polymer*, 49(8):1993–2007, 2008.

[245] Justyna Wiedemair, Michael J Serpe, Jongseong Kim, Jean-Francois Masson, L Andrew Lyon, Boris Mizaikoff, and Christine Kranz. In-situ afm studies of the phase-transition behavior of single thermoresponsive hydrogel particles. *Langmuir*, 23(1):130–137, 2007.

[246] Haruma Kawaguchi, Keiji Fujimoto, and Yoshiro Mizuhara. Hydrogel microspheres iii. temperature-dependent adsorption of proteins on poly-n-isopropylacrylamide hydrogel microspheres. *Colloid and Polymer Science*, 270(1):53–57, 1992.

[247] Saet Byul Debord and L Andrew Lyon. Influence of particle volume fraction on packing in responsive hydrogel colloidal crystals. *The Journal of Physical Chemistry B*, 107(13):2927–2932, 2003.

[248] Thomas Hellweg, Karl Kratz, Stephanie Pouget, and Wolfgang Eimer. Internal dynamics in colloidal pnipam microgel particles immobilised in mesoscopic crystals. *Colloids and Surfaces A: Physicochemical and Engineering Aspects*, 202(2-3):223–232, 2002.

[249] Karl Kratz, Thomas Hellweg, and Wolfgang Eimer. Influence of charge density on the swelling of colloidal poly (n-isopropylacrylamide-co-acrylic acid) microgels. *Colloids and Surfaces A: Physicochemical and Engineering Aspects*, 170(2-3):137–149, 2000.

[250] X Wu, RH Pelton, AE Hamielec, DR Woods, and W McPhee. The kinetics of poly (n-isopropylacrylamide) microgel latex formation. *Colloid and polymer science*, 272(4):467–477, 1994.

[251] Brian R Saunders and Brian Vincent. Thermal and osmotic deswelling of poly (nipam) microgel particles. *Journal of the Chemical Society, Faraday Transactions*, 92(18):3385–3389, 1996.

[252] Roberta Acciaro, Tibor Gilanyi, and Imre Varga. Preparation of monodisperse poly (n-isopropylacrylamide) microgel particles with homogenous cross-link density distribution. *Langmuir*, 27(12):7917–7925, 2011.

[253] Tim Still, Ke Chen, Ahmed M Alsayed, Kevin B Aptowicz, and AG Yodh. Synthesis of micrometer-size poly (n-isopropylacrylamide) microgel particles with homogeneous crosslinker density and diameter control. *Journal of colloid and interface science*, 405:96–102, 2013.

[254] D Duracher, A Elaissari, and C Pichot. Characterization of cross-linked poly (n-isopropylmethacrylamide) microgel latexes. *Colloid and Polymer Science*, 277(10):905–913, 1999.

[255] Werner Stöber, Arthur Fink, and Ernst Bohn. Controlled growth of monodisperse silica spheres in the micron size range. *Journal of colloid and interface science*, 26(1):62–69, 1968.

[256] Yanqing An, Miao Chen, Qunji Xue, and Weimin Liu. Preparation and self-assembly of carboxylic acid-functionalized silica. *Journal of Colloid and Interface Science*, 311(2):507–513, 2007.

[257] Jianhui Zhang, Huaiyong Liu, Zhenlin Wang, and Naiben Ming. Au-induced polyvinylpyrrolidone aggregates with bound water for the highly shape-selective synthesis of silica nanostructures. *Chemistry-a European Journal*, 14(14):4374–4380, 2008.

[258] Anke Kuijk, Alfons van Blaaderen, and Arnout Imhof. Synthesis of monodisperse, rodlike silica colloids with tunable aspect ratio. *Journal of the American Chemical Society*, 133(8):2346–2349, 2011.

[259] Nynke AM Verhaegh and Alfons van Blaaderen. Dispersions of rhodamine-labeled silica spheres: synthesis, characterization, and fluorescence confocal scanning laser microscopy. *Langmuir*, 10(5):1427–1438, 1994.

[260] Andrew Burns, Hooisweng Ow, and Ulrich Wiesner. Fluorescent core–shell silica nanoparticles: towards "lab on a particle" architectures for nanobiotechnology. *Chemical Society Reviews*, 35(11):1028–1042, 2006.

[261] Hooisweng Ow, Daniel R Larson, Mamta Srivastava, Barbara A Baird, Watt W Webb, and Ulrich Wiesner. Bright and stable core- shell fluorescent silica nanoparticles. *Nano letters*, 5(1):113–117, 2005.

[262] Seiichi Uchiyama, Yuriko Matsumura, A Prasanna de Silva, and Kaoru Iwai. Fluorescent molecular thermometers based on polymers showing temperature-induced

phase transitions and labeled with polarity-responsive benzofurazans. *Analytical chemistry*, 75(21):5926–5935, 2003.

[263] To Ngai, Sven Holger Behrens, and Helmut Auweter. Novel emulsions stabilized by ph and temperature sensitive microgels. *Chemical communications*, 3:331–333, 2005.

[264] Tao Wu, Gang Zou, Jinming Hu, and Shiyong Liu. Fabrication of photoswitchable and thermotunable multicolor fluorescent hybrid silica nanoparticles coated with dye-labeled poly (n-isopropylacrylamide) brushes. *Chemistry of Materials*, 21(16):3788–3798, 2009.

[265] Gero Maatz, Arkadius Maciollek, and Helmut Ritter. Cyclodextrin-induced host–guest effects of classically prepared poly (nipam) bearing azo-dye end groups. *Beilstein journal of organic chemistry*, 8:1929, 2012.

[266] Alexander M Breul, Martin D Hager, and Ulrich S Schubert. Fluorescent monomers as building blocks for dye labeled polymers: synthesis and application in energy conversion, biolabeling and sensors. *Chemical Society Reviews*, 42(12):5366–5407, 2013.

[267] Linda K Månsson, Jasper N Immink, Adriana M Mihut, Peter Schurtenberger, and Jérôme J Crassous. A new route towards colloidal molecules with externally tunable interaction sites. *Faraday discussions*, 181:49–69, 2015.

[268] Yoshinori Tamai, Hideki Tanaka, and Koichiro Nakanishi. Molecular dynamics study of polymer- water interaction in hydrogels. 1. hydrogen-bond structure. *Macromolecules*, 29(21):6750–6760, 1996.

[269] Martina Keerl, Vytautas Smirnovas, Roland Winter, and Walter Richtering. Interplay between hydrogen bonding and macromolecular architecture leading to

unusual phase behavior in thermosensitive microgels. *Angewandte Chemie International Edition*, 47(2):338–341, 2008.

Appendix A

Particle Synthesis

A.1 PMMA

PSHA stabilized PMMA colloidal spheres are one of the most popular candidates used to study particle dynamics, especially colloidal crystal/glass transition due to their nearly hard-sphere properties when prepared well. The synthesis of PSHA stabilized PMMA colloidal spheres has been throughly studied and well controlled [131, 132, 133, 136, 233, 234].

Here we are going to summarize the synthesis procedures. First, we will list chemicals and equipments used during the synthesis and then document the synthesis procedures. There are three stages for a typical synthesis: (1) purification of raw materials, (2) stabilizer synthesis, and (3) particle synthesis. The first stage is to purify the monomer–methyl methacrylate (MMA) and the catalyst–2,2'-azo-bis-isobutyronitrile (ADIB) to remove inhibitors and other impurities. The second stage is to synthesize comblike PSHA stabilizers (Fig. A.1). Well-made PSHA stabilizers are the key to have non-sticky PMMA spheres as a hard-sphere model. And the last stage is to prepare PMMA particles and lock PSHA onto surfaces of PMMA particles to provide steric stabilizations

(Fig. A.1).

The synthesis procedures are modified based on several published research articles and a handbook prepared by Parag Desai, Clare Dibble, Mike Kogan, and Laura Shereda [131, 132, 133, 136, 233, 234, 235].

A.1.1 Chemicals and Equipment

Chemicals

Methyl methacrylate (MMA), 2,2'-azo-bis-isobutyronitrile (ADIB), 12-hydroxystearic acid (HSA), toluene, methanesulphonic acid, glycidyl methacrylate (GM), 1-octanethiol, 1-dimethylaminododecane, hexane, dodecane, methacrylic acid (MA), *t*-butyl catechol, 2-dimethylethanolamine, ethyl acetate, butyl acetate, acetone, potassium hydroxide.

Equipment

1-MEHQ removal prepacked column, glass bottles with Teflon coated caps, 250 mL 3-neck round-bottom-flask, 500 mL 3-neck round-bottom flask, Dean Stark apparatus, glass extender, reflux condenser, 25 mL graduated cylinder, 100 mL graduated cylinder, 50 mL beakers, 100 mL beakers, 250 mL Erlenmeyer flask, addition funnel, glass funnel, glass stopper, sleeve stoppers, syringe, ring stands and clamps, spatulas, scale, Teflon centrifuge tubes, pipettes and tips, thermometers, thermometer adapter with 24/40 fitting, air tubes, oil bath, Teflon sleeves, green clips, nitrogen cylinder and nitrogen gas, magnetic stirring plate and stir bar.

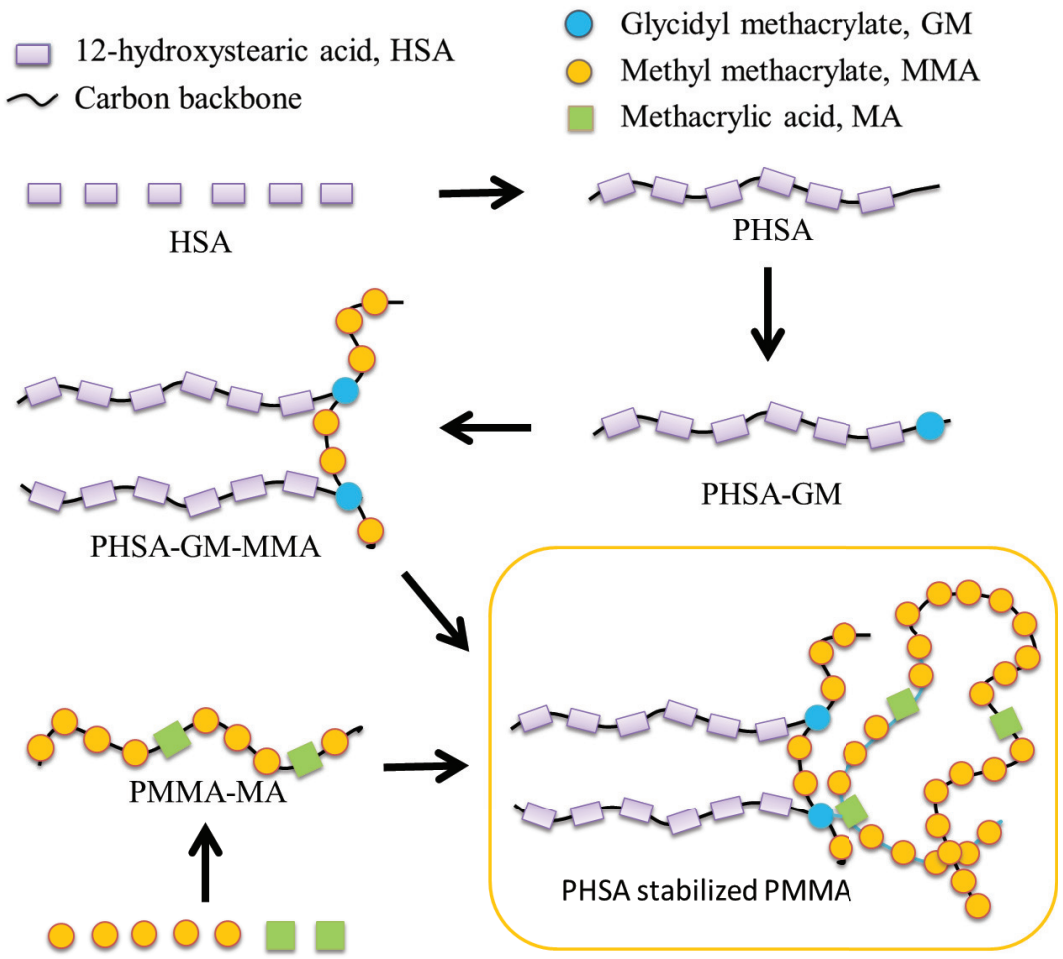

Figure A.1: Illustration of procedures of stabilizer synthesis and particle synthesis. For the stabilizer synthesis stage, HSA first polymerizes into PHSA, which covalently bonds with GM later. Then PHSA-GM copolymerizes with MMA and forms comblike PHSA-GM-MMA stablizers. For the particle synthesis stage, MMA and MA copolymerize and form main bodies of PMMA spheres. MA is added to provide joint points for stabilizer molecules. Lastly, the stabilizer prepared above is added and chemically bonds onto surfaces of PMMA spheres.

A.1.2 Purification of Raw Chemicals

Purification of MMA

1. Setup the filtration system in a chemical hood. From top to bottom there should be a glass funnel, an addition funnel, a prepacked MEHQ removal column and a glass bottle.
2. Add MMA dropwise from the top and collect the filtered MMA with a glass bottle.
3. Store the filtered MMA in a refrigerator for later use.
4. After the filtration, leave the column in the chemical hood for a few days to let the MMA evaporate.

Purification of ADIB

1. In a chemical hood, a desired amount of ADIB is dissolved into acetone in a centrifuge tube.
2. Store the solution in a freezer for as least 24 h.
3. Remove the solvent by centrifugation and dry the precipitated ADIB in a chemical hood.
4. Store the dried ADIB in a refrigerator for later use.

A.1.3 Stabilizer Synthesis

The synthesis of PHSA stabilizers needs three steps: (1) synthesis of PHSA, (2) copolymerization of PHSA-GM, and (3) copolymerization of PHSA-GM-MMA (Fig. A.1). The experimental setup is shown in Fig. A.2.

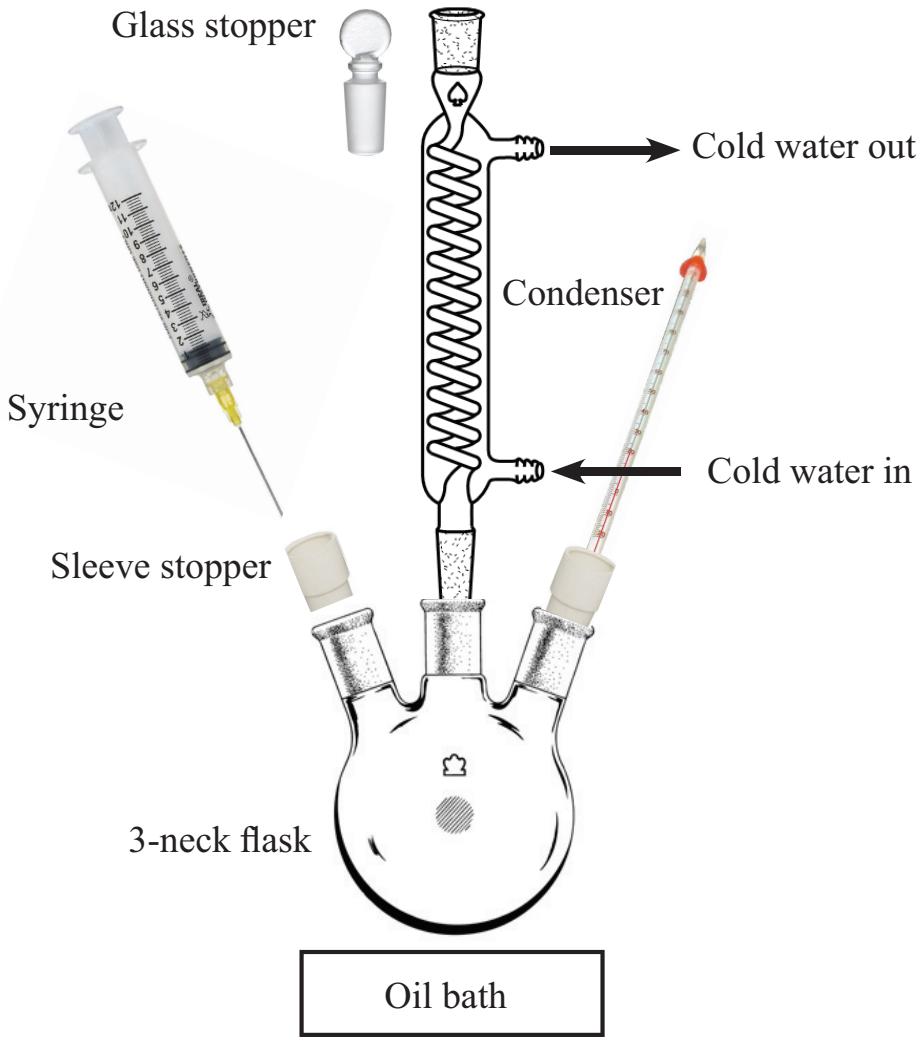

Figure A.2: Experimental setup for Stage two and three of PMMA synthesis. For some steps some modifications are needed such as replacing the condenser or a stopper to a Dean-Stark apparatus or a nitrogen adapter.

Synthesis of PHSA

1. Weigh 151 g of HSA and 27 g of toluene and then pour them into a 500 mL round bottom flask.
2. Place the flask into a oil bath. Add a glass extender in the middle neck of the flask then add a Dean-Stark apparatus onto the glass extender. Use ring stands and clamps to hold glassware tightly.
3. Put a nitrogen adapter into one side neck and a sleeve stopper into the other side neck. Be sure to place Teflon sleeves in all joints to seal the system well.
4. Turn on cooling water and the oil bath. Set the temperature to 100 °C.
5. Once all HSA is melted, add 236 µL of methanesulphonic acid to the flask using a syringe.
6. Open the nitrogen gas flow and replace the air inside of containers.
7. Slowly increase the temperature of the oil bath to 140 °C. Mark the time as the reaction's start point once it is 140 °C.
8. After 20 h of reaction, begin the titration process. Allow the reaction to proceed until the acid value is 35.2 mg KOH/g product or HSA stops polymerizing.
9. Proceed directly to step two once the titration is done.

Synthesis of PHSA-GM

1. Weigh 0.23 g of *t*-butyl catechol and 15 mL of toluene then mixed in a beaker.
2. Weigh 16.3 g of GM, another 15 mL of toluene and 787 µL of 1-dimethylaminododecane then pour them into a Erlenmeyer flask.

3. Mix the previous two mixtures and add them into the 3-neck flask using a clean syringe.

4. Continue refluxing the reaction at 140 °C for another 7 h.

5. Similar titration procedure is conducted after 7 h and then stop heating.

6. Add 100 g of toluene to the flask after the reaction is cooled down. Mix the chemicals and transfer them into a glass bottle with a Teflon coated lid.

Synthesis of PHSA-GM-PMMA

1. Weigh 25.55 g of ethyl acetate and 12.7 g of butyl acetate and then pour them into a 500 mL 3-neck round-bottom flask. Place the flask into the oil bath. Add a condenser in the middle neck and a addition funnel in one side neck of the flask. Turn on the cold water. Close all outlets with glass stoppers. Use ring stands and clamps to hold the glassware.

2. Slowly raise the temperature of the oil bath to 105 - 110 °C.

3. Weigh 0.57 g of ADIB, 33.49 g of filtered MMA, 67.8 g of PHSA-GM from step two, and 3.93 g of GM and then mix them in a Erlenmeyer flask.

4. Pour the mixture into the addition funnel and seal the funnel with a glass stopper.

5. Once the temperature reaches 105 - 110 °C, add the mixture slowly and evenly through the addition funnel for next 3.5 h. Mark the initial time when the addition starts.

6. Replace the addition funnel with a glass stopper and let the mixture reflux for another 6 h. Add 0.26 g of ADIB each at the time of 5.5 h and 7.5 h.

7. Turn off the oil bath and let the reaction cool down to about 80 °C.

8. Add 33.33 g of ethyl acetate and 16.7 g of butyl acetate into the flask and shake gently to mix the chemicals.

9. Transfer the mixture into a glass bottle, label it and then store it in a refrigerator.

A.1.4 Particle Synthesis

Now we can use the previous prepared PSHA stabilizers to synthesis PHSA stabilized PMMA spheres. Two steps are involved: copolymerization of PMMA-MA (step 1-5) and locking the PHSA stabilizers onto surfaces PMMA spheres (step 6-12). PMMA spheres usually have a narrow size distribution of about 5 %. Sizes of particles are controlled by the amount of MMA and MA added. Generally, a larger amount of MMA and MA yields a larger size of particles. The amount of MMA and MA provided below is chosen to prepare PMMA spheres with a target size of 1.8 µm.

1. Weigh 22.0 g of hexane, 11.0 g of dodecane, and 1.75 g of PHSA stabilizer prepared in stage two. Mix them a 250 mL 3-neck flask by shaking until the stabilizer is fully dissolved.

2. Place the flask into a oil bath. Put a condenser in the middle neck and a thermometer in a side neck of the flask. Turn on the cold water. Seal the other side neck with a sleeve stopper.

3. Turn on the oil bath and set the temperature as 80 °C.

4. Weigh 0.28 g of ADIB, 34.3 g of MMA, and 0.7 g of MA. After mixing them in a beaker, add 0.175 g of 1-octanethiol into the beaker.

5. After 30 min of heating at 80 °C, add the above mixture into the flask via a syringe. Let the reaction proceed for 2 h.

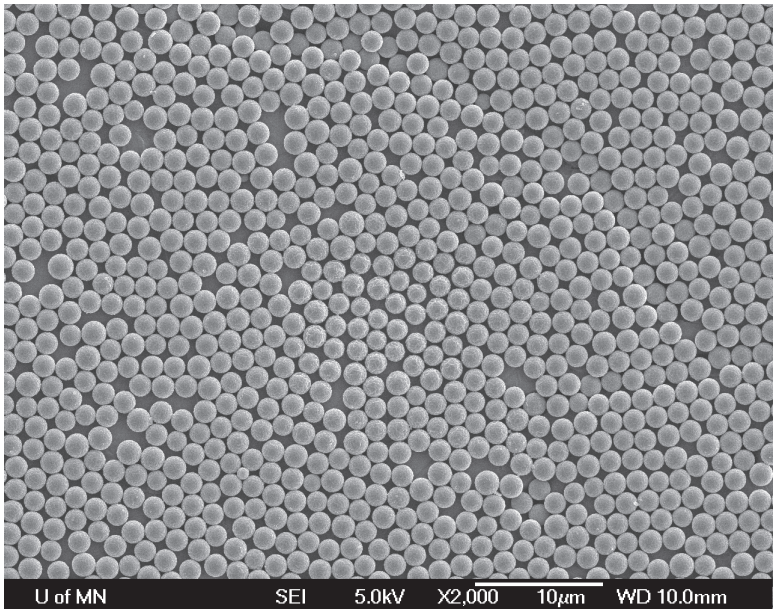

Figure A.3: SEM image of a typical batch of PMMA spheres.

6. Add a Dean-Stark apparatus between the condenser and the flask.

7. Add 22.0 g of dodecane and 0.15 g of 2-dimethylethanolamine to the flask.

8. Increase the temperature of the oil bath to 140 °C.

9. Distill hexane by the Dean-Stark apparatus until the temperature inside reaches 118 °C. Then remove the Dean-Stark apparatus.

10. Maintain the temperature in the flask at 120 °C and leave the reaction for 12 h.

11. Turn off the oil bath and let the flask cool down.

12. Transfer the mixture into a glass bottle, label it then store it in a refrigerator.

A.1.5 Particle Characterization

Fig. A.3 shows a SEM image of PMMA spheres prepared following above procedures. The size of particles is roughly same as the target size of 1.8 µm, showing the synthesis is well-controlled as designed. Products need to be washed by decalin or hexane for at least 7 times and dispersed into a desired solvent before used for any experiments. To be imaged by a confocal microscope PMMA particles need to be fluorescent labelled, which will be discussed in Appendix B.

A.2 PNIPAM

poly(*N*-isopropylacrylamide) (PNIPAM) microgel particles are crosslinked latex particles, which are swollen by a good solvent such as water [236, 237]. One fascinating feature of PNIPAM particles is sizes of particles can be well-controlled by the temperature. PNIPAM particles can thermally de-swell when the solution temperature increases above the lower critical solution temperature (LCST) of 32 °C in water [237]. The size change can be 5 times or even larger. Due to this unique feature, PNIPAM particles have been widely used as model colloids to study particle dynamics induced by the in situ change of volume fractions [42, 238, 239, 240, 241, 242]. PNIPAM particles also show many promising applications such as separation media, drug delivery and sensor design [243, 244, 245].

We have done some explorations on particle dynamics using PNIPAM particles, which will not be discussed here. Nevertheless, procedures of the synthesis are provided here. The synthesis of PNIPAM particles is comparably easier than that of PMMA particles because the open structures of PNIPAM particles provide natural steric hairs on surfaces of particles. The synthesis has two stages: purification of raw materials and particle synthesis. The first stage is to remove impurities in NIPAM monomers and

second stage to synthesize PNIPAM particles in a one-batch reaction. An experimental setup for the particle synthesis is shown in Fig. A.4.

The procedures are modified based on published research articles [236, 238, 246, 247, 248, 249, 250, 251, 252, 253].

A.2.1 Chemicals and Equipment

Chemicals

N-isopropylacrylamide (NIPAM), hexane, toluene, deionized water (DI water), N,N'-methylenebisacrylamide (MBA), potassium persulfate (KPS), acrylic acid (AAc).

Equipment

Glass bottles with Teflon coated lids, 100 mL 3-neck round-bottom flask, 50 mL graduated cylinder, 500 mL Erlenmeyer flask, 100 mL beakers, reflux condenser, scale, pipette, gas washing bottle, sleeve stopper, glass stopper, 2-hole rubble stopper, rubble tubes, nitrogen cylinder and gas, ring stands and clamps, syringes and needles, magnet stir bar, oil bath, magnetic stirring hotplate, green clips, spatulas, thermometer.

A.2.2 Purification of Raw Chemicals

NIPAM Recrystallization

1. In a fume hood, dissolve a desired amount of NIPAM into a 1:1 mixture of toluene and hexane in a bottle.

2. Close the bottle and store it in a freezer for at least 24 h.

3. Remove the upper liquid and dispose it into a waste bottle. Use a centrifuge if needed.

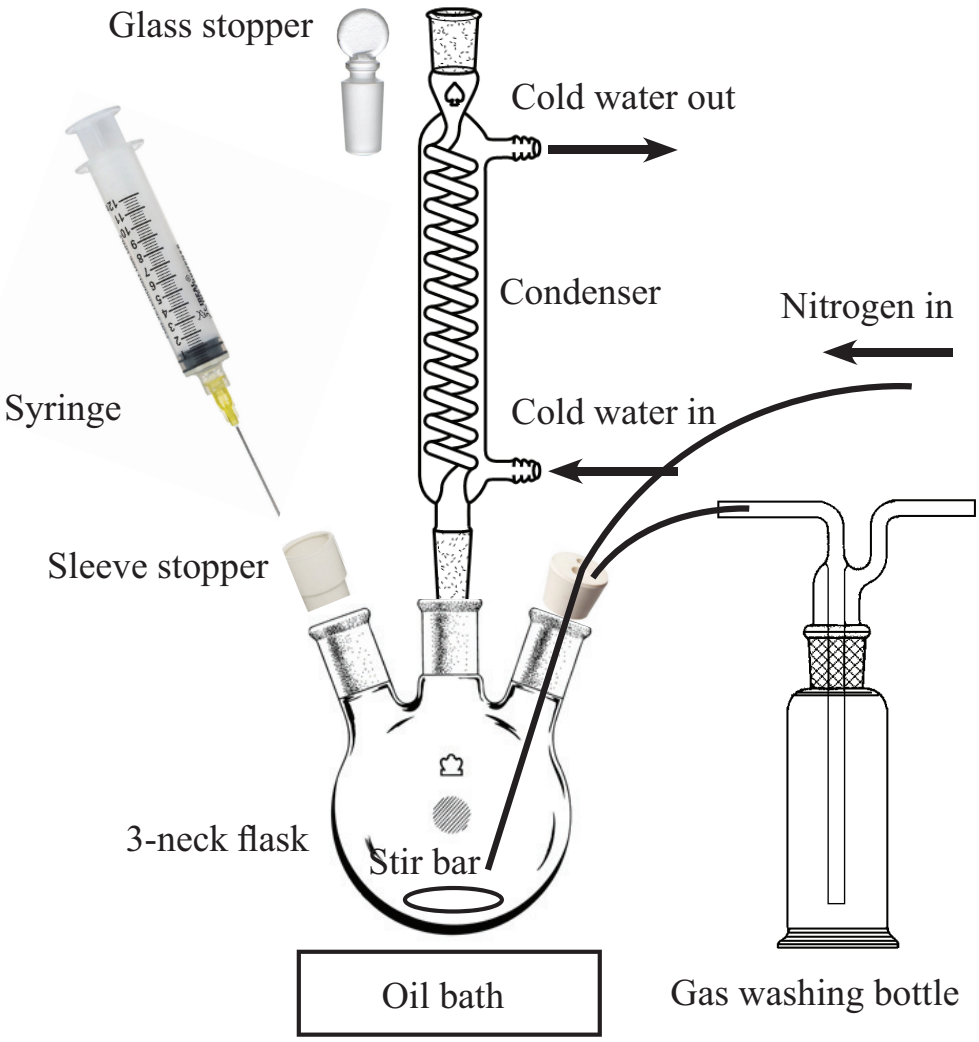

Figure A.4: Experimental setup for PNIPAM synthesis.

4. Leave the solid in the fume hood with cap open.

5. Store the dried crystals in a refrigerator for later use.

Water Degassing

1. Add 300 mL of DI water into a 500 mL Erlenmeyer flask.

2. Seal the flask with a 2-hole rubber stopper with 2 rubber tubes connected. One tube is connected to a nitrogen cylinder and the other one is linked to a gas washing bottle half-filled with silicon oil.

3. Turn on nitrogen gas and make sure the gas is flowing normally.

4. Place the flask onto a hotplate with the setting the temperature as 200 °C.

5. After the water boiling for 30 min, turn off the hotplate.

6. Keep the nitrogen gas flowing until the water is cooled down to room temperature.

7. Keep the degassed water for later use.

8. Degassing procedures should be done shortly before the particle synthesis.

A.2.3 Particle Synthesis

1. Turn on the oil bath and increase the temperature to 70 °C.

2. Weigh 50 g of degassed DI water, 2 g of NIPAM, 0.1 g of MBA, and 40 µL of AAc. Then transfer them into a 100 ml 3-neck round-bottom flask along with a magnetic stir bar.

3. Place the flask into the oil bath. Turn on the stirring system and set the stirring rate as 300 rps. Put a reflux condenser in the middle neck and put a sleeve stopper in one side neck of the flask. Open cold water.

4. Seal the other side neck of the flask with a 2-hole rubble stopper. Using rubber tubes to connect the flask to a gas washing bottle and a nitrogen cylinder.

5. Degas for 10 min then seal the condenser with a glass stopper. Then degas for another 30 min to fully remove air inside.

6. Weigh 0.02 g of KPS and dissolve it into 2 mL of degassed DI water.

7. Add the KPS solution into the flask via a syringe through the sleeve stopper to start the polymerization process. Mark the time and allow the reaction to proceed for 6 h.

8. The solution inside of the flask should turn cloudy within a few minutes after adding KPS. If not, degas longer and add another same amount KPS solution.

9. After 6 h, turn off the oil bath and let the product cool down.

10. Transfer the product into a glass bottle, label it and then store it in a refrigerator.

A.2.4 Particle Characterization

The product needs to be washed by DI water at least 7 times to fully remove impurities before used. Fig. A.5 shows a bright-field microscopic image of PNIPAM particles. The size of particles can be controlled by reaction temperatures (60 - 80 °C), crosslink densities and so on [236, 238, 246, 247, 248, 249, 250, 251, 252, 253]. The size of particles is typically in the range of 100 nm to 2 µm [237]. Even smaller sizes can be achieved by adding surfactants. Larger sizes can be prepared by adding sodium chloride to screen charges or using a monomer feeding procedure during the synthesis [252, 253]. As shown in Fig. A.5, the image contrast is low. Given PNIPAM particles typically contain about 80 wt% of water, the density and refractive index is very close to those of water [237]. Thus PNIPAM particles provide a very useful model system

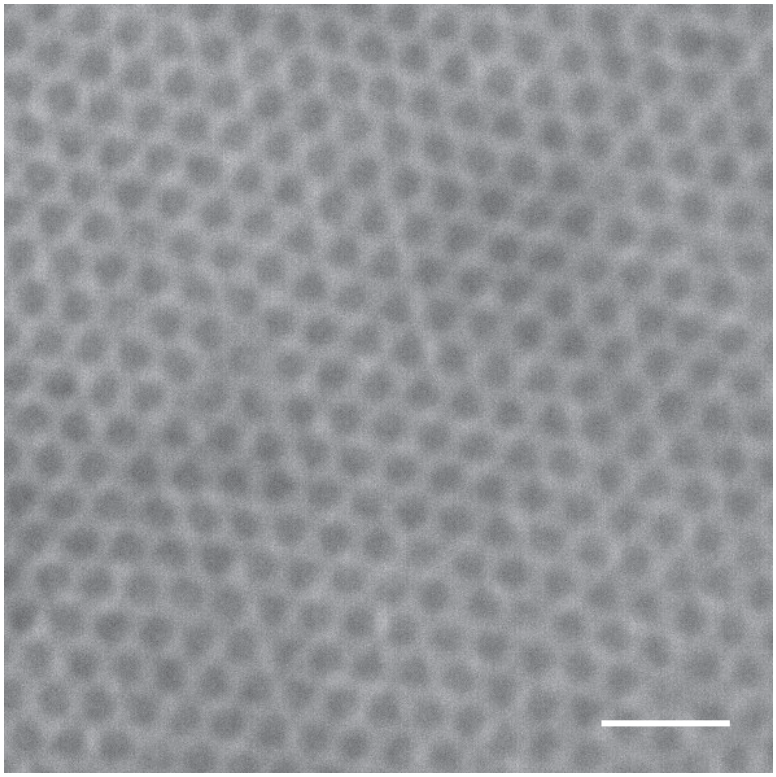

Figure A.5: Bright-field microscopic image of PNIPAM particles. The scale bar is 5 µm.

without any further density or index match for confocal studies of particle dynamics, on the premise of particles fluorescently labelled. Another similar microgel called poly(*N*-isopropylmethacrylamide) (PNIPMAM) shows a similar behavior as PNIPAM with a LCST about 44 °C [254]. Same synthesis procedures can also be applied to PNIPMAM synthesis. Fluorescent label of PNIPAM particles will be discussed in Appendix B.

A.3 Silica Spheres

Silica particles are another widely used model colloids [58, 179, 255]. Even though in this thesis we do not study silica particle dynamics, we do use them as spacers in the quasi-2D sample in Chap 4. They can be easily prepared by the widely used Söber process [255].

Here we summarize a simple synthesis method based the Söber process [189, 255, 256]. The Söber process is sol-gel approach to prepare spherical silica colloids. TEOS hydrolyzes in ethanol in the presence of ammonia as a catalyst. Due to a normal process is relatively sensitive to the liquid environment, here we provide a more robust synthesis method based the Söber process. We use commercial monodispersed silica particles as seeds and coat silica layer by layer on the seeds to prepared well-controlled larger silica particles. The size of particles can be accurately calculated and designed based on the mass ratio between seed silica particles and the source chemical–tetraethyl orthosilicate (TEOS).

A.3.1 Chemicals and Equipment

Chemicals

Tetraethyl orthosilicate (TEOS), ammonia hydroxide, ethanol, DI water, seed silica particles (d = 768 nm, 20 % solid).

Equipments

250 mL Erlenmeyer flask, 50 mL graduated cylinder, glass bottles, scale, centrifuge and centrifuge tubes, sleeve stopper, magnetic stirring hotplate, magnetic stir bar.

A.3.2 Particle Synthesis

1. Measure 5 mL of seed silica particles, 100 mL of ethanol, 10 g of ammonia hydroxide, and 10 g of DI water. Pour above chemicals into a 250 mL Erlenmeyer flask.

2. Add a magnetic stir bar into the flask and then place the flask onto a hotplate. Set the stirring rate as 300 rpm.

3. Add 1.6 g of TEOS into the flask.

4. Seal the flask with a sleeve stopper and leave the reaction untouched for 24 h.

5. Transfer the product into centrifuge tubes and wash it for several times.

6. Measure the size of silica particles.

7. If a larger size is needed, repeat above steps.

8. Transfer the final product into a glass bottle, label it and then store it in a refrigerator.

A.3.3 Particle Characterization

Fig. A.6 shows bright-field microscopic images of seed silica particles and five other coated silica particles. Particles are monodispersed without any further purification, demonstrating the synthesis is very robust. There is one thing needed to be aware. In order to grow monodispersed larger particles from the smaller seed particles, repeated

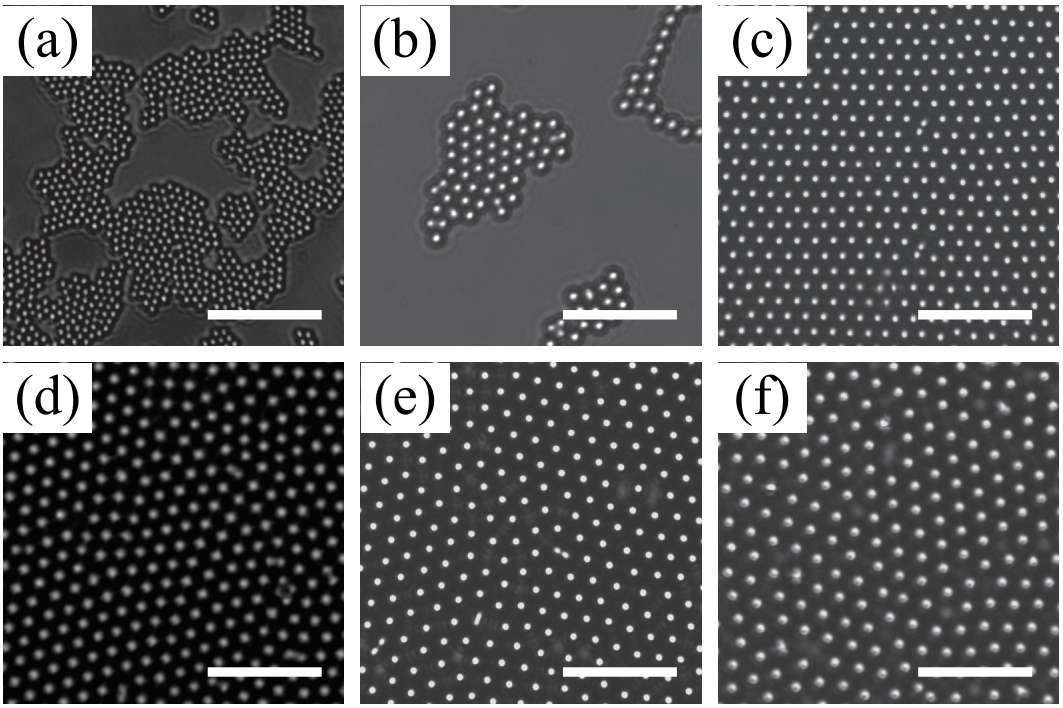

Figure A.6: Bright-field microscopic images of different sizes of silica particles. The sizes are 0.768 µm, 1.48 µm, 1.67 µm, 2.02 µm, 2.19 µm, and 2.37 µm. The scale bars are 10 µm.

steps may be needed to reduce the amount of TEOS added each time. If the amount of TEOS is added overwhelmingly, the hydrolysis of TEOS may not only happen on surfaces of seed particles but also in the solvent. This may cause the formation of binary particles or polydispersed particles.

A.4 Silica Rods

Asymmetric colloidal particles have been used widely due to their richness in shapes and interparticle interactions. In Chap. 4, we prepare PMMA and PS ellipsoidal or rodlike particles by a stretching process. Even though the particle size can be monodispersed if well-controlled, the yield of products is very low. Here use a simple wet-chemistry method to prepare monodispersed silica rods in a large quantity [207, 208, 257, 258]. There are two stages: particle growth in emulsions and particle second-growth by the Söber process. The first stage is to synthesize silica seed rods with certain tunability of aspect ratios. And the second stage is to coat silica seed rods to further tune sizes and aspect ratios of silica particles.

A.4.1 Chemicals and Equipment

Chemicals

Tetraethyl orthosilicate (TEOS), ethanol, DI water, ammonia hydroxide, polyvinylpyrrolidone (PVP, MW = 50,000), sodium citrate, 1-pentanol.

Equipments

250 mL Erlenmeyer flask, 50 mL graduated cylinder, glass bottles, scale, ultrasonic bath, centrifuge and centrifuge tubes, sleeve stoppers, magnetic stirring hotplate, magnetic stir bar, ring stands and clamps.

A.4.2 Particle Synthesis

1. Weigh 5 g of PVP and measure 50 mL of 1-pentanol. Transfer them into a 250 mL Erlenmeyer flask.

2. Seal the flask with a sleeve stopper and then sonicate them for 2 h to fully dissolve PVP.

3. Add 5 mL of ethanol, 1.4 mL of DI water, and 0.5 mL of 0.18 M sodium citrate into the flask. Shake the flask gently by hand.

4. Add 0.6 g of ammonia hydroxide into the flask. Then shake the flask gently by hand.

5. Add 0.5 mL of TEOS dropwisely into the flask. Shake the flask gently by hand then leave the reaction untouched for 24 h.

6. Transfer the product into centrifuge tubes and wash it for several times. By controlling the centrifuge speed and time, remove very small or very large particles and keep particles with the medium size.

7. Measure the size of silica particles.

8. Repeat the procedure in Appendix A.3.2 and Step 6 to coat one or more layers onto the seed rods.

9. Transfer the final product into a glass bottle, label it and then store it in a refrigerator.

A.4.3 Particle Characterization

Fig. A.7 shows a right-field microscopic image of seed silica rods synthesized above. Silica rods grow at the interfaces of emulsions of water droplets in 1-pentanol stabilized

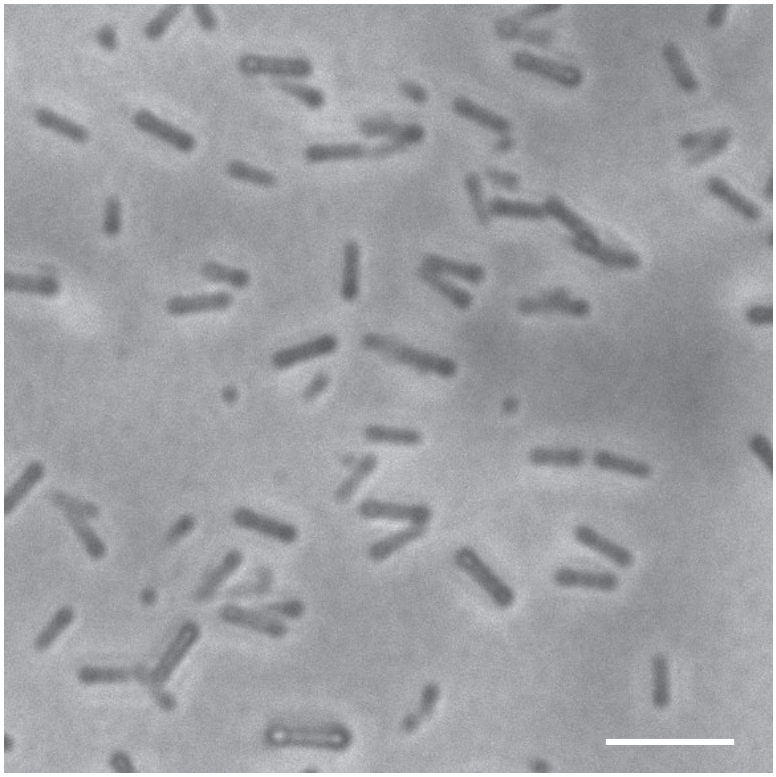

Figure A.7: Bright-field microscopic image of seed silica rods. Very small or large particles have not been removed.

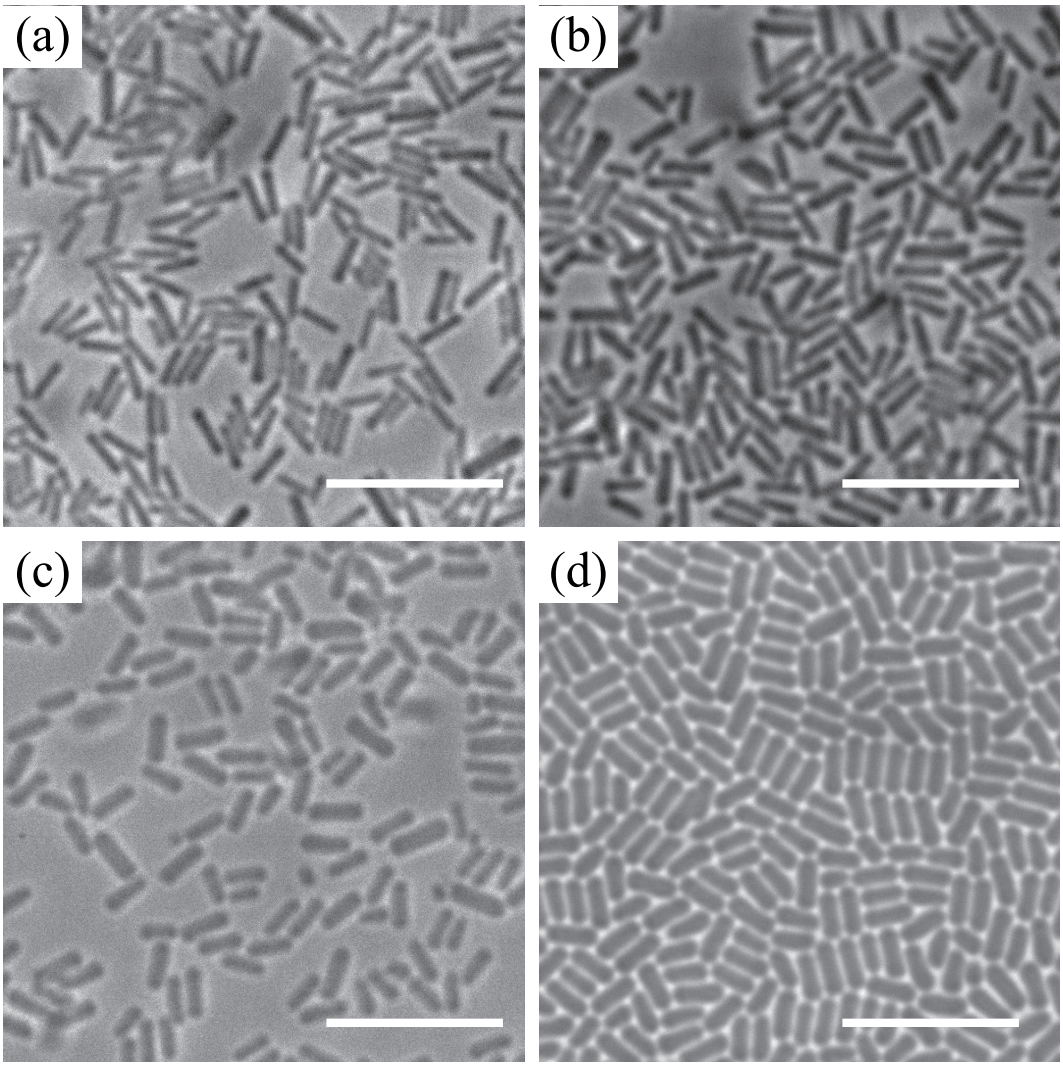

Figure A.8: Bright-field microscopic image of coated silica rods. The seed silica rods are coated once (a), twice (b), three times (c), and four times (d).

by sodium citrate and PVP [257, 258]. Particle sizes are controlled by emulsion sizes and reaction time. The size distribution of PVP polymers affects the size distribution of emulsion due to their micelle-like structure in emulsions. Thus, a batch of polydispersed particles is expected. The size distribution can be narrowed down by removing unwanted small and large particles. What's more, sizes and size distributions of silica rods can be further tuned by coating one or more layers of silica on the seed silica particles (Fig. A.8). Considering the less volume percentage of initial seed silica particles, polydispersities of particles can lower down with several layers of coatings. A polydispersity of 10 % or even lower is achievable.

Appendix B

Fluorescent Labelling

Preparation of particles with fluorescent labels is one of the keys to study particle dynamics by confocal microscopy. Except some special particles already with fluorescent labels such as fluorescent bacteria, most particles need to be fluorescently treated during or after particle synthesis. Depending on the interaction between fluorescent molecules and particles, the treatments can be either physical or chemical. The choice of a treatment method depends on many factors such as synthesis methods and properties of particles and their dispersed media. In this Appendix, we are going to address different methods of fluorescent labelling. Fig. B.1 shows molecular structures of several fluorescent dyes which are used in this Appendix.

B.1 Fluorescent Labelling during Particle Synthesis

B.1.1 Physical Treatment

Fluorescent molecules can be physically trapped inside of particles during a particle synthesis. In a dispersion polymerization or emulsion polymerization, if fluorescent

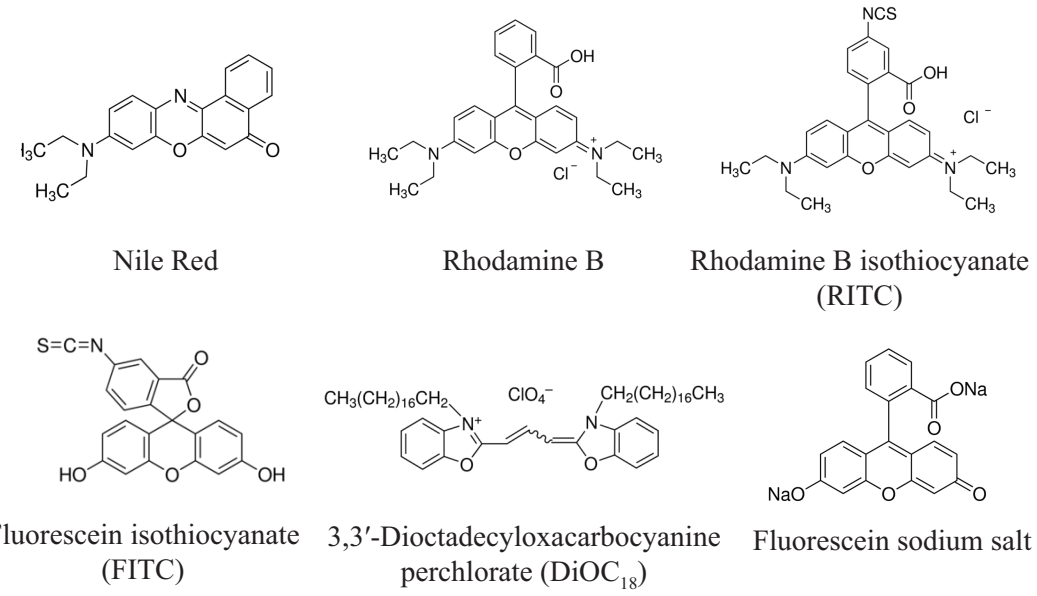

Figure B.1: Molecular structures of several commonly used fluorescent dyes. Structures are adopted from Sigma-Aldrich (www.sigmaaldrich.com). In our experiments, Nile Red, Rhodamine B, RITC are used with laser with a wavelength of 532 nm. Nile Red, FITC, $DiOC_{18}$, and fluorescein sodium salt are used with laser with a wavelength of 488 nm.

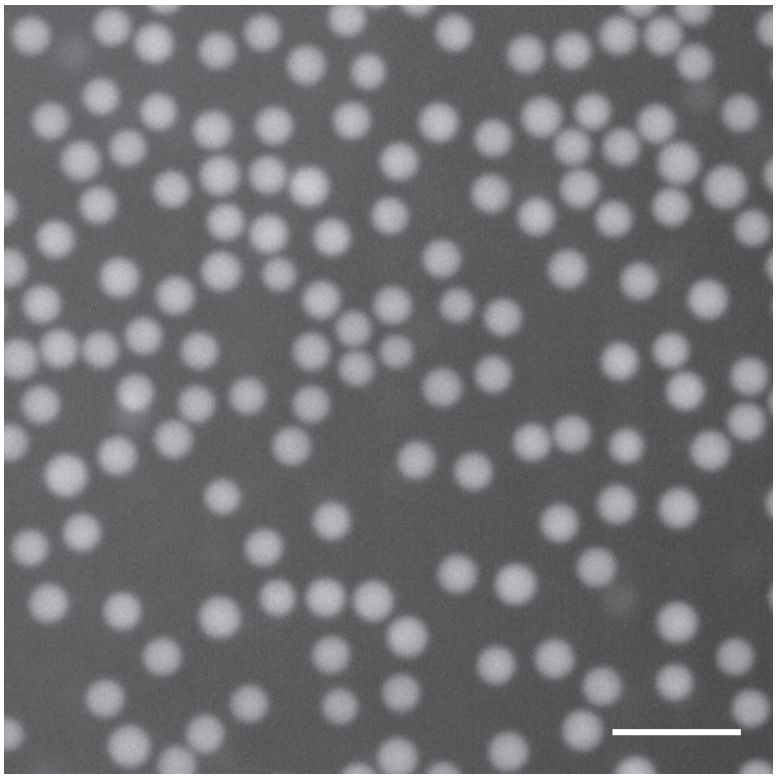

Figure B.2: Confocal microscopic image of Nile Red labelled PMMA spheres. Nile Red molecules are dissolved inside PMMA spheres after the particle synthesis stage. The scale bar is 5 µm.

molecules favor monomer or polymer phases instead of the dispersed media, they eventually distribute inside particles during particle growth. For example, during the synthesis of PHSA stabilized PMMA particles (Appendix A.1), fluorescent molecules such as Nile Red can be added as shown in Fig. B.2. There is no chemical reaction between Nile Red and MMA. Nile Red stays inside PMMA because Nile Red can dissolve better in PMMA phase. More discussions about fluorescent molecules being physically trapped inside of PMMA particles will be discussed in next section (Appendix. B.2.1).

B.1.2 Chemical Treatment

For many polymeric (such as PMMA, PS or PNIPAM particles) or silicon-based (such as silica) particles, fluorescent molecules can also be chemically bonded into particles via a polymerization or hydrolysis process. For example during a synthesis of PMMA particles, Rhodamine B isothiocyanate (RITC, fluorescent molecules) can be first linked to small molecules with carbon-carbon double bonds such as 4-aminostyrene to form fluorescent labelled monomer RITC-amonostyrene (RAS) [234]. Then RAS molecules copolymerize together with MMA monomers using the same procedures provided in Appendix A.1 to form RITC-labelled PMMA spheres. A similar approach can also be applied to fluorescent label of silica particles. RITC molecules first react with (3-aminopropyl)triethoxysilane (APS) to form fluorescent labelled RITC-APS monomers [259]. Then RITC-APS and TEOS hydrolyze together to form FITC labelled silica particles.

B.2 Fluorescent Label after Particle Synthesis

Fluorescent labelling of particles during particle synthesis is widely used for particle imaging. However, there are some limitations. Firstly, a pre-step of synthesis of fluorescent labeled monomer is usually needed [234, 259]. Fluorescent molecules need to be dissolved into reaction mixtures to provide uniform fluorescent labels of particles. What's more, it requires functional groups on the fluorescent molecules that can be chemically bonded with some monomers. Both requirements limit the choice of fluorescent dyes. Secondly, a chemical reaction requires certain reaction conditions such as temperature, PH, catalysts, and water/waterless environment [234]. Fluorescent molecules may have side reactions and not be stable at such conditions. Take the synthesis of PMMA spheres for example. The reaction needs catalyst ADIB and a temperature around 70

°C [235]. However not all dyes can survive at this condition. We show that Nile Red works well. But we also try another dye called 3,3'-dioctadecyloxacarbocyanine perchlorate ($DiOC_{18}$). $DiOC_{18}$ degrades during the particle synthesis stage and there is few functional $DiOC_{18}$ molecules left in PMMA particles or solvent. Thirdly, the present of fluorescent molecules may worsen the polydispersity of particles. Fluorescent molecules may serve as heterogeneous sites for particle growth. Once a reaction is not longer homogeneous, a batch of monodispersed particles is unlikely to be obtained.

There are also many other limitations where you want to fluorescently label some commercial undyed particles or where you want to fluorescently label one batch of particles with different dyes separately. Thus, fluorescent treatment methods for undyed particles after particle synthesis are also highly needed. Here, we discuss briefly about several popular methods and focus on two of them we explored in detail.

B.2.1 Physical Treatment

One of the simplest ways to fluorescently label particle physically is via electrostatic attractions between oppositely charged particles and fluorescent molecules. Take silica particles for example. Silica particles are slightly negatively charged in water. If positive charged fluorescent molecules such as RITC (Fig. B.1) are dissolved in water, RITC molecules can attach onto surfaces of silica particles due to electrostatic attractions. Under a confocal microscope, fluorescent rings outside of particles can be observed. Fluorescent dyes could also be negatively charged such as fluorescein sodium salt (Fig. B.1). In this case, fluorescent molecules stay in the water phase. A bright fluorescent background and blank circles (undyed particles) can be observed under a confocal microscope. For both cases, particle positions can be obtained after a normal imaging data analysis [115, 116].

One drawback of such methods is that image qualities are not as good as those

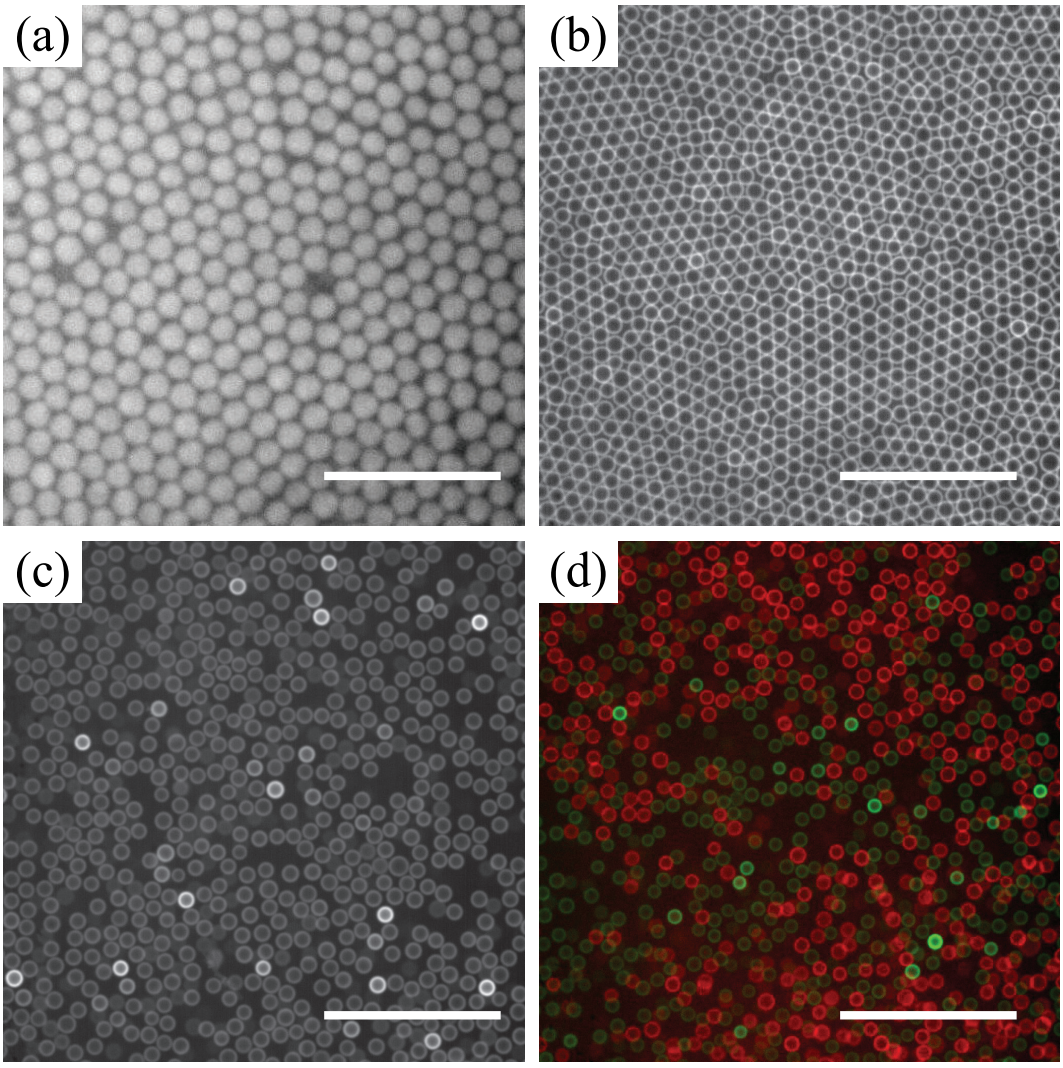

Figure B.3: Confocal microscopic images of PMMA spheres fluorescently labelled after the particle synthesis stage. (a) PMMA spheres are fully labelled by Nile Red. PMMA spheres are partially labelled by Nile Red (b), $DiOC_{18}$ (c), and both Nile Red (red) and $DiOC_{18}$ (green) (d). Red and green colors are artificial. Scale bars are 10 µm.

of particles with uniform fluorescent dyes. Thus, dissolving fluorescent molecules into particles is also worthy to study. Many polymeric particles can swell in a good solvent. If designed properly, fluorescent molecules can diffuse into swollen polymeric particles and stay inside even after the good solvent is changed to a poor solvent.

Here, we use this method to fluorescently label undyed PMMA particles. Undyed PMMA particles synthesized following the procedures described in Appendix A.1 are suspended in a over-saturated Nile Red/decalin solution. The suspension is heated at 90 °C for 3 h. The suspension is then washed by decalin for several times to remove extra Nile Red in the solvent. Fig. B.3a shows a confocal microscopic image of Nile Red labelled PMMA particles prepared by this method. PMMA particles are well-labeled. If the heating time is shorter, fluorescent molecules may only have time to diffuse into shells rather than cores of particles. Fig. B.3b shows Nile Red labelled PMMA particles with the heating time as 20 min. Bright ring structures indicates a density gradient inside of particles.

By this method, different fluorescent dyes such as $DiOC_{18}$ can also be used. Fig. B.3c shows PMMA particles labelled by $DiOC_{18}$. $DiOC_{18}$ is not stable at high temperature over a long time. It degrades when added into the reaction during the particle synthesis stage of PMMA since the reaction time is more than 14 h. Clearly, this labelling method can be applied to more fluorescent dyes than labelling during particle synthesis. This method also makes it possible that labelling same batch of particles with different dyes. Fig. B.3d shows a PMMA suspensions with two different dyes.

The idea of labelling polymeric particles by swelling them in a good solvent can also be used inversely to prepare PMMA particles with only cores labelled by dyes. Once the volume fraction of a PMMA suspension is high, particle-particle distance may be quite small and close to the length of PHSA hairs. It may cause trouble to distinguish particles in bulk samples. Thus preparation of particles with only cores labelled by dyed

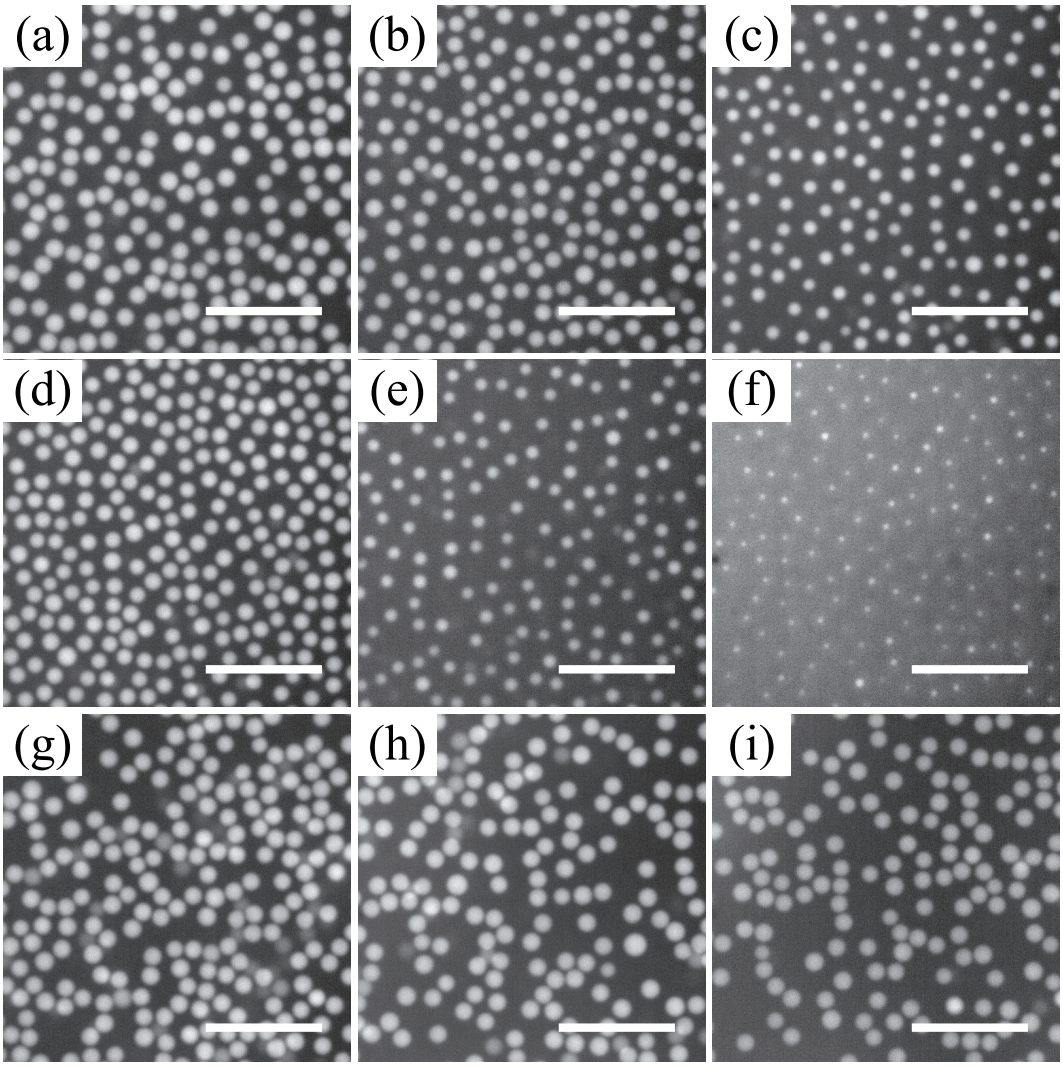

Figure B.4: Dye distributions after extractions of Nile Red from PMMA spheres at different temperatures and in different solvents. CXB/Decalin mixtures are used for (a-f) and pure decalin solvents are used for (g-i). Nile Red labeled PMMA suspensions are sealed into glass sample cells and then placed onto a hotplace for 10 s (a-c) or 20 s (d-i) at 90 °C (a, d, and g), 100 °C (b, e, and h), or 110 °C (c, f, and i). Scale bars are 10 µm.

is highly useful to study particle dynamics at high volume fractions. Some particles with fluorescent core-shell structures have been synthesized [45, 260, 261]. The process usually needs to synthesize fluoresecently labelled cores first then coat blank shells onto cores.

Here, we propose a simple method to prepare such particles. Nile Red labelled PMMA particles are suspended in a CXB (85 wt%) and decalin (15 wt%) mixture. The suspension is sealed in glass sample cells (Fig. 3.3) and then placed on a hotplate for 10 s. Fig. B.4a-c show fluorescent dye distributions after the extraction procedure at different temperatures. At $T = 90\ ^{\circ}\mathrm{C}$, particles contact with their neighbor particles and fluorescently labelled areas are roughly same as untreated particles (Fig. B.4a). When the temperature increase to 100 °C, particles stop contact with their neighbor particles, showing the extraction of dye molecules from outer layers (Fig. B.4b). This extraction is more obvious when $T = 110\ ^{\circ}\mathrm{C}$ (Fig. B.4c). Same procedures are conducted on samples heated for 20 s (Fig. B.4d-f), which show stronger extractions.

The experiments show that the higher temperature or longer time of heating, the stronger the extractions are. Even though we do not have quantitatively measurements on dye concentration distribution, it is easy to expect that there is a concentration gradient of Nile Red along the particle radius. Upon heating at higher temperature, Nile Red molecules start to diffuse outside of PMMA particles due to PMMA swelling inward in the low-polar solvent–CXB. Nile Red molecules near interfaces diffuse out sooner than inner molecules. By controlling the heating temperature and time, we can easily prepared particles with non-uniform distributions of dye molecules. The concentration of Nile Red molecules decreases from centers to interfaces of particles. With a proper threshold or contrast of images, only bright cores can be observed under a confocal microscope (Fig. B.4a-f).

We also study the effect of the polarizability of solvents. We replace the solvent from

CXB/decalin mixtures to pure decalin. Note that CXB is a low polar solvent and decalin is a non-polar solvent. Low-polar PMMA can swell in CXB but not in decalin. With same heating conditions, PMMA particles suspended in pure decalin show no change of the distribution of Nile Red (Fig. B.4g-i). Bright parts of particles still contact with their neighbor particles. These results indicate that a low-polar solvent such as CXB is needed to exact dye molecules from PMMA particles and prepare PMMA particles with only cores labelled.

To further confirm the fluorescent core-shell structures of PMMA particles. We compare the confocal microscopic image and bright-field microscopic image of same particles (Fig. B.5). On the confocal microscopic image, particles stay apart from their neighbor particles. While on the bright-field microscopic image, particles clearly contact with their neighbor particles. The difference between two images confirms the fluorescent core-shell structures of PMMA particles. The stability of such structures are also compared. Two confocal images at 0 and 13 h after extractions show core-shell structures with similar particle-particle distances. Nile Red molecules won't diffuse away and are locked inside of PMMA particles once the suspension is cooled down. If Nile Red labelled PMMA particles are suspended in a non-polar solvent such as decalin or hexane, we find that the supernatant liquid of suspensions stays clear even after several years. Whereas the supernatant liquid turns colored after several months, if PMMA particles are suspended in a low-polar solvent such as CXB. Thus, such fluorescent core-shell particles should be suspended in a non-polar solvent for storage.

This extraction of fluorescent molecules from swollen polymeric particles is a simple and controllable way to prepare fluorescent core-shell particles. And it could be very useful for studies of particle dynamics at high volume fractions.

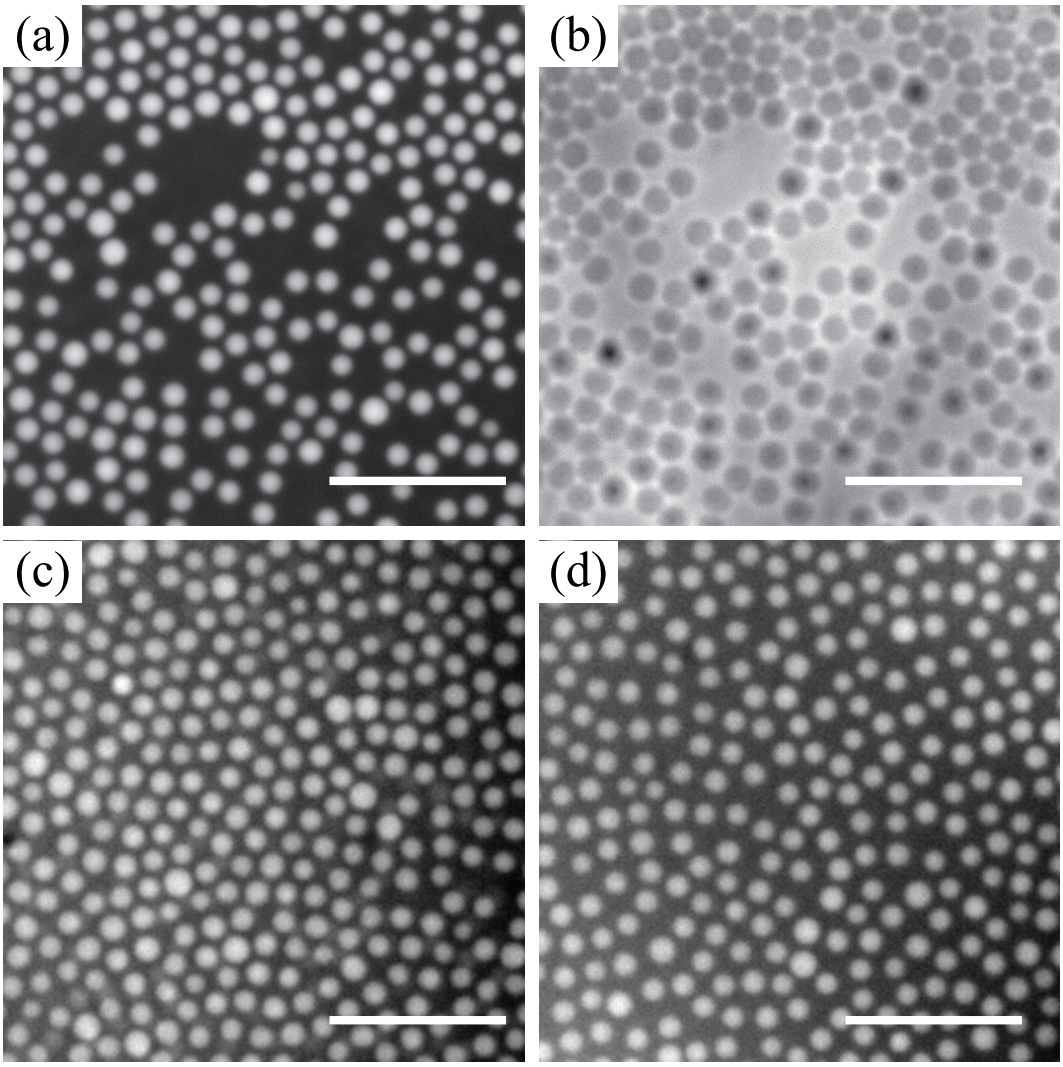

Figure B.5: Microscopic images of PMMA spheres with Nile Red partially extracted. PMMA spheres stored in glass bottles are heated at 100 °C for 3 min. The solvent is CXB/decalin mixture. (a) A confocal microscopic image of PMMA spheres with Nile Red partially extracted. Different sizes of PMMA may caused by an uneven distribution of temperature in glass bottles. (b) A bright-field microscopic image of same PMMA spheres. Confocal images of PMMA spheres with Nile Red partially extracted. Images are taken at 0 (c) and 13 h (d) after extractions. Scale bars are 10 µm.

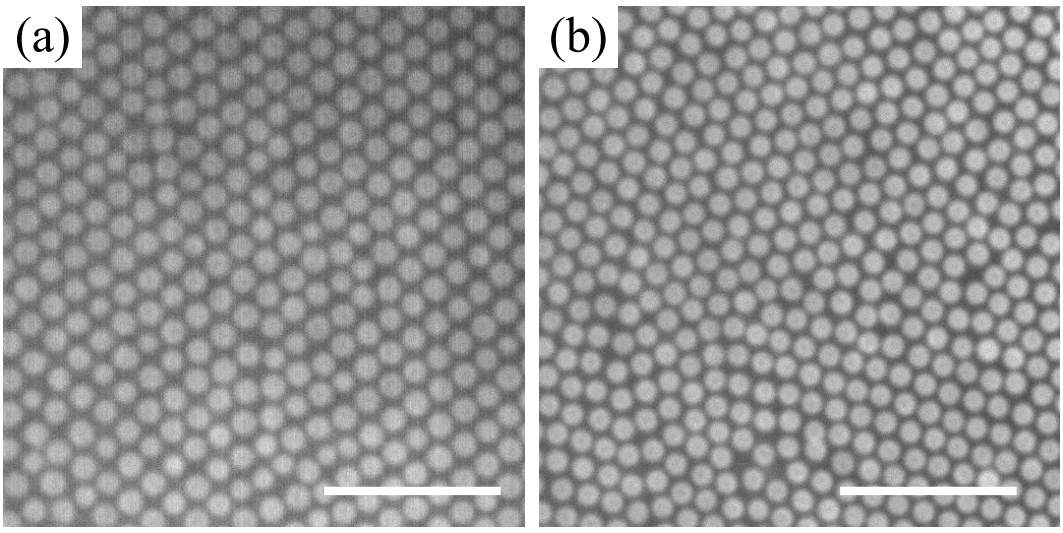

Figure B.6: Confocal microscopic images of PNIPAM particles dyed by Rhodamine B (a) and RITC (b). Scale bars are 10 µm.

B.2.2 Chemical Treatment

Besides physically fluorescent treatments of particle after particle synthesis, chemical treatments provide some other options. Surface modifications are usually needed to introduce some functional groups which can link with fluorescent molecules. For some polymeric particles which can swell in solvents such as PNIPAM, such chemical treatments can even prepare particles with an uniform distribution of dye molecules [239, 262, 263, 264, 265, 266, 267].

PNIPAM particles are very interesting due to their special temperature-control-size features [236, 237]. Water is a good solvent for PNIPAM at room temperature. Cross-linked PNIPAM microgels are swollen particles and typically contains about 80 wt% of water [237]. PNIPAM particles can be fluorescently labelled via physical treatments just like silica particles and PMMA particles in Appendix B.2.1. PNIPAM particles dyed by Rhodamine B is shown in Fig. B.6a. One drawback of this method is that

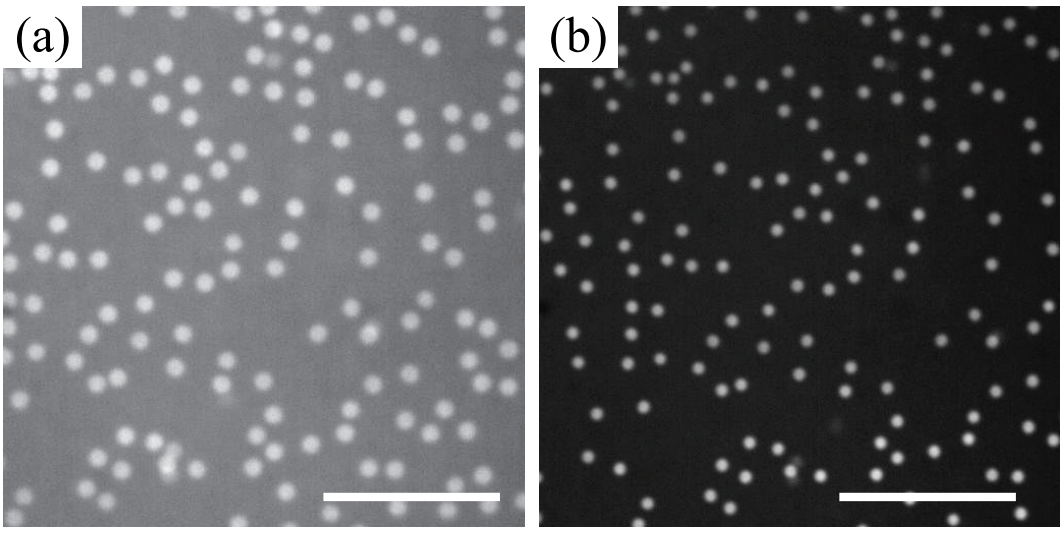

Figure B.7: Confocal microscopic images of PNIPAM particles at temperature of 20 °C (a) and 50 °C (b). Scale bars are 10 µm.

some Rhodamine B molecules are still dissolved in water, which may lower down images contrasts. Furthermore, particles can only be labelled by a single dye at once.

Here we use chemical treatments to prepare fluorescent PNIPAM particles. 2-Aminoethyl methacrylate hydrochloride (AEMA) is added during PNIPAM synthesis, adding amine groups to particles. Then RITC is mixed with PNIPAM suspensions for 12 h. The isothiocyanate groups from RITC chemically react with amine groups and form RITC labelled PNIPAM particles. Excess RITC can be removed by washing the mixture several times. Fig. B.6b shows a confocal microscopic image of RITC labelled PNIPAM particles. The image is more clear than Fig. B.6a, showing the advantage of chemical treatments over physical treatments for PNIPAM particles. PNIPAM particles can also be labelled by other fluorescent dyes using similar procedures [239, 266].

With PNIPAM particles uniformly labelled by fluorescent dyes, the size charge of

particles under different temperatures can be directly observed under a confocal microscope. Fig. B.7 shows PNIPAM particle at $T = 20$ °C and 50 °C. Note that PNIPAM particles have a LCST of 32 °C in water. Below the LCST such as at room temperature, PNIPAM particles swell in water and have large sizes. When the temperature increases above the LCST, PNIPAM particles collapse due to formation of hydrogen bonds between polymer chains [268, 269]. The sizes of particles decrease to about half of those sizes at room temperature. Such properties make PNIPAM particles very good models to study particle dynamics with volume fractions changed in situ [42, 238, 239, 240, 241, 242].

In sum, several fluorescent treatments have been discussed. Same particles may be dyed by different methods. To choose a proper fluorescent labelling method, many conditions such as particle synthesis methods and properties of particles and their dispersed media should be considered.